Carnegie Mellon University

CARNEGIE INSTITUTE OF TECHNOLOGY

THESIS

SUBMITTED IN PARTIAL FULFILLMENT OF THE REQUIREMENTS

FOR THE DEGREE OF Doctor of Philosophy

TITLE An Equation-based Framework for Large-scale Flowsheet Optimization and Applications for Oxycombustion Power System Design

PRESENTED BY Alexander Dowling

ACCEPTED BY THE DEPARTMENT OF

Chemical Engineering

Lorenz Biegler	5/4/15
ADVISOR AND DEPARTMENT HEAD	DATE

APPROVED BY THE COLLEGE COUNCIL

Vijayakumar Bhagavatula	5/4/15
DEAN	DATE

An Equation-based Framework for Large-Scale Flowsheet Optimization and Applications for Oxycombustion Power System Design

Submitted in partial fulfillment of the requirements for
the degree of
Doctor of Philosophy
in
Chemical Engineering

Alexander W. Dowling

B.S.E., Chemical Engineering, University of Michigan

Carnegie Mellon University
Pittsburgh, PA 15213

May, 2015

Acknowledgments

It has been a great honor to work with my advisor, Prof. Larry Biegler, for the past five years. I am greatly appreciative of his guidance, support, encouragement and sense of humor. He has instilled in me an appreciation for precise, thorough and meaningful research. I am continuously amazed both of his technical knowledge and excitement for the profession. I would also like to thank the members of my thesis committee, Prof. Igancio Grossmann, Prof. Nikolaos Sahinidis, Prof. Jeremy Michalek and Dr. David Miller, for their insights, advice and time.

A significant portion of the work encompassed in this thesis was a collaborative effort with several visiting researchers, Masters students and colleagues at the US Department of Energy. I would like to thank and acknowledge the following contributors: Yannic Vaupel (RWTH Aachen) for his contributions to the early ASU models (Chapter 4), Dominik Meinel (TU Müchen) for his work with Gibbs free-energy minimization based boiler models (Chapter 5), Qianwen Gao (MS student, Carnegie Mellon) for her work with the CPU model and conversations regarding the supercritical thermodynamics model (Chapters 2 and 3), Zixiang Gao (MS student, Carnegie Mellon) for his review of scrubber and pollution control technologies, Cheshta Balwani (MS student, Carnegie Mellon) for her refinement of the CPU model and investigation of cubic EoS model behavior (Chapters 2 and 3), and Dr. Michal Touš (Brno University of Technology) for discussion regarding the steam cycle models (Chapter 5). I would also like to thank John Eason (PhD student, Carnegie Mellon), who developed and implemented the trust region algorithm discussed in Chapter 5, and Dr. Jinliang Ma (URS/NETL), who created the hybrid boiler model used in Chapter 5. Although not included in this thesis, I also had the pleasure to work with Yajun Wang (MS student, Carnegie Mellon) and Dr. Sreeram Vetukuri (Carnegie Mellon) on a pressure swing adsorption optimization project. Our findings are reported in Dowling, Vetukuri, and Biegler (2012) and Wang et al. (2015).

There are two research communities I would like to acknowledge. First, I would like to thank the National Energy Technology Laboratory (NETL) for providing financial support for this research, and thank Dr. David Miller for assembling and managing the Carbon Capture Simulation Initiative (CCSI) project. I has been a pleasure to work with the entire interdisciplinary CCSI project team spread across the national laboratory system, academia and industry. I would also like to thank all of the professors, visitors, researchers and students in the Center for Advanced Process Decisions-making at Carnegie Mellon for create such a vibrant atmosphere to learn and conduct research. I really appreciate the time I've spent as a member of these communities.

I would also like to thank another community: my parents, my brother and sister, and my extended family. Most of all, I would like to thank my wife, Denise, for her friendship, support and encouragement throughout my graduate studies.

Finally, in recognition of funding through the National Energy Technology Laboratory (URS-RUA) and Lawrence Berkeley National Laboratory, I conclude these acknowledgement with a disclaimer:

Abstract

Over the past thirty years, flowsheet optimization methods have evolved from "black box" approaches to sophisticated equation-oriented methods for simultaneous flowsheet convergence and optimization. This thesis explores the next generation of flowsheet optimization tools that leverage completely open models (with exact first and second derivatives) and utilizes start-of-the-art nonlinear programming (optimization) solvers. A five part framework is proposed in this thesis:

1. Embedded cubic equation of state thermodynamic models with complementarity constraints to accommodate vanishing and reappearing phases
2. Simultaneous heat integration and process optimization using the pinch location method
3. Aggregate short-cut and rigorous tray-by-tray distillation models
4. Steam cycle equipment (e.g., turbine) and boiler models
5. Trust region optimization algorithm to incorporate models with expensive derivatives into the equations-based framework

A systematic initialization routine based on model refinement and multistart procedure are also presented as practical alternatives to global optimization. Complementarity constraints are used throughout the framework to model switches, such as vanishing phases. *Degeneracy Hunter*, an algorithm that identifies irreducible sets of degenerate constraints (i.e., constraints with a rank deficient Jacobian) is proposed and used to refine the models.

The framework is demonstrated in a series of case studies related to the design of oxycombustion power systems with CO_2 capture. Two case studies focus on the simultaneous optimization of gases separation systems and their accompanying multistream heat exchangers. In one of these case studies, the optimization procedure identifies common air separation unit configurations with comparable specific energy requirements to industrial designs. The framework is also used to optimize regenerate Rankine cycles, where steam flowrates from nine extraction points for boiler feedwater heating are considered as optimization variables. This allows for waste heat from compression to the completely integrated into the steam cycle. Steam table lookups (without derivatives) are incorporated using reduced models and a trust region optimization algorithm.

Table of Contents

List of Tables

List of Figures

Chapter 1

Introduction

Systematic methods for flowsheet optimization and synthesis are essential components of every process engineers' toolbox. They allow for automated (and intelligent) exploration nearly uncountable process configurations, which facilitates selection of the best designs, and ultimately reduces costs, increases efficiency and improves plant operability. Similarly, PSE (makers of gPROMs) promote three benefits of mathematical process modeling and optimization: "better decisions, faster decisions and safer decisions"[1]. Applied to tomorrow's power systems, large-scale optimization will help reduce the capital and operational costs of carbon capture, utilization and sequestration. Furthermore, optimization provides a framework to systematically screen promising technologies, ranging from single systems, such as membranes for CO_2 separation, to entire new flowsheets, such as coal oxycombustion. This offers qualitative insight regarding the potential value of new technologies throughout the development cycle.

Chemical process simulators and optimization tools have evolved over several (software) generations and the past forty years, with each generation embracing different mathematical formulations. Early process simulators were built around the *sequential modular* (SM) concept, where each unit (module) is simulated individually in the sequential order in the flowsheet. Converging a flowsheet with recycle loops is cast as a fixed point problem, and solved with repetitive iterations (direct substitution) or acceleration techniques. Each unit operation is treated as a input-output "black box", which allows for custom heuristics to accelerate individual unit model convergence to be embedded in each module. Furthermore, the SM modular strategy allowed for early codes focused on individual unit operations to be easily spliced together. In contrast, a flowsheet is treated as a large coupled system of nonlinear equations in the *equation oriented* (EO) approach, and solved using the Newton method. The EO approach typically experiences faster convergence for complex flowsheets that the SM approach, as consequence of quadratic local convergence for Newton methods and the mathematical structure of the flowsheet problem. For

[1] http://www.psenterprise.com/concepts/apm.html

example, EO methods can exploit either sparse or parallelized linear algebra routines to decrease computational times. Finally, EO methods have several benefits regarding optimization, as discussed below.

Early flowsheet optimization techniques coupled derivative free algorithms with sequential modular simulators, which produced less than satisfactory results. Derivative free optimization algorithms require a large number of function evaluations and SM methods require many iterations to converge a flowsheet, which together create large computational demands. Furthermore, this approach needs to accommodate convergence failures of the SM simulator. In the 1980s, Sequential Quadratic Programming (SQP) emerged as an alternate to "black box" optimization with SM simulators, due to two main benefits. First, SQP algorithms use derivative information to accelerate convergence. Second, with SQP methods flowsheet recycle streams can be "torn", i.e., converted to equality constraints, which allows for simultaneous flowsheet convergence and optimization. Much literature from this era is devoted to comparing different strategies for accommodating recycle streams (Lang and Biegler, 1987). First derivative information from sequential modular simulations are typically generated using finite difference perturbations and are noisy (due to rounding errors). The second derivatives (Hessian matrix) are approximated using the BFGS update, which slows the local convergence of the SQP algorithm to a superlinear rate. Furthermore, noisy first derivatives can impair identification of a stationary point that satisfies the Karush-Kuhn-Tucker optimality conditions. Nevertheless, the use of sequential modular simulators coupled with SQP methods for optimization is still in widespread use today.

Equation oriented approaches for flowsheet optimization are a natural extension of the tear stream concept, as the optimizer is used to converge all equations in the flowsheet. In contrast, the optimizer is used to converge only the tear streams in SM strategies and the remaining equations are encapsulated in the individual unit modules. Thus, EO methods result in large-scale optimization problems with many more constraints (e.g., mass and energy balances, thermodynamic property evaluations, etc.). SQP methods used with SM models, however, use dense linear algebra to solve the QP subproblems and perform poorly with large-scale problems. This promoted the development and application of reduced space SQP methods to flowsheet problems, where optimization is done in the null space of the constraints. This results in much smaller QP subproblems, as the flowsheet optimization problems typically have only 50 to 100 degrees of freedom. Similarly, with SM strategies the user identifies the degrees of freedom for optimization, and the remaining variables are "hidden" outputs of the unit operation models. Overall, efficient simultaneous optimization and flowsheet convergence is the key advantage of EO methods, especially for large systems. However, SM methods are more intuitive, as the user specifies the degrees of freedom, easier to debug, and easier to initialize given the (fairly) robust tailored procedures in each unit operation module. Thus, SM approaches remain popular for generic applications, whereas EO methods are preferred by experienced practitioners for

large-scale problems. For additional details regarding the history of flowsheet optimization methods, see Biegler, Grossmann, and Westerberg (1997).

Recently, Pattison and Baldea (2014) proposed a radically different approach to flowsheet optimization that uses pseudo-transient models. In order to converge the flowsheet, the models are integrated to steady-state for each iteration. The algorithm is implemented in gPROMs, and derivatives are evaluated at the steady-state point. The authors claim the approach requires less precise initialization and has a larger basin of convergence than traditional Newton methods, although convergence properties of the proposed optimization algorithm are not rigorously analyzed. Furthermore, this method requires integration of the differential algebraic equation (DAE) system for each optimization iteration. It is uncertain if this is more computationally efficient than using state-of-the-art NLP solvers with algebraic equation-based flowsheet formulations (as proposed in this thesis).

In parallel to the development of SQP-based flowsheet optimization methods, a community of researchers has also studied the application of integer and disjunctive programming methods to process design problems (Grossmann and Santibanez, 1980; Grossmann, 1985; Grossmann and Daichendt, 1996; Caballero and Grossmann, 2001; Kallrath, 2000; Mussati et al., 2008). In general, these problems are formulated with simplified process models, which result in mixed integer linear or mixed integer nonlinear programs with "mild" nonlinear features, e.g., only bilinear terms, convex or monotonic nonlinear terms, programs with nonlinear objective functions and linear constraints, etc. (Yee and Grossmann, 1990; Lee and Grossmann, 2001, 2003). See Trespalacios and Grossmann (2014) for a current review of MINLP and disjunctive programming methods. Recently, application of global optimization to these types of problems has become popular, especially with energy systems (Baliban, Elia, and Floudas, 2013; Gong and You, 2014; Martín and Grossmann, 2015). The major concern, however, is that the simplified models miss many important (nonlinear) features of the actual physical systems. For example, the thermodynamic models used in most process simulators are highly nonlinear and nonconvex. Another recent trend is to sample rigorous process simulators and construct surrogate models (i.e., reduce order models, meta-models) that are more suitable for optimization. Caballero and Grossmann (2008) proposed a framework for this with Kriging surrogate models. Similarly, Hasan et al. (2012) use Kriging models to optimize a pressure swing adsorption process for CO_2 capture. Alternately, Cozad, Sahinidis, and Miller (2014) developed the Automated Learning of Algebraic Models for Optimization (ALAMO) tool, which constructs the optimal surrogate model from a collection of basis functions, as defined by an information criterion. There are several important challenges for optimization with surrogate models, including developing strategies to ensure convergence to an optima of the original (detailed model) system and management of the computational cost and number of evaluations of the rigorous model, especially when it is computationally expensive.

In contrast, leveraging state-of-the-art nonlinear programming techniques

offers a more direct way to handle highly nonlinear and nonconvex flowsheet design problems, although it requires new platforms that use "open" models with exact first and second derivatives. Similarly, there are many ways to further improve EO flowsheet methods, such as the development of robust initialization procedures, the refinement of optimization formulations to avoid some instances of integer variables and the application of decomposition methods for design under uncertainty. These advancements require development of environments for EO flowsheet optimization that extend beyond existing commercial tools, both in terms of model flexibility and the ability to interface with numerous optimization algorithms.

1.1 A New Framework for EO Flowsheet Optimization

In thesis, a next generation framework for equation-based flowsheet optimization is developed and demonstrated. Emphasis is placed on using completely equation-based models with accurate first and second derivatives obtained from automatic differentiation. These derivatives enable the use of the next generation of mathematical programming algorithms, such as interior point methods, that exploit sparsity and are capable of considered nonlinear systems with 100,000+ variables and equations (including inequality constraints). Overall, these methods should be more reliable and efficient that existing SQP and reduced-space SQP approaches. A completely equation oriented framework offer four additional advantages:

1. **Modeling discrete events and decisions:** Many process synthesis tasks require modeling discrete events and decisions. These can be accommodated in EO frameworks with disjunctive programming and mixed integer nonlinear programming (MINLP) algorithms. Furthermore some discrete variables can be replaced with smoothing functions or complementarities (Gopal and Biegler, 1999; Stein, Oldenburg, and Marquardt, 2004; Kraemer, Kossack, and Marquardt, 2009), another active area of mathematical programming research. As discussed in Chapter 4, the solution of nonconvex MINLPs is not without its challenges. However, optimization of discrete variables with SM methods remains extremely challenging, as provable convergence to a local optimum is difficult to demonstrate.

2. **Optimization decomposition methods:** EO modeling allows the use of powerful decomposition methods (Lagrangian, Schur complement, etc.) that break the original problem into more manageable subproblems. For example, Zhu, Legg, and Laird (2010, 2011) applied decomposition methods to solve large-scale process design under uncertainty problems.

3. **Low cost sensitivity analysis:** Using EO methods, sensitivity information at the optimal solution is available as a byproduct of the solution

procedure; KKT multipliers report the linearized sensitivity of the objective function with respect to perturbations in each bound and constraint. This information is especially valuable in process optimization studies, where one may be forced to rely on assumptions or weakly validated models that constrain the optimal value. In contrast, performing sensitivity analysis around a solution with SM methods requires simulating the flowsheet at multiple design points around the optimal solution.

4. **Embedded multiscale models:** Using surrogate models, it is possible to embed multiscale models, such as a partial differential algebraic reactor models with expensive derivatives, in a large process design optimization problem without sacrificing the benefits of EO models for most of the flowsheet. Furthermore, trust region methods provide a framework for optimization with some guarantees regarding optimality of the original system (i.e., the computationally expensive model).

The mathematical models proposed in this thesis are also protyped in the General Algebraic Modeling System (GAMS). Three central themes are present throughout the framework: (1) modular equation-oriented models, and (2) refinement for robust initialization, and (3) use of complementarity constraints to model some switches, as an alternate to integer variables.

1.1.1 Modular Models and Implementation

Although motivated by the design of cost effective oxycombustion power generation systems, the proposed framework is flexible and applicable to many generic process design problems. Each section of the model is implemented as a separate module, which is automatically included or disabled based on the equipment in the flowsheet. Abstraction is used throughout the framework to maintain flexibility and compactness.

In the framework, a flowsheet is presented as a collection of *streams* and *units*. Each stream is assigned a vector of physical properties. Material and energy flow into and out of units, which manipulate the physical properties of connected streams. This abstraction is implemented in GAMS using numerous compound sets (indexed over multiple other sets), which are introduced as necessary throughout the thesis. Similarly, units are classified using various levels of abstraction. The most generic equipment type, *general equipment*, share common mass and energy balance equations. *Thermodynamic equipment* are a subtype of *general equipment*, and inherit[2] the balance equations. Furthermore, vapor-liquid equilibrium equations are also defined for *thermodynamic equipment*. Different types of units, such as flash vessels, heat exchanger, compressors, etc. are classified as *general equipment*, *thermodynamic equipment* and/or other equipment types. Finally, the GAMS code is organized such that all of the input data that define a flowsheet (connectivity, specifications, etc.)

[2]This mimics the concept of inheritance and classes from objected-oriented computer programming.

are separate from the models, initialization routines and generic optimization workflow. The models presented in the framework are organized into several modules:

1. Simple Thermodynamics Module (Chapter 2)
2. Cubic Equation of State Thermodynamics Module (Chapter 2)
3. Equilibrium-based Unit Operations Module (Chapter 2)
4. Pump and Compressor Module (Chapter 2)
5. Heat Integration Module (Chapter 3)
6. Shortcut Distillation Module (Chapter 4)
7. Rigorous Distillation Module (Chapter 4)
8. Steam Cycle Equipment Module (Chapter 5)
9. Steam Thermodynamic Module (Chapter 5)
10. Trust Region Algorithm for Optimization with Surrogate Models (Chapter 5)

Finally, implementation details are addressed in Chapter 6.

1.1.2 Initialization Procedure

Without careful initialization, the nonlinear programming solvers used for EO methods tend to prematurely terminate at infeasible points. Similar to the work of Kraemer, Kossack, and Marquardt (2009), an iterative initialization procedure is used in this thesis. Optimization is first performed with simple models, and the results are used to initialize variables in more complex rigorous models. Due to highly nonlinear thermodynamic models and flowrate-composition bilinearities, multiple local optima are both expected and observed. Multi-start initialization is considered as a particular alternative to deterministic global optimization, as the models are too large complex for current algorithms such as BARON (Tawarmalani and Sahinidis, 2005).

1.1.2.1 Model Refinement

The initialization routine is divided into six steps, ordered from lowest and highest model complexity. In each steps, a series of nonlinear programs is solved. The final solution from each step is used as an initial point for the next. In Steps 1, 3, 4 and 6, two model parameters are adjusted as part of the sequence of NLPs. ε^s, which is used in the smoothed max operators (2.54), (Balakrishna and Biegler, 1992), is decreased from $O(10^{-3})$ to $O(10^{-6})$ (or similar values). Too small values for ε^s cause CONOPT occasionally to terminate prematurely, especially from initial points with many infeasible equations. Similarly, theory requires the complementarity penalty weight to be sufficiently

large to guarantee the solution of (1.2e) is a solution of (1.1), but does not provide a means to calculated a suitable weight. We have also empirically found that very large values of the penalty weight can degrade CONOPT's performance with these models, especially infeasible initial points. Thus because a sequence of NLPs must already be solved to increment ε^s in (2.54), the complementarity penalty ρ is also incremented from $O(10^0)$ to $O(10^3)$ (or similar values). Any complementarity violations in the first solutions are typically removed with the successive solves. Finally, the range of values for ρ and ε^s may require problem specific tuning.

0. **Load initial point.** Load a previous solution or initial guesses for temperatures, pressures, compositions and flowrates for each stream.

1. **Optimization with ideal thermodynamics and shortcut cascade model.** In this step, the flowsheet is optimized using ideal/simplified thermodynamics and the shortcut cascade model from Kamath, Grossmann, and Biegler (2010). Optionally this step may be skipped.

2. **Cubic EoS initialization.** The temperatures, pressures and compositions for each stream (determined in the previous step(s)) are used to initialize Z and other variables for the cubic equation of state. This includes initialization of the bubble and dew point calculations by solving small NLPs.

3. **Optimization with cubic EoS thermodynamics and shortcut cascade model.** The flowsheet is reoptimized using the cubic EoS thermodynamics and the shortcut cascade model.

4. **Optimization with cubic EoS thermodynamics and MESH with bypass distillation model**. Using the solution from the previous section, the MESH-based model (Chapter 4) is initialized. Then the flowsheet is repeatedly reoptimized, with adjustment and re-initialization carefully implemented between each NLP solve such that number of trays is each cascade is allowed to increase.

5. **Heat exchange unit decomposition.** Next, all active heat exchange units (i.e., reboilers, condensers, heat exchangers) are decomposed into a specified number of subunits. Flash calculations for each subunit are initialized by solving a sequence of small NLPs.

6. **Optimization with decomposed heat exchange unit.** In the final step, the process is re-optimized using the cubic EoS thermodynamic model, modified MESH distillation model and the decomposed heat exchange subunits. This step is important, as it refines the constant heat capacity assumption with piece-wise linear heat capacities.

Additional details regrading the NLPs solved in each step are presented in Chapter 6.

1.1.2.2 Multi-start Search

Several important parameters including lower and upper bounds on thermodynamic intermediate variables, initial values for stream variables (T, P, x, F), modeling strategies (e.g., different options for phase constraints in pump/-compressor models), and initial values for incremented parameters (i.e., ρ and ε^s) all impact the path of the nonlinear solver, and can lead to different locally optimal solutions. A multi-start procedure is used as part of the flowsheet optimization framework to search over a full factorial design for these important initialization parameters. The efficacy of this method is demonstrated in two case studies in Chapters 3 and 6.

1.2 A Primer on Mathematical Programs with Complementarity Constraints

Complementarity constraints represent inclusive ORs in mathematical programs, and have a variety of modeling applications including market equilibrium (economics), transitions between static and kinetic friction (physics) and phase equilibrium (thermodynamics). More generally, complementarity constraints can be used to represent switches in mathematical models, including nonsmoothness in process correlations and piece-wise smooth equations, check-valves, controller saturation, compressor kick-backs and overflow conditions. For many nonconvex optimization problems, complementarities may offer an alternative to mixed integer programming. A general form for a complementarity constraint is $0 \leq x_i \perp y_i \geq 0$, indicating either $x_i = 0$ or $y_i = 0$ (or both), and x_i, y_i are non-negative. The $\perp$ operator means x_i complements y_i. Complementarity constraints can more generally be written with functions, say $0 \leq \psi_1(x) \perp \psi_2(x) \geq 0$. We seek to solve the following general mathematical program with complementarity constraints (MPCC):

$$\begin{aligned} \min\ f(x,y,z), \quad \text{s.t. } & h(x,y,z) = 0,\ g(x,y,z) \leq 0, \\ & 0 \leq x \perp y \geq 0 \end{aligned} \tag{1.1}$$

Robustly solving MPCCs requires special care. The simplest algebraic form for a complementarity constraints, $x_i y_i = 0$, violates NLP constraint qualifications at the solution ($x_i = 0$ and/or $y_i = 0$). For example, the Linearly Independent Constraint Qualification (LICQ) is violated because the Jacobian of active constraints (with complementarity) is rank deficient at the solution. Constraint qualifications are essential to guarantee that the Lagrange multipliers at the solution of the constrained optimization problem are unique and/or bounded. Furthermore, many nonlinear programming solvers experience degraded performance when constraint qualifications do not hold. Instead complementarity constraints are commonly reformulated using several

strategies to embed in nonlinear programs (Biegler, 2010):

$$\min f(x,y,z), \quad \text{s.t. } h(x,y,z)=0,\ g(x,y,z)\le 0, \quad x_i y_i \le \epsilon, \quad i=1,...,n_x, \quad x,y\ge 0 \tag{1.2a}$$

$$\min f(x,y,z), \quad \text{s.t. } h(x,y,z)=0,\ g(x,y,z)\le 0, \quad x_i y_i = \epsilon, \quad i=1,...,n_x, \quad x,y\ge 0 \tag{1.2b}$$

$$\min f(x,y,z), \quad \text{s.t. } h(x,y,z)=0,\ g(x,y,z)\le 0, \quad x^T y \le \epsilon, \quad x,y\ge 0 \tag{1.2c}$$

$$\min f(x,y,z), \quad \text{s.t. } h(x,y,z)=0,\ g(x,y,z)\le 0, \quad x_i - \max(0, x_i - y_i) = 0, \quad i=1,...,n_x, \quad x,y\ge 0 \tag{1.2d}$$

$$\min f(x,y,z) + \rho x^T y, \quad \text{s.t. } h(x,y,z)=0, \quad g(x,y,z)\le 0, \quad x,y\ge 0\ . \tag{1.2e}$$

In order to show that a solution of (1.1), (x^*, y^*, z^*), can be found with an NLP reformulation, (x^*, y^*, z^*) must also be a solution to the following relaxed NLP:

$$\begin{aligned} \min_{x,y,z} \quad & f(x,y,z) \\ s.t. \quad & h(x,y,z)=0 \\ & g(x,y,z)\le 0 \\ & x,y\ge 0 \\ & x_{(i)}=0, \quad i\in I_X\setminus I_Y \\ & y_{(i)}=0, \quad i\in I_Y\setminus I_X \\ & x_{(i)}\ge 0, \quad i\in I_X\cap I_Y \\ & y_{(i)}\ge 0, \quad i\in I_X\cap I_Y\ . \end{aligned} \tag{1.3}$$

where

$$I_X = \left\{ i : x^*_{(i)} = 0 \right\}, \quad I_Y = \left\{ i : y^*_{(i)} = 0 \right\}.$$

Such a solution is *Strongly Stationary* and if (1.3) satisfies LICQ, then the solution to (1.3) has unique, bounded multipliers and the so-called MPEC-LICQ property holds for problem (1.1).

In (1.2a) - (1.2c), known as regularization formulations, the NLP is resolved with a sequence of values for the positive relaxation parameter, ϵ, approaching zero. Convergence properties for these formulations have been analyzed by Ralph and Wright (2004). Similarly, formulation (1.2d) typically involves a positive relaxation parameter in a smoothed max operator (Balakrishna and Biegler, 1992; Gopal and Biegler, 1999) or other NCP-functions (Chen and Pan, 2008). In contrast, we consider the exact penalty formulation shown in (1.2e), where the complementarity constraints are transferred to the objective

function and solved with a sufficiently large ρ. Thus any stationary point of (1.2e) where $x^T y = 0$ is a strong stationary point of (1.1), and if LICQ holds for (1.2e) at this point, then MPEC-LICQ is also satisfied for (1.1). Furthermore, if second order sufficient conditions (SOSC) hold for (1.1) at the stationary point, then MPEC-SOSC is satisfied, and the point is a local minimizer of (1.1). Conversely, any solution to (1.1) that satisfies strong stationarity is also a stationary point of (1.2e) with a sufficiently large ρ. Likewise, if MPEC-LICQ and MPEC-SOSC hold at the stationarity point of (1.1), then LICQ and SOSC, respectively, hold for (1.2e) at the same point with a sufficiently large ρ (Ralph and Wright, 2004). Thus it is sufficient (but not necessary) to test LICQ and SOSC at a solution of (1.2e) where $x^T y = 0$ to guarantee the point is also a solution of (1.1). Finally, if strong stationarity does not hold for a solution of (1.1), there are no guarantees it may be found with a relaxed formulation. Thus explicit branching on complementarity constraints is preferred for global optimization of MPCCs (Zhang and Sahinidis, 2015).

MPCC formulation (1.2e) has several advantages. With a large enough penalty parameter, the MPCC may be solved in one shot, in contrast to (1.2a) - (1.2c) which are solved as a sequence of problems for a generic NLP solver. Baumrucker, Renfro, and Biegler (2008) reported comparisons of several MPCC formulations with both active set and interior point NLP solvers, and found that formulation (1.2e) is typically the most efficient and robust. Several interior point NLP solvers, including KNITRO (Byrd, Nocedal, and Waltz, 2006; Leyffer, López-Calva, and Nocedal, 2006) and IPOPT-C (Raghunathan and Biegler, 2005), along with the meta-solver NLPEC (Ferris and GAMS Development, 2015), also support declaration of MPCC models in the form of (1.1).

1.3 Oxycombustion Power Generation Systems

The impact of CO_2 emissions on climate change and the abundance of domestic coal resources motivates interest in "clean coal" technologies. Currently there are four popular methods of CO_2 abatement in coal power plants. The most direct method is *post-combustion* carbon capture, where CO_2 is separated from N_2 and other components in the fuel gas of a coal power plant. The captured CO_2 is pumped underground at high pressures for enhanced oil recovery and/or long term sequestration. The second approach, *pre-combustion* carbon capture, is specific to integrated gasification combine cycle (IGCC) power plants. Coal is first gasified to create syngas; next, the CO is shifted into CO_2; and finally the CO_2 is separated and sequestered. The remaining syngas (mainly H_2) is combusted to generate power and steam. In the third approach, *chemical looping*, oxygen is transported to the coal via a chemical carrier, such as a metal/metal oxide. This creates a CO_2 rich waste stream, which may not require an extensive separation step. In the fourth approach, *oxycombustion*, coal is combusted in a N_2 lean environment. The resulting flue gas contains mainly water and CO_2, and requires significantly less processing before seques-

tration. Oxycombustion technology may also be applied to other fuel sources such as biomass. Scheffknecht et al. (2011) provides an extensive review of oxyfuel technology.

1.3.1 Primary Subsystems

The oxycombustion process is divided into five main subsystems, which are shown in Figure 1.1. Each subsystem is described below.

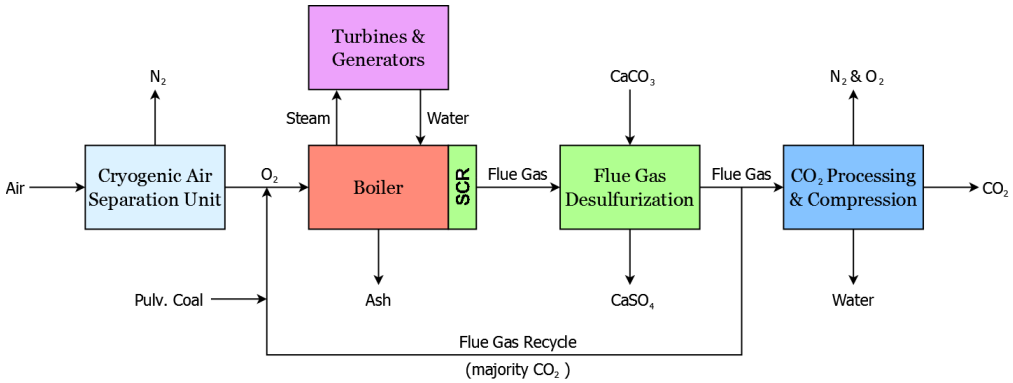

Figure 1.1: Simplified oxycombustion flowsheet

1.3.1.1 Air Separation

The first step of oxycombustion is to generate a N_2 lean air stream for combustion. Although several new technologies have been proposed, first generation oxycombustion plants are expected to utilize cryogenic air separation units (ASU) (Jordal, Yan, and Strömberg, 2004). This separation technique is mature, having originally been invented by Carl von Linde in the 1910s. Separation is achieved by distillation of air, but at cryogenic temperatures; at atmospheric pressure, the boiling points of N_2 and O_2 are $-196°$ C and $-183°$ C, respectively. These cold temperatures are achieved by compressing the inlet air, cooling it against exiting product streams in a multistream heat exchanger and then throttling the inlet air to a lower pressure, resulting in a temperature drop via the Joule-Thompson effect. Tight heat integration, with approach temperatures as small as 1° C in the multistream heat exchanger, helps reduce energy consumption but greatly complicates design and optimization.

1.3.1.2 Boiler and Flue Gas Recycle

The O_2 rich stream from the ASU is mixed with recycled flue gas (mainly CO_2 and water) and fed into the boiler, where pulverized coal is combusted. The CO_2 diluent helps control the boiler temperature. The recycle fraction is an important decision variable. Combustion of the coal produces heat, which is used to raise steam. Depending on coal quality, the amount of N_2 in the boiler feed air, boiler design and flame temperature, varying amounts of NO_x

and SO_x are formed. Comparison of combustion properties for coal in a CO_2 - O_2 versus a traditional N_2 - O_2 environment remains an active area of research; performance models for CO_2 - O_2 boilers involve a lot of uncertainty.

1.3.1.3 Power Generation

Steam from the boiler is converted to mechanical and electrical power by steam turbines and electric generators. As part of the steam cycle, a significant amount of heat is transferred from the flue gas to water (the working fluid) in the superheaters, reheaters, economizers and feedwater heaters. In the oxycombustion process, there is also a large amount of waste heat generated in the air compression (ASU) and CO_2 compression trains, which may be integrated into the steam cycle to improve efficiency. Finally, the upper bound on temperatures and pressures in the steam cycle, which are determined by available materials and metallurgy, greatly impact the overall efficiency of the oxycombustion process.

1.3.1.4 Flue Gas Treatment

Depending on the combustion conditions, recycle strategy and future sequestration regulations, SO_x and NO_x may need to be removed from the flue gas stream. In pulverized coal power plants, SO_2 is typically removed with a wet flue gas desulfurization unit. In this process limestone ($CaCO_3$) reacts with SO_2 to form $CaSO_4$ hydrate (gypsum) and CO_2 (Babcock & Wilcox Co., 2005d). NO_x is typically removed using a selective catalytic reduction (SCR) unit, where ammonia (NH_3) reduces NO_x, producing N_2 and H_2O (Babcock & Wilcox Co., 2005c). Due to the flue gas recycle in an oxycombustion plant, NO_x, CO and SO_3 all experience reburn near the nozzles, which are the hottest part of the boiler (Seltzer et al., 2010). Engineers at Foster Wheeler have proposed using this reburn phenomena to downsize the pollution control systems in certain oxyfuel plants (Hack, Fan, and Seltzer, 2010).

1.3.1.5 CO_2 Purification and Compression

The treated CO_2 rich flue gas is dried and compressed to high pressures (up to 150 bar) for utilization and/or sequestration. A multi-stage compressor train with inter-stage cooling is required for compression. Drying is typically done in two steps. First the flue gas is cooled, which knocks out most of the water. Next an absorption process (e.g., glycol drier) is used to remove the remaining water. The drying steps reduce pipeline corrosion from the acidic flue gas.

Specifications for pollutants (SO_2, NO_x), water and non-condensable gases (O_2, N_2, Ar) are still uncertain. Although it may be technically feasible to co-sequester CO_2 with pollutants, there are unknown environmental and political ramifications. Allowable water levels are dependent on the pollutants present and the pipeline materials. For enhanced oil recovery applications, it is desirable to maintain low O_2 levels in the CO_2 product. Pipitone and Bolland (2009) reviewed four pipeline specifications, and their findings are summarized

in Table 1.1.

Table 1.1: Summary of four reviewed pipeline specifications (Pipitone and Bolland, 2009).

Species	Lowest Limit Reported	Highest Limit Reported
CO_2	$\geq$ 95%	99.50%
CO	$\leq$ 10 ppm	0.1%
H_2O	$\leq$ 20 ppm	dew point at -5° C
SO_2	$\leq$ 10 ppm	$\leq$ 4500 ppm (weight) total sulfur
N_2	$\leq$ 300 ppm	4%
NO_x	$\leq$ 50 ppm	-
O_2	$\leq$ 10 ppm	$\leq$ 50 ppm
Glycol	4×10^{-5} L m^{-3}	-

Many have proposed some type of CO_2 purification unit (CPU) to remove O_2, N_2, Ar and other gases from the product CO_2 stream. Designs use either a series of cryogenic flashes or a distillation column (Pipitone and Bolland, 2009; Shah et al., 2011). Foster Wheeler is developing zero emissions oxycombustion designs with an extra vacuum pressure swing adsorption (VPSA) system to separate CO_2 and pollutants from the O_2, N_2 and Ar in the CPU distillate stream (Hack, Fan, and Seltzer, 2010; Fan, Seltzer, and Hack, 2011). This would allow for the CO_2 in the CPU gas stream to be recycled to the boiler, resulting in a near zero emissions power plant. Praxair is also developing a hybrid CPU-pollutant control system, which should be less expensive than traditional NO_x and SO_2 systems (Shah et al., 2011).

1.3.2 Previous Systems Analysis

Many researchers have studied coal oxycombustion technologies in the past decade, ranging from combustion experimentalists to CFD modelers. In the system analysis realm, researchers have focused on using exergy analysis, heat integration, process simulation and other tools to both quantify the expected efficiency of oxycombustion systems (for comparison with other carbon capture technologies) and identify pathways for efficiency improvement. For example, Fu and Gundersen (2010) used pinch analysis to estimate an overall system efficiency penalty of 10 percentage points due to the air separation unit and CO_2 processing in an oxycombustion power plant. They also used exergy analysis to improve the efficiency of air separation units tailored to the oxycombustion process (Fu and Gundersen, 2012, 2013). Recent work of Gundersen and coworkers (Fu, Anantharaman, and Gundersen, 2014; Soundararajan, Anantharaman, and Gundersen, 2014) has focused on applying heat integration methods to recover waste heat from compressors and other parts of the oxycombustion process in the steam cycle.

Chemical process simulators are also popular tools for oxycombustion system analysis. For example, Hagi et al. (2013) used a combination of Aspen Plus and exergy analysis to compare three flue gas recycle strategies. Simi-

larly, Li et al. (2014) explored sizing trade-offs between the air separation unit (ASU) and CO_2 processing unit (CPU) in an oxycombustion power plant. The advantages of operating an oxycombustion boiler slightly pressurized were explored by Soundararajan, Gundersen, and Ditaranto (2014) using simulations in Aspen Plus. Xiong et al. (2011) also used Aspen Plus to study the sensitivity of an 800 MWe oxycombustion facility to several key design variables.

Although the findings of these studies are valuable, there are several limitations. Many of these studies make drastic simplifying assumptions of various units in the oxycombustion process. For example, most Aspen Plus oxycombustion modelers use simplified models of the air separation unit instead of modeling the more difficult coupled double column system with accompanying multistream heat exchanger. As a result, these studies miss important interactions between the ASU and other systems, such as heat integration opportunities between the ASU and CPU. Zebian, Gazzino, and Mitsos (2012) and Zebian et al. (2013) demonstrated the shortcomings of these sensitivity-based studies by applying multi-variable numeric optimization to the oxycombustion process and found important interactions between key design variables. However, their work was restricted to 17 variables and used older optimization technology (SQP in Aspen Plus, i.e. sequential modular mode).

1.4 Thesis Organization

Thorough optimization of an oxycombustion power system requires both details modeled for each subsystem, and consideration of interaction between subsystems. To date, most systems analysis has either used extremely simplified models or considered individual subsystems in isolation. In contrast, this thesis uses the oxycombustion design problem as a test bed for the proposed equation-oriented flowsheet optimization framework, which allows for both detailed optimization of subsystems in isolation, and the power system as a whole. In Chapter 2, the thermodynamics and equipment modules are presented, along with set notation to manage flowsheet connectivity. The work of Kamath, Biegler, and Grossmann (2010) is used as the basis for the cubic equation of state (e.g., Peng-Robinson) thermodynamics module. In summary, they proposed rules based on the sign of the first and second derivatives of equation of state ($f(Z) = a + bZ + cZ^2 + Z^3 = 0$) to assigned roots for compressibility factor (Z) to phases. Two shortcomings of this model are explored and extensions are proposed. First, the original model misclassifies roots in the supercritical region, which is problematic for the CO_2 processing unit and compression train. A reformulation using complementarity constraints is proposed for proper phase identification. Second, nonphysical vapor-liquid equilibrium solutions are demonstrated with the cubic EoS formulation. These are problematic and occur during optimization as a means to cheat heat thermodynamics to artificially decrease the objective function. A strategy based on bubble and dew point calculations is presented and demonstrated to avoid a class of these nonphysical solutions.

In Chapter 3, models for simultaneous heat integration and process optimization based on the work of Duran and Grossmann (1986) and Kamath, Biegler, and Grossmann (2012) are presented. In summary, this approach embeds minimum utility calculations, which are analogous to the heat recovery pinch design method, in the process design problem as nonlinear equations. In the original formulation, the discrete nature of determining the active pinch point is handled with inequality constraints and smoothed max operators, which introduces some errors in the utility calculations. Three reformulations to reduce the number of smooth max operator instances (and associated errors) are presented and compared. Furthermore, decomposition of each heat exchange unit to refine the constant heat capacity assumption is discussed. The models from Chapters 2 and Chapter 3 are demonstrated with a CO_2 processing unit (CPU) case study, which includes optimization of the flash separators, subambient multistream heat exchangers and compression train. Sensitivity of the optimal solution to CO_2 purity and recovery specification is quantified.

In Chapter 4, two distillation columns models are presented. The first uses a modified version of the Edmister aggregate model to approximate column performance without considering each stage (Kamath, Grossmann, and Biegler, 2010). Optimization results obtained with this model are used to initialize a rigorous mass, energy, summation and heat (MESH) equation-based model. Bypass streams are considered for each tray, which allows for optimization of column size and feed tray location without integer variables. This new model is used to tailor cryogenic air separations units for use in oxycombustion systems. The accompanying multistream heat exchanger and columns are simultaneously optimized using the heat integration model presented in Chapter 3. Finally, heat integration opportunities between the ASU and CPU are discussed, and quantified by reoptimizing the CPU to use "waste" cooling from the ASU.

Equation-based models for turbine and other steam cycle equipment are presented in Chapter 5. Two approaches for incorporating water physical property calculations from standardized steam tables are discussed. The first approach uses static fitted nonlinear models, as common practice in many optimization studies. The optimizer, however, exploits errors in fitted models and proposes nonphysical steam cycle designs with system thermal efficiencies above the Carnot cycle upper bound. This failure motivates development of an adaptive strategy, where simple surrogate models for steam thermodynamics calculations are updated during optimization. A trust region algorithm is used to ensure convergence to a local optimum of the original system with the steam table lookup model. Unlike the first approach, optimization with these models results in meaningful steam cycle designs that are in agreement with the original steam table thermodynamics model within a small $O(10^{-8})$ tolerance. Furthermore, application of the adaptive model strategy for a zonal hybrid 1D/3D computational fluid dynamics boiler model is discussed. Finally, an air-fired steam cycle is reoptimized with varying amounts of low grade heat,

which demonstrates the capabilities of the framework to consider integration of waste heat from the ASU and CPU compression trains in the steam cycle.

In Chapter 6, additional implementation details are discussed. The sequence of NLPs solved in each step of the initialization procedure are presented. Furthermore, efficacy of the multi-start procedure is shown for the ASU case study. Finally, *Degeneracy Hunter*, a model analysis tool for identifying degenerate equations, is introduced. Speed-ups as consequence of removing degenerate, i.e. linearly dependent, constraints in the ASU case study are shown. Finally, conclusions are made and future work is suggested in Chapter 7. Table 1.2 shows the mapping between publications and chapters containing material included in this thesis.

Table 1.2: Publications containing material presented in this thesis

Publication	**Thesis Chapter**
Dowling, A. W., & Biegler, L. T. (2013). Optimization-based Process Synthesis for Sustainable Power Generation. *Chemical Engineering Transactions*, 35, 1-12.	1, 5
Dowling, A. W., & Biegler, L. T. (2014). Rigorous Optimization-based Synthesis of Distillation Cascades without Integer Variables. In: Klemeš, J. J., Varbanov, P. S., & Liew, P. Y., (Eds.), *Computer Aided Chemical Engineering*, 33, 55-60.	4
Dowling, A. W., Gao, Q., & Biegler, L. T. (2014). Equation-Oriented Optimization of Cryogenic Systems for Coal Oxycombustion Power Plants. In: Eden, M. R., Siirola, J. D., & Towler, G. P. (Eds.), *Computer Aided Chemical Engineering*, 34, 501-506.	3
Dowling, A. W., Eason, J. P., Ma, J., Miller, D. C., & Biegler, L. T. (2014). Coal Oxycombustion Power Plant Optimization Using First Principles and Surrogate Boiler Models. *Energy Procedia*, 63, 352-361.	5
Dowling, A. W., Balwani, C., Gao, Q., & Biegler, L. T. (2014). Equation-oriented Optimization of Cryogenic Systems for Coal Oxycombustion Power Generation, *Energy Procedia*, 63, 421-430.	3, 4
Dowling, A. W., & Biegler, L. T. (2015). A framework for efficient large-scale equation-oriented flowsheet optimization. *Computers & Chemical Engineering*, 72, 3-20.	1 - 4, 6
Dowling, A. W., Balwani, C., Gao, Q., & Biegler, L. T. (2015), Optimization of Sub-Ambient Separation Systems with Embedded Cubic Equation of State Thermodynamic Models and Complementarity Constraints. *Computers & Chemical Engineering* (in press).	1 - 4
Dowling, A. W., & Biegler, L. T. (2015). Degeneracy Hunter: An Algorithm for Determining Irreducible Sets of Degenerate Constraints in Mathematical Programs. In: Gernaey, K. V., Huusom, J. K, Gani, R., (Eds.), *12th International Symposium on Process Systems Engineering and 25th European Symposium on Computer Aided Process Engineering*.	6

Chapter 2

Thermodynamics and Equipment Models

Key Contributions and Results:

- Present reformulation of cubic EoS model for proper phase detection in the supercritical region
- Develop a strategy to avoid nonphysical phase equilibrium predictions with embedded cubic EoS models
- Extend flash calculation equation into modular models for various equilibrium-based unit operations

2.1 Overview

Phase equilibrium and thermodynamic property calculations are arguably the most computationally challenging aspects of flowsheet simulation and optimization. For most thermodynamic methods, determining equilibrium and physical properties (enthalpy, entropy, specific volume, etc.) requires the solution of highly nonlinear systems of equations. Furthermore, many complex flowsheets, such as applications in the oil and gas industry, may include fifty plus chemical species, most in trace quantities. Depending on the mathematical formulations in the thermodynamics model, this may lead to a poorly scaled system of equations and require significant amount of computer memory. Phase equilibrium calculations are nonconvex for most nonideal models, which makes rigorous calculations analogous to solving a global optimization problem. Furthermore, phase equilibrium calculations are also nonsmooth when the number of phases is not known *a priori*. Moreover, moderately sized flowsheets, especially those with distillation columns, typically include hundreds of phase equilibrium calculations.

Historically, thermodynamic packages have been treated as "black" or "gray boxes" that provide mixture properties at equilibrium and optionally first derivatives. This allows iterative procedures and logical conditions to be

used inside the thermodynamics package, similar to the sequential modular philosophy for flowsheet simulation. For example, in the famous inside-out algorithm (Boston and Britt, 1978), phase equilibrium calculations are decomposed into an inner and outer loop. In the inner loop, phase equilibrium is calculated with a simplified (i.e., surrogate) model for the component equilibrium coefficient (K_c), such as

$$\ln K_c = A_i + B_i(1/T - 1/T^r) \ , \tag{2.1}$$

where T^r is a reference temperature. In the outer loop, physical properties models are evaluated (e.g., fugacities) and used to update A_i and B_i. The iterative procedure continues until certain tolerances are met. Although usually robust, this procedure does not provide reliable derivatives for optimization. Consider a hypothetical, small perturbation in a unit's operating conditions (e.g., temperature) that causes the number of iterations required to converge insider-out algorithm to change. Unfortunately, the residual error in the equilibrium equations at the solution point is discontinuous (on a small scale) as the number of iterations for the inside-out algorithm changes. This phenomena explains why optimization with sequential-modular flowsheet simulators is difficult as first derivatives are noisy. Similarly, Reid, Prausnitz, and Poling (1987) describe different types of Newton steps that are preferred to converge phase equilibrium equations depending on the location in pressure-temperature-composition space relative to the critical point. As discussed later in this chapter, the Gibbs tangent plane criteria (Michelsen, 1982a,b) is commonly used to test the stability of multicomponent flash calculations. If the procedure fails, it generates a candidate compositions to use as a starting point with additional phases. All of these aspects of flash calculations require iterative procedures, which complicate calculation of exact first and second derivatives for optimization.

With this motivation, Kamath, Biegler, and Grossmann (2010) proposed a completely equation-based formulation for cubic equation of state (EoS) thermodynamic models. Assignment of roots of the cubic EoS to phases is handled with inequality constraints, instead of iterative procedures or heuristic rules. These models are the basis of the thermodynamics module in the proposed framework.

The remainder of this chapter is organized as follows. First, the derivation of a multi-component flash calculation model with complemenarity constraints is summarized. The model enables equation-based phase equilibrium calculations without either the number of phases specified *a priori* or integer variables. Next, the simple (ideal gas) thermodynamics module is presented, which is used as part of the initialization procedure in the framework. Then, the Kamath, Biegler, and Grossmann (2010) models for cubic EoS thermodynamics are discussed, and two improvements are proposed: [1] corrections for proper phase identification in the supercritical region and [2] strategies to avoid nonphysical phase equilbria solutions. Finally, the flash model is

extended to various equilibrium-based equipment models. These proposed models are demonstrated in case studies in Chapters 3 and 4.

2.2 Bilevel Optimization: Gibbs Free Energy Minimization

Depending on the specified parameters, phase equilibrium is defined as the minimum of a different state function. Common pairings include the following (Michelsen, 1993):

- Minimize $-S$ (entropy) for H-P flash calculations
- Minimize H (enthalpy) for S-P flash calculations
- Minimize A (Helmholtz free energy) for T-V flash calculations
- Minimize $-S$ (entropy) for V-U flash calculations

In flowsheet optimization problems, isothermal flash calculations are considered, and equilibrium occurs at the global solution of

$$\begin{aligned} \min_{l_c, v_c} \quad & G(T, P, l_c, v_c) && \text{(2.2a)} \\ \text{s.t.} \quad & l_c + v_c = m_c && \text{(2.2b)} \\ & l_c, v_c \geq 0, \quad \forall c \in \mathcal{C} \ , && \text{(2.2c)} \end{aligned}$$

where l_c and v_c represent the flowrate of component c in the liquid and vapor phases, respectively, and compositions are implicitly calculated from these flowrates. The overall mass flowrates (m_c), temperature (T) and pressure (P) are specifications or determined by optimizer in an outer loop. This formulation results in a bilevel optimization problem, where (2.2) is the inner problem embedded in the outer flowsheet design problem. In order to use generic nonlinear programming algorithms, the bilevel problem in converted into a mathematical program with complementarity constraints by examining the Karush-Kuhn-Tucker conditions (i.e., first order optimality conditions) of (2.2). The remainder of this derivation is based on the work of Biegler (2010). First, consider the Lagrange function for the Gibbs free energy minimization,

$$\mathcal{L} = G(T, P, l_c, l_v) - \sum_{c \in \mathcal{C}} \alpha_c^L l_c - \sum_{c \in \mathcal{C}} \alpha_c^V v_c + \sum_{c \in \mathcal{C}} \lambda_c (l_c + v_c - m_c) \tag{2.3}$$

where T, P and m_c are all constant, λ_c are the KKT multipliers for (2.2b), and α_c^V and α_c^L are the KKT multipliers for (2.2c). At a local solution of (2.2), the first derivatives of the Lagrange function, $\mathcal{L}$, with respect to the component flowrates in each phase are zero.

$$\nabla_{l_c}\mathcal{L} = \left(\frac{\partial G^L}{\partial l_c}\right)_{T,P,l_{i\neq c}} - \alpha_c^L + \lambda_c = 0 \tag{2.4a}$$

$$\nabla_{v_c}\mathcal{L} = \left(\frac{\partial G^V}{\partial v_c}\right)_{T,P,v_{i\neq c}} - \alpha_c^V + \lambda_c = 0 \ . \tag{2.4b}$$

The Gibbs free energy for each phase can be expressed in terms of chemical potential (μ_c^p),

$$\mu_c^p = \left(\frac{\partial G^p}{\partial n_c}\right)_{T,P,n_{i\neq c}} \ , \tag{2.5}$$

and (2.4) simplifies,

$$\nabla_{l_c}\mathcal{L} = \mu_c^L - \alpha_c^L + \lambda_c = 0 \tag{2.6a}$$

$$\nabla_{v_c}\mathcal{L} = \mu_c^V - \alpha_c^V + \lambda_c = 0 \ . \tag{2.6b}$$

Alternately the Gibbs free energy of a phase may be expressed in terms of partial molar Gibbs free energy of each component:

$$G^p = \sum_c n_c \bar{G}_c^p \ . \tag{2.7}$$

Differentiation of G with respect to n_c yields

$$\frac{\partial G^p}{\partial n_c} = \bar{G}_c^p + \sum_{i\in\mathcal{C}} n_i \left(\frac{\partial \bar{G}_i^p}{\partial n_c}\right) \ , \tag{2.8}$$

per the chain rule. This expression simplifies by realizing

$$\bar{G}_c^p = \mu_c^p \ , \tag{2.9}$$

and applying the Gibbs-Duhem equation,

$$0 = \sum_c n_c \ \mathrm{d}\mu_c^p \ , \tag{2.10}$$

which simplifies (2.8) to

$$\frac{\partial G^p}{\partial n_c} = \bar{G}_c^p = \mu_c^p \ . \tag{2.11}$$

This is consistent with (2.5). Next, the formula for potential chemical,

$$\mu_c^p = \mu_c^\circ + RT \ \ln\frac{f_c^p}{f_c^\circ} \ , \tag{2.12}$$

is substituted into the KKT conditions, (2.6), resulting in

$$\nabla_{l_c}\mathcal{L} = \mu_c^\circ + RT\,\ln\frac{f_c^L}{f_c^\circ} - \alpha_c^L + \lambda_c = 0 \tag{2.13a}$$

$$\nabla_{v_c}\mathcal{L} = \mu_c^\circ + RT\,\ln\frac{f_c^V}{f_c^\circ} - \alpha_c^V + \lambda_c = 0\ , \tag{2.13b}$$

where μ_c° and f_c° are the chemical potential and fugacity, respectively, of component c at the hypothetical gas phase reference state. Subtracting (2.13a) from (2.13b) gives

$$RT\,\ln\frac{f_c^V}{f_c^L} - \alpha_c^V + \alpha_c^L = 0\ . \tag{2.14}$$

Manipulation of (2.14) using the fugacity coefficient definition, $\phi_c^V = f_c^V/(y_c P)$ and $\phi_c^L = f_c^L/(x_c P)$ gives

$$\frac{f_c^V}{f_c^L} = \exp\left(\frac{\alpha_c^V - \alpha_c^L}{RT}\right) \tag{2.15a}$$

$$\frac{y_c\phi_c^V}{x_c\phi_c^L} = \exp\left(\frac{\alpha_c^V - \alpha_c^L}{RT}\right) \tag{2.15b}$$

$$y_c = \exp\left(\frac{\alpha_c^V - \alpha_c^L}{RT}\right)\left(\frac{\phi_c^L}{\phi_c^V}\right)x_c\ . \tag{2.15c}$$

Recall the definition of the equilibrium coefficient, $K_c = \phi_c^L/\phi_c^V$, and let $\gamma_c = \exp\left(\frac{\alpha_c^V - \alpha_c^L}{RT}\right)$. Then, (2.15c) becomes

$$y_c = \gamma_c K_c x_c\ . \tag{2.16}$$

Furthermore, the KKT conditions require complementarity between the inequality constraints (2.2c) and their KKT multipliers (α^V and α_c^L), thus

$$0 \le \alpha_c^V \perp v_c \ge 0 \tag{2.17a}$$

$$0 \le \alpha_c^L \perp l_c \ge 0\ . \tag{2.17b}$$

When $v_c > 0$ and $l_c > 0$, then $\alpha_c^V = \alpha_c^L = 0$ and $\gamma_c = 1$, thus (2.16) becomes $y_c = K_c x_c$, the standard vapor-liquid equilibrium formula. If $v_c = 0$ then $\alpha_c^V \ge 0$ and $\gamma_c \ge 1$, which in effect relaxes $y_c = K_c x_c$. This is equivalent to a component in the vapor stream disappearing. Similarly if $l_c = 0$, then $\alpha_c^L \ge 0$ and $\gamma_c \le 1$, which corresponds to a component disappearing in the liquid stream.

In the derivation of (2.19), Biegler (2010) assumes all components are present, i.e., $x_c, y_c > 0 \quad \forall c \in \mathcal{C}$. In place of (2.2c), $\sum_c l_c \ge 0$ and $\sum_c v_c \ge 0$

are considered. This is equivalent to applying $A^V = \sum_c \alpha_c^V$, $A^L = \sum_c \alpha_c^V$, $V = \sum_c v_c$ and $L = \sum_c l_c$ to (2.15) - (2.17), which yields

$$0 \leq A^V \perp V \geq 0 \tag{2.18a}$$
$$0 \leq A^L \perp L \geq 0 \tag{2.18b}$$
$$\beta = \exp\left(\frac{A^V - A^L}{RT}\right) \tag{2.18c}$$
$$y_c = \beta K_c x_c \tag{2.18d}$$

It is important to note the trade-offs between formulations (2.17) and (2.18). The former can accommodate cases where $x_c = y_c = 0$ (although this may lead to linearly dependent constraints), whereas the latter cannot. However, the latter is more compact and requires fewer slack variables. Thus, when using (2.18), it is important there are no extra components in flash calculations. With (2.18), consideration of the scenarios $A^V = 0$, $A^V > 0$, $A^L = 0$, $A^L > 0$ allows for formulation of the follow conditions for phase equilibrium with complementary constraints,

$$m_c = l_c + v_c, \quad \forall c \in \mathcal{C} \tag{2.19a}$$
$$L = \sum_c l_c \tag{2.19b}$$
$$l_c = x_c L, \quad \forall c \in \mathcal{C} \tag{2.19c}$$
$$V = \sum_c v_c \tag{2.19d}$$
$$v_c = y_c V, \quad \forall c \in \mathcal{C} \tag{2.19e}$$
$$y_c = \beta K_c x_c, \quad \forall c \in \mathcal{C} \tag{2.19f}$$
$$-\sigma^L \leq \beta - 1 \tag{2.19g}$$
$$\beta - 1 \leq \sigma^V \tag{2.19h}$$
$$0 \leq V \perp \sigma^V \geq 0 \tag{2.19i}$$
$$0 \leq L \perp \sigma^L \geq 0\ , \tag{2.19j}$$

where K_c is the equilibrium coefficient, L and V are overall flowrates for both phases, and σ^V and σ^L are slack variables for the vapor and liquid phases, respectively. β is a slack variable used to relax (2.19f), which is related to the Lagrange multipliers from (2.2). When both phases are present, $V, L > 0$ and $\sigma^V = \sigma^L = 0$ due to the complementarity constraint (2.19i) & (2.19j), thus $\beta = 1$ and (2.19f) is not relaxed. However, if the vapor phase disappears ($V = 0$), σ^V moves away from zero and $\beta \geq 1$, thus relaxing (2.19f). This approach results in a mathematical program with complementarity constraints (MPCC), due to (2.19i) - (2.19j). Applications include:

1. Distillation column simulation and design with dry trays (below the minimum reflux ratio) (Baumrucker, Renfro, and Biegler, 2008)

2. Startup of batch distillation columns with phase appearance and disappearance (Raghunathan, Diaz, and Biegler, 2004)

3. Heat integration of multiphase, multistream heat exchangers with phase determination and disappearance over the length of the equipment (Kamath, Biegler, and Grossmann, 2012)

In all of these studies, the exact penalty formulation (1.2e) successfully tracked phase changes and led to robust and efficient solutions to the large-scale NLPs. In this work, we propose the following modification of (2.19),

$$m_c = l_c + v_c, \quad \forall c \in \mathcal{C} \tag{2.20a}$$
$$L = \sum_c l_c \tag{2.20b}$$
$$l_c = x_c L, \quad \forall c \in \mathcal{C} \tag{2.20c}$$
$$V = \sum_c v_c \tag{2.20d}$$
$$v_c = y_c V, \quad \forall c \in \mathcal{C} \tag{2.20e}$$
$$\hat{y}_c = \hat{\beta} + \hat{K}_c + \hat{x}_c, \quad \forall c \in \mathcal{C} \tag{2.20f}$$
$$-\sigma^L \leq \hat{\beta} \tag{2.20g}$$
$$\hat{\beta} \leq \sigma^V \tag{2.20h}$$
$$0 \leq V \perp \sigma^V \geq 0 \tag{2.20i}$$
$$0 \leq L \perp \sigma^L \geq 0 \tag{2.20j}$$
$$x_c = \exp(\hat{x}_c), \quad \forall c \in \mathcal{C} \tag{2.20k}$$
$$y_c = \exp(\hat{y}_c), \quad \forall c \in \mathcal{C} \tag{2.20l}$$
$$\hat{K}_c = \ln(\phi_c^L) - \ln(\phi_c^V), \quad \forall c \in \mathcal{C}\ , \tag{2.20m}$$

where $\hat{x_c}$, $\hat{y_c}$, $\hat{K_c}$ and $\hat{\beta}$ are log transformations of x_c, y_c, K_c and β. This idea was inspired by early flash calculation literature that recommends Newton iterations with $\ln K$ for the high pressure region and other cases (Michelsen, 1980, 1993). System (2.20) is preferable for three reasons. With a cubic equation of state, the fugacity coefficient equations (ϕ_c) are simpler in the form $\ln(\phi_c)$, as shown in (2.35) and (2.36). Furthermore, the log transformation allows (2.19f) to be replaced with (2.20f), which is linear. In contrast, if $x_c \approx 0$ or $y_c \approx 0$, such as with trace components, the Jacobian of (2.19) may become ill conditioned due to (2.19f), whereas the bounds $\ln(10^{-16}) \leq \hat{x_c}, \hat{y_c} \leq 0$ ensure the derivatives of (2.20k) and (2.20l) are well behaved (e.g., reasonably scaled, non-singular).

In summary, the first order optimality conditions (i.e., KKT conditions) shown in (2.19) and (2.20) are equivalent to the equal fugacity definition of equilibrium, i.e., $y_c \phi_c^V = x_c \phi_i^L \ \ \forall c \in \mathcal{C}$. Using the slack variables σ^V, σ^L, β and $\hat{\beta}$, the nonsmooth nature of (2.2), i.e. determining the number of phases, is

formulated as a mathematical program with complementarity constraints. β and $\hat{\beta}$ are related to the KKT multipliers for (2.2c), as previously discussed. In contrast, *intrinsic phase stability* requires the Hessian (matrix of 2$^{\text{nd}}$ derivatives) of G "with respect to the independent composition variables" to be positive definite (Michelsen, 1993). This is analogous to the second order sufficient conditions for (2.2), which require the reduced Hessian (i.e., the Hessian projected into the null space of the constraints) to be positive definite. In practice, second order conditions are rarely used to predict equilibrium, as they require calculation of a reduced Hessian.

2.3 Prerequisites: Stream Model and Common Equations

Before discussing either thermodynamics module and their associated equations, it is important to establish some nomenclature. In this thesis, a flowsheet is treated as a collection of *streams* and *units*. Physical properties including flowrate F_s, component flowrate $f_{s,c}$, component mole fraction $x_{s,c}$ (or $y_{s,c}$), temperature T_s, pressure P_s, specific molar enthalpy H_s, specific molar entropy S_s, specific molar volume $V_{s,c}$ and fugacity $\phi_{s,c}$ are defined over the parent sets $\mathcal{S}$, which contain all possible streams in the flowsheet, and components $\mathcal{C}_{All}$, which contain all components in the flowsheet. The indices s and c are used for streams and components, respectively.

Several subsets of $\mathcal{S}$ are used throughout the framework. To reduce the number of equations in a flowsheet problem, enthalpy, entropy, fugacity and specific volume are only calculated for streams $\mathcal{S}^{H}_{Calc}$, $\mathcal{S}^{S}_{Calc}$, $\mathcal{S}^{\phi}_{Calc}$, and $\mathcal{S}^{V}_{Calc}$. All of these sets are subsets of $\mathcal{S}$ and are automatically populated based on the connectivity in the flowsheet. They are not shown with equation declarations below to simplify notation. Similarly, $\mathcal{S}$ is divided into mutually exclusive subsets based on phase classification: $\mathcal{S}_{Liq}$ and $\mathcal{S}_{Vap}$ contain liquid and vapor streams, respectively, that cannot vanish. In contrast $\mathcal{S}^{Flash}_{Liq}$ and $\mathcal{S}^{Flash}_{Vap}$ contain liquid and vapor streams used in flash calculations, and these may vanish. Other subsets of $\mathcal{S}$ are introduced as needed and listed in the nomenclature table (Appendix). All of these subsets are automatically populated in the optimization framework depending on the flowsheet connectivity discussed in Section 2.7.

In order to accommodate complex processes, the concept of multiple *flowsheet zones* is supported in the framework. A separate set, $\mathcal{C} = \{c_1, c_2, ..., c_{N_c}\}$, is specified for each zone such that $\mathcal{C} \subseteq \mathcal{C}_{All}$, and each stream is assigned to one (and only one) flowsheet zone by the modeler. This provides a simple mechanism to consider only the relevant chemical species for each part of a process (e.g., ignore SO_x in the ASU of an oxycombustion process, although it is an important chemical species in the flue gas processing section). To simplify notation, flowsheet zones are implied in most equation declarations in this thesis.

The basic stream model equations,

$$F_s = \sum_{c \in \mathcal{C}} f_{s,c} \qquad \forall s \in \mathcal{S} \tag{2.21a}$$

$$f_{s,c} = F_s \; x_{s,c} \qquad \forall c \in \mathcal{C} \setminus \{c_{N_c}\} \; , s \in \mathcal{S} \tag{2.21b}$$

$$1 = \sum_{c \in \mathcal{C}} x_{s,c} \qquad \forall s \in \mathcal{S} \; , \tag{2.21c}$$

include an overall mole flowrate definition, component flowrate definition and summation requirement. This model is mathematically equivalent to Rachford-Rice formulation, $\sum_c (x_c - y_c) = 0$, and is preferred for optimization. Instead of writing (2.21b) for all components, the final instance, c_{N_c}, is replaced with $\sum_c x_{s,c} = 1$ (or $\sum_c y_{s,c} = 1$)[1], which removes one bilinear term from the model. Finally, based on the phase equilibrium conditions presented in Section 2.2, the following complementarity constraints are enforced:

$$0 \leq F_s \perp \sigma_s^L \geq 0, \quad \sigma_s^V = 0, \qquad \forall s \in \mathcal{S}_{Liq}^{Flash}, \tag{2.22a}$$

$$0 \leq F_s \perp \sigma_s^V \geq 0, \quad \sigma_s^L = 0, \qquad \forall s \in \mathcal{S}_{Vap}^{Flash}, \tag{2.22b}$$

$$F_s \geq 0, \quad \sigma_s^L = \sigma_s^V = 0, \qquad \forall s \in \mathcal{S}_{Liq} \cup \mathcal{S}_{Vap} \; . \tag{2.22c}$$

In practice, these complementarity constraints are accommodated in this work by using the penalty formulation (1.2e).

2.4 Simple Thermodynamics Module

Optimization with the simple thermodynamics module produces a good initial point for the more rigorous cubic EoS models. Vapor pressure, P^{vap}, is calculated using the Antoine equation, (2.23a), and vapor-liquid equilibrium is calculated via Raoult's law, (2.23b). Phases boundaries are determined by calculating bubble and dew point pressures, (2.23c) & (2.23d), from the mixture vapor pressure. Stream pressures are constrained in accordance with (2.23e) & (2.23f). The index g represents thermodynamic equipment, which are discussed in Section 2.7, along with $\mathcal{G}_{out}^V$ and $\mathcal{T}$. The stream index s in (2.23b) corresponds to the vapor outlet of an equilibrium-based equipment model.

$$P_{s,c}^{vap} = \exp[\mathcal{A}_c^a - \mathcal{A}_c^b/(T_s + \mathcal{A}_c^c)], \qquad \forall s \in \mathcal{S} \tag{2.23a}$$

$$K_{g,c} \; P_s = P_{s,c}^{vap} \qquad \forall (s,g) \in \mathcal{G}_{out}^V \cap \{\mathcal{S} \times \mathcal{T}\} \tag{2.23b}$$

$$P_s^b = \sum_c x_{s,c} P_{s,c}^{vap}, \qquad \forall s \in \mathcal{S}_{Liq} \cup \mathcal{S}_{Liq}^{Flash} \tag{2.23c}$$

$$P_s^d \sum_c \frac{x_{s,c}}{P_{s,c}^{vap}} = 1, \qquad \forall s \in \mathcal{S}_{Vap} \cup \mathcal{S}_{Vap}^{Flash} \tag{2.23d}$$

[1] $x_{s,c}$ is used throughout this thesis to denote component mole fraction of liquid and occasionally vapor streams. When the distinction between phases is important, $y_{s,c}$ is used for vapors.

$$P_s \geq P_s^b, \quad \forall s \in \mathcal{S}_{Liq} \tag{2.23e}$$

$$P_s \leq P_s^d, \quad \forall s \in \mathcal{S}_{Vap} \ . \tag{2.23f}$$

Using the slack variables σ^L and σ^V from (2.19), the phase specification constraints are relaxed as follows:

$$P_s \geq P_s^b(x_s) - M\sigma_s^L \quad s \in \mathcal{S}_{Liq}^{Flash} \tag{2.24a}$$

$$P_s \leq P_s^d(y_s) + M\sigma_s^V \quad s \in \mathcal{S}_{Vap}^{Flash} \ . \tag{2.24b}$$

The enthalpy of an ideal gas is independent of pressure, and $\Delta H = \int_{T^1}^{T^2} C_p^{IG}(T)\mathrm{d}T$ does not predict Joule-Thompson cooling, which is essential to the operation of throttle valves in refridgeration cycles. As a workaround, correlations for gas and liquid enthalpies are regressed using thermodynamic data. This approach is consistent with the purpose of the simple thermodynamic models, which is to obtain reasonable results for initialization of rigorous models. Moreover, it avoids explicit consideration (and tuning) of Joule-Thomson equations for valves. For each component in the flowsheet, a large temperature and pressure space was sampled with the Peng-Robinson EoS in Aspen Plus for pure substances. Equations (2.25a) and (2.25b) were fit to the vapor and liquid data, respectively, using linear regression techniques. Stream enthalpies are obtained by assuming ideal mixing as follows:

$$\begin{aligned} H_s = \sum_{c\in\mathcal{C}} x_{s,c}[&\mathcal{H}_{v,c}^1 + \mathcal{H}_{v,c}^2 P_s + \mathcal{H}_{v,c}^3 P_s^2 + \mathcal{H}_{v,c}^4 T_s^* + \mathcal{H}_{v,c}^5 (T_s^*)^2 \\ &+ \mathcal{H}_{v,c}^6 (T_s^*)^3 + \mathcal{H}_{v,c}^7 T_s^* P_s + \mathcal{H}_{v,c}^8 (T_s^*)^2 P_s], \\ &\forall s \in \mathcal{S}_{Vap} \cup \mathcal{S}_{Vap}^{Flash}, \quad \forall c \in \mathcal{C} \end{aligned} \tag{2.25a}$$

$$\begin{aligned} H_s = \sum_{c\in\mathcal{C}} x_{s,c}[&\mathcal{H}_{l,c}^1 + \mathcal{H}_{l,c}^4 T_s^* + \mathcal{H}_{l,c}^5 (T_s^*)^2 + \mathcal{H}_{l,c}^6 (T_s^*)^3 + \mathcal{H}_{l,c}^7 T_s^* P_s] \\ &+ \mathcal{H}_{l,c}^8 (T_s^*)^2 P_s, \quad \forall s \in \mathcal{S}_{Liq} \cup \mathcal{S}_{Liq}^{Flash}, \quad \forall c \in \mathcal{C} \end{aligned} \tag{2.25b}$$

The framework supports different coefficients in these models for each flowsheet zone, which is essential for processes with multiple sections that operate at vastly different conditions (e.g., high versus low pressure).

2.5 Cubic Equation of State Thermodynamics Module

Cubic equations of state thermodynamic models, such as Peng-Robinson (PR) and Soave-Redlich-Kwong (SRK) models, are popular choices for process simulation with non-polar and slightly polar mixtures, as these models balance computational expense and accuracy. The most general form of cubic equations of state is

$$f(Z) = Z^3 - (1 + B - uB)Z^2 + (A + wB^2 - uB - uB^2)Z \\ -AB - wB^2 - wB^3 = 0 \ , \tag{2.26}$$

where A and B are dimensionless coefficients that depend on temperature, pressure and phase composition, and are defined as follows,

$$Z_s = \frac{P_s V_s}{RT_s} \tag{2.27a}$$

$$A_s = \frac{a_s^m P_s}{R^2 T_s^2} \tag{2.27b}$$

$$B_s = \frac{b_s^m P_s}{RT_s} \ , \tag{2.27c}$$

where a^m and b^m are mixture properties (defined below). Additional EoS specific values and formulas are given in Table 2.1. $\bar{t}_c$ and $\bar{p}_c$ are the critical point temperature and pressure for pure component c, respectively. $a_{s,c}$ is calculated for each stream as follows,

$$a_{s,c} = \frac{\underline{a} R^2 \bar{t}_c^2}{t_c} \hat{\alpha}_{s,c}, \quad \forall c \in \mathcal{C} \tag{2.28a}$$

$$\hat{\alpha}_{s,c} = [1 + f^\omega (1 - \sqrt{T_s / \bar{t}_c})]^2, \quad \forall c \in \mathcal{C} \tag{2.28b}$$

where ω_c is the component specific acentric factor. b_c and other constants are defined in Table 2.1. The formula for $\hat{\alpha}_{s,c}$ is cubic EoS specific, and (2.28b) applies for the SRK and PR models.

Table 2.1: Formulas and parameters for two popular cubic EoS models (Reid, Prausnitz, and Poling, 1987)

	Soave (SRK)	Peng-Robinson (PR)
u	1	2
w	0	-1
$\underline{a}$	0.42748	0.45724
b_c	$\underline{b} R \bar{t}_c / \bar{p}_c$	
$\underline{b}$	0.08664	0.07780
f_c^ω	$0.48 + 1.574\omega_c - 0.176\omega_c^2$	$0.37464 + 1.54226\omega_c - 0.26992\omega_c^2$

Mixing rules with interaction terms are used to improve the prediction of mixture properties and phase equilibria. For two constant cubic equations of state, including the SRK and PR models, Reid, Prausnitz, and Poling (1987) recommend the following mixing rules:

$$a_s^m = \sum_{i\in\mathcal{C}}\sum_{j\in\mathcal{C}} x_i x_j \sqrt{a_{s,i}a_{s,j}(1-k_{i,j})} \tag{2.29a}$$

$$b_s^m = \sum_{i\in\mathcal{C}} x_{s,i} b_i \ . \tag{2.29b}$$

The binary interaction parameters, $k_{i,j}$, are fit for each component-EoS combination. Values published by Knapp et al. (1982) are used in this thesis. Finally, $\forall s \in \mathcal{S}$ is implied for (2.26) - (2.29).

2.5.1 Property Calculations

Thermodynamic properties are calculated using departure functions,

$$\begin{aligned} H_s - H_s^\circ = &\left(a_s^m - T_s\frac{\partial a_s^m}{\partial T_s}\right)\frac{1}{b_s^m\sqrt{u^2-4w}}\ \ln\left[\frac{2Z_s + B_s(u-\sqrt{u^2-4w})}{2Z_s + B_s(u+\sqrt{u^2-4w})}\right] \\ &+ RT_s(Z_s-1) \end{aligned} \tag{2.30}$$

$$\begin{aligned} S_s - S_s^\circ = &R\ \ln\left(\frac{Z_s - B_s}{Z_s}\right) + R\ \ln\left(\frac{V_s}{V_s^\circ}\right) \\ &- \frac{\partial a_s^m}{\partial T_s}\frac{1}{b_s^m\sqrt{u^2-4w}}\ \ln\left[\frac{2Z_s + B_s(u-\sqrt{u^2-4w})}{2Z_s + B_s(u+\sqrt{u^2-4w})}\right] \end{aligned} \tag{2.31a}$$

$$\frac{\partial a_s^m}{\partial T_s} = -\frac{R}{2}\sqrt{\frac{\Omega_a}{T_s}}\sum_{i\in\mathcal{C}}\sum_{j\in\mathcal{C}} x_{s,i}x_{s,j}(1-k_{i,j})\left[f_{\omega,j}\sqrt{\frac{a_{s,i}\bar{t}_j}{\bar{p}_j}} + f_{\omega,i}\sqrt{\frac{a_{s,j}\bar{t}_i}{\bar{p}_i}}\right] \tag{2.31b}$$

where H° and S° are the enthalpy and entropy of the ideal gas mixture at a reference state with a specified (fixed) pressure, P°, and the actual stream temperature T_s. Specific volume for the reference state is calculated as follows,

$$V_s^\circ = \frac{RT_s}{P^\circ} \ . \tag{2.32}$$

The enthalpy of a corresponding ideal gas mixture at the reference state is calculate by integrating a polynomial model for constant pressure specific heat with respect to temperature:

$$\begin{aligned} H_s^\circ &= \sum_{c\in\mathcal{C}} x_{s,c}\int_{T^\circ}^{T_s}\left(\frac{\partial H}{\partial T}\right)_P \mathrm{d}t \\ &= \sum_{c\in\mathcal{C}} x_{s,c}\int_{T^\circ}^{T_s}\left(C_c^V t^4 + C_c^{IV}t^3 + ... + C_c^I\right)\mathrm{d}t \\ &= \sum_{c\in\mathcal{C}} x_{s,c}\left(\frac{C_c^{\mathrm{V}}(T^\circ)^5}{5}[(T_s^*)^5 - 1] + ... + C_c^{\mathrm{I}}(T^\circ)[(T_s^*) - 1]\right) \end{aligned} \tag{2.33}$$

where $T_s^* = T_s/T^\circ$[2] and $C_c^I, C_c^{II}, ..., C_c^V$ are component specific constants.

Similarly, ideal gas entropy is calculated by integrating the expression $\mathrm{d}S = C_V \mathrm{d}T + R\mathrm{d}V$, and substituting $C_p = C_v + R$:

$$\begin{aligned}
S_s^\circ &= \sum_{c\in\mathcal{C}} x_{s,c} \int_{T^\circ}^{T_s} \frac{\left(\frac{\partial H}{\partial T}\right)_V}{t}\mathrm{d}t + R\int_{V^\circ}^{V_s} \frac{v}{\mathrm{d}v} \\
&= \sum_{c\in\mathcal{C}} x_{s,c} \int_{T^\circ}^{T_s} \frac{\left(\frac{\partial H}{\partial T}\right)_V}{t}\mathrm{d}t + R\ln\left(\frac{V_s}{V^\circ}\right) \\
&= \sum_{c\in\mathcal{C}} x_{s,c} \int_{T^\circ}^{T_s} \frac{\left(\frac{\partial H}{\partial T}\right)_P - R}{t} - R\mathrm{d}t + R\ln\left(\frac{V_s}{V^\circ}\right) \\
&= \sum_{c\in\mathcal{C}} x_{s,c} \int_{T^\circ}^{T_s} \frac{\left(\frac{\partial H}{\partial T}\right)_P}{t}\mathrm{d}t - R\ln\left(\frac{T_s}{T^\circ}\right) + R\ln\left(\frac{T_s}{T^\circ}\right) \\
&= \sum_{c\in\mathcal{C}} x_{s,c} \int_{T^\circ}^{T} \left(C_v^V t^3 + C_v^{IV} t^2 + ... + C_c^I/t\right)\mathrm{d}t \\
&= \sum_{c\in\mathcal{C}} x_{s,c} \left(\frac{C_c^{\mathrm{V}}(T^\circ)^4}{4}[(T_s)^4 - 1] + ... + C_c^{\mathrm{I}}\ln(T_s/T^\circ)\right) \ .
\end{aligned} \tag{2.34}$$

Through the application of (2.32), $\ln\frac{V_s}{V^\circ} = \ln\frac{T_s}{T^\circ}$. Finally, the fugacity coefficient is defined as follows,

$$\forall c \in \mathcal{C},$$

$$\begin{aligned}
\ln(\phi_{s,c}) = \frac{b_c}{b_s^m}(Z_s - 1) - \ &\ln(Z_s - B_s) \\
&+ \frac{A_s}{B_s\sqrt{u^2-4w}}\left(\frac{b_c}{b_s^m} - \delta_{s,c}\right)\ln\left[\frac{2Z_s + B_s(u+\sqrt{u^2-4w})}{2Z_s + B_s(u-\sqrt{u^2-4w})}\right]
\end{aligned} \tag{2.35a}$$

$$\frac{b_c}{b_s^m} = \frac{\bar{t}_c/\bar{p}_c}{\sum_{j\in\mathcal{C}} x_j \bar{t}_j/\bar{p}_j} \tag{2.35b}$$

$$\delta_{s,c} = \frac{2\sqrt{a_{s,c}}}{a_s^m}\sum_{j\in\mathcal{C}} x_{s,j}\sqrt{a_{s,j}}(1-k_{c,j}) \ . \tag{2.35c}$$

In order to simply the above formulas, a constant (I_0) and four intermediate variables ($\hat{I}^1$ - $\hat{I}^4$) are defined,

[2]In the GAMS implementation, all stream temperatures are scaled by T°, which is typically specified as 273.15 K or 298.15 K. This scaling in not shown in the equation declarations for simplicity.

$$I_0 = \sqrt{u^2 - 4w} \tag{2.36a}$$

$$\exp(\hat{I}_s^1) = Z_s - B_s \tag{2.36b}$$

$$\exp(\hat{I}_s^2) = \frac{Z_s - B_s}{Z_s} \tag{2.36c}$$

$$\exp(\hat{I}_s^3) = \left[\frac{2Z_s + B_s(u + I_0)}{2Z_s + B_s(u - I_0)}\right] \tag{2.36d}$$

$$\exp(\hat{I}_s^4) = \frac{Z_s P^\circ}{P_s} = \frac{V_s}{V_s^\circ}\ , \tag{2.36e}$$

and substituted into (2.30), (2.31a) and (2.35a) to replace the $\ln(\cdot)$ terms. Finally, $\forall s \in \mathcal{S}$ is implied for (2.30) - (2.36).

2.5.2 Bubble and Dew Point Calculations

Streams contained in $\mathcal{S}_{bub}$ and $\mathcal{S}_{dew}$ are constrained to be at their bubble and dew points, respectively. To accomplish this, every stream in $\mathcal{S}_{bub}$, $\mathcal{S}_{dew}$ and $\mathcal{S}_{check}$ (discussed in Section 2.5.5) is assigned both a vapor and liquid shadow stream, which are contained in $\mathcal{S}_{shdw}^V$ and $\mathcal{S}_{shdw}^L$, respectively. In the framework, shadow streams are hypothetical and do not correspond to any pipes in the flowsheet, but are instead used for "internal" calculations (bubble and dew points, isentropic compressor efficiencies, etc.). The process stream-vapor shadow-liquid shadow mappings are contained in $\mathcal{S}_{shdw}^{map}$. Furthermore, the shadow streams are defined such that $\mathcal{S}_{shdw}^V \subset \mathcal{S}_{Vap}$, $\mathcal{S}_{shdw}^L \subset \mathcal{S}_{Liq}$,

$$\forall (s, \tilde{s}^v, \tilde{s}^l) \in \{\mathcal{S}_{bub} \times \mathcal{S}_{shdw}^V \times \mathcal{S}_{shdw}^L\} \cap \mathcal{S}_{shdw}^{map},$$
$$\sum_{c \in \mathcal{C}} (x_{s,c} - \tilde{y}_{\tilde{s}^v,c}) = 0 \tag{2.37a}$$

$$T_s = \tilde{T}_{\tilde{s}^v} \tag{2.37b}$$

$$P_s = \tilde{P}_{\tilde{s}^v} \tag{2.37c}$$

$$x_{s,c}\phi_{s,c} = \tilde{y}_{\tilde{s}^v,c}\tilde{\phi}_{\tilde{s}^v,c}, \quad \forall c \in \mathcal{C} \tag{2.37d}$$

for bubble point calculations and

$$\forall (s, \tilde{s}^v, \tilde{s}^l) \in \{\mathcal{S}_{dew} \times \mathcal{S}_{shdw}^V \times \mathcal{S}_{shdw}^L\} \cap \mathcal{S}_{shdw}^{map},$$
$$\sum_{c \in \mathcal{C}} \left(\tilde{x}_{\tilde{s}^l,c} - y_{s,c}\right) = 0 \tag{2.38a}$$

$$T_s = \tilde{T}_{\tilde{s}^l} \tag{2.38b}$$

$$P_s = \tilde{P}_{\tilde{s}^l} \tag{2.38c}$$

$$\tilde{x}_{\tilde{s}^l,c}\tilde{\phi}_{\tilde{s}^l,c} = y_{s,c}\phi_{s,c}, \quad \forall c \in \mathcal{C} \tag{2.38d}$$

for dew point calculations. Shadow streams properties are denoted as $\tilde{T}$, $\tilde{P}$, $\tilde{x}$, $\tilde{y}$ and $\tilde{\phi}$ in the equations above for clarity. Similarly, $\tilde{s}$ is used to index shadow streams. Other equations in the cubic EoS module, such as (2.26) - (2.36), also apply to shadow streams (as $\mathcal{S}_{shdw}^V \subset \mathcal{S}_{Vap}$, $\mathcal{S}_{shdw}^L \subset \mathcal{S}_{Liq}$).

2.5.3 Root Selection

There are up to three real roots for (2.26), depending on location in temperature-pressure-composition space. Kamath, Biegler, and Grossmann (2010) proposed an equation-based strategy to map roots to phases for cubic EoS thermodynamic models. Most notably, their approach avoids heuristics, iterations and logic conditions used in many traditional process simulators for root selection. In summary, they proved the first derivative of the cubic equation with respect to Z must be positive to avoid the erroneous middle root. Furthermore, the sign of the second derivative determines the phase (vapor or liquid):

$$f'(Z_s) = 3Z_s^2 - 2(1 + B_s - uB_s)Z_s + A_s + wB_s^2 - uB_s - uB_s^2 \geq 0, \quad \forall s \in \mathcal{S} \tag{2.39}$$

$$f''(Z_s) = 6Z_s - 2(1 + B_s - uB_s) \geq 0, \quad \forall s \in \mathcal{S}_{Vap} \tag{2.40a}$$

$$f''(Z_s) = 6Z_s - 2(1 + B_s - uB_s) \leq 0, \quad \forall s \in \mathcal{S}_{Liq}\ . \tag{2.40b}$$

These rules are further relaxed using the slack variables σ^V and σ^L,

$$f''(Z_s) = 6Z_s - 2(1 + B_s - uB_s) \geq -M\sigma_s^V, \quad \forall s \in \mathcal{S}_{Vap}^{Flash} \setminus \mathcal{S}_{sup} \tag{2.41a}$$

$$f''(Z_s) = 6Z_s - 2(1 + B_s - uB_s) \leq M\sigma_s^L, \quad \forall s \in \mathcal{S}_{Liq}^{Flash} \setminus \mathcal{S}_{sup}\ . \tag{2.41b}$$

Equation (2.39) may be optionally relaxed with σ_s^V and σ_s^L $\forall s \in \mathcal{S}_{Vap}^{Flash} \cup \mathcal{S}_{Liq}^{Flash}$. $\mathcal{S}_{sup}$ is defined later.

These constraint boundaries are shown in Figure 2.1, where the solid black line corresponds to $f'(Z) = 0$. Inside this triangle-like region there are three distinct real roots for Z in (2.26), whereas outside this region there is only one real root. The critical point is at the "tip" of the region. See the Appendix and Poling, Grens, and Prausnitz (1981) for further discussion of the relationship between $f'(Z) = 0$ and the number of real roots. The dashed black line corresponds to $f''(Z) = 0$, which is the transition between vapor and liquid phases in the single root region (outside the black triangle), per (2.41). The bubble and dew point curves for this fixed composition are also shown in blue and red, respectively, and the two phase region is located between these two curves. Further investigation of this figure leads to two observations:

1. The sign of $f''(Z)$ does not properly distinguish between phases outside of the three real root region. Consider a mixture at 200 K and 100 bar on Figure 2.1, which is properly classified as a liquid ($f''(Z) < 0$) and is well

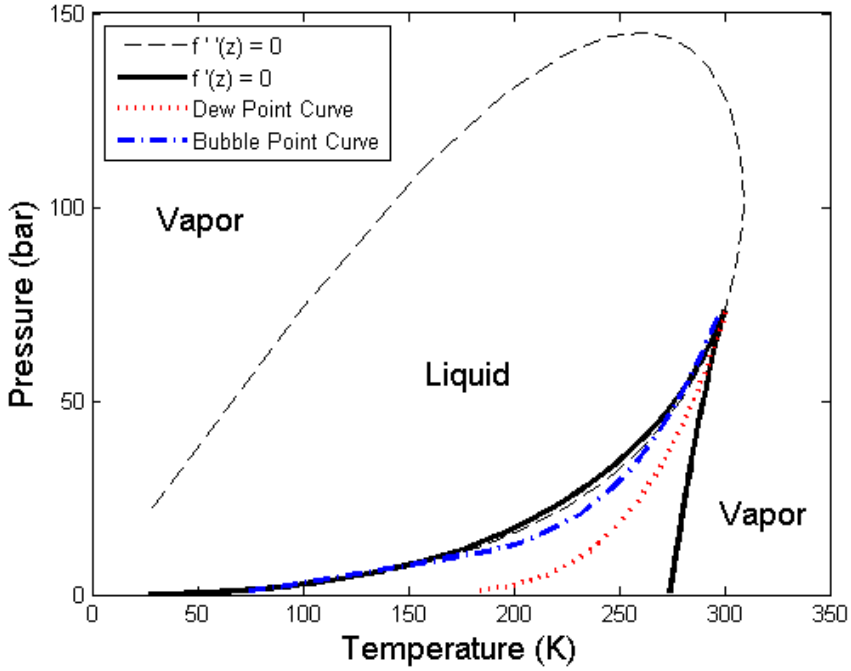

Figure 2.1: Visualization of $f''(Z)$ and $f'(Z)$ phase identification constraints for a mixture of 97 mol% CO_2 and 1% Ar, O_2 and N_2 (each).

above the bubble point curve. The sign of $f''(Z)$ predicts a transition to vapor as the mixture is isothermally (T = 200 K) compressed to 150 bar. This transition, however, is only a mathematical artifact and does not occur in nature.

2. The bubble and dew point curves, i.e., the boundaries of the two phase region, do not correspond to the boundary of the three root region. For example, consider the mixture at 250 K and 15 bar. This point is below the dew point curve, and thus must be only a vapor. However, this point is also in the three root region and a liquid root for Z exists at this point. Thus (2.40) are necessary but not sufficient to predict the proper number of phases. Additional information, such as component fugacities, must also be considered.

2.5.4 Correcting Supercritical Phase Classifications

Regarding observation 1, Kamath, Biegler, and Grossmann (2010) proved that (2.41) hold when there are three distinct real roots for Z. As shown by Figure 2.1, their conjecture that these equations extend to the single root region (only one distinct real root) fails, especially for a supercritical mixture. We propose an extension of the Kamath, Biegler, and Grossmann (2010) formulation that mimics the behavior in Figure 2.2 (and is consistent with simulators such as Aspen Plus). Here, the pressure-temperature (PT) phase diagram is divided

into four quadrants with the critical point, ($\bar{T}_s$,$\bar{P}_s$), at the origin. In quadrant I ($T_s > \bar{T}_s$, $P_s > \bar{P}_s$), i.e., the supercritical region, the mixture may be classified as either vapor or liquid. This allows pumps (liquid only) and compressors (vapor only) to operate in quadrant I without modification of the equipment models. Similarly, quadrants II ($T_s < \bar{T}_s$, $P_s > \bar{P}_s$) and III ($T_s > \bar{T}_s$, $P_s < \bar{P}_s$) correspond to liquid only and vapor only regions, respectively. The phase classification and equilibrium models from Kamath, Biegler, and Grossmann (2010) are maintained in the subcritical quadrant III ($T_s < \bar{T}_s$, $P_s < \bar{P}_s$). These models, however, must be relaxed in quadrants I and II. In quadrant IV, however, (2.40a) correctly classifies the mixture as a vapor, as shown in Figure 2.1. Thus, the models proposed by Kamath, Biegler, and Grossmann (2010) do not need to be relaxed here.

In many processes, the modeler knows *a priori* a majority of the streams will never be near the critical point. Therefore, the relaxations described below are only considered for streams in $\mathcal{S}_{sup}$, which is specified by the modeler. This helps reduce the number of equations in flowsheet optimization problems.

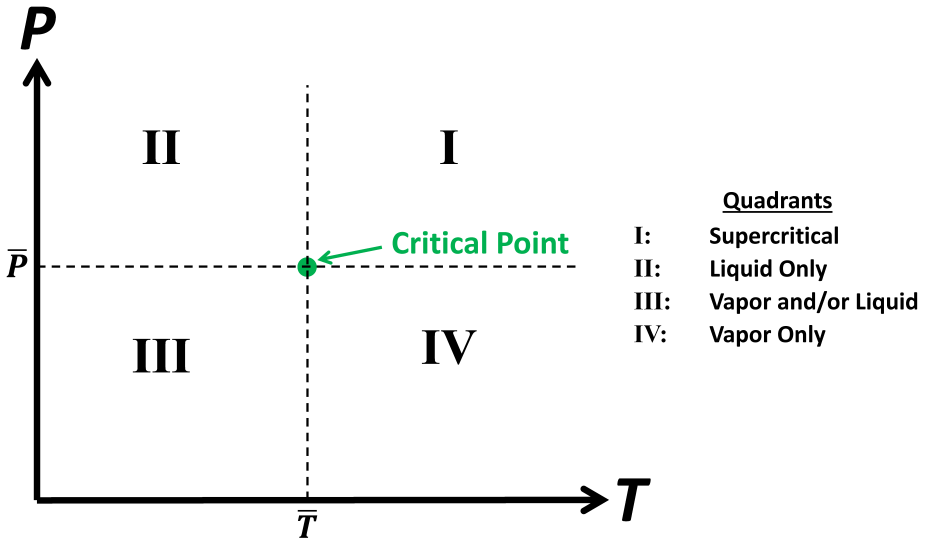

Figure 2.2: The PT phase diagram divided into four quadrants. Quadrant I corresponds to the supercritical region, which may be classified as either vapor or liquid. Quadrants II and IV correspond to liquid and vapor only regions, respectively. In quadrants I and II, the phase classifications rules based on $f''(Z)$ must be relaxed. Standard vapor-liquid equilibrium calculations are maintained in quadrants III and IV (subcritical P).

2.5.4.1 Equilibrium Relaxation

First consider relaxation of (2.20f), (2.20h) and (2.41), which occurs outside of quadrants III or IV, i.e., whenever $P_s > \bar{P}_s$. This switch is easily modeled using complementarities:

$$P_s + \sigma_s^P \geq \bar{P}_s, \quad \forall s \in \mathcal{S}_{sup} \tag{2.42a}$$
$$0 \leq \sigma_s^P \perp \xi_s \geq 0, \quad \forall s \in \mathcal{S}_{sup}\ , \tag{2.42b}$$

where σ_s^P is a slack variable for pressure. When outside quadrants III or IV, $\sigma_s^P = 0$, and the slack variable ξ_s may be greater than 0. The latter slack variable is used to relax the phase selection and equilibrium equations:

$$-(\sigma_s^L + \xi_s) \leq \hat{\beta}_g, \quad \forall (s,g) \in \{\mathcal{S}_{Liq}^{Flash} \cap \mathcal{S}_{sup} \times \mathcal{T}\} \cap \mathcal{G}_{out}^L \tag{2.43a}$$
$$\hat{\beta}_g \leq \sigma_s^V + \xi_s, \quad \forall (s,g) \in \{\mathcal{S}_{Vap}^{Flash} \cap \mathcal{S}_{sup} \times \mathcal{T}\} \cap \mathcal{G}_{out}^V \tag{2.43b}$$
$$f''(Z_s) \leq M(\sigma_s^L + \xi_s), \quad \forall s \in \mathcal{S}_{Liq}^{Flash} \cap \mathcal{S}_{sup} \tag{2.43c}$$
$$f''(Z_s) \geq -M(\sigma_s^V + \xi_s), \quad \forall s \in \mathcal{S}_{Vap}^{Flash} \cap \mathcal{S}_{sup}\ , \tag{2.43d}$$

where (2.43a) & (2.43b) replace (2.20g) & (2.20h). This strategy is also compatible with (2.19) if $\beta - 1$ is substituted for $\hat{\beta}$ in (2.43a) & (2.43b). $\mathcal{G}_{out}^L$, $\mathcal{G}_{out}^V$ and $\mathcal{T}$ are defined in Section 2.7 and are used to manage flowsheet connectivity.

2.5.4.2 Phase Selection in Quadrant II

Next, consider quadrant II and its liquid only logical constraint, which occurs when $P_s > \bar{P}_s$ and $T_s < \bar{T}_s$. This logical condition can be reformulated into a complementarity constraint using a few additional slack variables. First, define $\Omega_s = \max(\bar{P}_s - P_s, T_s - \bar{T}_s)$. When $\Omega_s < 0$, the stream is in quadrant II and there must be no vapor. Thus,

$$\forall s \in \mathcal{S}_{sup} \cap \left(\mathcal{S}_{Vap} \cup \mathcal{S}_{Vap}^{Flash}\right),$$
$$0 \leq \Omega_s - (\bar{P}_s - P_s) \perp \Omega_s - (T_s - \bar{T}_s) \geq 0 \tag{2.44a}$$
$$\Omega_s = \sigma_s^{2a} - \sigma_s^{2b} \tag{2.44b}$$
$$0 \leq \sigma_s^{2a} \perp \sigma_s^{2b} \geq 0 \tag{2.44c}$$
$$0 \leq \sigma_s^{2b} \perp F_s \geq 0\ , \tag{2.44d}$$

where the max operator is replaced by the addition complementarity constraint (2.44a). Because $f''(Z) \leq 0$ correctly classifies mixtures as vapor in quadrant IV, there is no need for additional equations in this region.

2.5.4.3 Critical Point Calculations

The final aspect of this reformulation is calculation of the critical point properties, $\bar{T}$ and $\bar{P}$, in a manner consistent with mixing rules used in the cubic EoS model. The critical point is defined as the temperature and pressure at which $\left(\frac{\partial P}{\partial V}\right)_T = 0$ and $\left(\frac{\partial^2 P}{\partial V^2}\right)_T = 0$. Using the chain rule, it is possible to show this is equivalent to (2.45b) and (2.45c). System (2.45) is solved for unique numeric values of Z, A, and B at the critical point, which depend on

cubic EoS specific coefficients, but are independent of mixture composition or mixing rule selection. Values for two popular cubic equations of state are shown in Table 2.2. The results for the SRK model ($\bar{Z} = 1/3$) are consistent with the observations of Gundersen (1982).

$$f(Z, A, B) = 0 \tag{2.45a}$$

$$\left(\frac{\partial f}{\partial Z}\right)_{A,B} = f'(Z, A, B) = 0 \tag{2.45b}$$

$$\left(\frac{\partial^2 f}{\partial Z^2}\right)_{A,B} = f''(Z, A, B) = 0\ . \tag{2.45c}$$

Table 2.2: Numeric values for Z, A and B at the critical point

	$\bar{Z}$	$\bar{A}$	$\bar{B}$
Peng-Robinson	0.30740...	0.45724...	0.077796...
Soave-Redlich-Kwong	1/3	0.42748...	0.086640...

Mixture properties $\bar{T}_s$ and $\bar{P}_s$ are obtained by solving the following nonlinear system of equations:

$$\bar{a}_{s,c} = \frac{aR^2\bar{t}_c^2}{\bar{p}_c}\alpha(\omega_c, \bar{t}_c, \bar{T}_s), \quad \forall c \in \mathcal{C}, \quad \forall s \in \mathcal{S}_{sup} \tag{2.46a}$$

$$\bar{a}_s^m = \sum_{i\in\mathcal{C}}\sum_{j\in\mathcal{C}} x_i x_j \sqrt{a_{s,i}a_{s,j}(1-k_{i,j})}, \quad \forall s \in \mathcal{S}_{sup} \tag{2.46b}$$

$$\bar{A} = \frac{\bar{a}_s^m \bar{P}_s}{\bar{T}_s^2 R^2}, \quad \forall s \in \mathcal{S}_{sup} \tag{2.46c}$$

$$\bar{B} = \frac{b_s^m \bar{P}_s}{\bar{T}_s R}, \quad \forall s \in \mathcal{S}_{sup}\ , \tag{2.46d}$$

where b_s^m is already calculated in (2.29b) and b_c is constant.

Unfortunately, (2.46) does not have a closed form solution for the PR and SRK models, due to the nonlinear nature of $\hat{\alpha}(\cdot)$, which is defined in (2.28b). Instead this system of equations is embedded in the flowsheet optimization problem with the numerical values for $\bar{A}$ and $\bar{B}$ taken from Table 2.2.

2.5.5 Avoiding Nonphysical Single-Phase Equilibrium Solutions

For most nonideal thermodynamic models the Gibbs free energy minimization problem (2.2) is nonconvex and may have multiple local solutions. Of course, the global minimum is preferred, as this is the most stable energy state. To

address the concerns of meta-stable solutions, Michelsen (1982a,b) proposes a numeric implementation of the Gibbs tangent plane criterion:

$$\psi(\tilde{\mathbf{z}}) = \sum_{i \in \mathcal{C}} \tilde{\mathbf{z}}_i \left(\mu_i(\tilde{\mathbf{z}}) - \mu_i(\mathbf{z}) \right) \geq 0 \ , \tag{2.47}$$

where $\mu_i(\cdot)$ is the chemical potential of species i at a specified composition, $\mathbf{z}$ is the composition at the equilibrium solution under analysis and $\tilde{\mathbf{z}}$ is a trial composition. (2.47) must be valid for all feasible trial compositions (i.e., $||\tilde{\mathbf{z}}||_1 = 1, \ \tilde{z}_i \geq 0 \ \forall i \in \mathcal{C}$), thus explicitly adding (2.47) to an optimization problem results in a semi-infinite program. Practically, this is implemented by checking $\psi(\tilde{\mathbf{z}}) \geq 0$ for all stationary points of min $\psi(\tilde{\mathbf{z}})$, s.t. $\sum_{i \in \mathcal{C}} \tilde{z}_i = 1$. If $\psi(\tilde{\mathbf{z}}) \leq 0$, then $\mathbf{z}$ is only a meta-stable solution, and flash calculations should be extended to consider an additional phase with $\tilde{\mathbf{z}}$ as its initial composition. Michelsen (1982a) recommends identifying these stationary points using multi-start initialization, which is not guaranteed to find all of the points.

Alternately, several studies apply rigorous, deterministic global optimization algorithms to phase equilibrium calculations (McDonald and Floudas, 1995; Harding and Floudas, 2000; Nichita, Gomez, and Luna, 2002b,a; Nichita and Gomez, 2009). Similarly, Mitsos and Barton (2007) proposed a global optimization algorithm based on a Lagrangian dual interpretation of Gibbs tangent plane stability criterion. Alternately, Hua, Brennecke, and Stadtherr (1998) proposed an interval arithmetic approach. Although global optimization and interval arithmetic provide guarantees that equilibrium calculations are correct, further work is required to efficiently embed these calculations in an equation-based flowsheet framework with hundreds of flash calculations. Multiple local solutions are closely related to the trivial root problem discussed by several others (Boston and Mathias, 1980; Poling, Grens, and Prausnitz, 1981; Gundersen, 1982). Reid, Prausnitz, and Poling (1987) recommend careful initialization as the best safeguard against trivial solutions. Furthermore, derivatives of physical property calculations may be undefined at the bubble and dew point when a phase vanishes, which would result in a nonsmooth optimization problem. In contrast, this work focuses on computationally efficient, robust and flexible approaches to avoid a specific class of nonphysical/false equilibrium solutions.

In order to better understand non-global solutions of (2.2), a mixture of 97 mol% CO_2 and 1 mol% Ar, O_2 and N_2 is considered at 225K and 8 bar, which is in the two phase region, i.e., between the bubble point and dew point curves, as shown in Figures 2.1. Phase equilibrium is calculated by solving

$$
\begin{aligned}
\min \quad & \zeta + \rho(L \cdot \sigma^L + V \cdot \sigma^V) \\
\text{s.t.} \quad & \zeta = \sum_{c\in\mathcal{C}} \Big[l_c(\ln \phi_c^L + \hat{x}_c) + v_c(\ln \phi_c^V + \hat{y}_c) \Big] && \text{(2.48a)} \\
& L = \sum_{c\in\mathcal{C}} l_c, \quad V = \sum_{c\in\mathcal{C}} v_c && \text{(2.48b)} \\
& \sum_{c\in\mathcal{C}} (x_c - y_c) = 0 && \text{(2.48c)} \\
& L, V \geq 0 && \text{(2.48d)} \\
& l_c + v_c = m_c && \text{(2.48e)} \\
& x_c = \exp(\hat{x}_c), \quad y_c = \exp(\hat{y}_c) && \text{(2.48f)} \\
& \ln \phi_c = \ldots \qquad \text{See (2.35) and (2.36)} \\
& \text{Other cubic EoS formulas: (2.26) - (2.29), (2.39), (2.41)} \\
& \varepsilon^x \leq \hat{x}_c, \hat{y}_c \leq 0 && \text{(2.48g)} \\
& 0 \leq x_c, y_c \leq 1 \ , && \text{(2.48h)}
\end{aligned}
$$

where m_c, T and P are constants, $\rho = 10$, $\varepsilon^x = \ln(10^{-16})$ and $\forall c \in \mathcal{C}$ is implied for (2.48e) - (2.48h). The complementarity constraints are incorporated as a penalty into the objective function. With temperature and pressure constant, $\arg\min \zeta = \arg\min G$.

Depending on the initialization for (2.48), CONOPT finds three local solutions ($L = 0$, $V = 0$ and $V, L > 0$), as shown in Table 2.3. The two phase solution ($V, L > 0$) is the global solution for this temperature and pressure. The single-phase solutions (Cases A and B in Table 2.3) are a consequence of the complementarity constraints, and more generally nonconvex features added to the vapor-liquid equilbrium problem when the number of phases is not known *a priori*. For the Case A and B solutions, $Z_L = Z_V$ and $x_c = y_c$, thus $\phi_c^V = \phi_c^L$ and $K_c = 1 \ \ \forall c \in \mathcal{C}$. When this occurs, $y_c = K_c x_c$ is always satisfied. These "$K = 1$" solutions were previously reported by Gundersen (1982), and now require either $\sigma^V > 0$ or $\sigma^L > 0$ to relax $f''(Z_V) \geq 0$ or $f''(Z_L) \leq 0$.

Table 2.3: Solutions of (2.48) from three different initial points. Cases A and B corresponds to vapor-only and liquid-only mixtures, which are non-global solutions of (2.48). In contrast, Case C predicts a two-phase mixture, which is the global solution of (2.48) at the specified $T = 225$ K, $P = 8$ bar and $m_c = z_c^f$. l_c and v_c are initialized to be consistent with the values of L, V, x_c and y_c shown below. The order of components for $\mathbf{x}$ and $\mathbf{y}$ is CO_2, Ar, N_2, O_2. Let $\mathbf{z^f} = [0.97, 0.01, 0.01, 0.01]^T$.

Initial Points	**Case A**	**Case B**	**Case C**
Z_L	0.8	0.02	0.02
$\mathbf{x}$	$\mathbf{z^f}$	$\mathbf{z^f}$	$[0.99, 0.003, 0.003, 0.003]^T$
L	0	1	0.5
σ^L	10	0	0
Z_V	0.8	0.02	0.8
$\mathbf{y}$	$\mathbf{z^f}$	$\mathbf{z^f}$	$[0.5, 0.167, 0.167, 0.167]^T$
V	1	0	0.5
σ^V	0	10	0
Solutions	**Case A**	**Case B**	**Case C**
Z_L	0.897	0.016	0.016
$\mathbf{x}$	$\mathbf{z^f}$	$\mathbf{z^f}$	$[0.998, 0.001, 0.000, 0.001]^T$
L	0	1	0.341
σ^L	10	0	0
Z_V	0.897	0.016	0.904
$\mathbf{y}$	$\mathbf{z^f}$	$\mathbf{z^f}$	$[0.916, 0.028, 0.029, 0.028]^T$
V	1	0	0.659
σ^V	0	10	0
K_{CO_2}	1.000	1.000	0.918
K_{Ar}	1.000	1.001	31.238
K_{N_2}	1.000	1.002	68.823
K_{O_2}	1.000	1.001	29.776
ζ	-0.266	-0.239	-0.291

Furthermore, we have also observed nonphysical single-phase equilibrium solutions with distinct values for x and y, $K_c \neq 1$, either $\sigma^V > 0$ or $\sigma^L > 0$ and with the two values for Z in the same phase region (either both $f''(Z) < 0$ or $f''(Z) > 0$). These nonphysical single-phase solutions were observed in the case studies as a means to cheat thermodynamics by adjusting stream temperatures used for heat integration, which resulted in low objective function values (and process designs that violated physics!).

As illustrated in Figure 2.3, this class of nonphysical single-phase solutions are located inside the two phase region. The most straightforward approach to eliminate these nonphysical solutions is to constrain the equilibrium temperature to be on the proper side of the bubble and dew point curves,

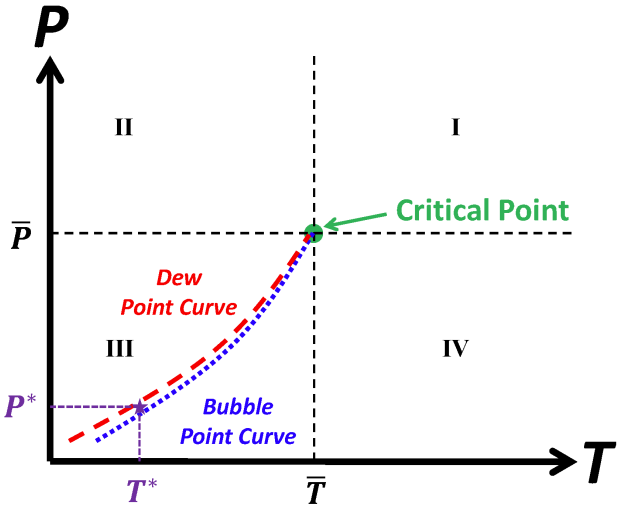

(a) Narrow boiling mixture (e.g., 79% N_2 - 21% O_2)

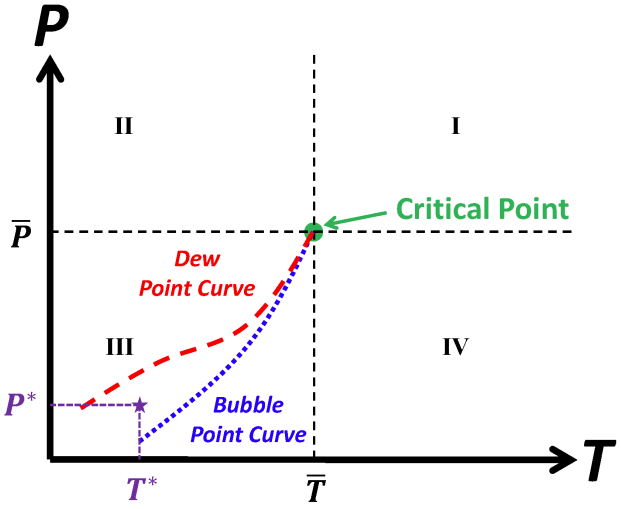

(b) Wide boiling mixture (e.g., 95% CO_2 - 5% N_2)

Figure 2.3: Bubble and dew point curves (fixed composition) overlaid onto the four quadrant phase diagram. Without (2.49), it is possible for a single phase solution of (2.19) - (2.41), denoted (T^*, P^*), to lie between the bubble and dew point curves, i.e., $T^{dew}(P^*) < T^* < T^{bub}(P^*)$.

$$\begin{aligned} &T_s \leq T_s^{bub}(P_s, x_s) + M\sigma_s^L, \\ &\forall s \in \left(\mathcal{S}_{Liq} \cup \mathcal{S}_{Liq}^{Flash}\right) \cap \mathcal{S}_{check} \end{aligned} \tag{2.49a}$$

$$\begin{aligned} &T_s \geq T_s^{dew}(P_s, y_s) - M\sigma_s^V, \\ &\forall s \in \left(\mathcal{S}_{Vap} \cup \mathcal{S}_{Vap}^{Flash}\right) \cap \mathcal{S}_{check} \ , \end{aligned} \tag{2.49b}$$

where T^{bub} and T^{dew} are bubble and dew point temperatures, respectively,

which depend on pressure and composition. These equations are only applied to streams in $\mathcal{S}_{check}$. For streams with the supercritical relaxation, (2.49) is modified to also include $M\xi$, similar to (2.43). For Case B of Table 2.3, requiring $\sigma^L = 0$ prevents the nonphysical single-phase solution.

Bubble point temperatures are calculated using the shadow streams introduced in Section 2.5.2, as follows

$$\forall (s, \tilde{s}^v, \tilde{s}^l) \in \{\mathcal{S}_{check} \cap \left(\mathcal{S}_{Liq} \cup \mathcal{S}_{Liq}^{Flash}\right) \times \mathcal{S}_{shdw}^V \times \mathcal{S}_{shdw}^L\} \cap \mathcal{S}_{shdw}^{map},$$

$$\tilde{T}_{\tilde{s}^v} = \tilde{T}_{\tilde{s}^l} = T_s^{bub} \tag{2.50a}$$

$$x_{s_c} = \tilde{x}_{\tilde{s}^l,c}, \quad \forall c \in \mathcal{C} \tag{2.50b}$$

$$\sum_{c \in \mathcal{C}} \left(\tilde{x}_{\tilde{s}^l,c} - \tilde{y}_{\tilde{s}^v,c}\right) = 0 \tag{2.50c}$$

$$P_s = \tilde{P}_{\tilde{s}^v} = \tilde{P}_{\tilde{s}^l} \ , \tag{2.50d}$$

$$\forall (s, \tilde{s}^v, \tilde{s}^l) \in \{(\mathcal{S}_{check} \setminus \mathcal{S}_{sup}) \cap \left(\mathcal{S}_{Liq} \cup \mathcal{S}_{Liq}^{Flash}\right) \times \mathcal{S}_{shdw}^V \times \mathcal{S}_{shdw}^L\} \cap \mathcal{S}_{shdw}^{map},$$

$$\hat{\tilde{x}}_{\tilde{s}^l,c} + \ln \tilde{\phi}_{\tilde{s}^l,c} = \hat{\tilde{y}}_{\tilde{s}^v,c} + \ln \tilde{\phi}_{\tilde{s}^v,c}, \quad \forall c \in \mathcal{C} \ , \tag{2.50e}$$

and dew point temperatures are calculated as follows,

$$\forall (s, \tilde{s}^v, \tilde{s}^l) \in \{\mathcal{S}_{check} \cap \left(\mathcal{S}_{Vap} \cup \mathcal{S}_{Vap}^{Flash}\right) \cap \times \mathcal{S}_{shdw}^V \times \mathcal{S}_{shdw}^L\} \cap \mathcal{S}_{shdw}^{map},$$

$$\tilde{T}_{\tilde{s}^v} = \tilde{T}_{\tilde{s}^l} = T_s^{dew} \tag{2.51a}$$

$$y_{s_c} = \tilde{y}_{\tilde{s}^v,c}, \quad \forall c \in \mathcal{C} \tag{2.51b}$$

$$\sum_{c \in \mathcal{C}} \left(\tilde{x}_{\tilde{s}^l,c} - \tilde{y}_{\tilde{s}^v,c}\right) = 0 \tag{2.51c}$$

$$P_s = \tilde{P}_{\tilde{s}^v} = \tilde{P}_{\tilde{s}^l} \tag{2.51d}$$

$$\forall (s, \tilde{s}^v, \tilde{s}^l) \in \{(\mathcal{S}_{check} \setminus \mathcal{S}_{sup}) \cap \left(\mathcal{S}_{Vap} \cup \mathcal{S}_{Vap}^{Flash}\right) \times \mathcal{S}_{shdw}^V \times \mathcal{S}_{shdw}^L\} \cap \mathcal{S}_{shdw}^{map},$$

$$\hat{\tilde{x}}_{\tilde{s}^l,c} + \ln \tilde{\phi}_{\tilde{s}^l,c} = \hat{\tilde{y}}_{\tilde{s}^v,c} + \ln \tilde{\phi}_{\tilde{s}^v,c}, \quad \forall c \in \mathcal{C} \ , \tag{2.51e}$$

where shadow stream properties are denoted as $\tilde{T}$, $\tilde{P}$, $\tilde{x}$, $\tilde{y}$ and $\tilde{\phi}$ are clarity, and $\exp(\hat{\tilde{x}}_c) = \tilde{x}$ and $\exp(\hat{\tilde{y}}_c) = \tilde{y}$, similar to (2.20). It is important to note (2.40) are applied to the shadow streams with $\sigma^V = 0$ and $\sigma^L = 0$, which prevents this class of nonphysical single-phase solutions.

The bubble/dew point calculations shown in (2.50e) and (2.51e) are problematic when $P_s \geq \bar{P}_s$ (only one phase exists), and are relaxed using the slack variable π_s in quadrants I and II in Figure 2.2 as follows:

$$\begin{aligned} T_s &\leq T_s^{bub}(P_s, x_s) + M(\sigma_s^L + \xi_s), \\ \forall s &\in \left(\mathcal{S}_{Liq} \cup \mathcal{S}_{Liq}^{Flash}\right) \cap (\mathcal{S}_{check} \cap \mathcal{S}_{sup}) \end{aligned} \tag{2.52a}$$

$$\begin{aligned} T_s &\geq T_s^{dew}(P_s, y_s) - M(\sigma_s^V + \xi), \\ \forall s &\in \left(\mathcal{S}_{Vap} \cup \mathcal{S}_{Vap}^{Flash}\right) \cap (\mathcal{S}_{check} \cap \mathcal{S}_{sup}) \end{aligned} \tag{2.52b}$$

$$-M\xi_s \leq \pi_{s,c} \leq M\xi_s, \quad \forall s \in \mathcal{S}_{check} \cap \mathcal{S}_{sup}, \quad \forall c \in \mathcal{C} \tag{2.52c}$$

$$\begin{aligned} &\forall (s, \tilde{s}^v, \tilde{s}^l) \in \{\mathcal{S}_{check} \cap \mathcal{S}_{sup} \cap \left(\mathcal{S}_{Liq} \cup \mathcal{S}_{Liq}^{Flash}\right) \times \mathcal{S}_{shdw}^V \times \mathcal{S}_{shdw}^L\} \cap \mathcal{S}_{shdw}^{map}, \\ &\hat{\tilde{x}}_{\tilde{s}^l,c} + \ln \tilde{\phi}_{\tilde{s}^l,c} = \pi_{s,c} + \hat{\tilde{y}}_{\tilde{s}^v,c} + \ln \tilde{\phi}_{\tilde{s}^v,c}, \quad \forall c \in \mathcal{C} \end{aligned} \tag{2.52d}$$

$$\begin{aligned} &\forall (s, \tilde{s}^v, \tilde{s}^l) \in \{\mathcal{S}_{check} \cap \mathcal{S}_{sup} \cap \left(\mathcal{S}_{Vap} \cup \mathcal{S}_{Vap}^{Flash}\right) \times \mathcal{S}_{shdw}^V \times \mathcal{S}_{shdw}^L\} \cap \mathcal{S}_{shdw}^{map}, \\ &\hat{\tilde{x}}_{\tilde{s}^l,c} + \ln \tilde{\phi}_{\tilde{s}^l,c} = \pi_{s,c} + \hat{\tilde{y}}_{\tilde{s}^v,c} + \ln \tilde{\phi}_{\tilde{s}^v,c}, \quad \forall c \in \mathcal{C} \ . \end{aligned} \tag{2.52e}$$

Thus, when $P_s \geq \bar{P}_s$ and $\xi_s > 0$, $\pi_{s,c}$ is free to move away from zero.

Analogous to the supercritical phase relaxation, (2.49) - (2.52) are not required for every stream in the flowsheet, as nonphysical single-phase solutions are rare. Instead, the following approach is recommended: initially, solve the flowsheet optimization problem with only total condenser and total reboiler outlet streams (and other streams specified by the modeler) in $\mathcal{S}_{check}$. Next, calculate the bubble and dew points for all streams with a post-processing routine. If there are any violations of (2.49), add the offending streams to $\mathcal{S}_{check}$, resolve and recheck. In the worst case, this algorithm would add all of these streams to $\mathcal{S}_{check}$, resulting in a large optimization problem (and most likely increased solution times).

According to Michelsen (1993), uniqueness is expected when different models are used for the vapor and liquid phases, except for a few extreme cases. Non-uniqueness or nonphysical/trivial solutions may occur when $x = y$ and the same thermodynamic model is used. For this case, Michelsen recommends using the tangent plane criterion to ensure phase stability (although the approach does not provide mathematical guarantees). We contend the procedures discussed above, including (2.49) - (2.52), should prevent these nonphysical solutions for cubic equation of state models. The nonphysical single-phase solutions cannot exist for the bubble and dew point calculations, as $\mathcal{S}_{shdw}^V \subset \mathcal{S}_{Vap}$ and $\mathcal{S}_{shdw}^L \subset \mathcal{S}_{Liq}$, thus $f''(Z_L) \leq 0$ and $f''(Z_V) \geq 0$ which ensures $Z_L \neq Z_V$. Finally, (2.49) restricts vapor and liquid solutions to be on the correct side of bubble and dew point curves, which prevents nonphysical single-phase solutions in the original flash calculation. A mathematical proof is left as future work.

2.5.6 Summary of the Modified Cubic EoS Model

In summary, two modifications of the cubic EoS model originally developed by Kamath, Biegler, and Grossmann (2010) are presented. PT space is divided into four quadrants with the critical point at the origin (Figure 2.2). In quadrants III and IV, the pressure is below the mixture's critical point and standard phase equilibrium calculations are used, i.e., (2.19) - (2.41). In the remaining two quadrants, pressure is greater than the critical value and only one phase exists. Thus, (2.20g), (2.20h), (2.40) and (2.41) must be relaxed. This is accomplished using the slack variable ξ and complementarity constraints. Thus for any stream specified as possibly supercritical, (2.42) - (2.44) are considered in place of (2.19g), (2.19h), (2.41a) and (2.41b) in the standard equilibrium model. Critical point properties are calculated as a function of mixture composition using (2.46). Furthermore, the existence of nonphysical single-phase solutions in between a mixture's bubble and dew point is demonstrated. These solutions may be prevented by constraining vapor phases to be above their dew point and liquid phases to be below their bubble point, as shown in (2.49). Bubble and dew point calculations are performed using (2.50) - (2.52). These two extensions of cubic EoS model are required for accurate phase equilibrium calculations in the CPU design case study in Chapter 3.

2.6 Constraints to Avoid Dry Ice

In order to avoid dry ice formulation in heat exchanger equipment for the CPU case study, the following constraints are considered:

$$\forall s \in \mathcal{S}_{CO_2} \ ,$$

$$a_s^{DI} = 0.0323 T_s - 6.2908 \tag{2.53a}$$

$$b_s^{DI} = 1.547889 T_s - 334.481 \tag{2.53b}$$

$$\log_{10}(P_s) \leq \widetilde{\max}(a_s^{DI} - b_s^{DI}, 0) + b_s^{DI} \tag{2.53c}$$

where (2.53) were fit using data from a CO_2 phase diagram (Praxair, 2009). $\mathcal{S}_{CO_2}$ contains only subambient streams carrying CO_2, e.g., streams in CPU section of an oxycombustion power plant. The smoothed max operator (Balakrishna and Biegler, 1992),

$$\widetilde{\max}(x, 0) = \frac{1}{2}\left(x + \sqrt{x^2 + \varepsilon^s}\right), \tag{2.54}$$

blends the two constraints together at their intersection, the triple point of CO_2. ε^s is a small constant, typically between 10^{-3} and 10^{-6}. Alternately, (2.53c) may be reformulated with complementarity constraints.

2.7 Equilibrium-Based Equipment Models

Many basic units share a similar structure, as shown in Figure 2.4, with one or more input streams and two possible outlet streams (vapor and liquid). These

units also share several equations, namely mass and enthalpy balances, and phase equilibria expressions for the outlet streams. Under the theme of modularity, flash separators, heat exchangers, partial reboilers, throttle valves, total condensers and compressors are classified as *general equipment* and inherit these common equations. All general equipment except total condensers and reboilers are also classified as *thermodynamic equipment*. The sets of general and thermodynamic equipment are represented by $\mathcal{G}$ and $\mathcal{T}$, respectively, and $\mathcal{T} \subseteq \mathcal{G}$. For units in $\mathcal{T}$, the outlet streams are in thermodynamic equilibrium.

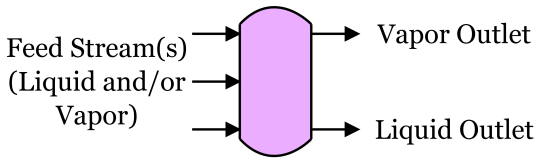

Figure 2.4: General and thermodynamic equipment structure

Flowsheet connectivity is managed using compound sets in GAMS. For example, $\mathcal{G}_{in}$ contains pairings of streams (index s) and general equipment (index g). If the pair (s^1, g^1) belongs to $\mathcal{G}_{in}$, it would imply s^1 is an inlet stream for equipment g^1. $\mathcal{G}^L_{out}$ and $\mathcal{G}^V_{out}$ establish the outlet liquid and vapor streams for all general equipment. These and similar sets are used to define flowsheet connectivity. Finally, to simplify notation, let

$$\mathcal{G}_{out} := \{(s^l, s^v, g) | (s^l, g) \in \mathcal{G}^L_{out},\ (s^v, g) \in \mathcal{G}^V_{out}\}\ .$$

The general equipment model consists of component mole balances, (2.55a), overall enthalpy balance, (2.55b), and bounds on heat duty, (2.55c):

$$\left(\sum_{(s^f, g) \in \mathcal{G}_{in}} f_{s^f, c}\right) = f_{s^l, c} + f_{s^v, c}, \quad \forall c \in \mathcal{C}, \quad \forall (s^l, s^v, g) \in \mathcal{G}_{out} \tag{2.55a}$$

$$\left(\sum_{(s^f, g) \in \mathcal{G}_{in}} F_{s^f} H_{s^f, c}\right) + Q^{in}_g = F_{s^l} H_{s^l} + F_{s^v} H_{s^v} + Q^{out}_g, \quad \forall (s^l, s^v, g) \in \mathcal{G}_{out} \tag{2.55b}$$

$$Q^{in}_g, Q^{out}_g \geq 0, \quad \forall g \in \mathcal{G}\ . \tag{2.55c}$$

The thermodynamic equipment model also includes equilibrium expressions,

$$\mathcal{T}_{out} := \{(s^l, s^v, g) | (s^l, g) \in \mathcal{G}^L_{out},\ (s^v, g) \in \mathcal{G}^V_{out}, g \in \mathcal{T}\}$$
$$T_{s^v} = T_{s^l}, \quad \forall (s^l, s^v, g) \in \mathcal{T}_{out} \tag{2.56a}$$

$$P_{s^v} = P_{s^l}, \quad \forall (s^l, s^v, g) \in \mathcal{T}_{out} \tag{2.56b}$$

$$\mathcal{T}^*_{out} := \{(s^l, s^v, g) | (s^l, g) \in \mathcal{G}^L_{out},\ (s^v, g) \in \mathcal{G}^V_{out}, g \in \mathcal{T},\ s^v \notin \mathcal{S}_{sup}, s^l \notin \mathcal{S}_{sup}\}$$

$$\hat{y}_{s^v,c} = \hat{\beta}_g + \ln K_{g,c} + \hat{x}_{s^l,c}, \quad \forall c \in \mathcal{C}, \forall (s^l, s^v, g) \in \mathcal{T}^*_{out} \tag{2.57a}$$

$$-\sigma^L_{s^l} \leq \hat{\beta}_g, \quad \forall (s^l, s^v, g) \in \mathcal{T}^*_{out} \tag{2.57b}$$

$$\hat{\beta}_g \leq \sigma^V_{s^v}, \quad \forall (s^l, s^v, g) \in \mathcal{T}^*_{out} \tag{2.57c}$$

where $x_{s^l,c}$ ($y_{s^v,c}$) corresponds to the mole fraction of component c in liquid (vapor) stream s^l (s^v). Alternately, the non-log transformed model may be used:

$$y_{s^v,c} = \beta_g K_{g,c}\ x_{s^l,c}, \quad \forall c \in \mathcal{C}, \quad \forall (s^l, s^v, g) \in \mathcal{T}^*_{out} \tag{2.58a}$$

$$-\sigma^L_{s^l} \leq \beta_g - 1, \quad \forall (s^l, s^v, g) \in \mathcal{T}^*_{out} \tag{2.58b}$$

$$\beta_g - 1 \leq \sigma^V_{s^V}, \quad \forall (s^l, s^v, g) \in \mathcal{T}^*_{out} \tag{2.58c}$$

For streams in $\mathcal{S}_{sup}$, (2.57b) or (2.57c) are replaced with either (2.43a) or (2.43b), respectively. Equations (2.21c) & (2.22), which are essential for correct flash calculations, are rewritten below (without numbers) for clarity.

$$\sum_{i \in \mathcal{C}} x_{s^l,i} = 1, \quad \forall s^l \in \mathcal{S}_{Liq} \cup \mathcal{S}^{Flash}_{Liq}$$

$$\sum_{i \in \mathcal{C}} y_{s^v,i} = 1, \quad \forall s^v \in \mathcal{S}_{Vap} \cup \mathcal{S}^{Flash}_{Vap}$$

$$0 \leq \sigma^L_{s^l} \perp F_{s^l} \geq 0, \quad \forall s^l \in \mathcal{S}^{Flash}_{Liq}$$

$$0 \leq \sigma^V_{s^v} \perp F_{s^v} \geq 0, \quad \forall s^v \in \mathcal{S}^{Flash}_{Vap}\ ,$$

In the remainder of this section, temperature and pressure specific relationships are specified for each type of equipment. A few additional compound connectivity sets are required for the models: $\mathcal{G}^1_{in}$ contains a single inlet stream for each unit, and $\mathcal{G}^1_{out}$ contains a single outlet stream for each unit. Thus, $\mathcal{G}^1_{in} \subseteq \mathcal{G}_{in}$ and $\mathcal{G}^1_{out} \subseteq \mathcal{G}^L_{out} \cup \mathcal{G}^V_{out}$. The sets $\mathcal{G}^1_{in}$ and $\mathcal{G}^1_{out}$ are automatically populated based on the type of equipment.

2.7.1 Flash Separation and Throttle Valves

The flash vessels and throttle valves are the simplest type of thermodynamic equipment, and are mathematically identical. The model consists of equations to specify a minimum pressure drop and ensure adiabatic operation,

$$\begin{gathered} P_{s^{out}} \leq \bar{\alpha}_g P_{s^{in}} - \bar{\beta}_g, \\ \forall (s^{in}, s^{out}, g) \in \{(s^1, s^2, g) | (s^1, g) \in \mathcal{G}^1_{in}, g \in \mathcal{F} \cup \mathcal{V}, (s^2, g) \in \mathcal{G}^1_{out}\} \end{gathered} \tag{2.59a}$$

$$Q_g^{in} = Q_g^{out} = 0, \quad \forall g \in \mathcal{F} \cup \mathcal{V} \tag{2.59b}$$

where $\mathcal{F}$ and $\mathcal{V}$ are the sets containing all flash separators and throttle valves, and are defined such that $\mathcal{F} \subseteq \mathcal{T} \subseteq \mathcal{G}$ and $\mathcal{V} \subseteq \mathcal{T} \subseteq \mathcal{G}$. $\bar{\alpha}_g$ and $\bar{\beta}_g$ are relative and absolute pressure drop constants, respectively, for each unit. Flash vessels are used throughout the framework as mixtures, typically with $\bar{\alpha} = 1$ and $\bar{\beta} = 0$, as non-isothermal mixing requires evaluation of an energy balance and vapor-liquid equilibrium calculations, which are already included in the flash vessel model.

2.7.2 Reboilers, Condensers and Heat Exchangers

Partial reboilers (set $\mathcal{R}^p$), partial condensers (set $\mathcal{N}^p$) and the fluid (i.e., non-utility) side of heat exchangers (set $\mathcal{X}$) are non-adiabatic extensions of the flash model. As expected, $\mathcal{R}^p \subseteq \mathcal{T} \subseteq \mathcal{G}$, $\mathcal{N}^p \subseteq \mathcal{T} \subseteq \mathcal{G}$, $\mathcal{X} \subseteq \mathcal{T} \subseteq \mathcal{G}$, $\mathcal{R}^p \subseteq \mathcal{R}$ and $\mathcal{N}^p \subseteq \mathcal{N}$. All of these units are further classified as cooling (removing heat, set $\mathcal{G}_{cool}$) or heating (providing heat, set $\mathcal{G}_{heat}$), such that $\mathcal{R} \subseteq \mathcal{G}_{heat}$, $\mathcal{N} \subseteq \mathcal{G}_{cool}$, $\mathcal{X} \subseteq \mathcal{G}_{heat} \cup \mathcal{G}_{cool}$ and $\mathcal{G}_{heat} \cap \mathcal{G}_{cool} = \{\varnothing\}$. The mathematical model for these units includes pressure and temperature relationships,

$$P_{s^{in}} = P_{s^{out}}, \quad \forall (s^{in}, s^{out}, g) \in \{(s^1, s^2, g) | (s^1, g) \in \mathcal{G}_{in}^1, g \in \mathcal{R} \cup \mathcal{N}, (s^2, g) \in \mathcal{G}_{out}^1\} \tag{2.60a}$$

$$P_{s^{out}} \leq \bar{\alpha}_g P_{s^{in}} - \bar{\beta}_g, \quad \forall (s^{in}, s^{out}, g) \in \{(s^1, s^2, g) | (s^1, g) \in \mathcal{G}_{in}^1, g \in \mathcal{X}, (s^2, g) \in \mathcal{G}_{out}^1\} \tag{2.60b}$$

$$T_{s^{in}} \geq T_{s^{out}}, \quad \forall (s^{in}, s^{out}, g) \in \{(s^1, s^2, g) | (s^1, g) \in \mathcal{G}_{in}^1, g \in \mathcal{G}_{cool}, (s^2, g) \in \mathcal{G}_{out}^1\} \tag{2.60c}$$

$$T_{s^{in}} \leq T_{s^{out}}, \quad \forall (s^{in}, s^{out}, g) \in \{(s^1, s^2, g) | (s^1, g) \in \mathcal{G}_{in}^1, g \in \mathcal{G}_{heat}, (s^2, g) \in \mathcal{G}_{out}^1\} \tag{2.60d}$$

$$Q_g^{in} = 0, \quad \forall g \in \mathcal{G}_{cool} \tag{2.60e}$$

$$Q_g^{out} = 0, \quad \forall g \in \mathcal{G}_{heat} \ , \tag{2.60f}$$

in addition to the relevant general equipment and thermodynamic equipment equations, (2.55) and (2.56) Flowrates and inlet/outlet temperatures for the utility side of the heat exchangers are not explicitly considered in this model, and are discussed in Chapter 3. Instead, this model calculations the heat addition, Q^{in}, and removal, Q^{out}, demands for each unit.

2.7.3 Total Condensers and Total Heat Reboilers

In contrast to the units previous considered, the outlets of total condensers (set $\mathcal{N}^t$) and total reboilers (set $\mathcal{R}^t$) are single phase. Therefore, these units are classified as *general equipment* and not *thermodynamic equipment*, i.e. $\mathcal{N}^t \subseteq \mathcal{G}$, $\mathcal{R}^t \subseteq \mathcal{G}$, $\mathcal{N}^t \cap \mathcal{T} = \{\varnothing\}$, and $\mathcal{R}^t \cap \mathcal{T} = \{\varnothing\}$. This classification restricts (2.56)

from be evaluated for these units. However, $\mathcal{R}^t \subseteq \mathcal{R}$ and $\mathcal{N}^t \subseteq \mathcal{N}$, such that (2.60) apply to total condensers and reboilers. Furthermore, the single phase outlet streams of total condensers and reboilers are automatically added to $\mathcal{S}_{check}$ to ensure proper thermodynamic calculations.

2.7.4 Splitters

The splitter model is very straightforward, and copies all stream intensive stream properties (e.g., x, T, P, H, etc.) from the single inlet stream to multiple outlet streams using equality constraints. In the processing and setup routines with the framework, the inlet streams inherit any special sets memberships, such as $\mathcal{S}_{Liq}^{Flash}$, $\mathcal{S}_{Vap}^{Flash}$, $\mathcal{S}_{sup}$ and/or $\mathcal{S}_{check}$, from the outlet streams. Thus, the thermodynamic model is not evaluated for splitter outlets to reduce the number of equations.

2.8 Compressor and Pump Models

Pumps and compressors are used to increase the pressure of streams, and only operate on a single phase. In this framework, pumps ($\mathcal{P}^p$) and compressors (set $\mathcal{P}^c$) are generalized as *pressure changers* (set $\mathcal{P}$), such that $\mathcal{P}^p \subseteq \mathcal{P}$ and $\mathcal{P}^c \subseteq \mathcal{P}$. The sets $\mathcal{P}_{in}$, $\mathcal{P}_{out}^L$, $\mathcal{P}_{out}^V$ are used to manage connectivity. Similar to general equipment, each pressure changer is assigned one vapor and one liquid outlet. Furthermore, it is assumed that if a pressure changer is assigned multiple inlet streams, they are at a common pressure and temperature from an upstream unit. This is typical of liquid-vapor pairs. $\mathcal{P}_{in}^1$ contains a single *liquid* inlet and $\mathcal{P}_{out}^1$ contains a single *liquid* outlet stream from each pump, whereas $\mathcal{P}_{in}^1$ contains a single *vapor* inlet and $\mathcal{P}_{out}^1$ contains a single *vapor* outlet stream from each compressor. Shared mole balances along with temperature and pressure relationship are defined using these connectivity sets:

$$\begin{aligned}
&\forall (s^{in}, s^{out}, p) \in \{(s^1, s^2, p) | (s^1, p) \in \mathcal{P}_{in}^1, (s^2, p) \in \mathcal{P}_{out}^1\}, \\
&f_{s^{in},c} = f_{s^{out},c}, \quad \forall c \in \mathcal{C} && \text{(2.61a)} \\
&T_{s^{in}} \leq T_{s^{out}} && \text{(2.61b)} \\
&P_{s^{in}} \leq P_{s^{out}} && \text{(2.61c)}
\end{aligned}$$

$$\begin{aligned}
&\forall (s^l, s^v, p) \in \{(s^1, s^2, p) | (s^1, p) \in \mathcal{P}_{out}^L, (s^2, p) \in \mathcal{P}_{out}^V\}, \\
&T_{s^l} = T_{s^v} && \text{(2.61d)} \\
&P_{s^l} = P_{s^v} \ . && \text{(2.61e)}
\end{aligned}$$

Furthermore, the pressure ratio for each compressor is restricted to κ^{max} or less,

$$\begin{aligned}
&P_{s^{out}} \leq \kappa^{max} P_{s^{in}}, \\
&\forall (s^{in}, s^{out}, p) \in \{(s^1, s^2, p) | (s^1, p) \in \mathcal{P}_{in}^1, (s^2, p) \in \mathcal{P}_{out}^1, p \in \mathcal{P}^c\} \ ,
\end{aligned} \tag{2.62}$$

where $\kappa^{max} = 5$ is a typical value. Separate models are required to calculate the work for pumps and compressors, depending on the selected thermodynamics module.

2.8.1 Ideal Thermodynamics

With the ideal thermodynamics module, pump work is calculated using the common $V\Delta P$ formula:

$$\forall (s^{in}, s^{out}, p) \in \{(s^1, s^2, p) | (s^1, p) \in \mathcal{P}^1_{in}, (s^2, p) \in \mathcal{P}^1_{out}, p \in \mathcal{P}^c\},$$
$$T_{s^{in}} + \epsilon \leq T_{s^{out}} \tag{2.63a}$$
$$W_p = F_{s^{out}} \left(\sum_{c \in \mathcal{C}} x_{s^{in},c} V_{s^{in},c} \right) (P_{s^{out}} - P_{s^{in}}) \ . \tag{2.63b}$$

Alternately, $\left(\sum_{c \in \mathcal{C}} x_{s^{in},c} V_{s^{in},c}\right)$ may be replaced with an (approximate) constant liquid specific volume. Compressor work is calculated using the ideal gas formula for adiabatic expansion,

$$\forall (s^{in}, s^{out}, p) \in \{(s^1, s^2, p) | (s^1, p) \in \mathcal{P}^1_{in}, (s^2, p) \in \mathcal{P}^1_{out}, p \in \mathcal{P}^c\},$$
$$T_{s^{out}} = T_{s^{in}} \left(\frac{P_{s^{out}}}{P_{s^{in}}} \right)^{\frac{\gamma - 1}{\gamma}} \tag{2.64a}$$
$$W_p = F_{s^{out}} \left(\frac{\gamma}{\gamma - 1} \right) R \ T_{s^{in}} \left[\left(\frac{P_{s^{out}}}{P_{s^{in}}} \right)^{\frac{\gamma - 1}{\gamma}} - 1 \right] \ , \tag{2.64b}$$

and interstage cooling is modeled using a series of compressors and heat exchangers.

2.8.2 Cubic Equation of State Thermodynamics

In contrast to the ideal gas model, enthalpy (H) and entropy (S) can be reliably calculated as a function of pressure (P) with a cubic equation of state. Thus, for pumps, work is calculated using an energy balance while ensuring no entropy destruction:

$$\mathcal{S}^{in}(p^*) := \{s | (s, p) \in \mathcal{P}_{in}, p = p^*\}$$
$$\mathcal{S}^{out}(p^*) := \{s | (s, p) \in \mathcal{P}^V_{out} \cup \mathcal{P}^L_{out}, p = p^*\}$$
$$W_p = \frac{1}{(\eta_{pump} \ \eta_{motor})} \left[\sum_{s \in \mathcal{S}^{out}(p)} F_s H_s - \sum_{s \in \mathcal{S}^{in}(p)} F_s H_s \right], \quad \forall p \in \mathcal{P}^p \tag{2.65a}$$
$$\sum_{s \in \mathcal{S}^{in}(p)} F_s S_s \leq \sum_{s \in \mathcal{S}^{out}(p)} F_s S_s, \quad \forall p \in \mathcal{P}^p \ , \tag{2.65b}$$

A shadow (i.e., hypothetical) stream is used to calculate the outlet conditions for isentropic compression. The shadow stream-compressor pairings are contained in $\mathcal{P}^c_{shdw}$, and the streams are defined such that,

$$\forall(s^{in}, s^{out}, s^*, p) \in \{(s^1, s^2, s^3, p) | (s^1, p) \in \mathcal{P}^1_{in}, (s^2, p) \in \mathcal{P}^1_{out}, (s^3, p) \in \mathcal{P}^c_{shdw}\},$$

$$S_{s^{in}} = \tilde{S}_{s^*} \tag{2.66a}$$

$$P_{s^{out}} = \tilde{P}_{s^*} \tag{2.66b}$$

$$y_{s^{out},c} = \tilde{y}_{s^*,c}, \quad \forall c \in \mathcal{C} \ , \tag{2.66c}$$

where shadow stream properties are denoted $\tilde{S}$, $\tilde{P}$ and $\tilde{y}$ for clarity.

The shadow streams are used to calculate the isentropic enthalpy change, Δh^{isn}_p, and an energy balance is used to calculate the actual ethalphy change, Δh^{act}_p, for each compressor. The ratio of these two terms is the isentropic efficiency, η^{isn}_{cmpr}. Finally, the mechanical compressor efficiency, η^{mech}_{cmpr}, is used to calculate work:

$$\Delta h^{act}_p = \left(\sum_{s \in \mathcal{S}^{out}(p)} F_s H_s \right) - \left(\sum_{s \in \mathcal{S}^{in}(p)} F_s H_s \right), \quad \forall p \in \mathcal{P}^c \tag{2.67a}$$

$$\Delta h^{isn}_p = \left(\sum_{s \in \mathcal{S}^{out}(p)} F^{out} \right) \tilde{H}_{s^*} - \left(\sum_{s \in \mathcal{S}^{in}(p)} F_s H_s \right), \quad \forall (s^*, p) \in \mathcal{P}^c_{shdw} \tag{2.67b}$$

$$\eta^{isn}_{cmpr} = \frac{\Delta h^{isn}_p}{\Delta h^{act}_p}, \quad \forall p \in \mathcal{P}^c \tag{2.67c}$$

$$W_p = \frac{\Delta h^{act}_p}{\eta^{mech}_{cmpr}}, \quad \forall p \in \mathcal{P}^c \ , \tag{2.67d}$$

This model is compatible with either fixed isentropic efficiencies or ones calculated from correlations. For the case studies in this work, fixed efficiencies are used to facilitate comparison with other studies.

2.8.3 Phase Constraints

Pumps and compressors are required to operate on liquid-only and vapor-only streams, respectively. If a pump or compressor (generalized as *pressure changers*) in known to always exist, the phases of the inlet and outlet streams are fixed in the optimization problem. For example, in the CPU case study in Chapter 3, the liquid streams into and out of compressors and vapor streams into and out of the pumps are automatically disabled. Otherwise,

$$\begin{aligned} &\mathcal{S}^V(p^*) := \{s \in \mathcal{S}^{Flash}_{Vap} \cup \mathcal{S}_{Vap} | (s,p) \in \mathcal{P}_{in} \cup \mathcal{P}^V_{out}, p = p^*\} \\ &0 \leq (\Delta T_p + \Delta P_p + W_p) \perp \left(\sum_{s \in \mathcal{S}^V(p)} F_s \right) \geq 0, \quad \forall p \in \mathcal{P}^p \end{aligned} \tag{2.68a}$$

$$\mathcal{S}^L(p^*) := \{s \in \mathcal{S}_{Liq}^{Flash} \cup \mathcal{S}_{Liq} | (s,p) \in \mathcal{P}_{in} \cup \mathcal{P}_{out}^L, p = p^*\}$$
$$0 \leq (\Delta T_p + \Delta P_p + W_p) \perp \left(\sum_{s \in \mathcal{S}^L(p)} F_s \right) \geq 0, \quad \forall p \in \mathcal{P}^c \ , \tag{2.68b}$$

where $\Delta T_p, \Delta P_p, W_p, F \geq 0$. This allows for pressure chargers and associated phase restrictions to be toggled "on" and "off". For example, if there is non-zero vapor flow into a pump, its temperature change (ΔT_p), pressure change (ΔP_p) and work (W_p) must all be zero.

2.9 Final Remarks

The thermodynamics and basic equipment models are presented in this chapter. In the remainder of the thesis, these models are used as basic building blocks to assemble large flowsheets. The models are build upon three principles. First, modularity is embraced by abstracting models whenever possible. For example, mass and energy balances are defined for *general equipment* unit, instead of individual equipment types (e.g., valves, reboilers, flash vessels, etc.). The heat integration model (Chapter 3) is also defined over the general equipment set, and whenever possible, the equipment models are independent of the thermodynamic models. This organization maintains a compact implementation and is extensible. Similarly, the compound sets used to manage flowsheet connectivity are introduced in this chapter. Second, complementarity constraints are used throughout the chapter to model switches, including vanishing and reappearing phases and the toggling "on" and "off" of pressure change units based on the inlet phase. A derivation of the complementarity model for phase equilibrium calculation is presented at the beginning of the chapter. Third, a model refinement strategy is used for initialization, and two thermodynamics modules are presented in this chapter. As described in Chapter 6, the flowsheet is first optimized with the ideal thermodynamics module, and the solution is used to initialize the more complex cubic equation of state (EoS) model.

The cubic EoS model presented in this chapter is based on the work of Kamath, Biegler, and Grossmann (2010). Inequality constraints are used for root assignment, instead of the iterative procedures preferred in most process simulators. The former is better suited for EO optimization, as derivatives are readily available. Furthermore, two contributions to the cubic EoS model are presented in this chapter. The first is a reformulation to properly classify phases in the supercritical region. The second is an embedded bubble and dew point calculation strategy to prevent a class of nonphysical equilibrium solutions. State-of-the-art alternatives use either non-rigorous iterative procedures (Gibb's tangent plane test) or global optimization, which is not practical for large flowsheets.

Chapter 3

Heat Integration Models and CPU Optimization

Key Contributions and Results:

- Discuss three improvements of the Duran-Grossmann formulation for simultaneous heat integration and process optimization
- Propose two alternate heat integration models that replaces instances of a smoothed max operator with inequality and complementarity constraints
- Demonstrate the efficacy of the heat integration models by considering simultaneous optimization of the CO_2 processing unit, compression train and accompanying multistream heat exchanger for an oxy-fired power system

3.1 Overview

Heat integration has a well establish track record for increasing efficiency, reducing costs and improving "sustainability" of process designs by reusing waste heat and cooling, thus minimizing the amount of heat rejected by a process. Furthermore, heat integration is an essential aspect of modern power generation system design. This chapter explores systemic methods for heat integration, and focuses on mathematical models to embed minimum utility calculations as part of the large process design optimization problem. The methods presented in the chapter are demonstrated in a CO_2 processing unit (CPU) design case study that seeks to minimize the compression costs in the system, while ensuring the embedded multistream heat exchangers are thermodynamically feasible, i.e., don't violate a minimum temperature difference (driving force) specification.

3.1.1 Literature Review

Masso and Rudd (1969) are credited with the first formula definition of the heat exchanger network synthesis (HENS) problem, which is typically cast as

the following (paraphrased) optimization problem: *Given stream data (i.e., heating and cooling demands), utility data and necessary cost data, minimize the total cost (equipment and utilities) for heat exchange subject to the laws of thermodynamics.* During the past forty-five years, heat integration has become a classic problem in process systems engineering, and two categories of techniques have emerged: systematic evolutionary rules based on design heuristics and mathematical programming techniques, which are subdivided into sequential and simultaneous formulations. The remainder of this review seeks to establish general trends and important milestones regarding heat integration methodological development. For extensive literature reviews, see Gundersen and Naess (1988), Linnhoff (1993), Furman and Sahinidis (2002) and Klemeš and Kravanja (2013).

Evolutionary design methods are a collection of iterative tools and heuristic to systematically improve heat integration networks while balancing energy consumption, capital costs and operability (flexibility, controllability, reliability and safety). Heat recovery pinch is considered the most important concept for evolutionary HENS methods (Gundersen and Naess, 1988). Independently invented by Umeda, Itoh, and Shiroko (1978) and Linnhoff and Flower (1978a,b) and motivated by the 1970s energy crisis, the heat recovery pinch is the point where the minimum temperature difference, $\Delta \underline{T}$, limits the reduction of utility demands by heat integration. This point may be found using graphical tools, such as composite curves and grand composite curves, and is fundamentally important to simplifying the design of HENs. The heat recovery pinch concept was combined with heuristic rules and procedures to form the pinch design method (Linnhoff and Hindmarsh, 1983). A common heuristic is to avoid heat integration across the pinch point, i.e., use vertical integration near the pinch. This decomposes the initial HENS problem into two (nearly) independent design problems, i.e., above and below the pinch. Furthermore, pinch calculations allow for a rigorous calculation of minimum utility/maximum energy recovery (MER) target before any network configurations are considered, which tells engineers how close their network designs are to the theoretical thermodynamic minimum (Linnhoff and Turner, 1981). Numerous additional heuristic rules have been proposed by Linhoff and colleagues for the pinch design method to evolve network designs. Common topics for these rules include procedures for breaking loops to reduce the number of matches, i.e., heat exchangers, or guidelines for splitting streams. Colbert (1982) and Trivedi, O'Neill, and Roach (1989) extended the idea of pinch analysis to consider two separate temperature differences: heat recovery approach temperature (HRAT) and exchanger minimum approach temperature (EMAT). This technique, known as the dual-temperate approach method (DTAM), allows designers to specify one approach temperature, HRAT, to determine the utility requirements/maximum recoverable energy, and a second, smaller approach temperature, EMAT, to govern exchanger design. Thus the designer may use EMAT to adjust the area versus number of matches tradeoff without impacting the energy (utility) requirements for the network. The

technique typically leads to networks with simpler topologies, fewer units and (hopefully) lower costs. The procedure was further developed by Rév and Fonyó (1986) and Trivedi et al. (1989) into the pseudo-pinch design method (PPDM), which add an arbitrary minimum heat load parameter to prevent numerous small exchangers and improve network capital costs. Pinch based methods have also been extended to include cost targeting (Linnhoff and Ahmad, 1990; Ahmad, Linnhoff, and Smith, 1990) and supertargeting (Linnhoff and Ahmad, 1989a), where HRAT is traded-off with capital costs before network synthesis. Other extensions consider resiliency (Colberg, Morari, and Townsend, 1989) and flexibility (Linnhoff and Smith, 1989), and heat-work trade-offs, such as heat pump placement (Townsend and Linnhoff, 1983a,b). Overall, evolutionary design methods emphasize the use of thermodynamic-based heuristics along with the designer's input and intuition.

In contrast, mathematical programming based techniques find rigorous optima for HENS problems, and don't rely on heuristics or engineer's intervention to iteratively improve designs. Early work focused on sequential methods for HENS. First, linear and integer programming techniques were applied to calculate the minimum utility requirements and number of matches (exchangers). For example, Cerda et al. (1983) proposed a transportation model for these two calculations, and extended it to consider forbidden/restricted matches (Cerda and Westerburg, 1983). Papoulias and Grossmann (1983a,c,b) proposed an alternate transshipment model, which is more compact (fewer equations) and generally preferred. Next, Floudas, Ciric, and Grossmann (1986) developed MAGNETS, a computer program that uses the minimal utility (LP) and minimum number of matches (MILP) results from the transshipment model, and automatically formulates a network superstructure to minimize the amount of area by solving a nonlinear program (NLP). These three optimization problems, LP to minimize utilities, MILP to minimize the number of matches and NLP to minimize area, are the basis of the sequential mathematical programming strategy for HENS. The sequential strategy has been extended to consider uncertainty and multi-period operation (Floudas and Grossmann, 1986, 1987b,a), and retrofit applications (Ciric and Floudas, 1989). Optimization of the approach temperature, $\Delta\underline{T}$, i.e., supertargeting, may be done in an outer loop around this procedure (Floudas, Ciric, and Grossmann, 1986).

Sequential algorithms were originally preferred, given the computational complexity of the HENS problem[1]. However, as shown by Biegler, Grossmann, and Westerberg (1997) and others, sequential synthesis does not always produce the lowest cost networks. Floudas and Ciric (1989, 1990) proposed a mixed integer nonlinear program (MINLP) to simultaneously optimize the match selection and heat exchanger sizing (area). Their approach, however, requires HRAT to be specified *a priori*. They extended the model to consider the pseudo-pinch problem (Ciric and Floudas, 1990, 1991), which allows for utility

[1] In fact, Furman and Sahinidis (2001) proved several HENS problems are NP-hard in the strong sense, and thus polynomial time algorithms cannot exist for these problems.

levels to be included in the simultaenous problem. Yee and Grossmann (1990); Yee, Grossmann, and Kravanja (1990a,b) proposed an alterante MINLP model for simultaneous optimization of utility costs, number of matches and area costs in HENs. Their model features a stagewise superstructure and makes several assumptions, such as isothermal mixing, no stream bypass and split streams only flow through one exchanger, which result in a linear constraint set. Overall, these two MINLP models enable simultaneous balancing of the three costs, utility, number of matches and area, in HENS problems.

The evolutionary methods and mathematically programming algorithms for HENS reflect two fundamentally different philosophies to process design. The former embrace physical insights and interventions from the user, whereas the latter uses mathematical program techniques to rigorously search the design space. As consequence of these differences, the communities of developers and practitioners for both methods have occasionally been in conflict. For example, the founding work on pinch based methods, E. C. Hohmann's PhD thesis (supervised by F. J. Lockhart), was rejected for publication twice because of "*very strong confidence in those days that the HENS problem could be automated and solved by mathematical methods*" (Gundersen and Naess, 1988). In early days, mathematically programming based approaches were severally limited to small size problems. For instance, Trivedi et al. (1989) wrote "*In the last 5 yr, systematic evolutionary methods have been accepted as the best available methods to generate alternative methods*" and cited long computational times and required mathematical skills to use early mathematical programming algorithms and tools. However, evolutionary approaches (e.g., pinch design method) are prone becoming stuck in *topology traps*, in which the heuristic rules and procedures cannot evolve the network design to the globally optimal structure (Trivedi et al., 1989; Linnhoff and Ahmad, 1990). Mathematical programming techniques are resilient against this problem, given their search of the design space. Furthermore, HENS problems are difficult given the mix of "hard" and "soft" input data (Gundersen and Naess, 1988). In many industrial problems, some specifications are closer to guidelines than requirements. Evolutionary design methods inherently handle these situations better, as the rely on frequent designer input, whereas most mathematical programming formulations threat all input specifications as strict requirements. These factors, i.e., limited computational burdens, more intuitive engineer-algorithm interactions, greater procedure flexibility and industry emphasis on good but not globally optimal solutions led evolutionary design methods to be preferred by many practitioners in the 1980s and 1990s. With advances in numeric optimization algorithms, development of numerous alternate formulations and availability of automated tools, mathematical programming approaches are now superior for many types of small to medium size HENS problems.

The evolutionary design and mathematical programming algorithms for HENS discussed thus far assume constant/fixed temperatures and flowrates in process streams. In the broader scope of process design, this assumption typically leads to suboptimal solutions. Instead, the additional degrees of

freedom from combining flowsheet optimization (adjustment of process operating conditions) with HENS yields significant cost saving, as demonstrated by Duran and Grossmann (1986). They proposed an equation-based model to embed heat recovery pinch calculations in flowsheet optimization problems. Nondifferentiable features associated with locating the pinch point(s) are accommodated with smooth max operators and inequality constraints, and are discussed below. Lang, Biegler, and Grossmann (1988) compared explicit and implicit forms of this model versus traditional sequential integration in the sequential-modular process simulator FLOWTRAN for two process optimization case studies. As consequence of the additional degrees of freedom, they found superior profits with the simultaneous approach, mainly due to raw material savings and increased yields. For results with both heat integration strategies, they used MAGNETS to automatically design a cost optimal network, and found capital costs were roughly the same. This justified their choice to ignore HEN capital costs in the case study objective functions. Gomez Giammattei (1994), under the supervision of L.B. Evans and J.W. Tester, embedded the cost targeting models from Linnhoff and Ahmad (1990) in a sequential modular process simulator for optimization. Their implementation is analogous to the implicit strategy in Lang, Biegler, and Grossmann (1988). Overall, this allows for the simultaneous flowsheet optimization and heat integration, with rigorous utility targets calculations with the Duran-Grossmann formulation, and approximate HEN capital cost (i.e., area) targets. In contrast, the sequential and simultaneous mathematical programming strategies for HENS synthesis design the cost optimal network, but miss possible interactions between flowsheet optimization (adjustment of process stream flowrate, temperatures, pressures, etc.) and HENS.

Several researchers have proposed improvements and extensions for the Duran-Grossmann model. Grossmann, Yeomans, and Kravanja (1998) replaced the smoothed max operators and temperature bumps for isothermal streams with disjunctions to reduce heat integration errors. The disjunctions are reformulated in a MINLP with big-M constraints, and the model is tested with several case studies. They found the NLP formulation (Duran-Grossmann) is ten to twenty-five times faster than the proposed MINLP model for test cases with non-isothermal streams. However, in the test cases with isothermal streams, the MINLP formulation was thirty to one hundred twenty five times faster, and correctly calculated the cooling requirements. Navarro-Amorós et al. (2013) proposed an alternate disjunctive programming model based on the the transshipment model, but with variable temperatures. Unfortunately, their constant heat flow (flowrate time heat capacity) assumption removes important degrees of freedom, and does not allow for full simultaneous heat integration and process optimization. For instance, most of the cost savings due to simultaneous optimization in the examples of Lang, Biegler, and Grossmann (1988) came from increased reaction conversion and decreased raw material demands, which required adjustment of process stream flowrates. Furthermore, it is unclear how well the mixed-integer heat integration mod-

els perform in conjunction with highly nonlinear thermodynamic calculations. Navarro-Amorós et al. (2013) avoid the issue in their examples by fitting quadratic models to distillation column data generated with Aspen-HYSYS. Although adequate for small problems, this procedure may be undesirable for large industrial examples.

Simultaneous heat integration and flowsheet optimization is especially important in sub-ambient separation systems, such as air separation units, to ensure feasibility of the accompanying multistream heat exchangers. For example, Kamath, Biegler, and Grossmann (2012) applied extensions of the Duran-Grossmann model to optimize the PRICO natural gas liquefaction process, which consists of multistream heat exchangers to cool the natural gas feed and one or more refrigeration loops. In conjunction with the embedded cubic equation of state model from Kamath, Biegler, and Grossmann (2010), they simultaneously optimized pressures and flowrates in the refrigeration cycle along with working fluid composition while ensuring thermodynamically feasibility of the multistream heat exchangers. Their designed systems require 12 to 15% less energy than the design proposed by Del Nogal et al. (2008), which were optimized using a genetic algorithm (i.e., stochastic derivative free optimization). Kamath, Biegler, and Grossmann (2012) also proposed two important extensions to the Duran-Grossmann formulation. First, they decomposed each heat exchanger into multiple subunits, which replaces the constant heat capacity assumption with a piecewise linear approximation. Second, they proposed a disjunctive model to locate phase transitions and place them at the boundary of these subunits. In order to avoid integer variables, they reformulate the disjunctions using complementarity constraints. Recently, Pattison and Baldea (2015) reoptimized the PRICO process using a more restrictive heat integration formulation, which requires the order of each stream to be specified *a priori*. This allows them to easily embed area calculations in the design problem, and balance area and energy costs. The ordering assumption, however, is more restrictive than the Duran-Grossmann model and not be applicable to the general flowsheet optimization problem.

3.1.2 Chapter Organization

The Duran-Grossmann formulation forms the basis for the heat integration models considered in the proposed flowsheet optimization framework. In this chapter, several modifications and extensions are considered. First, necessary nomenclature to link the heat integration and unit operation models are established. Next the Duran-Grossmann formulations is summarized, and three key extensions are discussed: introduction of heat integration zones, a reformulation to reduce smoothed max errors, and heat exchanger decomposition. Then, the smoothed max operators in the original model are replaced with inequality and complementarity constraints in two novel alternate formulations. Finally, the heat integration and thermodynamics modules of the proposed framework are demonstrated in CO_2 processing unit (CPU) design case study.

3.1.3 Generalized Heat Integration Units

Reboilers (set $\mathcal{R}$), condensers (set $\mathcal{N}$) and heat exchangers (set $\mathcal{X}$) are considered for heat integration in this framework. As discussed in Section 2.7, these units are abstracted as general equipment, leading to a compact heat integration model. These equipment are further classified as units that require external heating (set $\mathcal{G}_{heat}$) or units that require external cooling (set $\mathcal{G}_{cool}$). This definition is in contrast to the heat integration literature, where the primary goal is to synthesize a heat exchange network with fixed inlet/outlet stream data (temperatures, flows, etc). In this thesis a different problem is addressed: optimize a flowsheet while maintaining a minimum temperature difference (HRAT) without synthesizing the network, i.e., embed energy targeting into the flowsheet problem. "Streams" in classic HENS literature are analogous to units in this framework.

3.1.4 Heat Integration Zones

In this work, the heat integration models are extended to considering multiple zones, which allows for different groups of process units to be heat integrated separately. This is related to the forbidden match problem, but applied to groups of equipment. For example, in a cryogenic air separation unit (Chapter 4) equipment that comprise the multistream heat exchanger are assigned to one zone, whereas coupled reboiler/condenser are assigned to another. Furthermore, a minimum temperature difference, $\Delta\underline{T}$, is specified for each zone. $\mathcal{Z}^{HI}$ contains all of the heat integration zones, and is indexed with z. The mapping of equipment to zones in contained in $\mathcal{G}^{HI}_{zones}$ [2]. Finally, it is important to note heat integration zones are a completely different concept than flowsheet zones (Chapter 2).

3.2 Duran-Grossmann Model

In the Duran-Grossmann model, the pinch point(s) are located by calculating the utility requirements for every pinch candidate as if it were selected as an active pinch point. Inequality constraints then determine the worst-case utility requirements. The calculated utility demands are included in the objective function and minimized. Unlike the transshipment model for minimum utility calculations, the temperature of streams in the flowsheet are variable for the simultaneous heat integration and process optimization problem. Thus, the ordering of streams from coldest to hottest is not constant and temperature intervals are not considered. Instead, the discrete nature of locating the pinch point(s) is accommodated using inequality constraints and a smoothed max operator, such as (2.54) (shown below):

[2] Each unit may only be assigned to one heat integration zone.

$$\begin{aligned}\widetilde{\max}(x,0) &= \frac{1}{2}\left[x+\sqrt{x^2+\varepsilon^s}\right]\\ &\approx \max(x,0)\end{aligned}$$

Implementation of the Duran-Grossmann model in this framework is divided into six sections. In the first section, the temperatures of inlet and outlet streams for each generalized heat exchange unit are copied to the variables T_g^{in} and T_g^{out}. The smoothed max operator (2.54) is used in conjunction with a small number (α) to ensure nonzero temperature drops for phase changes. For a high purity stream undergoing phase change (e.g., boiling) the temperature change is near zero and the calculated heat capacity is nearly infinite, resulting in numerical difficulties. In Duran and Grossmann (1986), a 1 °C temperature bump is applied to all streams. In contrast,

$$\forall(s^{in},s^{out},g)\in\{(s^1,s^2,g)|(s^1,g)\in\mathcal{G}_{in}^1,(s^2,g)\in\mathcal{G}_{out}^1,g\in\mathcal{G}_{heat}\},$$

$$T_g^{in} = T_{s^{in}} \tag{3.1a}$$

$$T_g^{out} = \widetilde{\max}(T_{s^{out}} - T_{s^{in}} - \alpha, 0) + T_{s^{in}} + \alpha \tag{3.1b}$$

$$\forall(s^{in},s^{out},g)\in\{(s^1,s^2,g)|(s^1,g)\in\mathcal{G}_{in}^1,(s^2,g)\in\mathcal{G}_{out}^1,g\in\mathcal{G}_{cool}\},$$

$$T_g^{in} = \widetilde{\max}(T_{s^{in}} - T_{s^{out}} - \alpha, 0) + T_{s^{out}} + \alpha \tag{3.1c}$$

$$T_g^{out} = T_{s^{out}}\ , \tag{3.1d}$$

is considered in this model, which only bumps temperatures of near isothermal units. For cryogenic application $\alpha = 0.1$ to 0.2 °C is considered.

In the second section, the inlet and outlet temperatures for each heat exchange unit are considered as pinch candidates (set $\mathcal{S}^P$). For flowsheet design problems, extreme stream temperatures are generally not known *a priori*; thus all of the inlet and outlet streams are considered as pinch candidates in this framework, as opposed to only inlet streams in the original model. Although this increases problem size, it has little impact on the results. More precisely, the pinch candidate set is defined as follows for streams s and zones z:

$$\mathcal{S}^P := \{(s,z)|[(s,g)\in\mathcal{G}_{in}^1\cup\mathcal{G}_{out}^1],[(g,z)\in\mathcal{G}_{zone}^{HI}],[g\in\mathcal{G}_{cool}\cup\mathcal{G}_{heat}]\}\ ,$$

and contains all stream-heat integration zone pairs that are candidate pinch points. Notice that although each general unit may only be assigned to one heat integration zone, it is possible for a stream to be a pinch candidate in two zones (outlet for one unit and inlet for another). For convenience, unit-stream-zone mapping sets are also defined,

$$\mathcal{G}^P_{cool} := \{(s,g,z)|[(s,g) \in \mathcal{G}^1_{in} \cup \mathcal{G}^1_{out}], [(g,z) \in \mathcal{G}^{HI}_{zones}], [g \in \mathcal{G}_{cool}]\}$$
$$\mathcal{G}^P_{heat} := \{(s,g,z)|[(s,g) \in \mathcal{G}^1_{in} \cup \mathcal{G}^1_{out}], [(g,z) \in \mathcal{G}^{HI}_{zone}], [g \in \mathcal{G}_{heat}]\} \ ,$$

where $\mathcal{G}^P_{cool} \cup \mathcal{G}^P_{heat}$ contains all of the pairs in $\mathcal{S}^P$. Using these sets, the inlet and outlet temperatures of general units are copied to pinch candidate temperatures τ,

$$\tau_{s,z} = T^{in}_g, \quad \forall (s,g,z) \in \mathcal{G}^P_{cool} \tag{3.2a}$$
$$\tau_{s,z} = T^{out}_g, \quad \forall (s,g,z) \in \mathcal{G}^P_{cool} \tag{3.2b}$$
$$\tau_{s,z} = T^{in}_g + \Delta\underline{T}_z, \quad \forall (s,g,z) \in \mathcal{G}^P_{heat} \tag{3.2c}$$
$$\tau_{s,z} = T^{out}_g + \Delta\underline{T}_z, \quad \forall (s,g,z) \in \mathcal{G}^P_{heat}, \tag{3.2d}$$

and minimum driving force temperature constant $\Delta\underline{T}_z$ is added to the inlet and outlet temperatures of heating units (e.g., reboilers), which correspond to cold streams in Duran and Grossmann (1986).

In the third section of constraints, the average heat capacity-flowrate product Θ_g for each unit is calculated. The formulation assumes that the heat capacity for each stream is constant over the temperature interval considered.

$$Q^{in}_g = \Theta_g(T^{out}_g - T^{in}_g), \quad \forall g \in \mathcal{G}_{heat} \tag{3.3a}$$
$$Q^{out}_g = \Theta_g(T^{in}_g - T^{out}_g), \quad \forall g \in \mathcal{G}_{cool} \ , \tag{3.3b}$$

The heart of the model is contained in the final two sections. The heating (Q^{Ah}) and cooling (Q^{Ac}) available above each pinch candidate is defined as follows[3]:

$$C(z^*) = \{g|g \in \mathcal{G}_{cool}, (g,z) \in \mathcal{G}^{HI}_{zones}, z = z^*\}$$
$$H(z^*) = \{g|g \in \mathcal{G}_{heat}, (g,z) \in \mathcal{G}^{HI}_{zones}, z = z^*\}$$

$$Q^{Ah}_{s,z} = \sum_{g \in C(z)} \Theta_g[\widetilde{\max}(T^{in}_g - \tau_{s,z}, 0) - \widetilde{\max}(T^{out}_g - \tau_{s,z}, 0)], \quad \forall (s,z) \in \mathcal{S}^P \tag{3.4a}$$

$$\begin{aligned} Q^{Ac}_{s,z} = \sum_{g \in H(z)} \Theta_g[&\widetilde{\max}(T^{out}_g - \tau_{s,z} + \Delta\underline{T}_z, 0) \\ &- \widetilde{\max}(T^{in}_g - \tau_{s,z} + \Delta\underline{T}_z, 0)], \quad \forall (s,z) \in \mathcal{S}^P \ . \end{aligned} \tag{3.4b}$$

For each pinch candidate, the heating deficit, $Q^{Ac}_{s,z} - Q^{Ac}_{s,z}$, is calculated, and the minimum amount hot utility $\bar{Q}^s_z$ is the largest of these deficits. The minimum amount of cold utility $\bar{Q}^w_z$ is calculated using an energy balance:

[3]Note that cooling units provide heat Q^{Ah} to the heat exchange network.

$$\bar{Q}_z^s \geq Q_{s,z}^{Ac} - Q_{s,z}^{Ah}, \quad \forall (s,z) \in \mathcal{S}^P \tag{3.5a}$$

$$\bar{Q}_z^w = \bar{Q}_z^s + \sum_{g \in H(z) \cup C(z)} \left[Q_g^{out} - Q_g^{in} \right], \quad \forall (s,z) \in \mathcal{S}^P \ . \tag{3.5b}$$

Finally, the minimum utility demands for the overall process, Q^s and Q^w, are calculated by summing the individual demands for each zone:

$$Q^s = \sum_{z \in \mathcal{Z}^{HI}} \bar{Q}_z^s \tag{3.6a}$$

$$Q^w = \sum_{z \in \mathcal{Z}^{HI}} \bar{Q}_z^w \ . \tag{3.6b}$$

In the reminder of this section, two further improvements of the Duran-Grossmann formulations are presented: [1] reformulation to reduce the number of smoothed max instances and associated errors, and [2] refinement of constant heat capacity assumption. In Section 3.3, two alternate formulations to remove the smoothed max operators are presented.

3.2.1 Reformulation to Reduce Smoothed Max Errors

The smoothed max operator (2.54) blends the kink at the switching point ensuring differentiability for gradient based optimization. However this adds small numerical errors, especially near the switching point/kink. Near the switching point at $x = 0$, $\widetilde{\max}(0,0)$ returns 0.5ϵ, whereas $\max(0,0) = 0$. The smoothed max operator also contributes to large elements of $O(1/\epsilon)$ in the Hessian near the switching point, which may lead to poor optimizer performance. Most evaluations of $\widetilde{\max}(\cdot)$ near the switching point are inside the summations of (3.4) and occur when the inlet or outlet streams correspond to the pinch candidate stream. These cases can be removed by analyzing each $\widetilde{\max}$ term and unrolling the summations in (3.4).

To illustrate this idea, consider the amount of cold exchanged above the pinch for a specific heating unit (index g) as a function of pinch temperature (τ), as shown in Figure 3.1. When the pinch temperature is less then the inlet temperature for the unit (T_g^{in}), the entire heat duty for the the unit, Q_g^{in}, is transferred above the pinch. Likewise for pinch candidate temperatures above the outlet temperature (T_g^{out}), no heat integration for this unit occurs above the pinch. If the pinch temperature is between the inlet and outlet temperature, linear interpolation is used to calculate the amount of heat transfer above the pinch. $\tau = T_g^{in}$ and $\tau = T_g^{out}$ correspond to the switching points of the smoothed max operator (3.4b). Table 3.1 summarizes the amount of heat transferred above the pinch at all four switching points in (3.4a) and (3.4b). The first column of the table corresponds with the scenarios in Figure 3.1.

These scenarios provide justification to reformulate (3.4). The summations are unrolled and units whose inlet or outlet streams are the pinch candidates are considered separately (without the $\widetilde{\max}$ operator). This is best illustrated

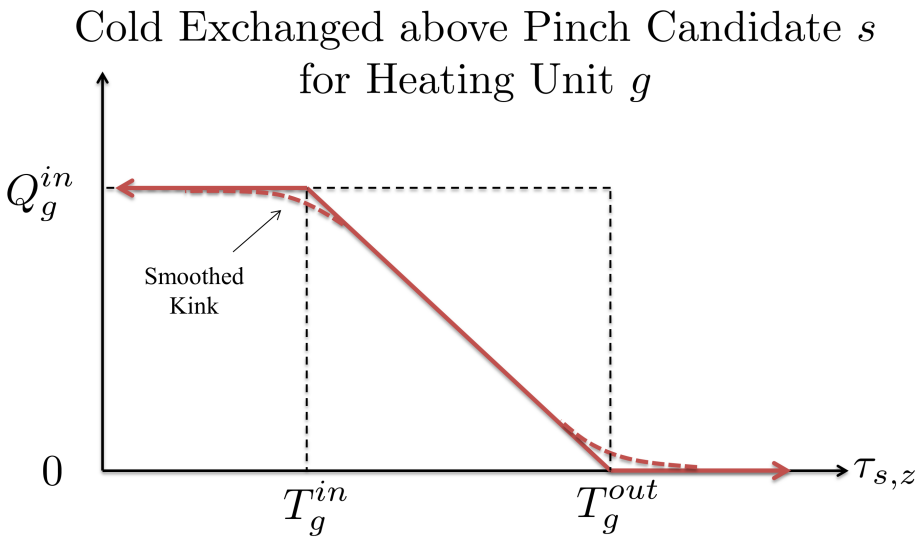

Figure 3.1: Cartoon showing the amount of heat integrated in the network for a specific heating unit g as a function of pinch temperature $\tau_{s,z}$.

Table 3.1: Heat Transfer Above the Pinch at Switching Points

	Heating Unit ($T_g^{in} \leq T_g^{out}$)	Cooling Unit ($T_g^{in} \geq T_g^{out}$)
$T_g^{out} = \tau_{s^P}$	0	Q_g^{out}
$T_g^{in} = \tau_{s^P}$	Q_g^{in}	0

by considering an example heating unit g^* and (3.4b). When the pinch candidate stream corresponds with the inlet stream for unit g^*, the contribution to the summation in (3.4b) is zero (see Table 3.1). Likewise when pinch candidate corresponds with the outlet stream the available heat for integration from g^* is $Q_{g^*}^{in}$. This leads to some set definitions:

$$
\begin{aligned}
H_{s,z}^1 &= \{g | (g,z) \in \mathcal{G}_{heat}^P \text{ and not } (s,g) \in \mathcal{G}_{in}^1 \cup \mathcal{G}_{out}^1\} \\
H_{s,z}^2 &= \{g | (g,z) \in \mathcal{G}_{heat}^P, (s,g) \in \mathcal{G}_{out}^1\} \\
H_{s,z}^3 &= \{g | (g,z) \in \mathcal{G}_{heat}^P, (s,g) \in \mathcal{G}_{in}^1\}
\end{aligned}
$$

Using these sets the summation in (3.4b) is unrolled and scenarios presented in Table 3.1 are applied to simplify the summations over H^2 and remove the summation over H^3, ultimately yielding

$$
\begin{aligned}
Q^{Ac}_{s,z} = & \sum_{g \in H^1_{s,z}} \Theta_g [\widetilde{\max}(T^{out}_g - \tau_{s,z} + \Delta \underline{T}_z, 0) - \widetilde{\max}(T^{in}_g - \tau_{s,z} + \Delta \underline{T}_z, 0)] \\
& + \sum_{g \in H^2_{s,z}} \Theta_g [\widetilde{\max}(T^{out}_g - \tau_{s,z} + \Delta \underline{T}_z, 0) - \widetilde{\max}(T^{in}_g - \tau_{s,z} + \Delta \underline{T}_z, 0)] \\
& + \sum_{g \in H^3_{s,z}} \Theta_g [\widetilde{\max}(T^{out}_g - \tau_{s,z} + \Delta \underline{T}_z, 0) - \widetilde{\max}(T^{in}_g - \tau_{s,z} + \Delta \underline{T}_z, 0)] \\
= & \sum_{g \in H^1_{s,z}} \Theta_g [\widetilde{\max}(T^{out}_g - \tau_{s,z} + \Delta \underline{T}_z, 0) - \widetilde{\max}(T^{in}_g - \tau_{s,z} + \Delta \underline{T}_z, 0)] \\
& + \sum_{g \in H^2_{s,z}} Q^{in}_g + \sum_{g \in H^3_{s,z}} 0, \qquad \forall (s,z) \in \mathcal{S}^P \ .
\end{aligned}
\tag{3.7}
$$

The same observations are also applied to the cooling units:

$$
\begin{aligned}
C^1_{s,z} &= \{g | (g,z) \in \mathcal{G}^P_{cool} \text{ and not } (s,g) \in \mathcal{G}^1_{in} \cup \mathcal{G}^1_{out}\} \\
C^2_{s,z} &= \{g | (g,z) \in \mathcal{G}^P_{cool}, (s,g) \in \mathcal{G}^1_{in}\}
\end{aligned}
$$

$$
\begin{aligned}
Q^{Ah}_{s,z} = & \sum_{g \in C^1(s,z)} \Theta_g [\widetilde{\max}(T^{in}_g - \tau_{s,g}) - \widetilde{\max}(T^{out}_g - \tau_{s,g}, 0)] \\
& + \sum_{g \in C^2(s,z)} Q^{out}_g, \qquad \forall (s,z) \in \mathcal{S}^P \ .
\end{aligned}
\tag{3.8}
$$

In summary, (3.7) and (3.8) replace (3.4) in the heat integration model and reduce the number of $\widetilde{\max}$ evaluations near the switching point.

3.2.2 Selection of Piecewise Constant Heat Capacities

The pinch based model proposed by Duran and Grossmann (1986) assumes constant heat capacities for each stream. This approximation is typically accurate, except when streams undergo a phase transition. At the bubble and dew point temperatures there is a non-smooth kink in heat capacity. Kamath, Biegler, and Grossmann (2012) propose an extension of the pinch heat integration model that decomposes streams into three substreams (vapor, liquid and two phase) that are separately considered for heat integration.

In this framework, multiple heat exchangers are considered in series for streams undergoing phase changes. For example, in cryogenic systems the feed stream (air) is cooled from a vapor to liquid. Three heat exchangers are used as shown in Figure 3.2. The outlet of the first exchanger is constrained to be at the dew point ($\sigma^L = \sigma^V = 0,\ F^L = 0$) and outlet of the second is at the bubble point ($\sigma^L = \sigma^V = 0,\ F^V = 0$). The exit of the final heat exchanger is constrained to be a liquid ($\sigma^V = 0$). These conditions are applied to thermodynamic equipment using the sets $\mathcal{T}^{dew}$, $\mathcal{T}^{dew}$ and $\mathcal{T}^{2p}$ as follows:

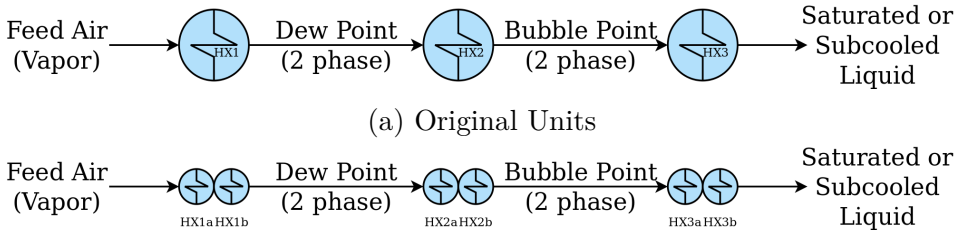

(a) Original Units

(b) Decomposed Units

Figure 3.2: Cooling heat exchangers in series

$$
\begin{aligned}
\mathcal{S}^L_{dew} &:= \{s|(s,g) \in \mathcal{G}^L_{out},\ \forall g \in \mathcal{T}^{dew}\} \\
\mathcal{S}^V_{dew} &:= \{s|(s,g) \in \mathcal{G}^V_{out},\ \forall g \in \mathcal{T}^{dew}\} \\
\mathcal{S}^L_{2p} &:= \{s|(s,g) \in \mathcal{G}^L_{out},\ \forall g \in \mathcal{T}^{2p}\} \\
\mathcal{S}^V_{2p} &:= \{s|(s,g) \in \mathcal{G}^V_{out},\ \forall g \in \mathcal{T}^{2p}\} \\
\mathcal{S}^L_{bub} &:= \{s|(s,g) \in \mathcal{G}^L_{out},\ \forall g \in \mathcal{T}^{bub}\} \\
\mathcal{S}^V_{bub} &:= \{s|(s,g) \in \mathcal{G}^V_{out},\ \forall g \in \mathcal{T}^{bub}\}
\end{aligned}
$$

$$\sigma^L_{s^l} = \sigma^V_{s^v} = F_{s^l} = 0, \quad \forall s^l \in \mathcal{S}^L_{dew}, \quad \forall s^v \in \mathcal{S}^V_{dew} \tag{3.9a}$$

$$\sigma^L_{s^l} = \sigma^V_{s^v} = 0, \quad \forall s^l \in \mathcal{S}^L_{2p}, \quad \forall s^v \in \mathcal{S}^V_{2p} \tag{3.9b}$$

$$\sigma^L_{s^l} = \sigma^V_{s^v} = F_{s^v} = 0, \quad \forall s^l \in \mathcal{S}^L_{bub}, \quad \forall s^v \in \mathcal{S}^V_{bub} \tag{3.9c}$$

Although this approach requires *a priori* specification of streams undergoing multiple phase transitions, it is easier to simulate and verify with commercial flowsheeting tools. The alternate approach from Kamath, Biegler, and Grossmann (2012) requires bubble and dew point calculations for each heat exchanger, which greatly complicates the model.

For large changes in temperature heat capacity may not be constant. In order to address this issue, heat exchange units are decomposed into N^{sub} subunits and the system is reoptimized. For example, the three units in series from Figure 3.2(a) are decomposed into two subunits each, as shown in Figures 3.2(b) & 3.3. Let $\mathcal{X}^{sub}$ contain the heat exchange subunits, where $\mathcal{X}^{sub} \subseteq \mathcal{X} \subseteq \mathcal{T} \subseteq \mathcal{G}$. Furthermore, let $\mathcal{G}^{sub}_{map}$ contain the mapping between "large" general equipment at their subunits. Finally, "large unit" with pressure drops are assigned to set $\mathcal{G}^{PD}$, along with all subunits of these large units. The subunits are equally spaced with respect to temperature, and pressure drops are modeled as follows:

$$
\begin{aligned}
T_{s^{in}} - T_{s^{out}} &= \delta T_g / N^{sub}, \\
\forall (s^{in}, s^{out}, x, g) \in \{(s^1, s^2, x, g) | &(s^1, x) \in \mathcal{G}^1_{in}, (s^2, x) \in \mathcal{G}^1_{out}, \\
&x \in \mathcal{X}^{sub}, (g, x) \in \mathcal{G}^{sub}_{map}\}
\end{aligned} \tag{3.10a}
$$

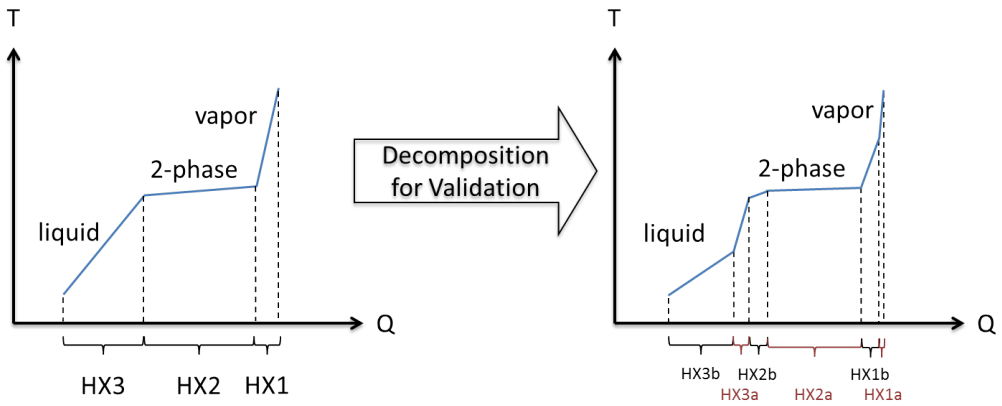

Figure 3.3: Decomposition of heat exchanges from Figure 3.2 into two subunits each

$$
\begin{aligned}
&P_{s^{in}} \geq P_{s^{out}}, \\
&\forall (s^{in}, s^{out}, x) \in \{(s^1, s^2, x) | (s^1, x) \in \mathcal{G}^1_{in}, (s^2, g) \in \mathcal{G}^1_{out}, \\
&x \in \mathcal{X}^{sub} \cap \mathcal{G}^{PD}\}
\end{aligned} \tag{3.10b}
$$

$$
\begin{aligned}
&P_{s^{out}} \leq \bar{\alpha}_g P_{s^{in}} - \bar{\beta}_g, \\
&\forall (s^{in}, s^{out}, g) \in \{(s^1, s^2, g) | (s^1, g) \in \mathcal{G}^1_{in}, g \in \mathcal{G}^{PD} \setminus \mathcal{X}^{sub}, \\
&(s^2, g) \in \mathcal{G}^1_{out}\}
\end{aligned} \tag{3.10c}
$$

$$
\begin{aligned}
&P_{s^{in}} = P_{s^{out}} \\
&\forall (s^{in}, s^{out}, x) \in \{(s^1, s^2, x) | (s^1, x) \in \mathcal{G}^1_{in}, (s^2, g) \in \mathcal{G}^1_{out}, \\
&x \in \mathcal{X}^{sub} \setminus \mathcal{G}^{PD}\}
\end{aligned} \tag{3.10d}
$$

It is important to note requiring both equal temperature spacing and equal pressure drops for subunits may cause Q to have the incorrect sign due to the Joule-Thomson effect. In Step 5 of the initialization procedure, each generalized heat exchanger unit is decomposed, and in Step 6, the flowsheet is reoptimized with the decomposed subunits. In Step 6, the "large units" are deactivated and completely replaced with their subunits. Furthermore, because the subunits are in $\mathcal{T}$, they inherit the mass, energy and phase equilibrium equations established in Chapter 2. Specific details for Steps 5 and 6 in the initialization procedure as discussed in Chapter 6.

3.3 Alternate Heat Integration Formulations

In the smoothed max operator (2.54), ε^s controls the "smoothness" of the kink. Large values of ε^s (e.g., 0.1 - 0.01) result in less extreme gradients but large smoothing errors. We have empircally observed, with too small of values for ε^s, CONOPT has a tendency to prematurely terminate at infeasible or non-optimal points with initial points far from an optimum. Thus, in the

optimization procedure described in Chapter 6, a series of flowsheet design NLPs are solved and ε^s is shrunk by an order of magnitude between each solve. This procedure works well for the ASU (Chapter 4) and CPU (this chapter) design case studies. In the steam cycle optimization studies (Chapter 5), however, CONOPT does not reliably solve the latter flowsheet NLPs after ε^s has been shrunk. This motivated development of two alternate heat integration model with fewer $\widetilde{\max}$ instances.

The basis of these reformulations come from a simple observation regarding (3.5a). It is not necessary to calculate $Q^{Ac}_{s,z}$ and $Q^{Ah}_{s,z}$ with equality constraints, as overestimation of $Q^{Ac}_{s,z}$ and underestimation of $Q^{Ah}_{s,z}$ will simply increase $\bar{Q}^s_w$ and $\bar{Q}^w_z$. Instead, inequality constraints may be used, which the optimizer will drive to active as Q^w and Q^s are in the objective function. This idea is illustrated in Figure 3.4, where $q^{Ac}_{s,g,z}$ and $q^{Ah}_{s,g,z}$ are the contributions for each unit g to either $Q^{Ac}_{s,z}$ or $Q^{Ah}_{s,z}$, respectively:

$$Q^{Ac}_{s,z} = \sum_{g \in H(z)} q^{Ac}_{s,g,z}, \quad \forall (s,z) \in \mathcal{S}^P \tag{3.11a}$$

$$Q^{Ah}_{s,z} = \sum_{g \in C(z)} q^{Ah}_{s,g,z}, \quad \forall (s,z) \in \mathcal{S}^P \tag{3.11b}$$

where $C(z) = \{g | g \in \mathcal{G}_{cool}, (g,z) \in \mathcal{G}^{HI}_{zones}\}$ and $H(z) = \{g | g \in \mathcal{G}_{heat}, (g,z) \in \mathcal{G}^{HI}_{zones}\}$.

3.3.1 Reformulation 1: Inequality Constraints

Examination of Figure 3.4 reveals the kinks at $T^{out}_g = \tau_{s,z}$ for both heating cooling units are convex, and may be replaced with inequality constraints,

$$\bar{H} = \{(s,g,z) | (g,z) \in \mathcal{G}^P_{heat}, (s,z) \in \mathcal{S}^P \text{ and not } (s,g) \in \mathcal{G}^1_{in} \cup \mathcal{G}^1_{out}\}$$
$$\bar{C} = \{(s,g,z) | (g,z) \in \mathcal{G}^P_{cool}, (s,z) \in \mathcal{S}^P \text{ and not } (s,g) \in \mathcal{G}^1_{in} \cup \mathcal{G}^1_{out}\}$$

$$q^{Ac}_{s,g,z} \geq 0, \quad \forall (s,g,z) \in \bar{H} \tag{3.12a}$$

$$q^{Ah}_{s,g,z} \leq Q^{out}_g, \quad \forall (s,g,z) \in \bar{C}\ , \tag{3.12b}$$

whereas the other two types of kinks are nonconvex. For this formulation, $\widetilde{\max}$ is used to accommodate the remaining kinks:

$$q^{Ah}_{s,g,z} \leq \Theta_g \widetilde{\max}(T^{in}_g - \tau_{s,z}, 0), \quad \forall (s,g,z) \in \bar{C} \tag{3.13a}$$

$$q^{Ac}_{s,g,z} \geq -\widetilde{\max}\left[Q^{in}_g - \Theta_g(T^{out}_g + \Delta \underline{T}_z - \tau_{s,z}), 0\right] + Q^{in}_g, \quad \forall (s,g,z) \in \bar{H}\ . \tag{3.13b}$$

Using the same unrolling argument as (3.7) and (3.8), Q^{Ac} and Q^{Ah} are calculated as follows:

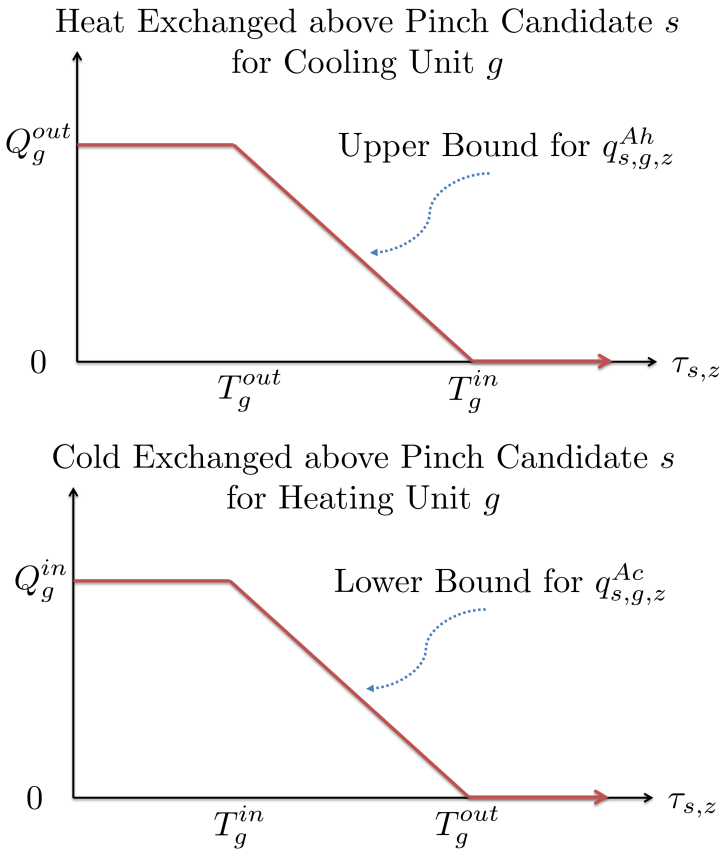

Figure 3.4: Central idea for reformulation to remove smoothed max

$$Q_{s,z}^{Ac} = \sum_{g \in H_{s,z}^1} q_{s,g,z}^{Ac} + \sum_{g \in H_{s,z}^2} Q_g^{in}, \quad \forall (s,z) \in \mathcal{S}^P \tag{3.14a}$$

$$Q_{s,z}^{Ah} = \sum_{g \in C_{s,z}^1} q_{s,g,z}^{Ah} + \sum_{g \in C_{s,z}^2} Q_g^{out}, \quad \forall (s,z) \in \mathcal{S}^P \tag{3.14b}$$

Thus this approach replaces half of the instances of $\widetilde{\max}$ compared to the modified Duran-Grossmann formulation, but increase the number of equations. This trade-off is discussed in detail in Section 3.3.3.

3.3.2 Reformulation 2: Complementarity Constraints

The second reformulation is an extension of the first, where the nonconvex kinks of Figure 3.4 are modeled with complementary constraints:

$$q_{s,g,z}^{Ac} \geq \Theta_g (T_g^{out} + \Delta \underline{T}_z - \tau_{s,z}) - \sigma_{s,g,z}^{c1}, \quad \forall (s,g,z) \in \bar{H} \tag{3.15a}$$

$$q_{s,g,z}^{Ac} \geq Q_g^{in} - \sigma_{s,g,z}^{c2}, \quad \forall (s,g,z) \in \bar{H} \tag{3.15b}$$

$$0 \leq \sigma_{s,g,z}^{c1} \perp \sigma_{s,g,z}^{c2} \geq 0, \quad \forall (s,g,z) \in \bar{H} \ , \tag{3.15c}$$

$$q^{Ah}_{s,g,z} \leq \Theta_g(T^{in}_g - \tau_{s,z}) - \sigma^{h1}_{s,g,z}, \quad \forall (s,g,z) \in \bar{C} \tag{3.16a}$$

$$q^{Ah}_{s,g,z} \leq \sigma^{h2}_{s,g,z}, \quad \forall (s,g,z) \in \bar{C} \tag{3.16b}$$

$$0 \leq \sigma^{h1}_{s,g,z} \perp \sigma^{h2}_{s,g,z} \geq 0, \quad \forall (s,g,z) \in \bar{C}\ , \tag{3.16c}$$

and σ^{c1} to σ^{h2} are slack variables. These constraints replace (3.13), and the other constraints from Reformulation 1 are retained.

3.3.3 Model Comparisons

In order to compare the number of equations in each formulation, let $n^H = |\mathcal{G}_{heat}|$ (number of heating units), let $n^C = |\mathcal{G}_{cool}|$ (number of cooling units), and assume $|\mathcal{Z}^{HI}| = 1$, i.e., there is only one heat integration zone. Finally, assume no streams are both the inlet of one unit and the outlet of another, i.e., each heating and cooling unit contributes two unique streams to the pinch candidate set, which is the worst case scenario regarding model size. Under these assumptions, there are $n^P = |\mathcal{S}^P| = 2n^H + 2n^C$ pinch stream candidates. Furthermore, let $n^* = |\bar{H}| + |\bar{C}| = 2n^H(n^H - 1) + 2n^C(n^C - 1) + 4n^H n^C$. Using these constants, Table 3.2 compares the number of equations in each formulation. The *Common* column refers to the group of equations that are found in each formulation, whereas the *Modified D-G*, *Reformulation 1* and *Reformulation 2* columns consider only the unique equations in each formulation. Finally, the last row of Table 3.2 shows the number of additional equations in reference to the *Modified D-G* formulation.

As seen in Table 3.2, Reformulation 1 replaces half of the $\widetilde{\max}$ operators in the modified D-G formulation with linear equations. The remaining $\widetilde{\max}$ operators are moved to individual inequality constraints. In Reformulation 2, the remaining $\widetilde{\max}$ operators are replaced with complementarity constraints. The primary disadvantage of the reformulations is the significantly increased problem size. However, the additional linear and bilinear equations are sparse, and should be efficiently handled by modern NLP codes. It is unclear from simple analysis which is version of the model is preferred, and computational comparisons are present as part of the case study in Section 3.4.4.

Table 3.2: Summary of Three Heat Integration Formulations. Let $n^* = 2n^H(n^H - 1) + 2n^C(n^C - 1) + 4n^H n^C$.

	Common	Modified D-G	Reformulation 1	Reformulation 2
Equations	(3.1) - (3.3), (3.5) - (3.6)	(3.7) & (3.8)	(3.12) - (3.14)	(3.12), (3.14), (3.15) & (3.16)
No. Linear Eqns.	$5(n^H + n^C) + 3$	0	$n^* + 2(n^H + n^C)$	$2n^* + 2(n^H + n^C)$
No. Eqns. w/ only Linear and Bilinear Terms	$n^H + n^C$	0	0	n^*
No. Eqns. w/ $\widetilde{\max}$	$n^H + n^C$	$2(n^H + n^C)$	n^*	0
No. Compl. Constraints	0	0	0	n^*
Total No. Eqns.	$7(n^H + n^C) + 3$	$2(n^H + n^C)$	$2(n^H + n^C) + n^*$	$2(n^H + n^C) + 3n^*$
No. $\widetilde{\max}$ operators	$n^H + n^C$	$2n^*$	n^*	0
No. additional variables	–	–	n^*	$3n^*$

3.4 Case Study: CO_2 Processing Unit Optimization

The purity requirements of CO_2 for utilization (e.g., enhanced oil recovery) depend on several location and application specific factors. Typically, the purified CO_2 product stream must contain less than 4 mol% "non-condensable gases" (i.e., O_2, N_2 and Ar) and trace amounts of other impurities (Pipitone and Bolland, 2009; Toftegaard et al., 2010). Furthermore, CO_2 product is preferred to be in a dense supercritical phase for efficient transportation and some utilization applications (Pipitone and Bolland, 2009). The flue gas after pollution controls in oxy-fired processes consists of CO_2 (58-70%), N_2 (8-18%), O_2 (2-5%), Ar (2-3%), H_2O (15-17%), trace NO_x, SO_x, Hg and particulate matter near atmospheric pressure (Darde et al., 2009). This does not meet the purity or pressure requirements, hence additional processing is necessary. Water is easily condensed by cooling the flue gas. Several methods, including absorption, adsorption, membrane separation and cryogenic distillation, have been proposed to remove the remaining "non-condensable gases" (Songolzadeh et al., 2014). Due to the large difference in boiling points between CO_2 and these gases, sub-ambient flash separation is one of the most promising commercially available technologies.

Several researchers have studied CO_2 purification processes in oxy-combustion power plants. Pipitone and Bolland (2009) compared energy requirement for sub-ambient separation and compression of boiler flue gas for natural gas and pulverized coal fuels in three cases: no separation (reference), a two flash unit separation system and a distillation column separation system. Similarly, Besong, Maroto-Valer, and Finn (2013) compared sub-ambient separation using single flash and three flash units with respect to various CO_2 recovery, purity and power requirements for the process, using feed gas compositions and thermodynamic data from Darde et al. (2009). They also analyzed the sensitivity of CO_2 recovery and purity to perturbations of the inlet pressure specifications for the flash vessels. Zanganeh, Shafeen, and Salvador (2009) investigated the behavior of three flash unit pilot plant system for a wide spectrum of inlet CO_2 concentration gas streams. All of these studies found similar results; separation with more equilibrium units required less energy but greater capital costs. The major drawback to many of these studies is their reliance on simulation tools and single-variable parametric case studies; systematic multivariable optimization was not considered.

Fu and Gunderson (2012) used engineering insight and exergy analysis to optimize the sub-ambient CO_2 conditioning process for one-stage flash, two-stage flash and three-stage flash units. They analyzed the system with respect to the CO_2 recovery rate, power consumption, exergy losses, capital costs and plant economics, while keeping the outlet CO_2 purity constant (96.3 mole%) and searching for the optimal operating conditions manually. Although their approach is quite successful for a single subsystem in the oxycombustion pro-

cess, it is difficult to extend to the entire flowsheet, and balance trade-offs between subsystems (e.g., ASU and CPU) in an oxycombustion process.

Similarly, our optimization case study considers the flowsheet in Figure 3.5 based on the two-stage flash case of Fu and Gunderson (2012), with a single multistream heat exchanger to replaces the two sub-ambient heat exchangers in the original work. The heat exchange units boxed in Figure 3.5 are assigned to multistream heat exchanger zone (heat integration zone 2) and integrated together. The remaining heat exchange units are assigned to the chilled water zone (heat integration zone 1), and subject to the following constraints:

$$\forall (g,z) \in \{\mathcal{G}_{cool} \times \text{Zone 1}\} \cap \mathcal{G}^{HI}_{zones},$$

$$T^{out}_g + T^{slack}_g \geq T^{utility}_z + \Delta \underline{T}_z \tag{3.17a}$$

$$0 \leq Q^{out}_g \perp T^{slack}_g \geq 0 \ . \tag{3.17b}$$

where $T^{utility}_1 = 283.15$ K (chilled sea water) and $\Delta \underline{T}_1 = 5$ K for the CPU case study. Addition specifications are shown in Table 3.3.

Table 3.3: Additional specifications for CPU case study

	Zone 1	Zone 2
$\Delta \underline{T}_z$	5 K	1.5 K
$\mathcal{G}_{cool}$	{HX601 - HX605, HX611, HX613 - HX618, HX620}	{HX606 - HX607, HX621}
$\mathcal{G}_{heat}$	$\{\varnothing\}$	{HX608 - HX610, HX612, HX619}
$\mathcal{T}^{bub}$	$\{\varnothing\}$	
$\mathcal{T}^{2p}$	{F601, F602, HX606, HX607}	
$\mathcal{T}^{dew}$	{HX621}	
$\mathcal{S}_{check}$	{S631, S632, S336, S640, S644, S646,S648, S650 S654, S656, S658, S660, S662, S644-S667, S671, S678-S680}	
$\mathcal{S}_{sup}$	{S654 - S671}	

Treated and dried flue gas (83.5 mol% CO_2) is fed into the CPU, compressed using a five stage compressor with intermediate cooling, cooled in multistream heat exchanger and flashed (F601), resulting in partial liquefaction. The vapor outlet of F601 in Figure 3.5 (rich in O_2, N_2 and Ar) is further cooled in the multistream heat exchanger and flashed again (F602) to recover more CO_2 (liquid) before venting the vapor. The liquid outlets of both the flash vessels are expanded adiabatically, heated (in order to balance the multistream heat exchanger), compressed and mixed (F603). The mixed stream is then compressed using a three stage compressor with intermediate cooling before liquefaction (or transition to the dense supercritical phase) and pumped

to the required pressure (150 bar). The location of the transition to the supercritical region is determined by the pressures for each stream, which are optimization variables. The required CO_2 purity and recovery are specified as 96.3 and 94.6 mol% to be consistent with Fu and Gunderson (2012). Similarly, all heat exchangers are modeled with 2% pressure drops. Heat exchangers in series, such as HX616 - HX618, are modeled with equal pressure drops ($\sqrt[3]{2}\%$) that combine to 2%.

3.4.1 Optimization of the Reference Case

The two-flash CPU system design problem is formulated as the following nonlinear program:

$$\min \quad \text{Shaft Work} + Q^s + 0.01Q_1^w + 5Q_2^w + \text{Complementarity Penalties}$$

s.t.	Flowsheet Topology	Figure 3.5
	Peng-Robinson Thermo.	(2.21), (2.22), (2.26) - (2.40), (2.42) - (2.44), (2.49) - (2.52e)
	Avoid Dry Ice	(2.53)
	Unit Operation Models	(2.55), (2.56), (2.59), (2.60)
	Compressor and Pump Models	(2.61) - (2.67)
	Heat Integration Model	(3.1) - (3.3), (3.5) - (3.8) & (3.17)
	CO_2 Recovery $\geq$ 94.6 mol%	
	CO_2 Purity = 96.3 mol%	
	$T \geq 180$ K ,	

where Q^s is the required heating (typically zero), Q_1^w is the required chilled water utility, and Q_2^w is the required cooling for the multistream exchanger (typically zero due to the high cost).

The multi-start optimization procedure, described in Chapters 1 and 6, was used to consider hundreds of initial point and initialization parameter combinations. In the best local solution, the CO_2 is initially pressurized to 28.7 bar. The stream is then cooled to 242.8 K in the multistream heat exchanger (MHEX) in Zone 2 and depressurized to 27.9 bar, resulting in a 33.2% vapor mixture. The vapor outlet of the first flash vessel, S264, is then cooled to 217.7 K and fed into the second flash vessel (F602). 45.9% of S264 leaves the second flash vessel as liquid in S631. The remaining non-condensable gases, S630, are expanded and used to provide cooling in the MHEXs. The liquid effluents of the second flash vessel, S631, is then heated to 223.7 K in MHEX. Similarly the effluent of the first flash vessel (S625) is adiabatically expanded to 21.6 bar and heated to 297.9 K. These heat loads drive cooling in other parts of the multistream heat exchanger. These two streams are then compressed and mixed in F603, which operates at 34.5 bar and 288.2 K. The CO_2 product stream is further pressurized and cooled with chilled water to the desired pressure of 150 bar. Although the optimized operating conditions are different than the ones reported by Fu and Gunderson (2012), the objective function (shaft work) is very similar, as shown in Table 3.4.

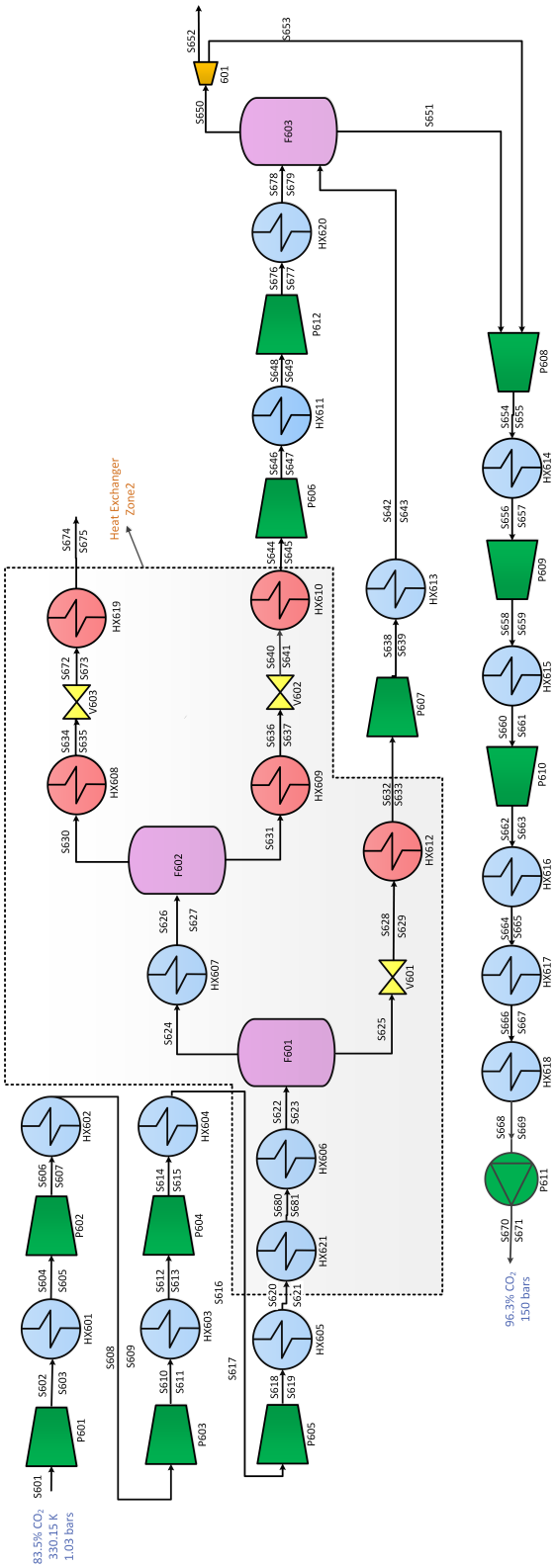

Figure 3.5: Flowsheet for two flash CPU system based on Fu and Gunderson (2012). Heat exchanger units inside the shaped region comprise the sub-ambient multistream heat exchanger.

Table 3.4: Comparison of CPU optimization results with Fu and Gunderson (2012)

	Fu & Gunderson	**This Work**
Shaft Work ($kWh/kgCO_2$)	0.114	0.113
Cooling Utility Requirement ($kWh/kgCO_2$)	Not Reported	0.186

3.4.2 Pareto Analysis

The CPU design optimization problem was resolved for a variety of CO_2 purity and recovery specifications resulting in the Pareto curve shown in Figure 3.6. For each data point, over one hundred different initialization parameter combinations were considered using the multi-start procedure to identify good locally optimal solutions. Each of the three curves in Figure 3.6, which correspond to 90%, 92% and 94.6% CO_2 recovery, exhibit the same trend: as CO_2 purity increases, the specific energy requirement decreases (with constant CO_2 recovery), which is expected: as CO_2 purity increases, the amount of contaminant gas (N_2, O_2, Ar) in the product decreases, and less energy is required to pressurize the product gas from separation operating conditions (around 15 - 20 bar) to the 150 bar product specification. After a certain critical purity, the slopes of the Pareto curves change, and the energetic benefits of increasing CO_2 purity becomes larger. Figure 3.7 explores this trend for the 90% recovery curve, and shows the operating conditions of both vessels as a function of CO_2 purity for the total CPU system. At 96.5% CO_2 purity, the flash vessels switch from operating at substantially different pressures (30 – 55 bar for Flash 1 (F601) and 15 – 20 bar of Flash 2 (F602)) to nearly the same pressure in both vessels. The shift in equilibrium is achieved by the multistream heat exchanger, which allows Flash 2 to operate 5 – 20 K cooler than Flash 1. With lower operating pressures for the flash vessels, less pressure drop is required for the multistream heat exchangers, and the process is more energy efficient.

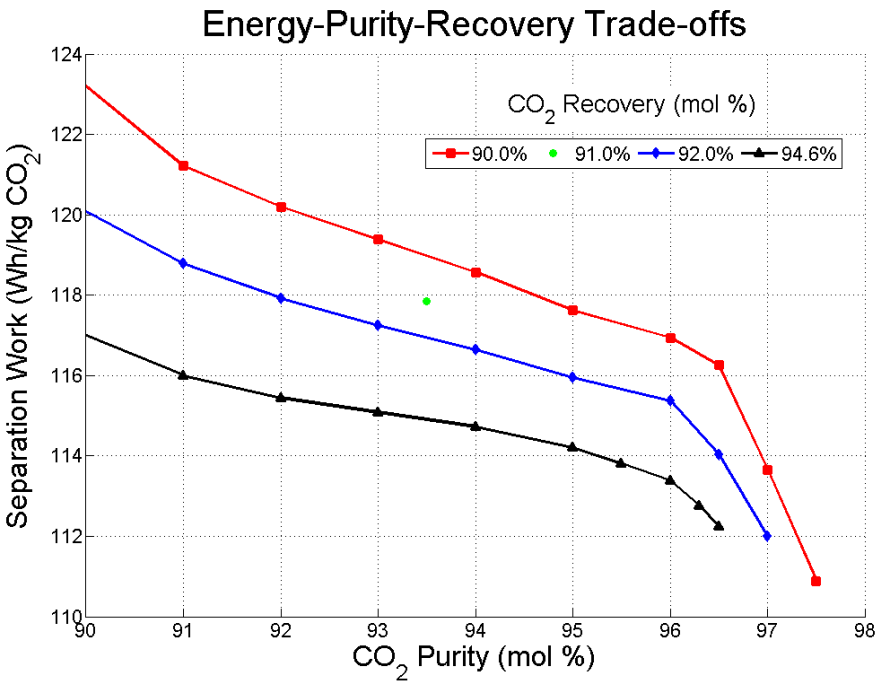

Figure 3.6: Trade-offs between CO_2 purity (horizontal axis), CO_2 recovery (three curves) and specific energy (vertical axis) for the two flash CPU system. Each point represents an optimized design for specified purity and recovery rates. The 91% recovery point is from Section 3.4.4.

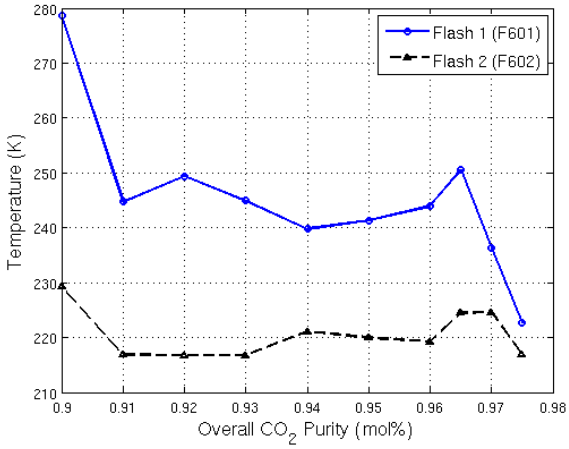

(a) Temperature

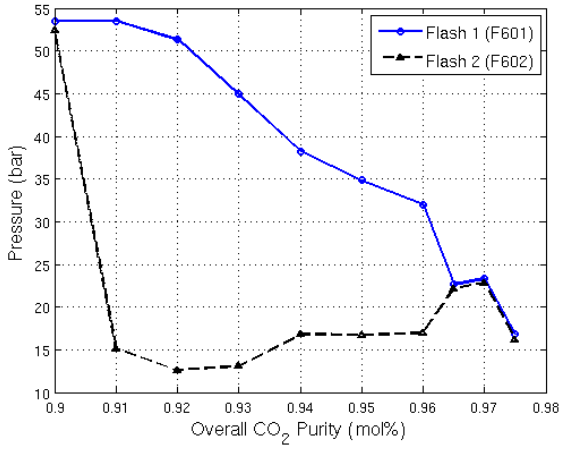

(b) Pressure

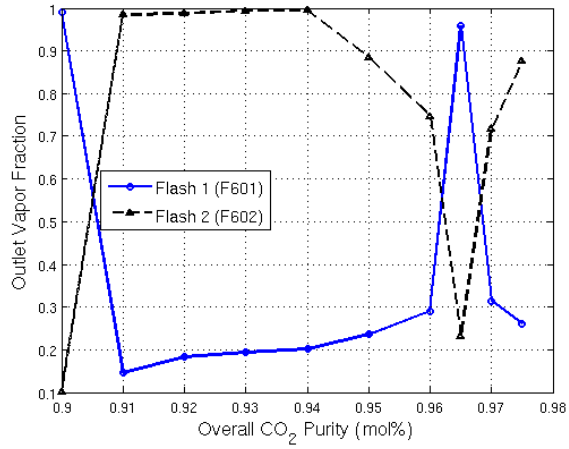

(c) Effluent Vapor Fraction

Figure 3.7: Operating conditions in the two flash vessels for the best solution at various purities and 90% CO_2 recovery

3.4.3 Heat Exchanger Decomposition Sensitivity Analysis

Nonlinear heat capacities are accounted for by decomposing each heat exchange unit (red and blue icons in Figure 3.5) into a fixed number of subunits, which approximates heat capacity as a piecewise linear function of temperature. The previously discussed results, including Figure 3.8(a), were generated using four subunits per original heat exchanger unit, and require work and cooling water duties of 0.1128 and 0.1850 kWh/kg captured CO_2, respectively. As a verification step, the system was reoptimized with ten subunits per original heat exchange unit. The best solution required only slightly more work and cooling water, 0.1133 and 0.1859 kWh/kg CO_2, respectively. The composite curves for the best solution with ten subunits are shown in Figure 3.8(b). The additional subunits provide better resolution of the nonlinear heat capacities around $Q = 2$ to $Q = 4$. Similarly, the pinch point at $Q = 11$ (four subunits per exchanger) is replaced with a pinch point near $Q = 4$ in the ten subunit case. However, the most important performance metric, compression specific energy, changes by only 0.5% with the additional subunits, which suggests four units are adequate for most systems level analyses. Four subunits are used to generate all of the other CPU results.

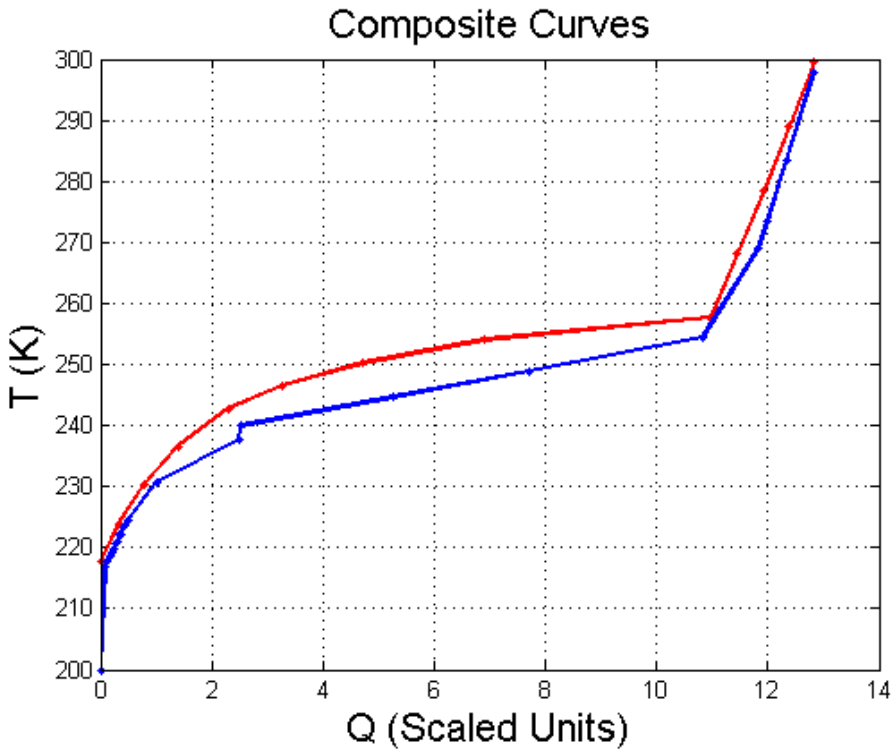

(a) Four subunits per original heat exchange unit

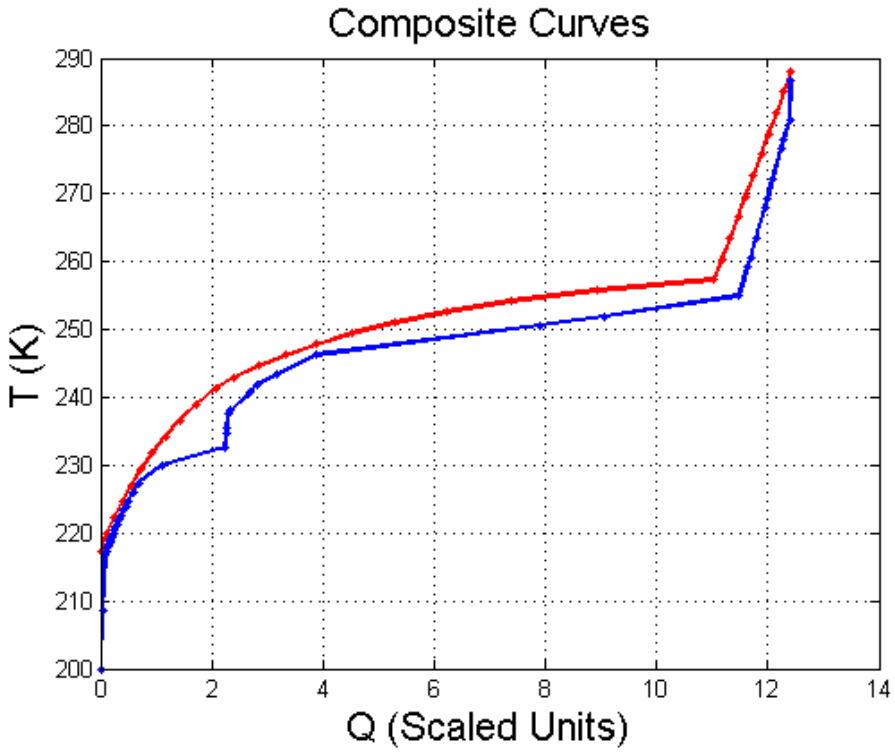

(b) Ten subunits per original heat exchange unit

Figure 3.8: Hot (top) and cold (bottom) composite curves for the multistream heat exchanger with four and ten subunits per heat exchange equipment (see Figure 3.5).

3.4.4 Comparison of Heat Integration Formulations

Using the multi-start procedure described in Chapter 6, the CPU system was reoptimized for 91% CO_2 recovery and 93.5% CO_2 purity requirements. 48 combinations of discrete options for three following initialization parameters are considered for each heat integration model:

1. Reinitialize component flowrates using mole fractions after Step 2 of the initialization algorithm (two options: yes/no)?

2. Either fix $\Delta\underline{T}_z$ in the heat integration model or treat it as a variable with a lower bound (two options)

3. Load values for F, x_c, T, P and Z from a solution in Figure 3.6 with a CO_2 purity between 92 and 95% and a recovery of 90%, 92% or 94.6% (twelve options)

For these results, only steps 0, 2, 5 and 6 in the initialization procedure are considered (see Chapter 6). Overall, this approach is very effective, as shown in Table 3.5 and Figure 3.9. For the modified Duran-Grossmann formulation, all but one of the solutions are classified as locally optimal by CONOPT. The scaled objective function values are shown in Figure 3.9. 39 out of the 48 points resulted in objective function values within 0.5% of the best solution. Furthermore, there are 12 unique designs among these 39 results. Each unique design is a small step in Figure 3.9. Out of the 48 points considered, all but one solution has no complementarity violations. Finally, the best solution from this test case is shown in Figure 3.6, and is in agreement with overall trends in the Pareto analysis. As demonstrated by these results, the proposed multi-start procedure provides a practical and effective alternative to deterministic global optimization.

Furthermore, Table 3.5 shows a comparison of the modified Duran-Grossmann formulation with the two alternate reformulations. With all three heat integration models, CONOPT found solutions with the same best objective function value. Steps 2 and 5 in the initialization procedure are independent of the heat integration model, and as expected the average times for these steps are approximately the same for each model. Step 6 (optimization with decomposed heat integration units) requires 86% and 268% more time on average with reformulations 1 and 2, respectively. This is most likely due to the increased number of constraints with the reformulations. Problem sizes are shown in Table 3.6. Optimization with alternate algorithms, such as IPOPT, that efficiently accommodate sparse constraints may produce better results with the alternate heat integration formulations. Nevertheless, Reformulation 1 is used for the case studies in Chapter 5, as CONOPT occasionally terminates at infeasible points when ε^s is small with the modified D-G model.

The results for Tables 3.5 and 3.6 were obtained using GAMS 24.3.3 (64 bit) on a desktop computer with a AMD FX-6350 (3.9 GHz) processor and 16

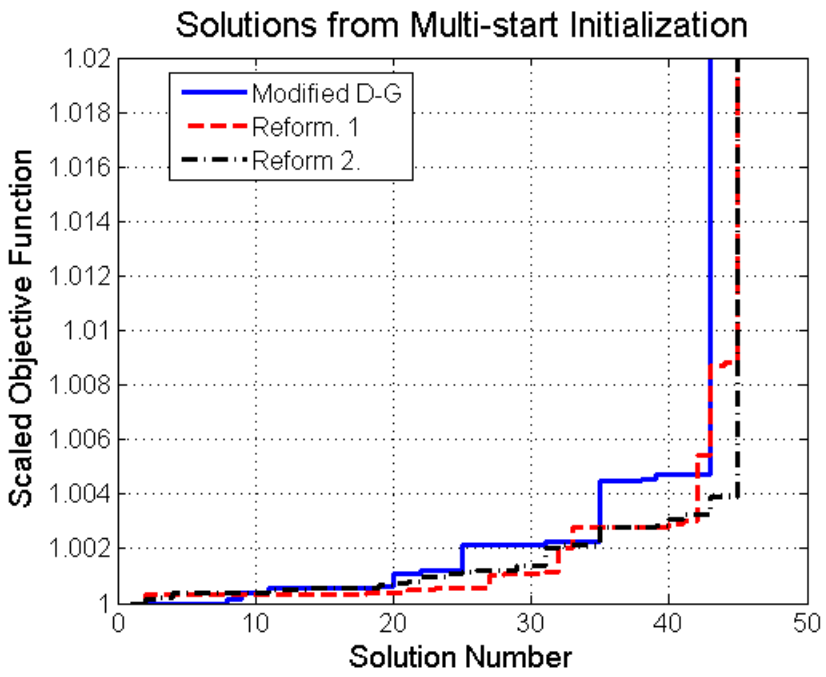

Figure 3.9: Comparison of results with different heat integration models sorted by objective function value

GB of RAM running Windows 7. Up to five solves/initial points were considered in parallel, each running on a separate core. The "Other" row in Table 3.5 includes compiling, loading necessary data files, the additional (inactive) steps, and other GAMS overhead. Initialization procedures are included in the times for each corresponding step. CONOPT was used as the primary solver, although IPOPT (with HSL routines) is used in Step 2 and 5 and SNOPT is used in Step 5 if CONOPT's preprocessing routine fails. The remaining CPU results were obtained using GAMS 24.4.1 on a server with dual Xeon E5-2440 processors (2.4GHz), 16 GB of GAM and ten solves in parallel. For all of these results, the initialization and multi-start procedure described in Chapter 6 was used to generate solutions for the CPU flowsheet.

Table 3.5: Computational results and comparison of the three heat integration formulations. Regarding the solution classification, [1] corresponds to points with feasible complementarity constraints and classified by GAMS as locally optimal. [2] corresponds to points with feasible complementarity constraints and with the following termination status in GAMS: "solver terminated early and model was feasible but not yet optimal".

	Modified D-G	Reform. 1	Reform. 2
Best Objective Function Value	14.681	14.681	14.681
Number Total Solutions within 0.5% of Best Obj.	42	41	44
Number Unique Solutions within 0.5% of Best Obj.	12	11	21
Number Locally Optimal Solutions[1]	46	43	19
Number Feasible Only Solutions[2]	0	2	28
Average Time (CPU-seconds)			
Step 2 (Ch. 6)	79.82	79.24	79.86
Step 5 (Ch. 6)	68.98	69.29	69.63
Step 6 (Ch. 6)	146.90	272.61	394.15
Other (Ch. 6)	12.80	14.84	14.45

Table 3.6: Problem size comparison for heat integration models at the best solution for 91% recovery and 93.5% purity. Note that fixed variables contribute one strongly active and one weakly active variable bound in GAMS.

	Modified D-G	Reform. 1	Reform. 2
Equality constraints	10,223	10,223	10,225
Inequality constraints	1062	9162	13,518
Strongly active	46	2379	9276
Weakly active	85	121	146
Inactive	931	2258	9130
Variables	11,808	16,292	25,004
Active variable bounds	1453	1850	6960
Strongly	1185	1241	4812
Weakly	531	868	2413
Degrees of freedom	1 to 354	1840 to 4707	upto 9821

3.5 Conclusions and Future Work

In this chapter, models for simultaneous heat integration and process optimization are considered. Unlike the heat exchanger network synthesis (HENS) problem, stream flowrates and temperatures are varied in the flowsheet opti-

mization problem and not considered fixed. As discussed by Lang, Biegler, and Grossmann (1988), this adds degrees of freedom to the flowsheet design problem and results in better solutions. The work of Duran and Grossmann (1986) is the basis for the models presented in this chapter, and three extensions are developed:

1. The flowsheet is separated into multiple **heat integration zones**, and the equations in the Duran-Grossmann model are indexed accordingly. This concept allows for restricted heat integration, and is useful for large systems that are too far apart to heat integrated or units that require different utilities. This concept is related to forbidden matches in HENS literature.

2. The Duran-Grossmann model is **reformulated to reduce the number of smooth max operators**, which removes some nonlinear terms. More specifically, (3.4) is replaced with (3.7) and (3.8).

3. Inspired by Kamath, Biegler, and Grossmann (2012), all heat exchange units are **decomposed into subunits** in the last stage of optimization, which refines the constant heat capacity assumption with a piecewise linear approximation.

These models are demonstrated in a case study to optimize the CO_2 processing unit and compression train in an oxycombustion power plant. The goal of this system is to remove N_2, O_2 and Ar from the flue gas, resulting in a nearly pure stream of CO_2, which is compressed to 150 bar for sequestration. The CPU contains three main sections: compression with interstage cooling, separation in flash vessels and additional compression/pumping. The middle section operates at sub-ambient temperatures (220 - 280 K) and includes multistream heat exchangers (MHEXs) to increase energy efficiency. The embedded heat integration models presented in this chapter are used to ensure the MHEXs remain thermodynamics feasible (i.e., don't violate a specified minimum approach temperature) as the optimizer manipulates flowrates, temperatures and pressures in the flowsheet. Furthermore, the multiple heat integration zone concept is used to distinguish interstage coolers serviced by cooling water from the MHEX. Using the models from this and Chapter 2, the CPU system is optimized, and the results require slightly less energy than the reference case from Fu and Gundersen (2012). Furthermore, the system is re-optimized with various purity and recovery requirements to generate a Pareto curve (Figure 3.6), which shows the complex trade-offs between energy, CO_2 purity and CO_2 recovery. Optimization results with four and ten subunits per heat exchange unit are compared. Although the composite curves are more refined with the additional units, the objective function values differ by only 0.5%, thus four units are deemed adequate for this system.

Two reformulations of the Duran-Grossmann are also proposed, in which instances of the smoothed max operator are replaced with inequality and complementarity constraints. The CPU system is used to compare the performance of

these two reformulations to the Duran-Grossmann model. The alternate models require 86% to 268% more CPU-time in Step 6 of the optimization routine for the CPU system, which is due to the additional variables and constraints. Nevertheless, the reformulated models are used in Chapter 5, as CONOPT experiences numerically difficulties with the Duran-Grossmann model. As future work, these alternate models should be tried with alternate solvers, such as IPOPT, that are tailored for large-scale sparse problems. This will require some refinement, as there are degenerate equations in the formulation when flows go to zero, which is discussed in Chapter 6.

Possible synergies between the constraints to avoid nonphysical vapor-liquid equilibrium solutions (Section 2.5.5) and the heat integration model from Kamath, Biegler, and Grossmann (2012) should be investigated as future work. In the latter, a disjunctive program is formulated to position the boundaries of heat exchange subunits at phase transitions. This requires bubble and dew point calculations, however, which are expensive and need shadow streams with cubic EoS models. Instead in this framework, the modeler is required to decompose heat exchange units undergoing phase changes manually. However, with the models presented in Section 2.5.5, bubble and dew point temperatures are already calculated from streams in $\mathcal{S}_{check}$ to ensure correct phase equilibrium predictions. Thus, it should be possible to reuse those calculations and consider the model of Kamath, Biegler, and Grossmann (2012) without a significant increase in problem complexity.

Chapter 4

Distillation Column Models and ASU Optimization

Key Contributions and Results:

- Present novel MESH with tray bypass distillation model for optimization of column size and feed tray location without integer variables
- Discuss initialization strategies for MESH distillation model, including use of optimization results with an approximate cascade model
- Optimize a cryogenic Air Separation Unit (ASU) and accompanying multistream heat exchanger for oxycombustion power plants with the proposed distillation model

4.1 Overview

Distillation is a fundamentally important unit operation in chemical engineering. Humphrey (1995) estimates distillation accounts for more than 90% of separations in the United States, and Soave and Feliu (2002) notes distillations accounts for approximately 3% of the total US energy consumption. In essence, distillation is an extension of the flash separation unit operation, organized in a countercurrent flow. Energy is typically removed and added at the top and bottom of the distillation column, in the condenser and reboiler, respectively, which condense and vaporize the light and heavy products. Some fraction of these products are split and recycled into the distillation column, which is know as reflux (light product, "tops") and reboiler (heavy product, "bottoms"). Distillation columns can contain hundreds of equilibrium stages (i.e., theoretical trays), which make them well suited to separate compounds with similar boiling points.

4.1.1 Literature Review

Optimization of complex distillation systems was pioneered by Sargent and Gaminibandara (1976) and continues to remain a challenging design paradigm

for several reasons. First, distillation requires evaluation of vapor-liquid equilibrium models (Chapter 2), which are highly nonlinear for nonideal models, especially with systems that form an azeotrope. Second, distillation system design requires several discrete decisions, including the number of tray, location of the feed stream(s) and the sequence of separations for multicomponent systems. Finally, heat integration is commonly used to reduce the energy requirements of modern distillation systems.

Severally researchers have applied mathematical programming techniques to automate distillation system design. Andrecovich and Westerberg (1985) developed a mixed integer linear programming (MILP) formulation to optimize heat integrated distillation sequences using approximate models. Several assumptions (constant split fractions calculated *a priori*, fixed column costs that only vary with condenser pressure, etc.) are made to avoid nonlinearities. Viswanathan and Grossmann (1990) developed a rigorous mixed integer nonlinear programming (MINLP) model for distillation column optimization. Integer variables are used to select the optimal feed tray location and activate/deactivate trays. The model has been extended to consider a variable number of trays and multiple feeds (Viswanathan and Grossmann, 1993a,b). The model was also reformulated using disjunctive programming methods (Yeomans and Grossmann, 2000a,c).

Recent work has focused on reformulation of the MINLP distillation column model to remove the integer variables. Embedding the full MINLP column model into a flowsheet with many other nonlinear reactors and separation units may lead to intractable optimization problems. Also, rigorous thermodynamics models add significant nonlinearity and nonconvex constraints to the distillation optimization problem, which complicates the solution of the original MINLP problem. By formulating the optimization problem as a pure NLP, the combinatorial nature of the mixed integer problem can be mitigated. This motivated Lang and Biegler (2002) to propose the distributed stream-tray optimization method for distillation column design. Feed, product and reflux stream locations are represented with continuous variables. The distribution of material flows from these streams onto trays are calculated using a differential distribution function. Complementarity constraints are used to allow dry tray (zero vapor or liquid flowrates), similar to vanishing phases discussed in Chapter 2. Smoothing techniques described by Gopal and Biegler (1999) are used to accommodate the complementarity constraints. Similarly, Raghunathan and Biegler (2003) used the complementarity formulation to optimize distillation columns below the minimum reflux ratio with dry trays. Baumrucker, Renfro, and Biegler (2008) revisited the model of Lang and Biegler (2002), and explored alternate treatments for the complemnarity constraints. More recently, Kamath, Grossmann, and Biegler (2010) proposed a revised shortcut model as an approximate distillation model. Unfortunately, there can be significant mismatch between their model and more rigorous mass, equilibrium, summation and heat (MESH) equations for certain distillation systems. Alternately, Kraemer, Kossack, and Marquardt (2009) investigated relaxations of the in-

teger variables in the formulation of Viswanathan and Grossmann (1990) to continuous and inclusion of a nonlinear Fischer-Burmeister function constraint to drive these variables to 0 or 1 values. The approach has some drawbacks; most notably the interior of relaxed integer variables (non-binary values) are ill-defined, leading to local solutions and even infeasibilities when the problem is not carefully initialized. This key downside has motivated development of a new MESH model with bypass that has physically realizable relaxations.

4.1.2 Chapter Organization

Robust distillation models for the equation-based framework are developed in this chapter. Given the highly nonlinear equations required for vapor-liquid equilibrium with cubic EoS models, integer variables are avoided. First, a general cascade structure and the necessary connectivity sets are introduced. Next, shortcut models based on the Edmister approximation are summarized. These models allow for the number of trays (equilibrium stages) to be approximated with continuous variables. The results from these models are used to initialize a novel mass, energy, summation and heat (MESH) equation-based model that features tray bypasses instead of integer variables to optimize the feed location and number of trays. Finally, these models are demonstrated in an air separation unit (ASU) design case study. The ASU is tailored to produce O_2 for an oxycombustion power plant and operates at cryogenic temperatures. The accompanying multistream heat exchanger is modeled using the heat integration methods described in Chapter 3, similar to the CPU case study.

4.2 General Cascade Structure

In this framework, cascades (set $\mathcal{E}$, index e) are defined as a sequence of equilibrium stages, and may be linked together to form distillation, absorption and stripping columns. Flash vessels are used to model feed trays. A general superstructure for a distillation column is shown in Figure 4.1. The feed stream, *S1*, is split into *S2*, *S3* and *S4* via splitter 1. These streams act as feeds for flash vessels *F1*, *F2* and *F3*, which correspond to the bottom, a middle and the top trays in the column. Cascade sections are located between the flash vessels. This superstructure allows for selection of an absorption, stripping or distillation column, along with hybrid configurations. Also shown in Figure 4.1 are the four main streams for each cascade section: inlet vapor (*S6*, *S12*), inlet liquid (*S4*, *S14*), outlet vapor (*S5*, *S13*) and outlet liquid (*S7*, *S11*). The sets $\mathcal{E}^V_{in}$, $\mathcal{E}^L_{in}$, $\mathcal{E}^V_{out}$ and $\mathcal{E}^L_{out}$ are used to manage this connectivity.

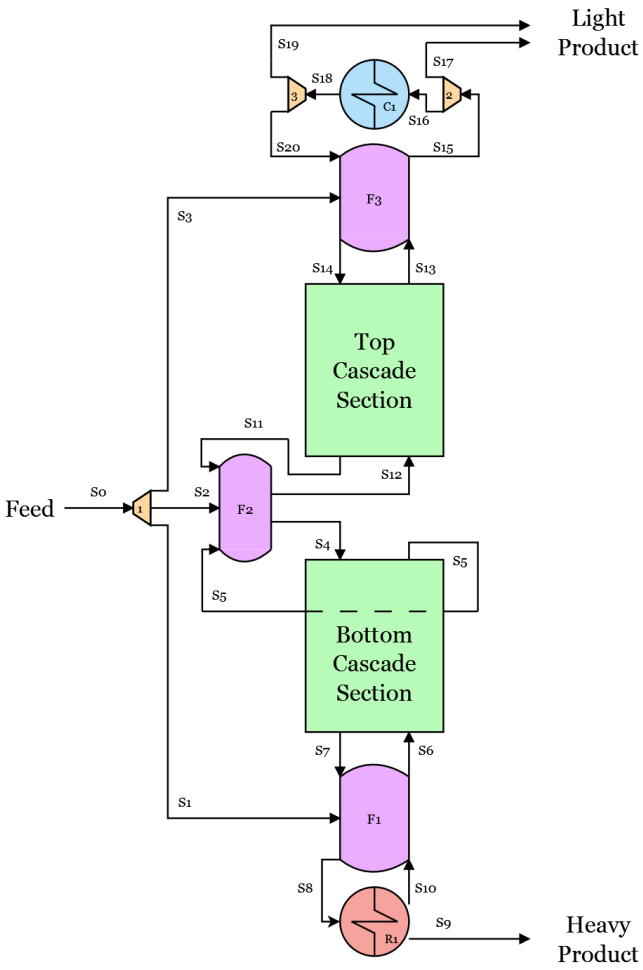

Figure 4.1: Distillation Column Structure with Variable Feed Location

4.3 Group Method Models

Numerous engineers have proposed empirical-based models to approximate the performance of separation columns. A classic example is the Fenske-Underwood-Gilliland method, in which the Fenkse equation is used to predict the minimum number of theoretical trays at total reflux and the Underwood equation approximates the minimum number of reflux ratio for a multicomponent separation (Fenske, 1932; Underwood, 1949). Finally, the Gilliland correlation uses these two quantities to predict the number of theoretical trays for a separation as a function of reflux ratio (Gilliland, 1940). Erbar and Maddox (1961) and many others have proposed alternate correlations to predict the number of theoretical trays and other key design parameters. These models avoid the need for rigorous tray-by-tray simulations, which are computationally expensive in large multicomponent systems, but are only provide approximations. Typical assumptions include constant relative volatility and constant molal reflux.

Similarly, group methods approximate separation cascade performance by calculating the average separation quality of a tray and duplicating said tray for the entire cascade. Recently, Kamath, Grossmann, and Biegler (2010) proposed a modified Edmister/Kremser group method, which is general purpose and suitable for superstructure optimization. At the heart of the model are component mole balances (4.1a), an enthalpy balance (4.1b) and performance equation (4.1c). The recoveries for component c in cascade e for absorption, $\varphi^A_{c,e}$, and stripping, $\varphi^S_{c,e}$, are used in the performance equation and are calculated from (4.2a) and (4.2b). These equations are log transformations of the original model in Kamath, Grossmann, and Biegler (2010) and include two intermediate variables, I^A and I^S, which are defined in (4.2c) and (4.2d). Based on empirical observations, this reformulation provides better scaled derivatives and improved numeric performance.

$$\forall (s^{iv}, s^{il}, s^{ol}, s^{ov}, e) \in \{(s^1, s^2, s^3, s^4, e) | (s^1, e) \in \mathcal{E}^V_{in}, (s^2, e) \in \mathcal{E}^L_{in}, \\ (s^3, e) \in \mathcal{E}^V_{out}, (s^4, e) \in \mathcal{E}^L_{out}\},$$

$$f_{s^{il},c} + f_{s^{iv},c} = f_{s^{ov},c} + f_{s^{ol},c}, \quad \forall c \in \mathcal{C} \tag{4.1a}$$

$$F_{s^{il}} H_{s^{il}} + F_{s^{iv}} H_{s^{iv}} = F_{s^{ov}} H_{s^{ov}} + F_{s^{ol}} H_{s^{ol}} \tag{4.1b}$$

$$f_{s^{ov},c} = f_{s^{iv},c} \varphi^A_{e,c} + f_{s^{il},c}(1 - \varphi^S_{e,c}), \quad \forall c \in \mathcal{C} \tag{4.1c}$$

$$L^1_e - F_{s^{ol}} = F_{s^{ov}} - V^N_e \tag{4.1d}$$

$$P_{s^{iv}} = P_{s^{il}} = P_{s^{ov}} = P_{s^{ol}} \tag{4.1e}$$

The absorption factors are calculated from equilibrium expressions at the column outlets, which require separate implementations for each thermodynamics module: (4.4) for the simple thermodynamics module, and (4.5) for the cubic EoS module. The stripping factors are related to the absorption factors, as shown in (4.2g) & (4.2h). A^1, A^N, S^1 and S^N represent the absorption and stripping phenomena at the top and bottom of the cascade. These factors are averaged using the original formula proposed by Edmister, (4.2e) & (4.2f), which produces A^E and S^E that are reflective of the "average" separation phenomena in the column.

$$\forall c \in \mathcal{C}, \quad \forall e \in \mathcal{E},$$

$$(N_e + 1)\ln(A^E_{e,c}) = \ln(I^A_{e,c}) - \ln(\varphi^A_{e,c}) \tag{4.2a}$$

$$(N_e + 1)\ln(S^E_{e,c}) = \ln(I^S_{e,c}) - \ln(\varphi^S_{e,c}) \tag{4.2b}$$

$$I^A_{e,c} = A^E_{e,c} - 1 + \varphi^A_{e,c} \tag{4.2c}$$

$$I^S_{e,c} = S^E_{e,c} - 1 + \varphi^S_{e,c} \tag{4.2d}$$

$$A^E_{e,c} = \sqrt{A^N_{e,c}\left(A^1_{e,c} + 1\right) + 0.25} - 0.5 \tag{4.2e}$$

$$S^E_{e,c} = \sqrt{S^1_{e,c}\left(S^N_{e,c}+1\right)+0.25}-0.5 \tag{4.2f}$$

$$S^1_{e,c}A^1_{e,c} = 1 \tag{4.2g}$$

$$S^N_{e,c}A^N_{e,c} = 1 \tag{4.2h}$$

This model contains two modifications proposed by Kamath, Grossmann, and Biegler (2010). The first modification is an approximate mole balance, shown in (4.1d). This replaces the absorber and stripping specific equations in Edmister (1957), making the model general to either stripping or absorbing cascades. In the second modification, the temperature approximations are replaced by bubble and dew point calculations for the outlet liquid and vapor streams, respectively. This requires separate implementations for each thermodynamic module. Calculation of the bubble and dew point is already part of the simple thermodynamics model, making (4.3) straightforward:

$$P_s = P^d_s, \quad \forall (s,e) \in \mathcal{E}^V_{out} \tag{4.3a}$$

$$P_s = P^b_s, \quad \forall (s,e) \in \mathcal{E}^L_{out} \tag{4.3b}$$

In the simple thermodynamics module, P^{vap} is used to calculate the adsorbtion factors A^1 and A^N and the top and bottom of each cascade.

$$A^1_{e,c}F_sP^{vap}_{s,c} = L^1_eP_s, \quad \forall (s,e) \in \mathcal{E}^V_{out}, \quad \forall c \in \mathcal{C} \tag{4.4a}$$

$$A^N_{e,c}V^N_eP^{vap}_{s,c} = F_sP_e, \quad \forall (s,e) \in \mathcal{E}^L_{out}, \quad \forall c \in \mathcal{C} \tag{4.4b}$$

Specifying streams to operate at their bubble or dew point with the cubic EOS thermodynamics model requires the introduction of shadow streams, which are discussed in Section 2.5.2. The constraints are repeated below:

$$\forall (s,\tilde{s}^v,\tilde{s}^l) \in \{\mathcal{S}_{bub} \times \mathcal{S}^V_{shdw} \times \mathcal{S}^L_{shdw}\} \cap \mathcal{S}^{map}_{shdw},$$

$$\sum_{c\in\mathcal{C}} (x_{s,c} - \tilde{y}_{\tilde{s}^v,c}) = 0$$

$$T_s = \tilde{T}_{\tilde{s}^v}$$

$$P_s = \tilde{P}_{\tilde{s}^v}$$

$$x_{s,c}\phi_{s,c} = \tilde{y}_{\tilde{s}^v,c}\tilde{\phi}_{\tilde{s}^v,c}, \quad \forall c \in \mathcal{C}$$

$$\forall (s,\tilde{s}^v,\tilde{s}^l) \in \{\mathcal{S}_{dew} \times \mathcal{S}^V_{shdw} \times \mathcal{S}^L_{shdw}\} \cap \mathcal{S}^{map}_{shdw},$$

$$\sum_{c\in\mathcal{C}} \left(\tilde{x}_{\tilde{s}^l,c} - y_{s,c}\right) = 0$$

$$T_s = \tilde{T}_{\tilde{s}^l}$$

$$P_s = \tilde{P}_{\tilde{s}^l}$$

$$\tilde{x}_{\tilde{s}^l,c}\tilde{\phi}_{\tilde{s}^l,c} = y_{s,c}\phi_{s,c}, \quad \forall c \in \mathcal{C}\ ,$$

where streams in $\mathcal{S}^{bub}$ and $\mathcal{S}^{dew}$ are constrained to their bubble and points, respectively. In the framework, all streams in $\mathcal{E}^L_{out}$ and $\mathcal{E}^V_{out}$ are automatically assigned to $\mathcal{S}^{bub}$ and $\mathcal{S}^{dew}$, respectively.

The shadow streams (above) are also used to calculate the absorption factors, as follows:

$$\begin{aligned}\forall(s,\tilde{s}^v,\tilde{s}^l,e) \in &\{(s,s^1,s^2,e)|(s,e)\in\mathcal{E}^V_{out}, s^1\in\mathcal{S}^V_{shdw},\\ &s^2\in\mathcal{S}^L_{shdw},(s,s^1,s^2)\in\mathcal{S}^{map}_{shdw}\}\end{aligned}$$

$$A^1_{e,c}\ F_s\ \phi_{\tilde{s}^l,c} = L^1_e\ \phi_{s,c}, \quad \forall c\in\mathcal{C} \tag{4.5a}$$

$$\begin{aligned}\forall(s,\tilde{s}^v,\tilde{s}^l,e) \in &\{(s,s^1,s^2,e)|(s,e)\in\mathcal{E}^L_{out}, s^1\in\mathcal{S}^V_{shdw},\\ &s^2\in\mathcal{S}^L_{shdw},(s,s^1,s^2)\in\mathcal{S}^{map}_{shdw}\}\end{aligned}$$

$$A^N_{e,c}\ V^N_e\ \phi_{s,c} = F_s\ \phi_{\tilde{s}^v,c}, \quad \forall c\in\mathcal{C}\ . \tag{4.5b}$$

4.4 Tray-by-Tray Model with Bypass

Kremser's shortcut model assumes the separation factor remains constant in the cascade[1]; in real cascades this can lead to approximation error. For these systems rigorous mass, equilibrium, summation and heat (MESH) models for each discrete tray should be considered, which requires either the number of trays to be fixed *a priori* or use of integer variables, such as in Viswanathan and Grossmann (1990). Before introducing the rigorous tray-by-tray model, it is important to establish some nomenclature. Each cascade (set $\mathcal{E}$) is made up of a sequence of trays (set $\mathcal{D}$). The cascade-tray mapping is captured in the ordered set $\mathcal{D}^E$. Furthermore, each tray has an inlet-vapor, inlet-liquid, outlet-vapor and outlet-liquid stream. Similar to cascades, the stream-tray pairings are contained in the sets $\mathcal{D}^V_{in}$, $\mathcal{D}^L_{in}$, $\mathcal{D}^V_{out}$ and $\mathcal{D}^L_{out}$. Finally, let

$$\begin{aligned}S^{in}_d &:= \{s|(s,d)\in\mathcal{D}^L_{in}\cup\mathcal{D}^V_{in}\}\\ S^{out}_d &:= \{s|(s,d)\in\mathcal{D}^L_{out}\cup\in\mathcal{D}^V_{out}\}\ .\end{aligned}$$

The model for each tray is straightforward, consisting of component mole and heat balances (4.6) and equilibrium calculations (4.7). The summation equations are part of the stream model (2.21c). Pressure drop is also included in the tray model. (4.8) and (4.9), where ΔP_e represents the pressure drop per tray coefficient (typically constant). N_e represents the number of trays per cascade which is initially fixed. In this framework, the MESH cascade model is only implemented with the cubic EoS thermodynamics module.

[1] See Biegler, Grossmann, and Westerberg (1997) for a derivation.

$$\sum_{s \in S_d^{in}} f_{s,c} = \sum_{s \in S_d^{out}} f_{s,c}, \quad \forall c \in \mathcal{C}, \quad \forall d \in \mathcal{D} \tag{4.6a}$$

$$\sum_{s \in S_d^{in}} F_s H_s = \sum_{s \in S_d^{out}} F_s H_s \tag{4.6b}$$

$$\forall (s^v, s^l, d) \in \{(s^1, s^2, d) | (s^1, d) \in \mathcal{D}_{out}^V, (s^2, d) \in \mathcal{D}_{out}^L\},$$

$$K_{d,c}\ \phi_{s^v,c} = \phi_{s^l,c}, \qquad \forall c \in \mathcal{C} \tag{4.7a}$$

$$y_{s^v,c} = K_{d,c}\ x_{s^l,c}, \qquad \forall c \in \mathcal{C} \tag{4.7b}$$

$$T_{s^l} = T_{s^v} \tag{4.7c}$$

$$P_{s^l} = P_{s^v} \tag{4.7d}$$

$$\forall (s^v, s^l, e) \in \{(s^1, s^2, e) | (s^1, e) \in \mathcal{E}_{in}^V, (s^2, e) \in \mathcal{E}_{in}^L\},$$

$$P_{s^v} = P_{s^l} + (N_e)(\Delta P_e) \tag{4.8}$$

$$\forall (s^i, s^o, d) \in \{(s^1, s^2, d) | (s^1, d) \in \mathcal{D}_{in}^V, (s^2, d) \in \mathcal{D}_{out}^V\},$$

$$P_{s^o} = P_{s^i} - \Delta P_e\ . \tag{4.9}$$

The standard MESH model is extended by considering bypass streams for each tray, as shown in Figure 4.2. The liquid and vapor flows into tray n, L_{n+1} and V_{n-1}, respectively, are split creating the bypass streams L_i^* and V_n^*. The non-bypassed remainder of the vapor and liquid flows enter tray n. If no bypass occurs (flows in L_n^* and V_n^* are zero), the standard MESH model is obtained and the outlet streams (L_n and V_n) are in vapor-liquid equilibrium. In contrast, with total bypass no separation is achieved and the inlet streams are identical to the outlets. As a result, partially bypassed trays are well defined and the feasible region is not disjoint.

Connectivity for this bypass model in managed with several sets. $\mathcal{D}_b^V$ and $\mathcal{D}_b^L$ contain the stream-tray pairs for the bypass streams, and $\mathcal{D}_e^V$ and $\mathcal{D}_e^L$ contains stream-tray pairs for the equilibrium streams, which leave the cascade and are denoted $\hat{V}_n$ and $\hat{L}_n$ in Figure 4.2. Finally, to simplify notation in this section, let

$$\begin{aligned}
V_{n-1} &= F_s, \quad \forall s \in \{s | (s,n) \in \mathcal{D}_{in}^V\} \\
v_{n-1,c} &= f_{s,c}, \quad \forall s \in \{s | (s,n) \in \mathcal{D}_{in}^V\}, \quad \forall c \in \mathcal{C} \\
y_{n-1,c} &= y_{s,c}, \quad \forall s \in \{s | (s,n) \in \mathcal{D}_{in}^V\}, \quad \forall c \in \mathcal{C} \\
H_{n-1}^V &= H_s, \quad \forall s \in \{s | (s,n) \in \mathcal{D}_{in}^V\}
\end{aligned}$$

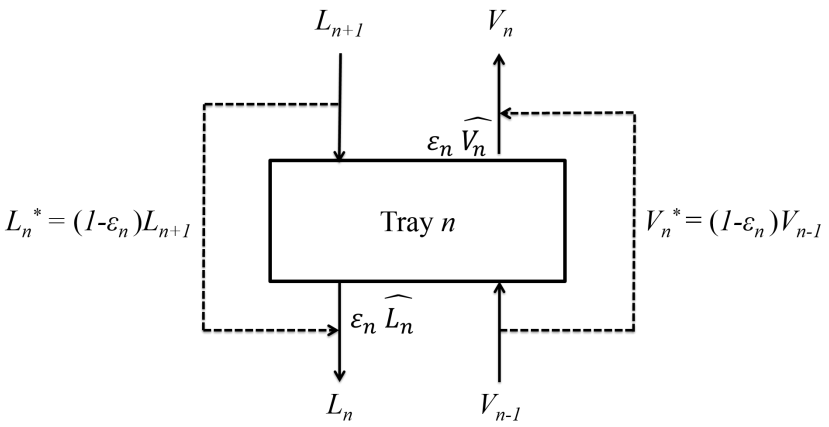

Figure 4.2: Single Tray with Bypass Streams

$$
\begin{aligned}
L_{n+1} &= F_s, \quad \forall s \in \{s|(s,n) \in \mathcal{D}_{in}^L\} \\
l_{n+1,c} &= f_{s,c}, \quad \forall s \in \{s|(s,n) \in \mathcal{D}_{in}^L\}, \quad \forall c \in \mathcal{C} \\
y_{n+1,c} &= y_{s,c}, \quad \forall s \in \{s|(s,n) \in \mathcal{D}_{in}^L\}, \quad \forall c \in \mathcal{C} \\
H_{n+1}^L &= H_s, \quad \forall s \in \{s|(s,n) \in \mathcal{D}_{in}^L\}
\end{aligned}
$$

$$
\begin{aligned}
V_n &= F_s, \quad \forall s \in \{s|(s,n) \in \mathcal{D}_{out}^V\} \\
v_{n,c} &= f_{s,c}, \quad \forall s \in \{s|(s,n) \in \mathcal{D}_{out}^V\}, \quad \forall c \in \mathcal{C} \\
y_{n,c} &= y_{s,c}, \quad \forall s \in \{s|(s,n) \in \mathcal{D}_{out}^V\}, \quad \forall c \in \mathcal{C} \\
H_n^V &= H_s, \quad \forall s \in \{s|(s,n) \in \mathcal{D}_{out}^V\} \\
P_n^V &= P_s, \quad \forall s \in \{s|(s,n) \in \mathcal{D}_{out}^V\}
\end{aligned}
$$

$$
\begin{aligned}
L_n &= F_s, \quad \forall s \in \{s|(s,n) \in \mathcal{D}_{out}^L\} \\
l_{n,c} &= f_{s,c}, \quad \forall s \in \{s|(s,n) \in \mathcal{D}_{out}^L\}, \quad \forall c \in \mathcal{C} \\
x_{n,c} &= x_{s,c}, \quad \forall s \in \{s|(s,n) \in \mathcal{D}_{out}^L\}, \quad \forall c \in \mathcal{C} \\
H_n^L &= H_s, \quad \forall s \in \{s|(s,n) \in \mathcal{D}_{out}^L\} \\
P_n^L &= P_s, \quad \forall s \in \{s|(s,n) \in \mathcal{D}_{out}^L\}
\end{aligned}
$$

$$
\begin{aligned}
V_n^* &= F_s, \quad \forall s \in \{s|(s,n) \in \mathcal{D}_b^V\} \\
v_{n,c}^* &= f_{s,c}, \quad \forall s \in \{s|(s,n) \in \mathcal{D}_b^V\}, \quad \forall c \in \mathcal{C} \\
y_{n,c}^* &= y_{s,c}, \quad \forall s \in \{s|(s,n) \in \mathcal{D}_b^V\}, \quad \forall c \in \mathcal{C}
\end{aligned}
$$

$$
\begin{aligned}
L_n^* &= F_s, \quad \forall s \in \{s|(s,n) \in \mathcal{D}_b^L\} \\
l_{n,c}^* &= f_{s,c}, \quad \forall s \in \{s|(s,n) \in \mathcal{D}_b^L\}, \quad \forall c \in \mathcal{C} \\
x_{n,c}^* &= x_{s,c}, \quad \forall s \in \{s|(s,n) \in \mathcal{D}_b^L\}, \quad \forall c \in \mathcal{C}
\end{aligned}
$$

$$
\begin{aligned}
\hat{V}_n &= F_s, \quad \forall s \in \{s|(s,n) \in \mathcal{D}_e^V\} \\
\hat{v}_{n,c} &= f_{s,c}, \quad \forall s \in \{s|(s,n) \in \mathcal{D}_e^V\}, \quad \forall c \in \mathcal{C} \\
\hat{y}_{n,c} &= y_{s,c}, \quad \forall s \in \{s|(s,n) \in \mathcal{D}_e^V\}, \quad \forall c \in \mathcal{C} \\
\hat{H}_n^V &= H_s, \quad \forall s \in \{s|(s,n) \in \mathcal{D}_e^V\} \\
\hat{P}_n^V &= P_s, \quad \forall s \in \{s|(s,n) \in \mathcal{D}_e^V\} \\
\hat{T}_n^V &= T_s, \quad \forall s \in \{s|(s,n) \in \mathcal{D}_e^V\} \\
\hat{\phi}_{n,c}^V &= \phi_{s,c}, \quad \forall s \in \{s|(s,n) \in \mathcal{D}_e^V\}, \quad \forall c \in \mathcal{C}
\end{aligned}
$$

$$
\begin{aligned}
\hat{L}_n &= F_s, \quad \forall s \in \{s|(s,n) \in \mathcal{D}_e^L\} \\
\hat{l}_{n,c} &= f_{s,c}, \quad \forall s \in \{s|(s,n) \in \mathcal{D}_e^L\}, \quad \forall c \in \mathcal{C} \\
\hat{x}_{n,c} &= x_{s,c}, \quad \forall s \in \{s|(s,n) \in \mathcal{D}_e^L\}, \quad \forall c \in \mathcal{C} \\
\hat{H}_n^L &= H_s, \quad \forall s \in \{s|(s,n) \in \mathcal{D}_e^L\} \\
\hat{P}_n^L &= P_s, \quad \forall s \in \{s|(s,n) \in \mathcal{D}_e^L\} \\
\hat{T}_n^L &= T_s, \quad \forall s \in \{s|(s,n) \in \mathcal{D}_e^L\} \\
\hat{\phi}_{n,c}^L &= x_{s,c}, \quad \forall s \in \{s|(s,n) \in \mathcal{D}_e^L\}, \quad \forall c \in \mathcal{C} \ ,
\end{aligned}
$$

where the index n is used in place of d for this section. The definitions are used to simplify the notation below. These intermediate variables are not implemented in the GAMS code. Also note $\hat{x}$ and $\hat{y}$ does not refer to log-transformed compositions in this chapter, but instead compositions of the "equilibrium streams" in the tray-bypass model. With these definitions the following relationships hold:

$$
\begin{aligned}
l_{n,c} &= x_{n,c}\, L_n \\
v_{n,c} &= y_{n,c}\, V_n
\end{aligned}
$$

Let the ratio of non-bypassed flow to total flow into the tray section be defined as the bypass efficiency, ε_n,

$$
\varepsilon_n = 1 - \frac{V_n^*}{V_{n-1}} = 1 - \frac{L_n^*}{L_{n+1}} \ . \tag{4.10}
$$

and the number of trays in each cascade is computed by summing the tray efficiencies:

$$
\text{Number of Trays } (N_e) \approx \sum_{n \in \mathcal{D}} \varepsilon_n \quad \forall e \in \mathcal{E} \ . \tag{4.11}
$$

With total bypass there is no feed flow ($V_{n-1} - V_n^* = 0$ and $L_{n+1} - L_n^* = 0$) and the equilibrium equations in the MESH model are degenerate. To avoid this problem, the bypass equations are reformulated such that equilibrium is calculated with L_{n+1} and V_{n-1}. The bypass fraction is applied for the mass and

enthalpy balances around mixers. Let $\hat{L}_n$ and $\hat{V}_n$ represent the total flowrate for hypothetical streams exiting tray n without bypass (as with the standard MESH equation model).

First consider equilibrium calculations to determine the flows and composition of $\hat{L}_n$ and $\hat{V}_n$. Recall these stream properties are calculated without bypass, ensuring flowrates used for the equilibrium calculations are non-zero. L_{n+1} and V_{n-1} are bounded away from zero, preventing vanishing phases at the final solution. β_n is included in (4.12c) to assist with convergence.

$$v_{n-1,c} + l_{n+1,c} = \hat{v}_{n,c} + \hat{l}_{n,c}, \qquad \forall c \in \mathcal{C} \tag{4.12a}$$

$$V_{n-1}H^V_{n-1} + L_{n+1}H^L_{n+1} = \hat{V}_n\hat{H}^V_n + \hat{L}_n\hat{H}^L_n \tag{4.12b}$$

$$\hat{y}^V_{n,c} = \beta_n \; K_{n,c} \; \hat{x}^L_{n,c}, \qquad \forall c \in \mathcal{C} \tag{4.12c}$$

$$\hat{T}^V_n = \hat{T}^L_n \tag{4.12d}$$

$$K_{n,c} \; \hat{\phi}^V_{n,c} = \hat{\phi}^L_{n,c}, \qquad \forall c \in \mathcal{C} \tag{4.12e}$$

Next, consider mass and enthalpy balances for two mixers that combine the bypass and streams in equilibrium. These equations are used to calculate the composition and temperature of streams L_n and V_n. Note the definition of ε_n (4.10) is used to implicitly calculate flowrates for bypass streams (L^*_n and V^*_n), and is not included the flowsheet optimization problems.

$$v_{n,c} = \varepsilon_n \; \hat{V}_{n,c} + (1-\varepsilon_n)v_{n-1,c}, \qquad \forall c \in \mathcal{C} \tag{4.13a}$$

$$l_{n,c} = \varepsilon_n \; \hat{L}_{n,c} + (1-\varepsilon_n)l_{n+1,c}, \qquad \forall c \in \mathcal{C} \tag{4.13b}$$

$$L_nH^{L_n} = \varepsilon_n \; \hat{H}^L_n\hat{L}_n + (1-\varepsilon_n)L_{n+1}H^L_{n+1} \tag{4.13c}$$

$$V_nH^V_n = \varepsilon_n \; \hat{H}^V_n\hat{V}_n + (1-\varepsilon_n)V_{n-1}H^V_{n-1} \tag{4.13d}$$

$$0 \le \varepsilon_n \le 1 \tag{4.13e}$$

Overall energy and mass balances for the entire tray with bypass, shown below, can be reconstructed from the equations above and thus are unnecessary.

$$v_{n-1,c} + l_{n+1,c} = v_{n,c} + l_{n,c}, \qquad \forall c \in \mathcal{C}$$

$$H^V_{n-1}V_{n-1} + H^L_{n+1}L_{n+1} = H^V_nV_n + H^L_nL_n$$

Finally the pressure drop relations are specified. The cascade outlet streams are in pressure equilibrium, (4.14a), and pressure of the hypothetical equilibrium stream also match the pressure of the outlet streams, (4.14b) and (4.14c). The ability to activate and deactivate trays is retained by modeling the pressure drop on each tray as proportional to the bypass fraction (4.14d). Equation (4.8) is retained to relate the top and bottom pressures in the entire cascade.

$$P^L_n = P^V_n \tag{4.14a}$$

$$P_n^L = \hat{P}_n^L \tag{4.14b}$$

$$P_n^V = \hat{P}_n^V \tag{4.14c}$$

$$P_n^V = P_{n-1}^V - \varepsilon_n \Delta P_n \tag{4.14d}$$

Finally, $\forall n \in \mathcal{D}$ is implied for (4.10), (4.12) - (4.14).

4.4.1 Simple Cascade Demonstration

A cascade with two equilibrium trays is simulated to demonstrate a preference for binary values for bypass efficiencies. Equal molar flowrates and a constant equilibrium coefficient are assumed for simplicity. As shown in the Figure 4.3, the largest $K_{effective}$ (y_{out}/x_{out}) is realized when both trays are active $(\varepsilon_1 = \varepsilon_2 = 1)$. If the problem is constrained such that $\varepsilon_1 + \varepsilon_2 = 1$, the sharpest separation (largest $K_{effective}$) is observed if one tray is complete active and the other is completely bypassed. These results make physical sense, as partial bypass results in inefficient mixing between trays, which explains why optimization with the new model typically results in binary values for bypass fractions. Finally this example shows that non-unique solutions exist (either $\varepsilon_1 = 1$ or $\varepsilon_2 = 1$) and can be prevented with an optional ordering constraint, e.g., $\varepsilon_n \geq \varepsilon_{n+1}$, or careful initialization.

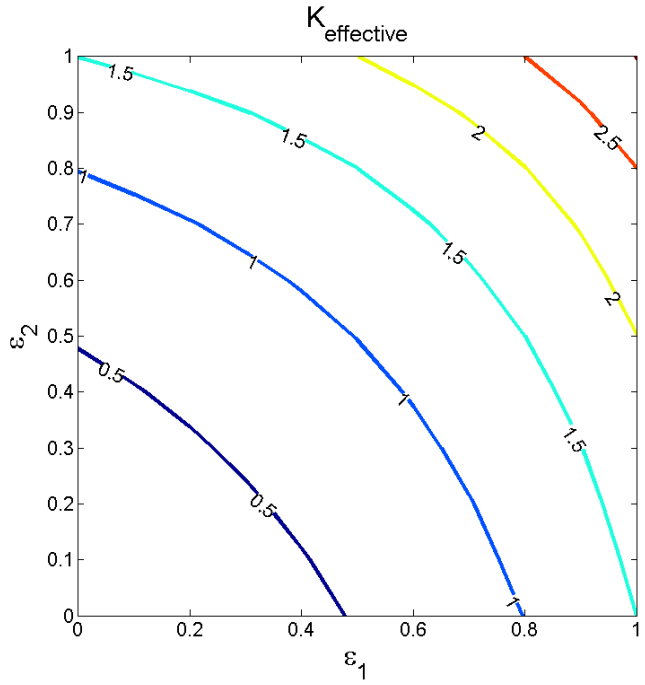

Figure 4.3: Demonstration of bypass model with two trays in series

4.4.2 Initialization

Careful initialization is required for successful optimization with the proposed MESH model (and most NLPs in general). The MESH distillation model with

bypass is solved as a sequence of NLPs and initialization steps, described below and illustrated in Figure 4.4:

1. First, the entire flowsheet is optimized and the shortcut cascade model is used for any distillation cascades. If the optimized flowsheet includes any non-integer number of trays, these values are rounded and fixed, and the entire flowsheet is then reoptimized. This provides a flowsheet solution with an integer number of trays that is used to initialize the MESH model.

2. Next, the MESH with tray bypass model is initialized using the same number of active (non-bypassed) trays as the previous solution. A specified number of additional trays (e.g. ten) are also included in the distillation superstructure. These trays are initialized as inactive (bypassed). This permits the optimizer to turn on additional trays and expand the cascade, similar to the approach from Viswanathan and Grossmann (1990), thus making the number of trays an optimized variable.

3. After initialization the flowsheet is optimized using the MESH with tray bypass model for all distillation cascades.

4. Next the solution is analyzed and additional trays are added or removed in order to reinitialize a fixed number of inactive trays (e.g. ten).

5. The flowsheet is then reoptimized and the process either terminates or repeats by returning to step 4. Potential termination criteria include the following: [1] stop if there is no change in the number of trays from the previous iteration; [2] stop if there is at least one completely inactive tray for each cascade or the maximum number of trays are allocated for each cascade; or [3] stop after a fixed number of iterations. Detailed analysis of the proposed termination criterion is left as future work. In this case study we found terminating after three cycles is sufficient and the simplest to implement.

Experience with the ASU case study has shown using ten to twenty initially inactive trays balances the ability of cascades to grow with computational complexity. If too many initially inactive trays are used the full flowsheet NLP will require noticeably more time to solve. In some cases, CONOPT was observed to terminate at infeasible points with 50+ initially inactive trays for the ASU case study. (The ideal number of initially inactive trays is likely different for other distillation systems and flowsheets. We also found the number of initially inactive trays can impact the local solution found when solving the model. For this reason the number of initially inactive trays is considered as an initialization parameter in the multi-start procedure described in Chapter 6.)

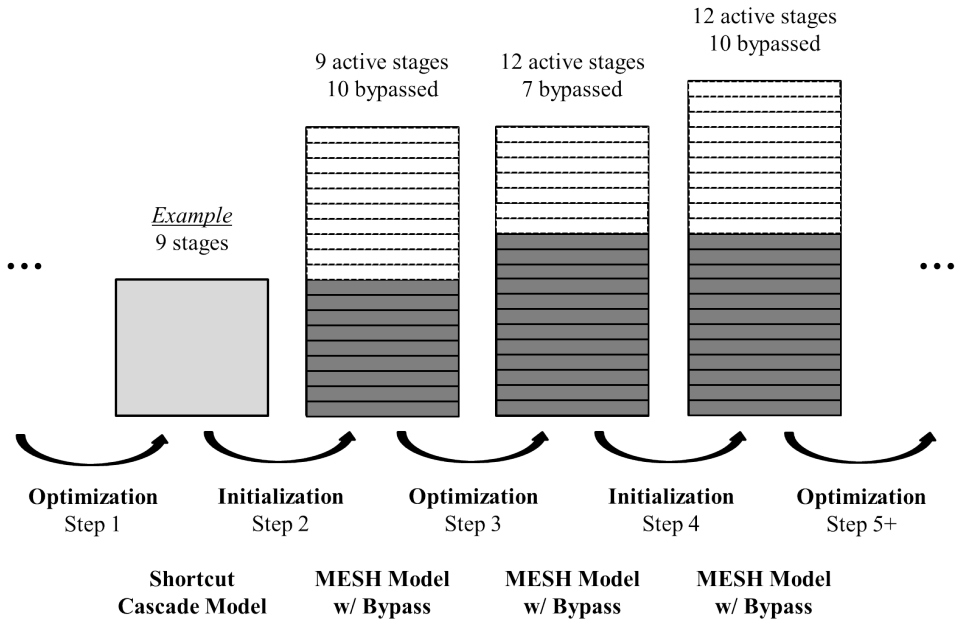

Figure 4.4: Distillation initialization schematic and example. Dark trays are active and light trays are bypassed. During the initialization step the cascade model is resized such that there are ten initially bypassed trays.

Initialization Step: Additional Details

In order to promote solutions where all active trays on at the bottom of a cascade, the "initialization" step in Figure 4.4 in decomposed into substeps. After optimization, the number of inactive cascades ($\varepsilon_d = 0$) is reset to N^+ (user specified parameter). First the number of active trays in each cascade is calculated by rounding ε_d to 0 or 1 and summing these values. Then the trays in each cascade are reordered such that all active trays are at the bottom of the cascade. Finally the cascade is resized such that there are N^+ initially inactive trays above the active trays.

This is best understood with the example in Figure 4.5. Suppose optimization terminates with 6 fully active trays with $\varepsilon_d = 1$, 5 partially bypassed trays with $0 < \varepsilon_d < 1$ and 8 completely bypassed trays with $\varepsilon_d = 0$. First, the bypass efficiencies are rounded, yielding 1 additional active tray and 4 additional bypassed trays in this example. Next, the cascade is reordered such that all 7 active trays are at the bottom. Third, the cascade is resized such that there are 10 (N^+ for this example) inactive trays. Finally, cubic equation of state variables are initialized using analytic expressions, which is not shown in the figure. This concludes the adjustment/initialization algorithm and the flowsheet is reoptimized. It is important to note this example case is extreme and rare. Typically all of the active trays are in one continuous block and $\varepsilon_d \approx 0$ or 1 for each tray after an optimization step.

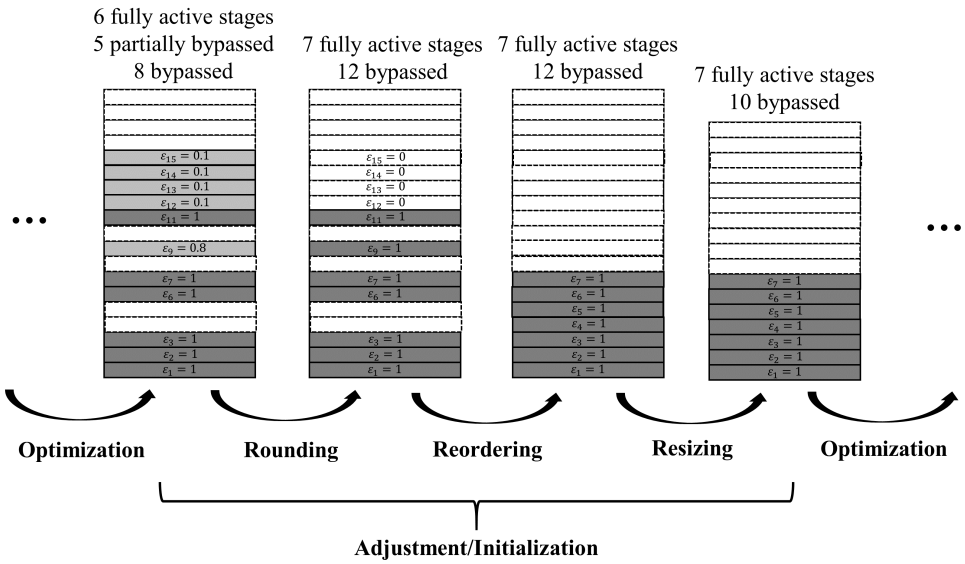

Figure 4.5: Additional details for the "initialization step"

4.5 Case Study: Design of Air Separation Units and Accompanying MHEXs

Purification of air into O_2, N_2, and Ar has many industrial applications, ranging from medical supplies to metallurgical processing. Next generation coal power plants with carbon capture may also use O_2 enriched streams for increased efficiency compared to post-combustion capture designs. For example, in oxycombustion power plants coal is combusted in a N_2 lean environment, producing CO_2, water and some pollutants. This effluent requires significantly less processing and purification than traditional coal power plants to prepare the CO_2 for enhanced oil recovery and sequestration (as most of the N_2 has already been removed). In this case study, the framework is used to synthesize cryogenic air separation units tailored for coal oxycombustion power plants.

After more than a century the original mechanism for separating large quantities of air remains: distillation at cryogenic temperatures (Foerg, 2002). Typically, two or three coupled/heat integrated columns are used for the separation. Air is first compressed at ambient temperature, cooled and throttled to produce additional cooling via the Joule-Thomson effect. The air is fed into a high pressure column, producing N_2 rich distillate and O_2 rich bottoms. These streams are throttled and fed into a lower pressure column for additional separation, resulting in high purity N_2 and O_2 product streams. An optional third column is used to produce especially high purity gases and/or Ar as a product.

Economic operation of cryogenic air separation units requires tight heat integration to minimize the compressor energy requirement (used to drive the

refrigeration cycle). Two strategies are typically employed: [1] the cold product streams cool the warm feed air to cryogenic temperatures in one or more multistream heat exchangers, and [2] heat from the condensing N_2 rich vapor in the high pressure column's condenser is used to vaporize high purity O_2 in the low pressure column's reboiler. With advanced designs these linked reboiler-condenser heat exchangers require a driving force temperature difference as small as 0.4 K (Castle, 2002). Despite these efficiency improving measures, cryogenic air separation remains energy intensive, requiring 4.7 times more energy than the theoretical minimum (Fu and Gundersen, 2012).

A variety of approaches have been use to improve cryogenic air separation process efficiencies. Numerous engineers have focused on improvements in equipment design, allowing for smaller minimum driving forces in heat integration equipment, reduced losses in compressors and expanders and lower pressure drops enabled by high efficiency structured packing materials (Foerg, 2002). Other researchers have focused on tailoring air separation units to specific applications. For example, Fu and Gundersen (2012) applied exergy analysis methods to identify efficiency losses in air separation units for coal oxy-combustion power plants. Jones et al. (2011) compared various ASU configurations for Integrated Gasification Combined Cycle (IGCC) coal power plants by manually adjusting the flowsheet in Aspen Plus. Similarly researchers at Air Liquide have used optimization methods to improve ASU designs for oxy-combustion, but offer no algorithm specifics (Darde et al., 2009). Zhu, Legg, and Laird (2010, 2011) apply EO methods with decomposition techniques and large-scale NLP solvers to design ASUs under uncertainty. In their study, the recycle strategy, feed locations and the number of trays are fixed. In contrast, this case study considers ASU optimization where the number of trays and feed locations are not specified *a priori*, and the accompanying multistream heat exchangers are considered in the design problem.

The remainder of the case study is organized as follows. First the optimal design problem formulation is stated along with the air separation unit superstructure. Next, detailed flowsheet results are described with the optimal column configuration highlighted. The heat integration results are then discussed and compared with literature, and a sensitivity analysis for O_2 purity is presented. Finally, verification with Aspen Plus is considered and numerical performance metrics are disclosed.

4.5.1 Problem Formulation

In this case study, ASU specific energy is minimized subject to O_2 product purity specifications of at 95 mole%, which is common for oxyfuel applications (Fu and Gundersen, 2012; Matuszewski, 2010). In future work, the oxygen purity constraint will be removed, and O_2 purity will be considered as a decision variable in the full power plant optimization problem (along with capital costs). In the problem statement below some equations are deactivated in accordance with the initialization procedure described in Chapter 6.

min	Specific Compression Energy (kWh/kg O_2)	
s.t.	Flowsheet Connectivity	Figure 4.6
	Stream Models	(2.21) & (2.22)
	Thermodynamics Models	[(2.23) - (2.25)] or [(2.26) - (2.41)*, (2.49) - (2.51)]
	Equipment Models	(2.55), (2.56), (2.58) - (2.60)
	Distillation Models	[(4.1) - (4.4)] or [(4.1), (4.2), (4.5)] or [(4.10) - (4.14)]
	Heat Integration Models	(3.1) - (3.3), (3.5) - (3.8)
	Objective Function Calculations	(4.15) - (4.16)
	O_2 Purity $\geq$ 95 mol%	

*A non-log transformed version of (2.36) is used in this case study.

Compressor energy is calculated using the ideal gas formula,

$$E^{cmpr} f_{feed,O_2} = \left(\frac{F_{feed}\ N^{cmpr}\ R\ T^{cool}\ \Gamma}{1.152 \times 10^5\ \text{J} \cdot \text{tonne/kWh}} \right) \times \sum_{s \in \mathcal{S}_{feed}} \left[\left(\frac{P_s}{1\ \text{bar}} \right)^{1/(\Gamma N^{cmpr})} - 1 \right] \tag{4.15}$$

where the number of compressor stages ($N^{cmpr} = 3$), interstage cooling temperature ($T^{cool} = 300$ K) and feed basis ($f_{feed,O_2} = 0.42$ mol/s, $F_{feed} = 2$ mol/s) are fixed, $\Gamma = \frac{\gamma}{\gamma - 1}$ with $\gamma = 1.4$, and $\mathcal{S}_{feed}$ contains the feed streams for the flowsheet (SF0 and SF10 in Figure 4.6).

The objective function considers only compression specific energy (E^{cmpr}) minimum utility loads (Q^s,Q^w) and complementarity violations:

$$\text{obj. func.} = E^{cmpr} + \rho(\text{Compl. Violations}) + Q^s + Q^w \tag{4.16}$$

Thus the complementarity constraints are accommodated using the penalty formulation (1.2e). The penalty weight is increased from $\rho = 10$ to $\rho = 1000$ in the initialization procedure, as described in Chapter 6. For the best ASU solutions, there are no complementarity violations and $Q^s = Q^w = 0$, which indicates no external heating or cooling is required for the MHEXs.

4.5.2 ASU Superstructure

The superstructure shown in Figure 4.6 allows for many common ASU configurations (Castle, 2002; Jones et al., 2011) to be considered. In the superstructure each column is decomposed into two cascade sections (rectifying and stripping). Flash vessels represent trays where feeds are allowed. To accommodate different configurations, each feed stream is split and allowed to enter the columns on the first, last and/or an intermediate tray (flash vessel). The number of trays in the cascade sections are variable (but ≥ 2 for the shortcut

model), and feed tray location is an optimization variable. The superstructure is formulated with only continuous variables to simplify the optimization problem.

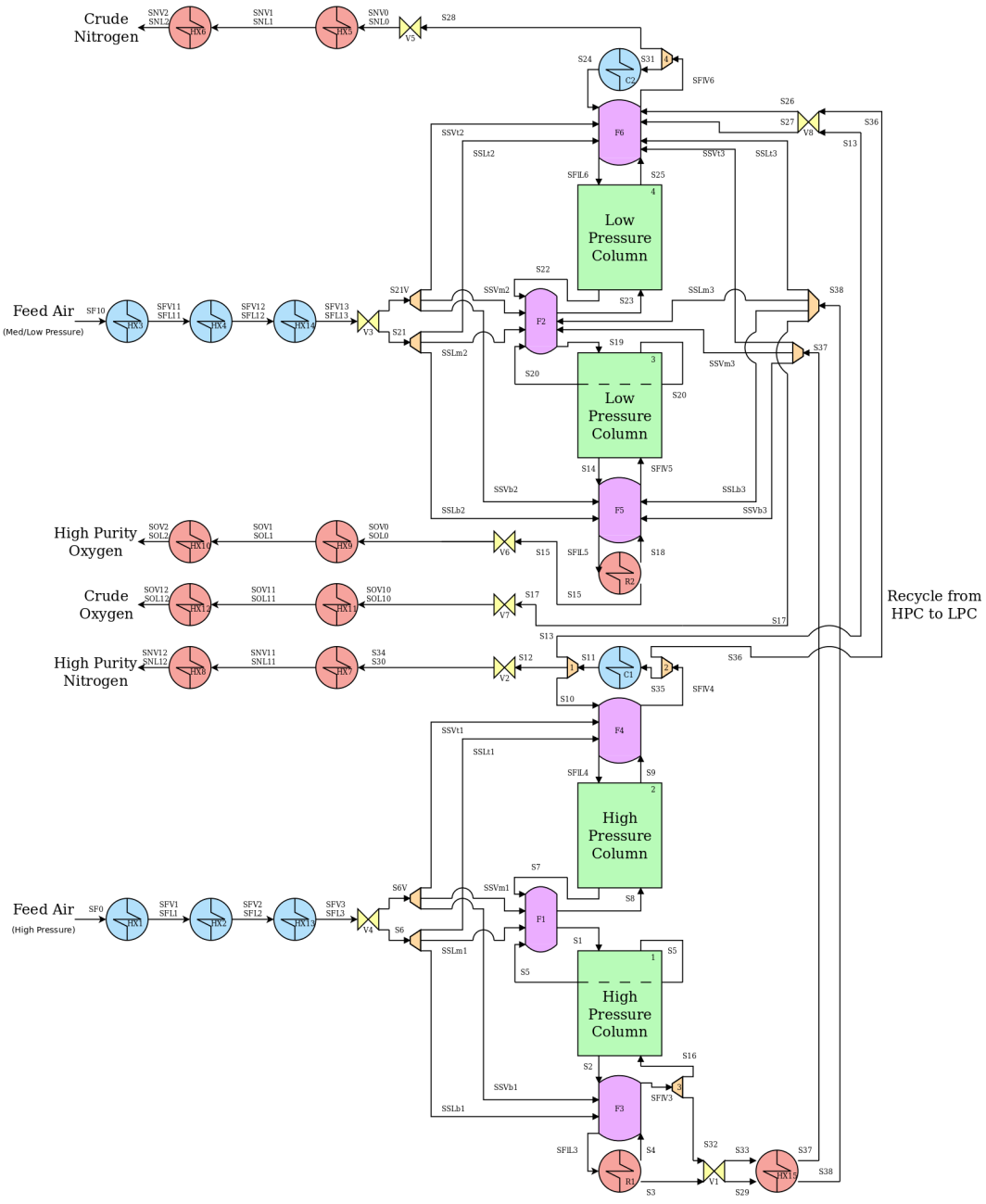

Figure 4.6: ASU Flowsheet Superstructure

4.5.3 Optimal Double Column Configuration

One of the best local solutions from the optimization procedure is shown in Figure 4.7 and has moderately small columns compared to other ASU designs;

there are only 10 and 21 theoretical stages in the high (bottom) and low (top) pressure columns (HPC and LPC), respectively. This is expected as ASUs are typically designed for high O_2 purity (99.9+ mole%) applications. In the optimized design 91.6% of the feed air is compressed to 3.5 bar, partially liquefied in the multistream heat exchanger and fed into the bottom tray of the high pressure column. The bottom of the HPC produces an oxygen enriched liquid stream (63.5 mol% N_2, 35.0% O_2, 1.5% Ar) at 93.2 K. This stream is throttled to near atmospheric pressure, vaporizing 12.3% and decreasing its temperature to 80.7 K. The stream is fed into the bottom and middle of the low pressure column. The distillate of the high pressure column is a nitrogen rich (98.4% N_2, 1.3% O_2, 0.3% Ar) liquid at 89.7 K. This stream is recycled to the top of the low pressure column, providing reflux and eliminating the need for a LPC condenser.

The remaining 8% of the feed air is compressed to 40 bar, cooled from 320 K to 79.1 K (all liquefied) and fed into the 8th tray (from the bottom) of the low pressure column. The low pressure column produces oxygen product (2.4% N_2, 95.0% O_2, 2.6% Ar) at 89.6 K resulting in 98.0% O_2 recovery from the air feed streams. The HPC distillate is the nitrogen product (98.9% N_2, 0.5% O_2, 0.6% Ar), which is produced at 77.5 K as a vapor. Detailed stream information is given in Table 4.1.

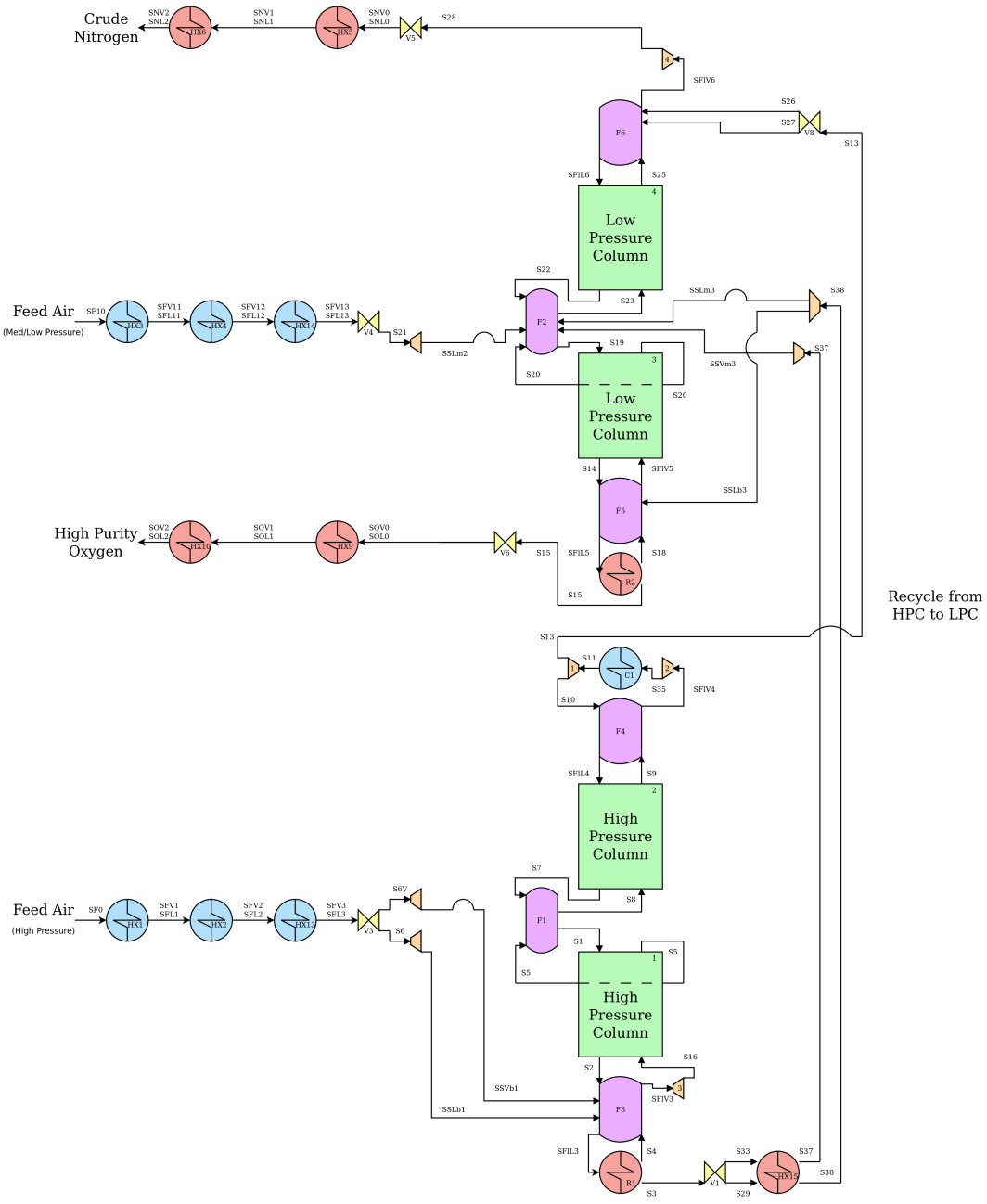

Figure 4.7: Optimal ASU Topology with $\Delta\underline{T}_1 = 1.5$ K, 95% O_2 purity, 0.196 kWh/kg (86% eff. ideal gas compressors)

Table 4.1: Stream Properties Corresponding to Figure 4.7

Stream	F	x_{N_2}	x_{O_2}	x_{Ar}	T	P	Z	H	σ^V or σ^L
S1	0.6870	0.9289	0.0619	0.0092	90.2041	3.4740	0.0152	-11.4705	0
S2	0.6393	0.6860	0.2993	0.0147	92.6538	3.5232	0.0142	-11.6463	0
S3	1.0699	0.6348	0.3503	0.0149	93.2236	3.5314	0.0140	-11.6843	0
S4	0.1982	0.8304	0.1605	0.0092	93.2236	3.5314	0.9043	-6.18758	0
S5	1.4490	0.9578	0.0361	0.0060	90.5025	3.4740	0.8997	-6.29784	0
S6	0.6310	0.6581	0.3284	0.0135	92.9758	3.5314	0.0141	-11.669	0
S7	0.6936	0.9589	0.0348	0.0063	89.9510	3.4740	0.0154	-11.4515	0
S8	1.4556	0.9720	0.0234	0.0046	90.2041	3.4740	0.8989	-6.31215	0
S9	1.4556	0.9720	0.0234	0.0046	90.2041	3.4740	0.8989	-6.31215	0
S10	0.6992	0.9839	0.0130	0.0031	89.7436	3.4740	0.0155	-11.4371	0
S11	1.4612	0.9839	0.0130	0.0031	89.7436	3.4740	0.0155	-11.4371	0
S13	0.7620	0.9839	0.0130	0.0031	89.7436	3.4740	0.0155	-11.4371	0
S14	1.2853	0.0737	0.8848	0.0415	88.2299	1.0508	0.0036	-12.6865	0
S15	0.4332	0.0240	0.9500	0.0260	89.5742	1.0532	0.0035	-12.7242	0
S16	1.4013	0.8480	0.1436	0.0084	92.8990	3.5314	0.9036	-6.20201	0
S18	1.1157	0.0874	0.8765	0.0361	89.5742	1.0532	0.9680	-5.99944	0
S19	1.3762	0.4944	0.4674	0.0382	81.6232	1.0388	0.0042	-12.4622	0
S20	1.2303	0.6856	0.2771	0.0373	83.1286	1.0388	0.9638	-6.28815	0
S21	0.1681	0.7800	0.2100	0.0100	80.1096	6.2731	0.0277	-12.2319	0
S22	0.5865	0.5077	0.4483	0.0441	81.4544	1.0364	0.0042	-12.4406	0
S23	1.3913	0.7889	0.1879	0.0231	81.6232	1.0388	0.9625	-6.37626	0
S25	1.4667	0.9814	0.0080	0.0106	77.6601	1.0100	0.9594	-6.55338	0
S26	0.0486	0.9942	0.0043	0.0014	84.0070	2.0463	0.9308	-6.43638	0
S27	0.7134	0.9832	0.0135	0.0032	84.0070	2.0463	0.0094	-11.7777	0
S28	1.5668	0.9890	0.0054	0.0056	77.5299	1.0100	0.9593	-6.56762	0
S29	0.9384	0.6040	0.3802	0.0158	80.7089	1.0532	0.0044	-12.419	0
S33	0.1315	0.8542	0.1373	0.0086	80.7089	1.0532	0.9610	-6.44187	0
S35	1.4612	0.9839	0.0130	0.0031	89.9510	3.4740	0.8983	-6.3249	0
S37	0.1315	0.8542	0.1373	0.0086	80.7089	1.0532	0.9610	-6.44187	0
S38	0.9384	0.6040	0.3802	0.0158	80.7089	1.0532	0.0044	-12.419	0
S6V	1.2009	0.8440	0.1478	0.0082	92.9758	3.5314	0.9038	-6.19934	0
SF0	1.8319	0.7800	0.2100	0.0100	300.0000	3.5314	0.9982	0.0257	0
SF10	0.1681	0.7800	0.2100	0.0100	320.0000	40.0000	0.9904	0.3734	0
SFV1	1.8319	0.7800	0.2100	0.0100	94.1247	3.5314	0.9062	-6.14956	0
SFV2	1.3218	0.8338	0.1576	0.0085	93.1638	3.5314	0.9042	-6.19114	0
SFV3	1.2009	0.8440	0.1478	0.0082	92.9758	3.5314	0.9038	-6.19934	0
SFL2	0.5101	0.6405	0.3456	0.0139	93.1638	3.5314	0.0140	-11.6819	0
SFL3	0.6310	0.6581	0.3284	0.0135	92.9758	3.5314	0.0141	-11.669	0
SFV11	0.1681	0.7800	0.2100	0.0100	133.5664	40.0000	0.3056	-7.60382	0
SFL12	0.1681	0.7800	0.2100	0.0100	81.4764	40.0000	0.1729	-12.1032	0
SFL13	0.1681	0.7800	0.2100	0.0100	79.0601	40.0000	0.1760	-12.2319	0
SNV0	1.5668	0.9890	0.0054	0.0056	77.5299	1.0100	0.9593	-6.56762	0
SNV1	1.5668	0.9890	0.0054	0.0056	92.9011	1.0100	0.9743	-6.09087	0
SNV2	1.5668	0.9890	0.0054	0.0056	298.5064	1.0100	0.9996	0.0026	0
SOV0	0.0013	0.0875	0.8764	0.0362	89.1740	1.0100	0.9690	-6.00849	0
SOV1	0.4332	0.0240	0.9500	0.0260	90.1870	1.0100	0.9697	-5.98566	0
SOV2	0.4332	0.0240	0.9500	0.0260	306.8343	1.0100	0.9992	0.2442	0
SOL0	0.4319	0.0238	0.9502	0.0260	89.1740	1.0100	0.0034	-12.7451	0
SSVm3	0.1315	0.8542	0.1373	0.0086	80.7089	1.0532	0.9610	-6.44187	0
SSLm2	0.1681	0.7800	0.2100	0.0100	80.1096	6.2731	0.0277	-12.2319	0
SSLm3	0.6511	0.6040	0.3802	0.0158	80.7089	1.0532	0.0044	-12.419	0
SSVb1	1.2009	0.8440	0.1478	0.0082	92.9758	3.5314	0.9038	-6.19934	0
SSLb1	0.6310	0.6581	0.3284	0.0135	92.9758	3.5314	0.0141	-11.669	0
SSLb3	0.2873	0.6040	0.3802	0.0158	80.7089	1.0532	0.0044	-12.419	0
SFlL3	1.2681	0.6653	0.3207	0.0140	92.8990	3.5314	0.0141	-11.6624	0
SFlL4	0.6936	0.9589	0.0348	0.0063	89.9510	3.4740	0.0154	-11.4515	0
SFlL5	1.5489	0.0696	0.8971	0.0333	88.3798	1.0532	0.0036	-12.7031	0
SFlL6	0.6619	0.9663	0.0199	0.0139	77.5299	1.0100	0.0048	-12.1422	0
SFlV3	1.4013	0.8480	0.1436	0.0084	92.8990	3.5314	0.9036	-6.20201	0
SFlV4	1.4612	0.9839	0.0130	0.0031	89.9510	3.4740	0.8983	-6.3249	0
SFlV5	1.1394	0.2263	0.7328	0.0409	88.3798	1.0532	0.9673	-6.0489	0
SFlV6	1.5668	0.9890	0.0054	0.0056	77.5299	1.0100	0.9593	-6.56762	0

4.5.4 Heat Integration Results

Using the models discussed in Chapter 3, minimum utility calculations are embedded in the process optimization problem. The composite curves, shown in Figure 4.8, reveal the process is tightly heat integrated and with no external heating or cooling required ($Q^w = Q^s = 0$). This last point is especially important, as it means cooling from product streams and the Joule-Thomson effect is sufficient to maintain cryogenic operating temperatures at steady-state. Multiple pinch points in the composite curves make the process challenging to heat integrate.

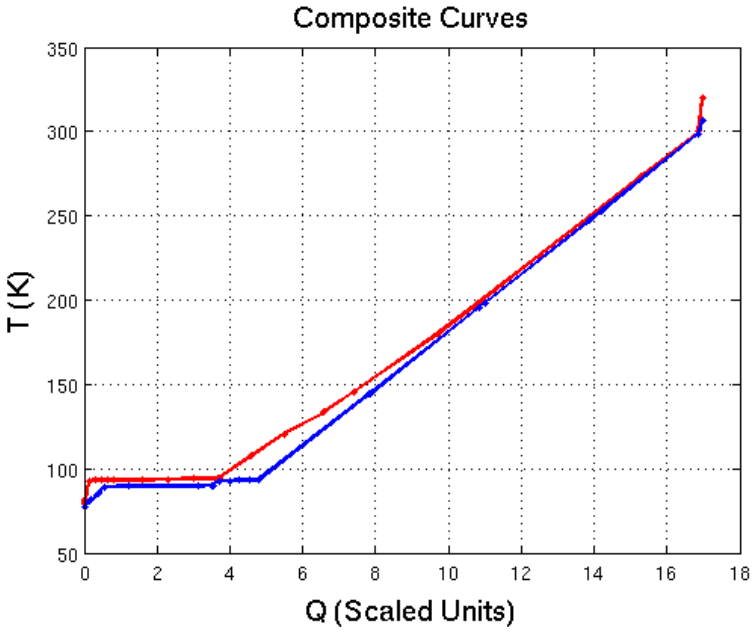

Figure 4.8: Composite curves for optimal ASU (Figure 4.7) with $\Delta\underline{T}_1 = 1.5$, 95% O_2 purity

Phase transitions are accommodated using multiple heat exchangers in series, as discussed in Section 3.2.2 and shown in Figure 4.6. Using only the heat exchangers shown in the superstructure, the process was optimized with $\Delta\underline{T}_1 = 1.5$K for the multistream heat exchangers. The linked condenser-reboiler is heat integrated separately with $\Delta\underline{T}_2 = 0.4$K as suggested by Castle (2002). As discussed in Chapter 3, each heat exchange unit is decomposed into four subunits with equal temperature spacing and the flowsheet is reoptimized to mitigate constant heat capacity assumption errors. Empirically we found that four subunits per heat exchanger balance accuracy with computational costs. Moreover, with five or more subunits, we observed little change in the composite curves or energy requirements. The composite curves in Figure 4.8 include four subunits for all shown heat exchangers, reboilers and condensers. The stream data used to generate composite curves for both heat integration zones are shown in Tables 4.2 and 4.3

Table 4.2: Multistream Heat Exchanger Streams for Optimal ASU with $\Delta\underline{T}_1$ = 1.5K (Zone 1), 95% O_2 purity

	Unit-Subunit		In		Out	Q
Cooling Units	HX1-SHX363	SF0	300 K	L363	248.5312 K	-2.7661
	HX1-SHX364	V363	248.5312 K	L364	197.0624 K	-2.7821
	HX1-SHX365	V364	197.0624 K	L365	145.5935 K	-2.8232
	HX1-SHX366	V365	145.5935 K	SFL1	94.1247 K	-2.9412
	HX2-SHX367	SFV1	94.1247 K	L367	93.8845 K	-0.66173
	HX2-SHX368	V367	93.8845 K	L368	93.6443 K	-0.69288
	HX2-SHX369	V368	93.6443 K	L369	93.4041 K	-0.73426
	HX2-SHX370	V369	93.4041 K	SFL2	93.1638 K	-0.78841
	HX3-SHX371	SF10	320 K	L371	273.3916 K	-0.24526
	HX3-SHX372	V371	273.3916 K	L372	226.7832 K	-0.25484
	HX3-SHX373	V372	226.7832 K	L373	180.1748 K	-0.27861
	HX3-SHX374	V373	180.1748 K	SFL11	133.5664 K	-0.56213
	HX4-SHX375	SFV11	133.5664 K	L375	120.5439 K	-0.34441
	HX4-SHX376	V375	120.5439 K	L376	107.5214 K	-0.15852
	HX4-SHX377	V376	107.5214 K	L377	94.4989 K	-0.13247
	HX4-SHX378	V377	94.4989 K	SFL12	81.4764 K	-0.12086
	HX13-SHX395	SFV2	93.1638 K	L395	93.1168 K	-0.16192
	HX13-SHX396	V395	93.1168 K	L396	93.0698 K	-0.16475
	HX13-SHX397	V396	93.0698 K	L397	93.0228 K	-0.16772
	HX13-SHX398	V397	93.0228 K	SFL3	92.9758 K	-0.17086
	HX14-SHX399	SFV12	81.4764 K	L399	80.8723 K	-0.0054297
	HX14-SHX400	V399	80.8723 K	L400	80.2682 K	-0.0054174
	HX14-SHX401	V400	80.2682 K	L401	79.6642 K	-0.0054055
	HX14-SHX402	V401	79.6642 K	SFL13	79.0601 K	-0.0053939
Heating Units	R1-SHX351	SF1L3	92.899 K	L351	92.9801 K	0.28092
	R1-SHX352	V351	92.9801 K	L352	93.0613 K	0.27
	R1-SHX353	V352	93.0613 K	L353	93.1425 K	0.25995
	R1-SHX354	V353	93.1425 K	S3	93.2236 K	0.2507
	HX5-SHX379	SNV0	77.5299 K	L379	81.3727 K	0.18799
	HX5-SHX380	V379	81.3727 K	L380	85.2155 K	0.18709
	HX5-SHX381	V380	85.2155 K	L381	89.0583 K	0.18629
	HX5-SHX382	V381	89.0583 K	SNL1	92.9011 K	0.18559
	HX6-SHX383	SNV1	92.9011 K	L383	144.3024 K	2.4382
	HX6-SHX384	V383	144.3024 K	L384	195.7037 K	2.3908
	HX6-SHX385	V384	195.7037 K	L385	247.1051 K	2.3657
	HX6-SHX386	V385	247.1051 K	SNL2	298.5064 K	2.3524
	HX9-SHX387	SOV0	89.174 K	L387	89.4272 K	0.62582
	HX9-SHX388	V387	89.4272 K	L388	89.6805 K	1.8956
	HX9-SHX389	V388	89.6805 K	L389	89.9338 K	0.39469
	HX9-SHX390	V389	89.9338 K	SOL1	90.187 K	0.0031683
	HX10-SHX391	SOV1	90.187 K	L391	144.3488 K	0.67172
	HX10-SHX392	V391	144.3488 K	L392	198.5107 K	0.6703
	HX10-SHX393	V392	198.5107 K	L393	252.6725 K	0.67487
	HX10-SHX394	V393	252.6725 K	SOL2	306.8343 K	0.68201

Table 4.3: Linked Condenser-Reboiler Streams for Optimal ASU with $\Delta\underline{T}_2$ = 0.4K (Zone 2), 95% O_2 purity

	Unit-Subunit		In		Out	Q
Cooling Units	C1-SHX359	S35	89.951 K	L359	89.8992 K	-0.85833
	C1-SHX360	V359	89.8992 K	L360	89.8473 K	-1.2315
	C1-SHX361	V360	89.8473 K	L361	89.7955 K	-1.9257
	C1-SHX362	V361	89.7955 K	S11	89.7436 K	-3.4543
Heating Units	R2-SHX355	SF1L5	88.3798 K	L355	88.6784 K	0.92562
	R2-SHX356	V355	88.6784 K	L356	88.977 K	1.2699
	R2-SHX357	V356	88.977 K	L357	89.2756 K	1.9207
	R2-SHX358	V357	89.2756 K	S15	89.5742 K	3.3536

4.5.5 Comparison with Literature

These results are compared with two optimized designs by Air Liquide described in Matuszewski (2010). The first design is a low capital case with a specific energy usage of 225 kWh/ton (248 kWh/tonne) of O_2 product. The second design is optimized with a low energy usage of 167 kWh/ton (184 kWh/-tonne). Although their report includes approximate capital costs, it does not indicate $\Delta\underline{T}$ used to design the heat exchangers. To compare with the NETL report the ASU models in this paper are reoptimized at various $\Delta\underline{T}$ values. Next a polytropic compressor efficiency of 86% is assumed for the designs in

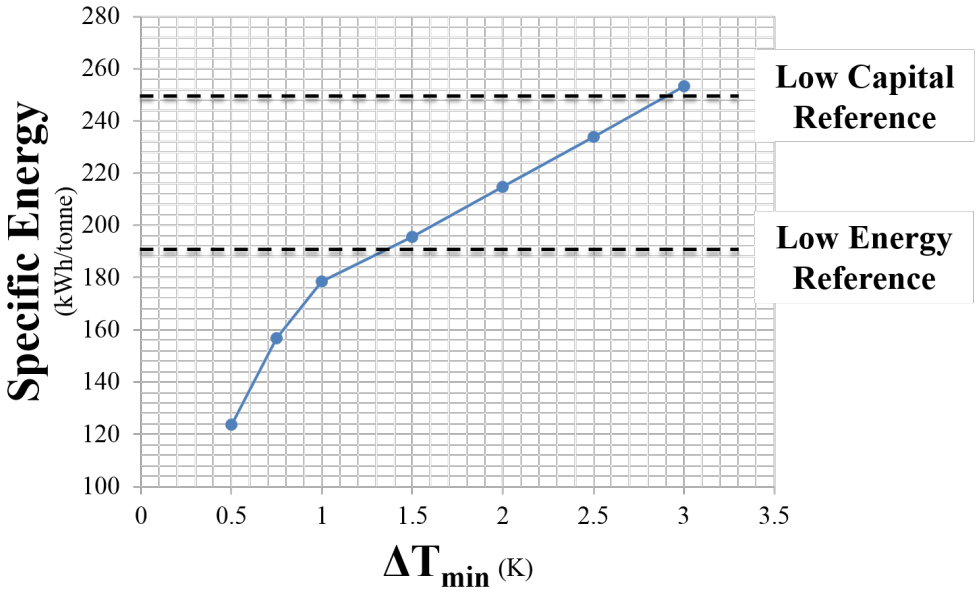

Figure 4.9: Optimal ASU designs with various $\Delta\underline{T}$ specification, 95% O_2 purity product and 86% polytropic efficient compressors

Matuszewski (2010). Although this efficiency is not explicitly stated in the report, it is consistent with other NETL studies (Black, 2014). The specific energies for the two designs are shown in Figure 4.9. The energy performance for the results in this thesis corresponds with the reported low energy and low capital designs with $\Delta\underline{T}$ of 1.3 K and 2.8 K, respectively.

4.5.6 Oxygen Purity Sensitivity

In future work O_2 purity will be considered as an optimization variable instead of a fixed value. This will allow separation efficiency of the ASU and CO_2 processing unit (CPU) to be balanced in the full power plant optimization problem. The O_2 purity specification is varied and the ASU flowsheet is reoptimized using the multi-start procedure discussed in Chapter 6, to produce the Pareto optimal frontier shown in Figure 4.10. This demonstrates the flexibility of the ASU model for future full power plant optimization studies.

A benefit to the equation oriented approach is the availability of sensitivity information at the optimal solution. The KKT multipliers provide a linearized sensitivity of the objective function to perturbations for each constraint and bound. This type of sensitivity is valuable for identifying influential assumptions and parameters that guide more detailed analysis (i.e. generation of a Pareto frontier). As a consistency check the KKT multiplier for the O_2 purity constraint (204 kWh/tonne O_2/mole fraction) is compared with the slope of the linear regression fit through the Pareto curve (228 kWh/tonne/mole frac) and found to be consistent.

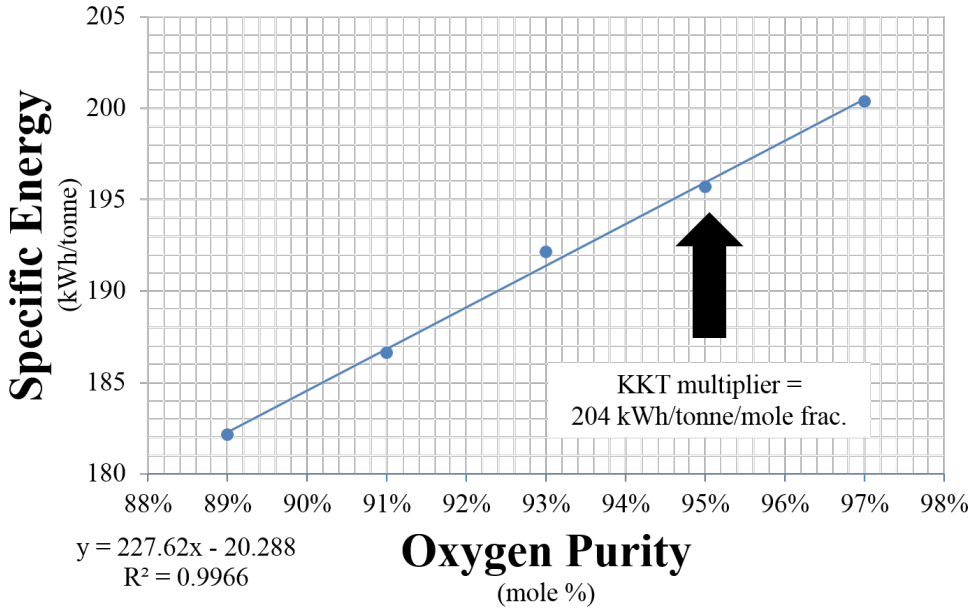

Figure 4.10: Optimal ASU designs at various O_2 purities with $\Delta\underline{T}_{MHEX} = 1.5$K and 86% polytropic efficient compressors

4.5.7 Verification with Aspen Plus

In order to validate the thermodynamic mode, optimization results are compared against Aspen Plus simulations for the low pressure reboiler and top tray in the low pressure column for an ASU design. Both the GAMS optimization results and Aspen verification use the Peng-Robinson equation of state. For both units, the outlet pressure and inlet stream properties (mole fractions, molar flowrate, vapor fraction and pressure) are specified in Aspen Plus to match the optimization results. For the reboiler, the outlet vapor fraction is specified and the heat duty is calculated. For the top tray, adiabatic operation is specified and the vapor fraction is calculated. Outlet stream compositions and temperatures are compared in Table 4.4 and found to match between GAMS and Aspen Plus. Compositions of the N_2 and O_2 products are shown in bold font. The largest discrepancy is seen with the prediction of bubble and dew point temperature. This is most likely due to differences in the correlations used for ideal gas properties required by the departure functions. The heat duties reported in Table 4.4 assume a basis of 2 mol/time of air into the ASU (consistent with Table 4.1 in the supplemental material). Overall, this comparison confirms the cubic EoS models are correctly implemented in GAMS and leads to confidence in the optimization results.

4.5.8 Numerical Performance

228 starting points were considered for the base case ASU ($\Delta\underline{T}_1 = 1.5$K, 95% O_2 purity) in order to quantify the performance of the multi-start initialization

Table 4.4: Comparison of Flash Calculation Outlet Streams

	LPC Top Tray			LPC Reboiler		
	GAMS	Aspen		GAMS	Aspen	
SFlL6	0.9663	0.9713	x_{N_2}	0.0240	0.0241	S15
	0.0199	0.0184	x_{O_2}	**0.9500**	**0.9496**	
	0.0220	0.0103	x_{Ar}	0.0136	0.0263	
common	77.53	77.85	T (in K)	89.57	89.54	common
	1.010	1.010	P (in bar)	1.0532	1.0532	
	0.7030	0.6954	vapor fraction	0.7203	0.7203	
	0	0	heat duty (kJ/time)	7.848	7.468	
SFlV6	**0.9890**	**0.9908**	y_{N_2}	0.0874	0.0873	S18
	0.0054	0.0051	y_{O_2}	0.8765	0.8767	
	0.0056	0.0041	y_{Ar}	0.0361	0.0360	

procedure outlined in Chapter 6. 72% of these points produced feasible designs with both negligible thermodynamic complementarity violations and external utility loads (Q^s, Q^w). For these designs, the sequence of NLPs described in Chapter 6 took 15 CPU-minutes to complete on average, using 2.4 GHz Intel Xeon processors (one thread per starting point) running Ubuntu Linux[2]. The CONOPT solver (version 3.15I, available in GAMS version 24.0.2) was used to solve the NLPs. Refinements of the initialization procedures could result in further speedups. The best 50 locally optimal solutions' objective function values are within 5% of the best solution's objective function value.

Although it is possible to find locally optimal solutions with partial bypass fractions using the new MESH model, they are rare. The reason is that partial bypass requires mixing, which is thermodynamically inefficient. Thus solutions with partial bypass (mixing) should require more separation energy. In the ASU case study, we found the best 20 solutions (out of 288 initial points considered) all had integer solutions for the number of trays. Furthermore in the best 150 solutions ($150/288 = 52.1\%$), only 11 ($11/150 = 7.3\%$) have partially bypassed trays.

Note that the problem size varies with steps of the initialization strategy. Each NLP in the initialization procedure may have a different size depending on the initial point, the equipment set pruned and the number of MESH trays considered. For the final NLP of the solution reported in Figure 4.7, there are 15,893 equations (14,615 equality constraints, 282 active inequality constraints and 996 inactive inequality constraints) and 15,534 variables. 574 variable bounds are strongly active at the solution resulting in 261 degrees of freedom with the active set selected by CONOPT.

[2]In order to obtain consistent timings, the authors found hyperthreading should be disabled for this processor (Intel Xeon), as the optimization calls are CPU intensive.

4.5.9 ASU-CPU Heat Integration Opportunities

The ASU and CPU are the major contributors to the efficiency penalty of oxy-combustion power plants. Through optimization, this penalty can be reduced by balancing the power consumption trade-offs between these two systems. For example, increasing the O_2 purity increases the energy consumption for the ASU, but also reduces the CPU energy requirements, as less N_2 needs to be removed post-combustion. Li et al. (2013) studied the energy consumption of a traditional ASU with a two stage flash CPU, by performing sensitivity analysis in Aspen Plus. They found 80 mol% O_2 production in the ASU and a large CPU is beneficial over traditional designs with 95 mol% purity O_2 from the ASU. Their study, however, did not consider detailed multivariable optimization or deeper integration between the ASU and CPU.

Using the framework presented in this thesis, we intend to optimize an entire oxy-combustion power plant, and determine the optimal balance between the ASU and CPU using rigorous models. Further, we also seek to evaluate synergies between the ASU and CPU, including heat integration of the sub-ambient multistream heat exchangers, which are shown in Figure 4.11. As the first step of this analysis, the heat integration opportunities between the ASU and CPU are quantified by introducing an extra heat exchanger in the CPU flowsheet (Chapter 3), which provides cooling from 89.2 K to 250 K using the waste N_2 from the optimized ASU to the multistream heat exchanger for the CPU, (Zone 2 in Figure 3.5). The Pareto curve in Figure 4.12 was generated by varying the amount cooling provided by the waste N_2 stream and reoptimizing the CPU (using the multi-start procedure). Initially, one unit of additional cooling energy reduces the separation work requirement by approximately 0.6 units of energy. As expected, the system experiences diminishing returns and as the amount of auxiliary cooling increase, the effectiveness of its utilization decreases. This happens because the phases in Figure 3.5 are specified *a priori*. The liquid streams exiting the flash vessels must be vaporized (which is necessary to balance the multistream heat exchanger) and then compressed to the target product pressure (150 bar). In this configuration, additional cooling cannot be used to reduce the product CO_2 compression requirement.

However, with a modified flowsheet, such as Figure 4.12, it may be possible to drive the multistream heat exchanger in the CPU with the waste N_2 stream from the ASU. The would eliminate the need to vaporize the streams exiting the flash vessels, and allow the CO_2 product stream to remain liquid and instead be pumped to 150 bar (with significant energy savings). Most importantly, this small integration demonstration highlights a key advantage of the optimization framework: all of the streams in the sub-ambient process can be easily exposed to possible heat integration.

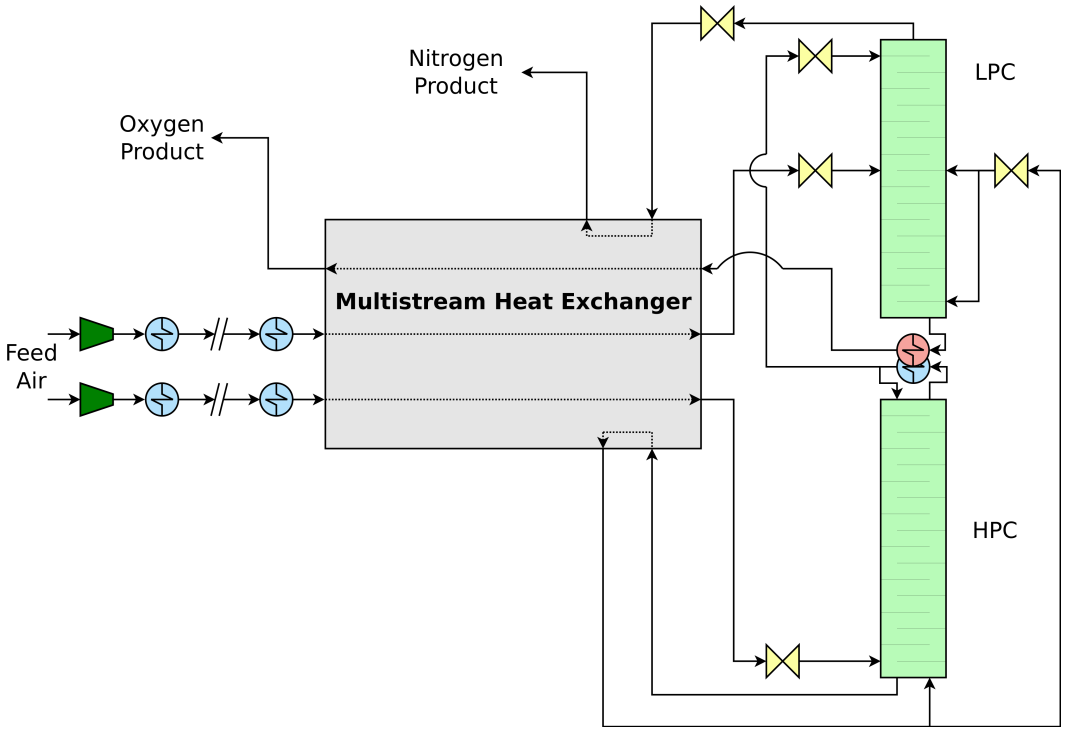

(a) Air Separation Unit

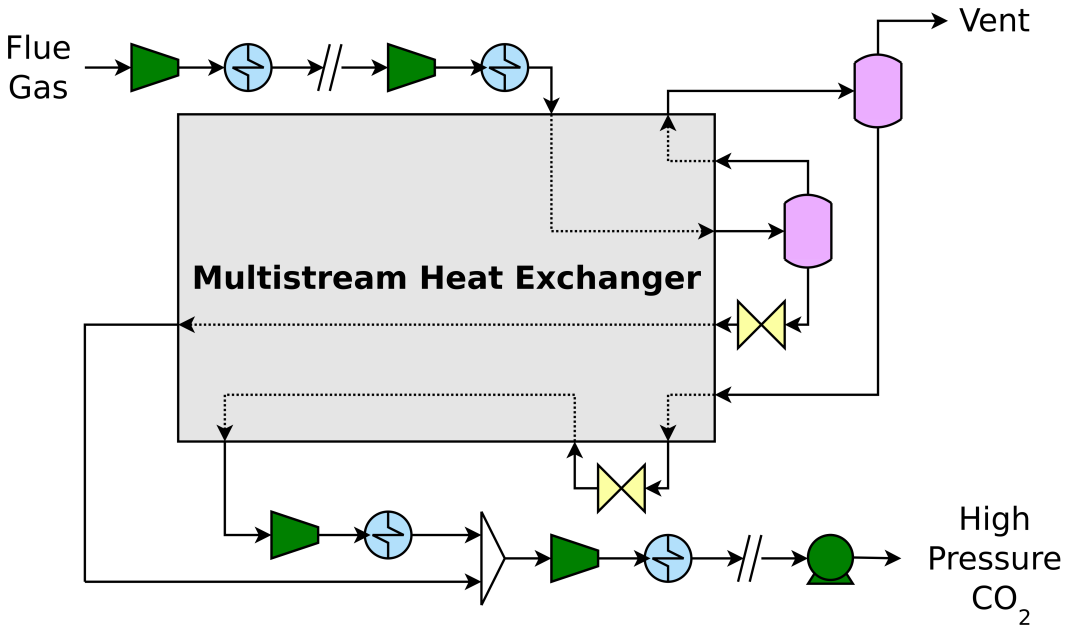

(b) CO_2 Processing Unit and Compression Train

Figure 4.11: With heat integration, the ASU and CPU multistream heat exchangers are combined (share a common HEN)

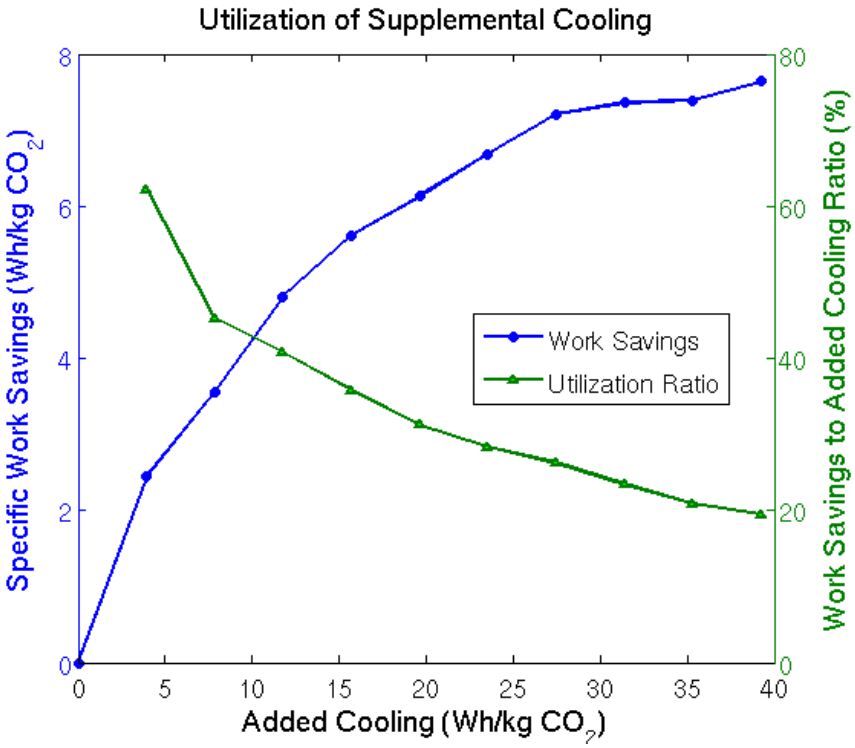

Figure 4.12: Preliminary evaluation of heat integration opportunities between the ASU and CPU

4.6 Conclusions and Future Directions

The equation-based framework is extended with two distillation models in this chapter. The first model is based on an extension of the Edmister approximation from Kamath, Grossmann, and Biegler (2010), which allows for the number of trays in a column section to be treated as a continuous variable. In contrast, rigorous vapor-liquid equilibrium calculations are considered for each theoretical tray in the second model. A novel tray bypass formulation is introduced, which allows for the number of trays to be optimized without integer variables using the rigorous MESH equations. Consistent with the model refinement theme used throughout the framework, results form the first distillation model are used to initialize the second.

The efficacy of these models and initialization strategies are demonstrated in an air separation unit case study, which features two heat integration columns and an accompanying multistream heat exchanger. A superstructure is used to simultaneous optimize the column configuration and operating conditions. Similar to the CPU case study, the heat integration models from Chapter 3 are used to ensure feasibility of the MHEXs. Overall, the ASU systems designed by the optimization procedure are very tightly heat integrated and energy competitive with other industrial systems. Pareto curves are generated with respect to O_2 purity and the $\Delta\underline{T}$ assumption to demonstrate the

flexibility of the models. The latter are used to estimate the unpublished $\Delta\underline{T}$ assumptions for some industrial designs. Finally, the thermodynamic models are verified again flash calculations in Aspen Plus.

Regarding the novel MESH with bypass model, a conjecture is presented that mixing is inefficient and solutions with $\varepsilon_d = 1$ and $\varepsilon_d = 0$ are preferred by the optimizer. Furthermore, the conjecture holds for the ASU case study, but a more detailed mathematical analysis should be considered as future work. Furthermore, the new distillation model should be benchmarked against the MINLP model of Viswanathan and Grossmann (1990). The ASU case study should be used to compare the original (2.19) and log-transformed (2.20) versions of the phase equilibrium model with complementarity constraints. Presently, only the original version is used for the ASU case study.

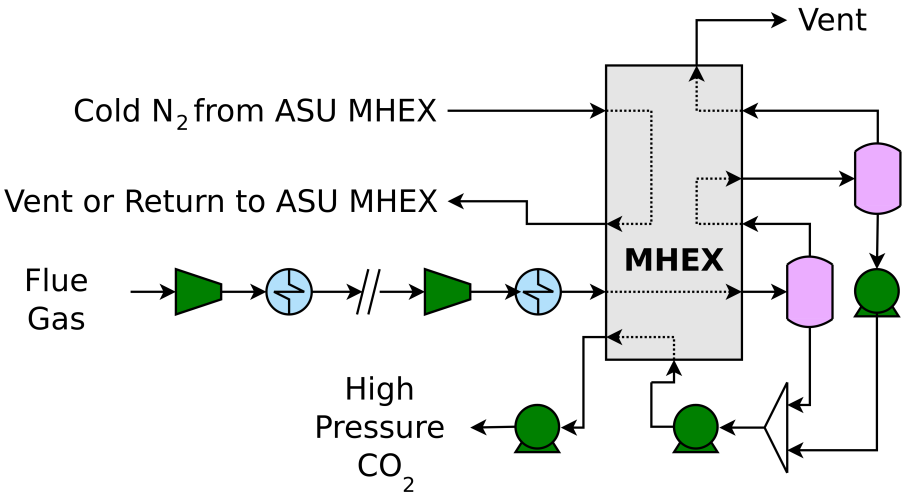

Figure 4.13: Alternate CPU configuration with the ASU providing cooling for the multistream heat exchanger

Finally, heat integration between the ASU and CPU (Chapter 3) with detailed models for both systems should be considered as future work. The CPU system considered in this chapter requires the CO_2 rich liquid effluents of the flash vessels to be vaporized to balance the multistream heat exchangers. With intimate ASU-CPU integration, it may be possible to use an ASU design that produces liquid N_2 product to completely drive the refrigeration cycle in the CPU. This would allow for the CO_2 rich streams to remain liquid and be pumped to 150 bar instead of compressed, which requires significantly less work. This concept is illustrated in Figure 4.13. Given the heat integration capabilities of these models, the framework developed in this thesis is uniquely positioned to evaluate this proposed design.

Chapter 5

Steam Cycle Models and Optimization

Key Contributions and Results:

- Present a collection of models and superstructures suitable for optimization of power plant steam cycles
- Motivate the need for accurate thermodynamic models using a small demonstration system
- Apply a trust-region optimization strategy to integrate accurate models without exact derivative information (i.e., steam thermodynamics table lookups, boiler simulations) into the equation-based framework
- Demonstrate this methodology by optimizing an entire air-fired coal combustion steam cycle, including integration of waste heat into the boiler feedwater preheating system

5.1 Overview

The steam cycle portion of a power or chemical plant converts heat to useful shaft work. In a cogeneration system, both heat (in the form of steam) and power is produced. These combined heat and power (CHP) systems are common in large chemical processing facilities, such as oil refineries, where there are significant electricity and steam demands. A basic steam cycle consists of four components: heat source (e.g., furnace), steam turbine, condenser and pump. Inside the walls of the furnace and other heat transfer surfaces, water is vaporized and/or superheated, creating high pressure steam. Some of the energy carried in the steam is converted to work in the turbine(s) through expansion. Low energy steam exiting the turbine is condensed at pressures as low as 1 inch Hg (3400 Pa) absolute. Finally, the water is compressed to high pressure and fed into the furnace, completing the steam cycle.

Traditional steam cycle equipment models conflict with the central tenet of this thesis, which is that equation-based models with exact first and second

derivatives enable more sophisticated optimization algorithms and problems to be considered. More specifically, steam cycle process models typically rely on calls to external packages for thermodynamic property calculations and computational fluid dynamics to resolve complex phenomena in boilers and combusters. Exact derivatives are difficult to obtain in both of these cases.

Two strategies to incorporate steam cycle models into the equation-based optimization framework are presented in this chapter. First, the simplest approach is considered; nonlinear regression models are fit using data generated from an external steam table library, which are then used in the optimization framework. These models are static (i.e., only fit once), and as consequence, the optimizer finds operating conditions that exploit inaccuracies in the fitted thermodynamic correlations. This results in too-good-to-be-true objective function values and solutions that violate thermodynamics when checked with the original steam table (e.g., destroy entropy in a turbine). In contrast, for the second approach, simple regression models for the steam thermodynamic properties are adjusted as part of the optimization procedure using a trust region strategy. A filter is employed to trade-off convergence of the equality constraints (e.g., mass balances, energy balances, etc.) with improvements in the objective function. This approach is also used to embed a CFD-based boiler models into power system optimization problems.

5.1.1 Background

A Carnot cycle is the simplest type of heat engine. It contains four pieces of equipment (a heat source, a heat sink, a pump and a turbine), as shown in Figure 5.1. As heat moves from the hot source to the cold sink via the working fluid in the closed system, some of the energy is transformed into useful shaft work. In the Carnot cycle model, the working fluid is ideal and may be isentropically heated and expanded, as shown in Figure 5.2(a). The maximum efficiency of a Carnot cycle is

$$\eta_{Carnot} = 1 - \frac{T_{sink}}{T_{source}} \tag{5.1}$$

where T_{sink} and T_{source} are the absolute temperatures of the cold sink and hot source, respectively. This efficiency is an upper bound for all heat engines.

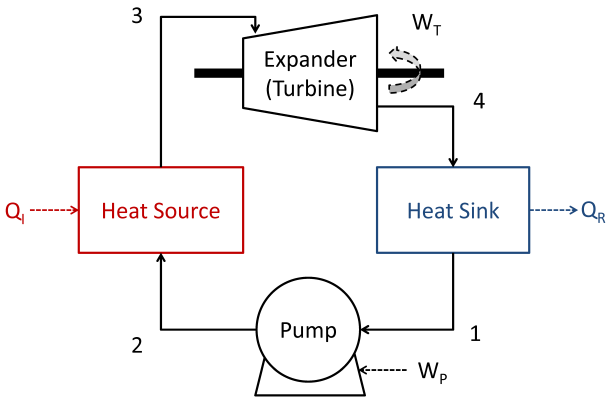

Figure 5.1: A simple Carnot and Rankine cycle

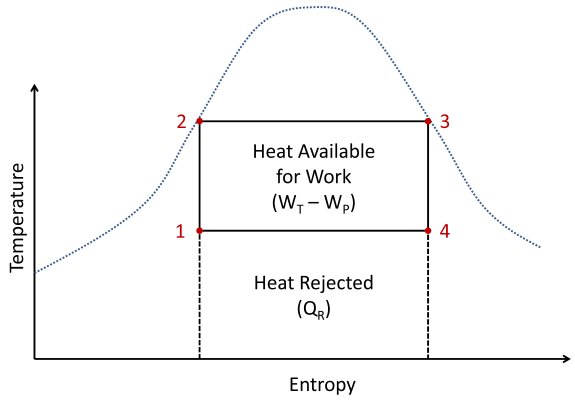

(a) Carnot Cycle

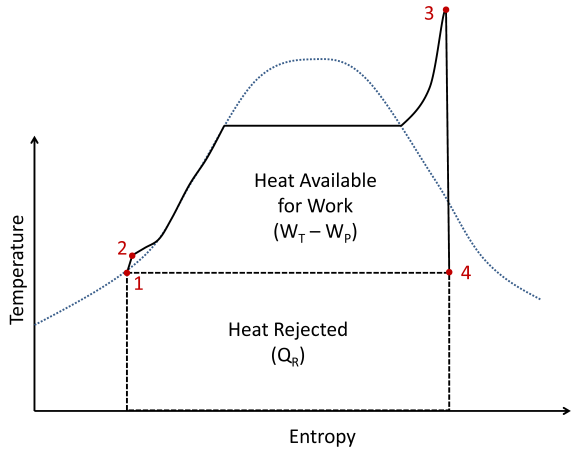

(b) Rankine Cycle

Figure 5.2: T-S Diagrams (without reheat)

More generally, the efficiency of a heat engine is

$$\eta = \frac{W_T - W_P}{Q_I} \tag{5.2}$$

where Q_I is the input heat (from the heat source), W_T is the useful work produced by the expander/turbine and W_p is the work required by the pump. A geometric interpretation of this formula is shown in Figure 5.2(a). The input and rejected heats are calculated from

$$Q_I = \int_{p_2}^{p_3} T\mathrm{d}S \tag{5.3a}$$

$$Q_R = -\int_{p_4}^{p_1} T\mathrm{d}S \tag{5.3b}$$

where points p_1 to p_4, which are shown in Figure 5.2(a), correspond with the numbered steams in Figure 5.1. The net work, $W_T - W_P$, is calculated using an energy balance:

$$W_T - W_P = Q_I - Q_R \tag{5.4}$$

Thus the efficiency of the simple Carnot cycle is the ratio of the area of the rectangle labeled *Heat Available for Work* to the sum of the area of itself and the rectangle labeled *Heat Rejected* in Figure 5.2(a).

$$\eta = \frac{\text{Heat Available for Work}}{\text{Heat Available for Work} + \text{Heat Rejected}} \tag{5.5}$$

In contrast, the Rankine cycle considers non-isentropic vaporization and superheating of the working fluid, as shown in Figure 5.2(b). Water exhibits these properties, thus the Rankine cycle is preferred to model actual steam cycles. An approximate efficiency for a Rankine cycle may be calculated using a graphical approach with the TS diagram, i.e., (5.5), similar to a Carnot cycle. If pumping (p_1 to p_2) and expansion (p_3 to p_4) are far from isentropic, the areas labeled in Figure 5.2(b) are inaccurate. Instead, new shapes must be drawn to represent (5.3) in order to accurately calculate cycle efficiency.

In large steam power plant or co-generation facilities, four design features are typically used to increase Rankine cycle efficiency:

1. Supercritical operation
2. Utilization of waste heat from the flue gas
3. Steam reheat
4. Steam extraction for feedwater preheating

When saturated steam is expanded in a steam turbine, there is some condensation, which imposes both operational restrictions and decreases the cycle efficiency. In other words, a significant amount of energy input to the boiler/-furnace goes to vaporization, which cannot be recovered in the steam turbines. In contrast, virtually all of the energy added to high pressure ($>$ 3200 psi) and high temperature ($>$ 705 °F) steam may be recovered in a turbine (Babcock & Wilcox Co., 2005a). The efficiencies and steam cycle conditions for an example subcritical and supercritical power plant are compared in Table 5.1. In a supercritical steam cycle, water is pumped to high pressure and heated in tubes inside the walls of the boiler. Additional heat is then transferred to the steam via hot flue gas in the primary superheater, which is located next to the boiler. The steam is then sent the secondary superheater, located at the top of the boiler, where thermal radiation is the dominant heat transfer mechanism. See Figure 5.15 for a graphical depiction of the gas and steam sides of a double reheat cycle.

Table 5.1: Comparison net efficiency and operating conditions for 550 MWe subcritcal and supercritical power plants. See Cases 9 and 11 in Black (2010) for additional details.

	Subcritical	**Supercritical**
Steam Cycle Conditions		
Pressure (Throttle Steam)	2400 psig	3500 psig
Temperature (Throttle Steam)	1050 °F	1100 °F
Temperature (Reheat)	1050 °F	1100 °F
Condenser Conditions		
Pressure	2 in Hg	2 in Hg
Cooling Water Temperature	60 °F	60 °F
Net Plant Efficiency (HHV)	36.8%	39.3%

The flue gas exiting a coal furnace is typically 1700 to 1900 °F and contains a significant amount of heat, which is transferred to water and steam in various parts of the Rankine cycle. After exiting the boiler (secondary superheater), the hot flue gas is sent to either the primary superheater or reheater(s). Next, the slightly cooled flue gas is sent to the economizer, which heats water after the pump and before entering the boiler. Finally, some of the remaining energy from the flue gas is used to preheat air fed into the boiler. This tight heat integration boosts efficiency by utilizing waste energy in the flue gas.

In a reheat Rankine cycle, steam is directed back to the heat source (e.g., furnace) typically once or twice to be reheated before it is completely expanded. A simple single reheat Rankine cycle is shown in Figure 5.3. Comparison TS diagrams for Rankine cycles with and without reheat (Figures 5.3(b) and 5.2(b), respectively) reveals a higher overall cycle efficiency in the

former. This is because most of the energy transferred to steam at high pressures and temperatures is recoverable in the steam turbines, unlike the latent heat of vaporization. From an exergy perspective, reheat is also beneficial, as the hot exiting flue gas is used to heat the partially expanded steam (p_{3b} to p_{3c} in Figure 5.3(a)) instead of water in the economizer. This reduces the temperature difference (i.e., driving force) between the flue gas and steam and involves smaller irreversibilities. Furthermore, reheat also reduces the moisture content in the low pressure turbine section and decreases moisture losses. Selection of the number of reheats (zero to two are common) in a steam cycle requires balancing the additional capital costs and pressure drops associated with reheaters against cycle efficiency improvements.

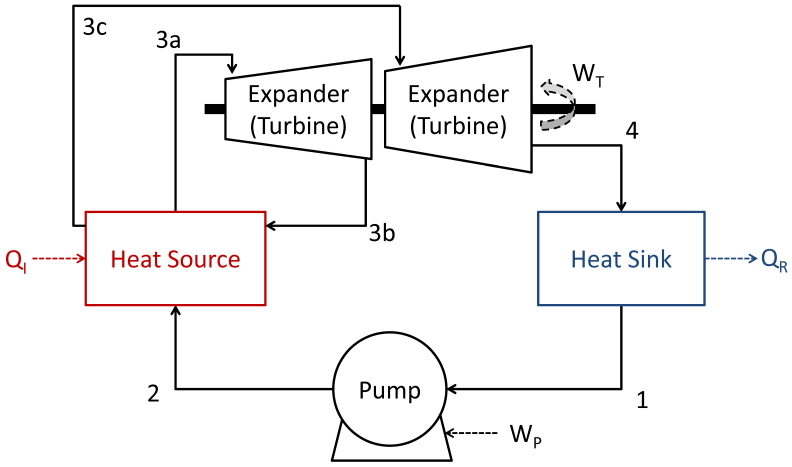

(a) Configuration

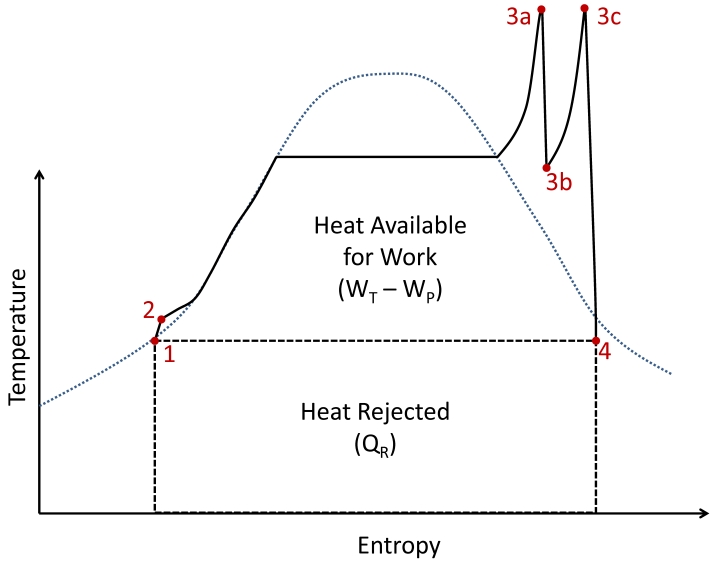

(b) TS Diagram

Figure 5.3: Single Reheat Rankine Cycle

Turbines are used to generate both shaft work and steam in CHP systems at up to three pressure levels: high, medium and low. Similarly, steam turbines are decomposed into three main sections, high, intermediate and low pressure, although multiple sections are commonly contained in the same housing. Extraction for steam utility demand occurs between these sections. Depending on the requirements for low pressure steam, a turbine is either classified as *back pressure* or *condensing*. Back pressure turbines output high quality steam at a specified pressure, whereas the low pressure section of a condensing turbine is immediately followed by a condenser, which allows the turbine outlet to be under vacuum. In most power plants, condensing turbines are preferred.

In a regenerative Rankine cycle, small quantities of steam are extracted from each section of the turbine for boiler feedwater heating. This improves overall cycle efficiency by raising the temperature of water fed to the boiler, which reduces the boiler heat (and fuel) input requirements. Furthermore, feedwater preheating also reduces the rejected heat in the condenser. Decisions regarding the number of feedwater heaters requires balancing turbine performance, capital costs and pressure drops in the feedwater heaters.

5.1.2 Literature Review

In the following literature review, previous work is classified into two broad categories: systematic methods for combined heat and power system optimization, and applications of these methods to large-scale electricity generation systems, including oxycombustion plants. Additional model specific literature reviews (e.g., turbine performance, thermodynamics) are included in individual sections throughout the chapter as appropriate.

5.1.2.1 Combined Heat and Power System Optimization

Given the potential for increased efficiency and energy savings in chemical manufacturing facilities, it is not surprising numerous researchers have sought systematic methods to improve combined heat and power generation systems over the past thirty years. Early work focused on balancing tradeoffs between shaft work and steam (heat) production using simplified models. Townsend and Linnhoff (1983a,b) applied insights from graphical pinch-based analysis to address the placement of heat engines and pumps in process networks. That same year, Papoulias and Grossmann (1983a,c,b) published a mixed integer linear programming (MILP) approach to design combined heat and power systems. Their method uses a superstructure to consider a larger number of possible utility system configurations. In order to use simple linear models, the authors assume power and heat demands are fixed, along with the steam utility pressure levels. Petroulas and Reklaitis (1984) consider both header pressure selection and driver allocation using a two staged approach. The outer problem optimizes header pressures using dynamic programming methods, while the inner problem considers driver allocation using linear programming techniques. Colmenares and Seider (1989) also consider pressure level optimization by modeling the utility systems as an network of Rankine

cycles with mass integration. This results in a nonlinear program (NLP), which they show replicates the performance of complex utility systems configurations found in existing processes. Maréchal and Kalitventzeff (1997) combine targeting techniques with mixed integer linear programming to determine optimal pressure levels in combined heat and power systems. They use Rankine cycle approximations to estimate shaft work production. Alternatively, Bruno, Fernandez, and Grossmann (1998) extended the previous work of Papoulias and Grossmann (1983a,c,b) to consider variable pressure levels, resulting in a mixed integer nonlinear program (MINLP). Their approach considers pressure level optimization, turbine configuration selection (e.g., backpressure versus condensing) and turbine-load pairings simultaneously. Instead of assuming Rankine cycle efficiencies, individual steam turbine sections are considered with approximate efficiency models. Li et al. (2014) augmented the MINLP model proposed by Bruno, Fernandez, and Grossmann (1998) with more complex (and accurate) turbine efficiency models. In parallel to development of optimization-based approaches for utility system design, Linnhoff and others also continued work on graphical methods (Linnhoff and Ahmad, 1989b; Linnhoff, 1989; Dhole and Linnhoff, 1993; Morton and Linnhoff, 1984; Hui and Ahmad, 1994; Marechal and Kalitventzeff, 1996; Klemes et al., 1997; Bandyopadhyay, Varghese, and Bansal, 2010; Botros and Brisson, 2011).

As time progressed, researchers began exploring optimal design of flexible utility systems and optimization of operations strategies. Iyer and Grossmann (1997) applied popular scheduling techniques for chemical processes to utility system operation. Unlike previous work (Nath and Holliday, 1985; Ito et al., 1987; Kalitventzeff, 1991), their approach considers multi-period operation with turnover costs. They formulate a mixed integer linear program (MILP) with constant turbine efficiencies and proposed an efficient decomposition-based solution algorithm. The authors also extended this work to consider utility system design (Iyer and Grossmann, 1998). Oliveira Francisco and Matos (2004) extended the framework from Iyer and Grossmann (1997) to include CO_2 and SO_2 emissions. They used an ε-constrained method to construct Pareto curves for the multi-objective optimization problem, which balances plant economics with emissions. Shang and Kokossis (2005) applied the Turbine Hardware Model (THM) and Boiler Hardware model (BHM) from previous work (Mavromatis and Kokossis, 1998a,b; Shang, 2000), along with the Condensing Turbine Hardware Model (CTHM) and Gas Turbine Hardware model to explore the optimal design of flexibility utility systems. They proposed a three step approach. First, total site analysis is used to identify design targets and evaluate the potential for integration. These results, in combination with the thermodynamic efficiency curve (TEC), are used to construct a set of minimal primal design components and propose a superstructure. Finally, they formulate and solve a multi-period mixed integer linear program (MILP). Unlike the work of Iyer and Grossmann (1997), this approach does not consider turnover costs but does consider variations in turbine efficiency with partial load operation. Aguilar et al. (2007a,b) extended the Turbine Hardware

model with a more straightforward procedure to calculate multi-stage turbine efficiency, and proposed a framework to consider grassroots (greenfield) and retrofit design problems, along with operational optimization problems. This work was then extended by the authors to address reliability and availability by formulating a multi-scenario MILP with several operational situations such as specific equipment unavailable due to maintenance, etc. (Aguilar et al., 2008).

These studies focus on economically balancing steam and electric generation. However, in most fossil fuel power plants, little extracted steam is required to run chemical reactors or separations (with the exception of some CO_2 capture systems). Instead, emphasis is placed on converting as much thermal energy into electric energy. Thus, optimal design of power generation systems is substantially different than CHP systems in two ways:

1. There are fewer practical configuration options, as production of large quantities of extracted steam at various pressure levels is not required.

2. Steam turbines used in power plants may be significantly larger than CHP systems.

However, many of the models and systematic design strategies presented in previous CHP studies are applicable to fossil fuel power plants (with modification).

5.1.2.2 Oxycombustion Steam Cycle Integration

As summarized in Section 1.3, most previous oxycombustion studies focused on simulation and technoeconomic analysis, with Aspen Plus being the preferred modeling environment. With the exception of Zebian, Gazzino, and Mitsos (2012) and Zebian et al. (2013), optimization is not consider to investigate the complex trade-offs between subsystems. Instead single variable sensitivity analysis is preferred, and subsystems in the oxycombustion process are considered in isolation (e.g. boiler). This thesis aims to reverse the trend, and optimize the oxycombustion process with rigorous models.

Another important limitation of most oxycombustion studies is the reliance on simplified reactor models in process simulations, such as a *Gibbs Reactor* block in Aspen Plus. In actuality, the boiler in an oxycombustion process is very complex. Over 90% of the heat transfer is radiative, which requires attention when determining the amount of heat absorbed by various parts of the boiler (e.g., walls versus superheaters). Furthermore, the combustion properties of an oxycombustion boiler are drastically different than a similar boiler (e.g., same geometry, etc.) operating in an air-fired mode. This is because the emissivity and fluid properties of CO_2 and N_2 are drastically different, causing different thermal and flow profiles in oxy-fired versus air-fired boilers. Consequently, most of the correlations typically used to design air-fired boilers (Babcock & Wilcox Co., 2005b) don't apply to oxy-fired systems. Understanding combustion properties in oxycombustion boilers has been the focus

on many pilot-scale and computational experiments. See Chen, Yong, and Ghoniem (2012) for an overview of combustion research and open questions related to coal oxy-firing. With this motivation, Edge et al. (2012, 2013) coupled simplified boiler models based on data from CFD studies with flowsheet simulators.

Overall, there is limited application of combined heat and power system optimization methods to design oxycombustion (and other fossil fuel) power plants. Dowling and Biegler (2013) consider the MINLP utility system model (Bruno, Fernandez, and Grossmann, 1998) in conjunction with a Gibbs free energy minimization boiler model and simplified ASU model to optimize an oxycombustion power system. This work, however, did not consider detailed steam turbine models, steam extraction for feedwater preheating or any other heat integration. Few researchers have gone beyond pinch analysis to explore the interactions between the steam cycle and utilization of low grade waste heat (e.g., from compressor inter-stage coolers). For example, Gundersen and colleagues (Fu, Anantharaman, and Gundersen, 2014; Soundararajan, Anantharaman, and Gundersen, 2014) consider only fixed steam pressure levels and extractions rates during their integration analysis. Similarly, Luo et al. (2012) applied a two stage approach to optimally integrate low-temperature waste process heat with a regenerative Rankine cycle. First, they used graphical pinch analysis to identify candidate pinch points. This information was then incorporated into a nonlinear program to optimize the use of waste heat for feedwater preheating. Detailed turbine models from their previous work (Luo et al., 2011) were considered as part of the optimization problem. However, their study assumed the temperatures and flowrates of the waste heat were fixed. This assumption may lead to suboptimal results with an oxycombustion system, as it does not consider additional degrees of freedom to adjust the balance of plant during heat integration. For example, some researchers have proposed near-adiabatic compression of CO_2 (Fu, Anantharaman, and Gundersen, 2014), which generates medium quality heat that may be integrated into the steam cycle. Rigorous evaluation and optimization of this strategy requires simultaneous optimization of the steam cycle system and balance of plant.

Thorough optimization of the oxycombustion process requires four key steam cycle model components:

1. Detailed steam turbine models that include extraction and adjustable operating conditions (flowrates, temperatures and pressures).

2. A heat integration model to consider interactions between the steam cycle and balance of plant, such as waste heat from compression.

3. Accurate steam thermodynamic calculations (e.g., calls to standardized steam table packages).

4. A detailed boiler model that considers the impact of feedwater and air inlet conditions on combuster efficiency.

5.1.3 Chapter Organization

The remainder of this chapter presents a unified modeling and optimization strategy with the aforementioned components. First, equation-based models for steam cycle equipment are presented along with a simple Rankine cycle demonstration system. These models are independent of the steam thermodynamic model. An extensive review of steam turbine modeling literature is considered in this section. Next, steam thermodynamics are considered with two different approaches. In Strategy A, a nonlinear surface model is proposed to calculate steam thermodynamic properties as a function of temperature and pressure. Ultimately this approach is shown to be inadequate through a small example problem. This motivates discussion of Strategy B, in which models are adaptively adjusted as part of a trust region with filter optimization algorithm. Next, a hybrid 1D/3D zonal boiler model developed by collaborators is summarized. Finally, all of the elements are combined and demonstrated in an air-fired steam cycle optimization case study.

5.2 Equipment Models

The steam cycle portion of the power plant is modeled as a collection of connected equipment, including mixers, turbines, the boiler, heat exhangers (reheaters, economizer, boiler feed water heater) and pumps, as shown in Figure 5.15. This section details algebraic models for all of these units, except the boiler. All of these models are independent of the thermodynamics models, which calculate enthalpy (H), entropy (S) and compressibility (Z) or specific volume (V) as a function of temperature (T), pressure (P) and phase for steam.

5.2.1 Steam Turbine Model

A steam turbine converts heat into useful work. Hot, high pressure steam is expanded through a nozzle, increasing its velocity. The steam's kinetic energy is then transferred to a rotating blade, where it is converted into torque (useful shaft work). The total energy and available energy (enthalpy) for steam are calculated as follows,

$$\text{Total Energy} = C_v T + PV + \frac{1}{2}v^2 \tag{5.6}$$

$$\text{Available Energy} = C_v T + PV \tag{5.7}$$

where T is temperature, C_v is the constant volume heat capacity, P is pressure, V is specific volume and v is velocity. Superheated steam behaves similarly to an ideal gas, i.e.,

$$PV = RT \tag{5.8}$$

where R is the gas constant. For adiabatic expansion, $PV^\gamma = \text{constant}$ and

$$P_2 V_2 = P_1 V_1 \left(\frac{P_2}{P_1}\right)^{\frac{\gamma-1}{\gamma}} \tag{5.9}$$

where P_1 and V_1 are the initial pressure and specific volume, P_2 and V_2 are the final pressure and specific volume, and $\gamma = C_p/C_v$. This equations simplifies as follows:

$$V_2 = V_1 \left(\frac{P_1}{P_2}\right)^{\frac{1}{\gamma}} \tag{5.10}$$

There are two different types of simple turbines: impulse (e.g., windmill) and reaction (e.g., rotating garden sprinkler). In a simple impulse turbine, the working fluid is expanded (typically in a nozzle), which decreases its pressure and temperature and increases its velocity, as shown in (5.10). The high speed steam spins the turbine blade creating useful shaft work. In contrast, the nozzle is incorporated into the rotating blades in a simple reaction type turbine. Compound turbines consist of multiples rows of rotating and stationary blades. The stationary blades redirect flow into the rotating blades. A pair of rotating and stationary blades are known as a stage. In an impulse type compound turbine, all of the pressure drop occurs over the stationary blades, which are shaped like nozzles. In contrast, in a 50% reaction type turbine, pressure drop is evenly distributed across stationary and rotating blades. As a consequence, impulse type turbines require higher steam velocities and greater frictional losses, whereas 50% reaction type turbines have higher pressure drops across rotating blades, and consequently greater leakage losses. Overall, the efficiencies of well designed turbines of both types are approximately equal. Furthermore, the classification of impulse or 50% reaction type is somewhat simplistic. In reality, the percent reaction of a turbine varies from stage to stage, and radially along each blade.

(a) The windmill, an impulse turbine[a]

(b) The sprinkler, a reaction turbine[a]

[a] Original photo by Patrick Bolduan, licensed under CC

[a] Original photo from alegriphotos.com, lic. under CC

Figure 5.4: Simple examples of impulse and reaction type turbines

The performance equations for the stage of a steam turbine are easily derived from mass and energy balances, and the ideal gas law. First, consider an energy balance across the nozzle of an impulse type turbine stage:

$$\frac{1}{2}v_{in}^2 + P_{in}V_{in} + C_vT_{in} = \frac{1}{2}\hat{v}^2 + \hat{P}\hat{V} + C_v\hat{T} \tag{5.11}$$

where $\hat{P}$, $\hat{V}$, $\hat{v}$, and $\hat{T}$ represent the pressure, specific volume, velocity and temperature of steam after the nozzle. $v^{in} \approx 0$ and may be dropped from (5.11). Adiabatic expansion occurs in the nozzle, and substitution of (5.8) and (5.10) into (5.11) yields

$$\frac{1}{2}\hat{v}^2 = P_{in}V_{in} - \hat{P}\hat{V} + C_v(T_{in} - \hat{T}) \tag{5.12a}$$

$$= \left(\frac{C_v}{R} + 1\right)\left(P_{in}V_{in} - \hat{P}\hat{V}\right) \tag{5.12b}$$

$$= \left(\frac{C_p}{C_p - C_v}\right)\left[P_{in}V_{in} - \hat{P}V_{in}\left(\frac{P_{in}}{\hat{P}}\right)^{1/\gamma}\right] \tag{5.12c}$$

$$= \left(\frac{\gamma}{\gamma - 1}\right)V_{in}P_{in}\left[1 - \left(\frac{\hat{P}}{P_{in}}\right)^{\frac{\gamma-1}{\gamma}}\right] \tag{5.12d}$$

$$= \left(\frac{\gamma}{\gamma - 1}\right)T_{in}R\left[1 - \left(\frac{\hat{P}}{P_{in}}\right)^{\frac{\gamma-1}{\gamma}}\right] \tag{5.12e}$$

and the steam velocity after the nozzle is given by

$$\hat{v} = \sqrt{2\left(\frac{\gamma}{\gamma - 1}\right)T_{in}R\left[1 - \left(\frac{\hat{P}}{P_{in}}\right)^{\frac{\gamma-1}{\gamma}}\right]} \tag{5.13}$$

Similarly, consider the energy balance over the rotating blade:

$$\frac{1}{2}\hat{v}^2 + \hat{P}\hat{V} + C_v\hat{T} = \frac{1}{2}v_{out}^2 + P_{out}V_{out} + C_vT_{out} + W_{stage} + Q_{stage} \tag{5.14}$$

where W_{stage} is the work extracted on the stage. In an impulse type turbine, all of the pressure drop occurs across the nozzles (i.e., stationary blades) and thus $\hat{P} = P_{out}$ for the rotating blade. Similar to the nozzle, $v_{out} \approx 0$ and the energy balance simplifies:

$$\frac{1}{2}\hat{v}^2 + C_p(\hat{T} - T_{out}) = W_{stage} + Q_{stage} \tag{5.15}$$

where $\hat{v}^2 = 2W_{stage}$ and $C_p(\hat{T} - T_{out}) = Q_{stage}$. From an entropy perspective, it does not make sense to remove heat from steam in a turbine (besides cooling required due to friction) and $Q_{stage} = 0$. More specifically, the temperature of the steam already decreases in the nozzle of the turbine due to adiabatic expansion. Additional reduction in temperature means less pressure drop can

occur before the steam begins to condense. This is also why reheat is beneficial. The combination of (5.12e) and (5.15) gives

$$W_{stage} = \left(\frac{\gamma}{\gamma - 1}\right) T_{in} R \left[1 - \left(\frac{P_{out}}{P_{in}}\right)^{\frac{\gamma-1}{\gamma}}\right] \tag{5.16}$$

which is the common formula for specific work from a adiabatic ideal gas expansion (e.g., compressor).

Several factors impact the isentropic efficiency of a turbine stage, including boundary layer losses, leakage losses, leaving losses (related to exit velocity of the steam) and moisture losses. More importantly, however, the efficiency of a turbine stage depends of the ratio of the steam and rotating blade velocities, which impacts the amount of energy transferred to the blade. In an ideal stage with a stationary blade angle of 0°, stage efficiency is calculated as follows,

$$\eta_{ideal} = 2\left(\frac{w}{\hat{v}}\right)\left[\left(\sqrt{1 - R_x} - \frac{w}{\hat{v}}\right) + \sqrt{\left(\sqrt{1 - R_x} - \frac{w}{\hat{v}}\right)^2 + R_x}\right] \tag{5.17}$$

where $\hat{v}$ is the velocity after isentropic expansion in the nozzle, w is the rotating blade (linear) velocity and R_x is the fraction of energy released on the rotating blade (i.e., a quantification of reaction). The maximum efficiency occurs when

$$\frac{w}{\hat{v}} = \frac{1}{2\sqrt{1 - R_x}} \tag{5.18}$$

For power generation applications, it is important that the rotating blade velocity remains constant, as the frequency of the generated electricity must be 50 or 60 Hz. Thus, it is desirable for the steam velocity to also remain constant, and the optimal w to $\hat{v}$ ratio to be maintained. As consequence of (5.13), steam turbines are designed such that the pressure ratio (and thus $\hat{v}$) is constant even under load variations for every stage except governing stages and the final few stages in the low pressure section.

A throttle valve is used in the governing stage(s) of the high pressure (HP) turbine to adjust the steam flowrate and maintain a constant output pressure from the boiler (US designs). For partial load operation, this means the steam flowrate is reduced, which impacts the performance of each type of stage differently. The efficiency of the governing stage(s), located at the beginning of the HP turbine, decreases as the pressure ratio deviates from the optimal value. The pressure ratios in the remaining stages in the high, intermediate and low pressure turbines, however, are maintained and the stage efficiencies are near constant despite partial load operation. The exception to this rule is the last few stages of the low pressure section, which operate in the wet region. The efficiency of these stages depends mainly on the condenser operating pressure and outlet velocity of the steam. Thus the efficiency of the governing stage(s) and final stages of the LP turbine decrease under partial load operation.

There are two types of stream extractions: *controlled* and *uncontrolled*. Governing stages and/or throttle valves are used to regulate the pressure of controlled steam extractions by manipulating the area along the steam path. These are commonly used in co-generation facilities where steam must be extracted at a fixed pressure for utility steam headers to meet the demands of the coupled processes. For example, the pressures at the exit of the high, medium and low pressure turbines are typically regulated. Controlled (e.g. regulated pressure) extractions may also be incorporated into the turbine casing and occur between stages. In contrast, for uncontrolled steam extractions the area along the steam path is fixed, and the pressure of extracted steam varies during off-design operation. Due to the improved turbine efficiency from not using governor stage(s), uncontrolled extractions are preferred feedwater preheating in power systems. The *constant flow coefficient* formula is the simplest way to calculate the pressure of steam from an uncontrolled extraction:

$$\phi_i = \frac{m_i}{\sqrt{P_i/V_i}} = \text{constant} \tag{5.19}$$

where ϕ_i is the mass flow coefficient, P_i is the pressure, m_i is the mass flowrate of steam remaining in the turbine (not extracted), and V_i is the specific volume at the entrance of stage i (more specifically, the nozzle throat). Equation (5.19) holds for utility cycles with expansion from high to vacuum pressure. Thus, during off-design operation, the flowrate of not extracted steam, m_i, must adjust to changes in steam conditions (P_i and V_i). Unfortunately, (5.19) does not hold for co-generation back-pressure steam turbines. Instead, Stodola's formula is preferred:

$$\phi_i = K_i \sqrt{1 - \left(\frac{B_i}{P_i}\right)^2} \tag{5.20}$$

where K_i is the Stodola constant for stage (group) i, B_i is the backpressure at the end of i and P_i is the pressure at the beginning of i. Theoretically, a group with an infinite number of stages may be treated as an analogous single nozzle (stage). Empirically, (5.20) may be applied to an unchocked stage group with at least eight 50% reaction type stages with virtually no error[1]. Stodola's formula is typically implemented in an alternate form,

$$\frac{\phi_i}{\phi_i^D} = \frac{\sqrt{1 - \left(\frac{B_i}{P_i}\right)^2}}{\sqrt{1 - \left(\frac{B_i^D}{P_i^D}\right)^2}} \tag{5.21}$$

where ϕ_i^D, P_i^D and B_i^D are at the design point. In utility systems the pressure ratio, B_i/P_i, for most stages is constant and (5.20) simplifies to (5.19).

[1] See Cooke (1985) for corrections with fewer stages in a group, or operation with chocked nozzle(s)

There are three categories of mathematical models to predict the impact of **off-design operation** on turbine section efficiency. Section models (coarse grain) only consider the variations in the overall section efficiency. These models are the least accurate. In contrast, stage-by-stage models (fine grain) calculate the efficiency of each individual section. Although these models are the most accurate, they require the most input information and are only appropriate for existing, well characterized turbines (Chacartegui et al., 2011). Stage group models (medium grain) are the most popular for design applications. These models cluster similar stages together, and calculate an overall group efficiency using a nozzle analogy. Steam extractions may occur between stage groups. This type of model requires less information for accurate implementation, and is more realistic then the section type model. In general, course and medium grain models are preferred by chemical engineers studying combined heat and power systems, whereas all three classes of models are used by mechanical and power systems engineers to studying electricity generation systems.

5.2.1.1 Turbine Hardware Model and Extensions

Many of the combined heat and power system optimization studies previously reviewed either use simplified steam turbine efficiency models (e.g., fixed overall efficiency) or assume a Carnot or Rankine cycle efficiency. In other words, these studies do not consider detailed efficiency calculations for off-design operation. In response to this shortcoming, Mavromatis and Kokossis (1998a) proposed the Turbine Hardware Model (THM) for backpressure steam turbine, which is a medium grain model. At its core, this model is based on the Willans line, a linear relationship between steam flowrate (M) and power output (W), as shown below:

$$W = nM - W^{loss} \tag{5.22}$$

The linear intercept, W^{loss}, represents internal losses of the steam turbine and is assumed equal to 20% of the maximum output, W^{max}. The slope of Willans line, n, is approximately proportional to the inverse of the turbine efficiency. Thus the linear relationship shown in the Willans line corresponds to a non-linear relationship between power output and turbine efficiency. Furthermore, using decomposition theory, a multi-stage turbine may be modeled as multiple simple turbines in series, with each simple turbine representing a section (Chou and Shih, 1987).

Regression analysis reveals a near linear relationship between the ratio of max power and turbine efficiency,

$$\frac{W^{max}}{\eta_{is}^{max}} = A + BW^{max} \tag{5.23}$$

where η_{is}^{max} is the isentropic efficiency at the maximum power output for the turbine and A and B are coefficients. Mavromatis and Kokossis (1998a) propose another linear relationship for the regressed coefficients,

$$A = a_1 + a_2 \cdot T_{in}^{sat} \tag{5.24a}$$
$$B = b_1 + b_2 \cdot T_{in}^{sat} \tag{5.24b}$$

where $a_1 - b_2$ are fitted constants (see Table 5.2) and T_{in}^{sat} is the temperature of saturated steam at the inlet pressure. Combining (5.22) and (5.23) results in the following formula:

$$W = \frac{6}{5}\frac{1}{B}\left(\Delta\bar{H}_{is} - \frac{A}{M^{max}}\right)\left(M - \frac{1}{6}M^{max}\right) \tag{5.25}$$

where $\Delta\bar{H}_{is}$ is the isentropic enthalpy change, M^{max} is the maximum steam flowrate and M is the operating steam flowrate. Equation (5.25) enables the off-design calculation of steam turbine performance. Isentropic efficiency is implicitly considered in the model, and may be explicitly calculated using

$$\eta_{is} = \frac{W}{M\Delta\bar{H}_{is}} = \frac{6}{5}\frac{1}{B}\left(1 - \frac{A}{\Delta\bar{H}_{is}M^{max}}\right)\left(1 - \frac{1}{6}\frac{M^{max}}{M}\right) \tag{5.26}$$

Several researchers have proposed extensions to this model to improve its accuracy. For example, Shang (2000) extend the THM to condensing turbines with a set of alternate correlations,

$$A = a_1^c + a_2^c \cdot T_{in}^{sat} \tag{5.27a}$$
$$B = b_1^c + b_2^c \cdot T_{in}^{sat} \tag{5.27b}$$

with the regressed coefficients given in Table 5.2. They used these model (THM and CTHM) to optimize the operation of utility systems (Shang and Kokossis, 2005). Varbanov, Doyle, and Smith (2004) further refined the THM in three ways. First, instead of assuming W^{loss} is 20% of W^{max}, they generalized the model such that $W^{loss} = L \cdot W^{max}$, where L is the *intercept ratio*, a fitted parameter determined from performance data. Second, the terms A and B are calculated using a different correlation,

$$A = \hat{a_1} + \hat{a_2} \cdot \Delta T^{sat} \tag{5.28a}$$
$$B = \hat{b_1} + \hat{b_2} \cdot \Delta T^{sat} \tag{5.28b}$$

where $\hat{a_1}$ - $\hat{b_2}$ are regressed coefficients (see Table 5.2) and ΔT^{sat} is the difference in saturation temperature between the inlet and outlet pressures. This model takes into account the pressure drop across the turbine, where the original form, (5.24) & (5.27), only considers the inlet pressure. These improvements result in the following revisted steam turbine model,

$$W = \frac{L+1}{B}\left(\Delta\bar{H}_{is} - \frac{A}{M^{max}}\right)\left(M - \frac{L}{L+1}M^{max}\right) \tag{5.29}$$

which reduces to (5.25) when $L = 0.2$. Finally, Varbanov, Doyle, and Smith (2004) considered mechanical efficiency (friction, etc.) of single-stage steam turbines. They selected a linear relationship between total energy removed from the working fluid, W^{total}, and net work out of the turbine, W,

$$W^{total} = a_{total} + b_{total} \cdot W \tag{5.30}$$

where a_{total} and b_{total} are fitted coefficients. They report good agreement with manufacture's data: maximum error between 3.0 - 3.8% and an average error less than 1%. Furthermore, they found a linear relationship between ΔT_{sat} and L, the *intercept ratio*,

$$L = a_L + b_L \cdot \Delta T_{sat} \tag{5.31}$$

where a_L and b_L are also fitted coefficients. These coefficients were determined by analyzing a large dataset of single-stage backpressure and condensing turbines ranging from approximately 1MW to 60MW in size. See Varbanov, Doyle, and Smith (2004) for the coefficient values[2].

Table 5.2: Reported coefficients for the THM and extensions.

(Backpressure) **Turbine Hardware Model** (Mavromatis and Kokossis, 1998a)				
	a_1	a_2	b_1	b_2
$W^{max} < 1.2$ MW	-0.0131	0.00117	0.989	0.00152
$W^{max} > 1.2$ MW	-0.928	0.00623	1.12	0.00047
Condensing Turbine Hardware Model (Shang, 2000)				
	a_1^c	a_2^c	b_1^c	b_2^c
$W^{max} < 1.5$ MW	-0.0981	0.001	1.2059	0.0006
$W^{max} > 1.5$ MW	-0.0376	0.0014	1.1718	0.0003
Revised Steam Turbine Model (Varbanov, Doyle, and Smith, 2004)				
Backpressure	$\hat{a_1}$	$\hat{a_2}$	$\hat{b_1}$	$\hat{b_2}$
$W^{max} < 2$ MW	0	0.00108	1.097	0.00172
$W^{max} > 2$ MW	0	0.00423	1.155	0.000538
Condensing	$\hat{a_1}$	$\hat{a_2}$	$\hat{b_1}$	$\hat{b_2}$
$W^{max} < 2$ MW	0	0.000662	1.191	0.000759
$W^{max} > 2$ MW	-0.463	0.00353	1.220	0.000148

Similar, Medina-Flores and Picón-Núñez (2010) customized the turbine hardware model with alternate correlations for coefficients in the Willans line:

[2]There appears to be incorrect units and/or values for b_{total} reported in the original publication.

$$W = \frac{1}{\tilde{\beta}}\left(M\Delta\bar{H}_{is} - \tilde{\alpha}\right) \tag{5.32a}$$

$$\tilde{\alpha} = 0.1854 + 0.0433P^{in} \tag{5.32b}$$

$$\tilde{\beta} = 1.2057 + 0.0075P^{in} \tag{5.32c}$$

where P^{in} is the inlet pressure in MPa, W is the output work in MW, M is the steam flowrate and $\Delta\bar{H}_{is}$ is the isentropic change in enthalpy (with consistent units). The authors used data from Peterson and Mann (1985), in the form of isentropic efficiency curves, to fit the models. These curves are for a constant inlet temperature of 540 °C, an outlet pressure 0.1 MPa and inlet pressures ranging from 1.4 to 10.2 MPa for turbines rated up to 100 MW. It is unclear how this model accounts for off-design operation (i.e., variations in steam flowrate). Using three single-stage and two multi-stage reference turbines (data from open literature), the authors demonstrate this new model outperforms those presented by Mavromatis and Kokossis (1998a) and Varbanov, Doyle, and Smith (2004). Furthermore, additional extensions to the Turbine Hardware Model have been recently proposed by Sun and Smith (2015).

Luo et al. (2011) present one of the most rigorous steam cycles models in CHP literature. They distinguish between controlled and uncontrolled steams extractions in the turbines and water preheater systems. Each turbine section (e.g., high, intermediate or low pressure) with uncontrolled extraction is further decomposed into stage groups and Stodola's formula is used to calculate the appropriate extracted steam pressure,

$$P^u = \sqrt{(P^{out})^2 + \frac{M^u}{\bar{M}^u}\left((\bar{P}^u)^2 - (\bar{P}^{out})^2\right)} \tag{5.33}$$

where P^u is the uncontrolled extraction pressure, P^{out} is the outlet pressure, M^u is the uncontrolled extracted steam flowrate, and $\bar{P}^u$, $\bar{P}^{out}$, and $\bar{M}^u$ are the design (nominal case) values of these variables. Eq. (5.33) is only applicable when the difference bewteen P^u and $\bar{P}^u$ is small. These models were used to optimize the operation of a utility system with four multistage turbines with steam extraction and the associated boiler feed water system. In a subsequent study, the authors investigated process waste heat integration into the utility system using these models (Luo et al., 2012).

Overall, the Turbine Hardware Model and its extensions may be classified as either course grain (section only resolution) or medium grain (stage group resolution). However, this model is likely inappropriate for the intermediate pressure section of a utility steam cycle, as it assumes turbine efficiency decreases as steam flowrate decreases. In contrast, steam turbines are designed for power systems such that the intermediate pressure efficiency remains nearly constant (Cotton, 1998; Spencer, Cotton, and Cannon, 1963). The THM is

most appropriate for co-generation systems, as controlled extractions are preferred (to deliver steam at constant pressure levels) which require additional governing stages. Furthermore, it is unclear if the performance data used to tabulate the fitted model parameters represent an entire turbine (high, medium and low sections lumped together) or distinguish between the individual sections. Finally, most studies using the THM and its derivatives recommend calibration with manufactures data (which is rarely published in open literature).

5.2.1.2 The Spencer, Cotton and Cannon Model

Spencer, Cotton, and Cannon (1963)[3] published a collection of correlation-based models to predict the impact of off-design operation on steam turbine efficiency for power plant size equipment. In contrast to a majority of CHP studies, these models are specific to type of turbine sections. Their models are extensions of the work by Hegetschweiler and Bartlett (1957), and were fit using performance data for turbines built by General Electric Company, their employer. They proposed efficiency correction for eight factors and seven different turbine configurations, as shown in Table 5.3. Each "Yes" corresponds to graph and/or regression model in Spencer, Cotton, and Cannon (1963), which is used to calculate a percentage change in efficiency relative to base value given for each turbine type. Alternately, the base value may be calculated from the "thermal kit" provided by the turbine manufacture, which contains heat balance specifications for the design point. Table 5.3 does not include intermediate pressure (IP) sections, because the efficiencies of these sections are minimally affected by off-design operation.

Table 5.3: Summary of the factors and configurations consider in Spencer, Cotton, and Cannon (1963). This is an adaptation of Table 1 in the original article.

	Nonreheat	**HP Sections**		**Reheat Sections**		
Efficiency Corrections:	3600 rpm condensing 2-row gov. stage	3600 rpm noncondensing 1-row gov. stage	3600 rpm noncondensing 2-row gov. stage	3600 rpm condensing w/o gov. stage	3600/1800 rpm condensing w/o gov. stage	1800 rpm condensing w/o gov. stage
Volume flow	Yes	Yes	Yes	Yes	Yes	Yes
Governing stage	Yes	Yes				
Pressure ratio		Yes	Yes			
Initial conditions	Yes			Yes	Yes	Yes
Gov. stage at partial load	Yes	Yes				
Partial load	Yes	Yes	Yes			
Subs. of 1800 rpm, LP section					Yes	
Mean-of-loops	Yes	Yes	Yes			

The Spencer-Cotton-Cannon (SCC) models are used as the basis for off-design turbine performance calculations in several commercial steam cycle sim-

[3]An updated version of the model was published in *A Method for Predicting the Performance of Steam Turbine-Generators... 16,500 KW and Larger* General Electric Co., Publication GER-2007C, July 1974. This report, however, is extremely difficult to find. We were unable to locate and review it for this thesis.

ulators including IPSEPro[4], GateCycle[5] and PEPSE[6], although it is possible the software vendors have updated the model correlations in their products. Furthermore, these models are also featured in several academic studies. For example, Chacartegui et al. (2011) developed a computer program based on the SCC model, and validated it with performance data from a 565 MW steam power plant. The tool was then used to simulate alternate feedwater heater configurations and out of service scenarios. Chi et al. (2010) implement the SCC model in gPROMs, validate it with GateCycle and use the model to explore off-design operation of a chemical looping combustion (CLC) system. Overall, the SCC model provides a more detailed way to calculate off-design performance of utility steam turbines compared to the (modified) Turbine Hardware Model. Although the empirical correlations in the SCC model are based on performance data for systems over 50 years old, the model is still widely used in practice with adjustment (tuning) factors.

5.2.1.3 Proposed Turbine Model

The scope of this work is limited to design point operation, and does not consider the impact of variable steam flowrates on turbine section efficiency. Thus, the models in this work assume a fixed isentropic efficiency for each turbine stage group. An energy balance around the stage group gives

$$H^{out} = H^{in} - \eta^{is}\Delta H^{is} \tag{5.34}$$

$$W^{turbine}/\eta^{mech} = H^{in} - H^{out} \tag{5.35}$$

where H^{in} and H^{out} are the inlet and outlet enthalpy, respectively. ΔH^{is} and η^{is} are the isentropic enthalpy and isentropic efficiency, respectively, $W^{turbine}$ is the work produced in the stage group and η^{mech} is the mechanical efficiency. Typical values of isentropic efficiencies and pressure ratio as shown in Table 5.4 (Black, 2014). These pressure ratios are considered as bounds in the turbine model. Alternately, a relationship similar to (5.23) may be developed to link design point (i.e., maximum) isentropic efficiency and power output. The model coefficients fit by Mavromatis and Kokossis (1998a) and other, however, are for CHP turbines and are likely inappropriate for power system applications.

Table 5.4: Recommended Turbine Section Performance Parameters

	HP Section	**IP Section**	**LP Section**
Isentropic Efficiency	90.3 - 91.5 %	93.5 - 94.0 %	88.2 - 89.2 %
Pressure Ratio	25 - 35	6.6 - 14	0.7 - 1.5

Unlike the turbine hardware model (Mavromatis and Kokossis, 1998a) and extensions (Luo et al., 2011) that use an approximation for ΔH^{is}, the isen-

[4]SimTech Simulation Technology, http://www.simtechnology.com
[5]GE Measurement & Control, http://www.ge-mcs.com
[6]Scientech, http://famos.scientech.us/PEPSE.html

tropic enthalpy change is calculated exactly by introducing a shadow stream for each turbine ($\tilde{T}$, $\tilde{P}$, $\tilde{H}$, $\tilde{S}$),

$$P^{out} = \tilde{P} \tag{5.36a}$$

$$S^{in} = \tilde{S} \tag{5.36b}$$

$$\Delta H^{is} = H^{in} - \tilde{H} \tag{5.36c}$$

All entropies and enthalpies are calculated using the methods discussed in Sections 5.3 and 5.5. The outlet of each stage group is constrained to be in the vapor phase (0% moisture), with the exception of the last stage group of the low pressure sections. Its outlet may be up to 10 - 15% moisture (Babcock & Wilcox Co., 2005a), although 8 - 10% is a common recommendation (Black, 2014). Unless otherwise noted, 10% moisture is used as the upper bound for the LP exhaust in this work. Extraction is allowed between each stage group, as shown in Figure 5.15.

In order to extend these calculations to off-design calculations, either (5.19) or (5.20) should be used to calculate uncontrolled steam extraction pressures and flowrates. Depending on the application, either the THM or SCC equations should be used as the basis for off-design stage efficiency. For cogeneration applications, the THM model is preferred, as the SCC equations are intended for units with minimal steam extraction. For utility systems, the selection between a THM or SCC approach depends on the required accuracy. Although the SCC approach considers the impact of many different factors on efficiency for off design operation, the model is based on correlations developed for 50 years old equipment. If the THM approach is selected, it is best to refit the model with data from the turbine manufacture. Alternately, data generated from GateCycle or another commercial tool could be used to develop different correlations for each turbine section type (HP or LP).

5.2.2 Pump Model

Work demands for pumps are calculated using an enthalpy balance and entropy inequality,

$$W^{pump} = F(H^{out} - H^{in})/(\eta^{pump}\eta^{motor}) \tag{5.37a}$$

$$S^{out} \geq S^{in} \tag{5.37b}$$

where η^{pump} and η^{motor} are the pump and motor efficiencies. Without (5.37b), it is possible for the optimizer to find a point where an increase in the pressure of steam does not result in an enthalpy difference, and zero work is predicted. Unless otherwise noted, $\eta^{pump} = 0.736$ and $\eta^{motor} = 1.0$ are used in the optimization case studies. Finally, the temperature of the working fluid is constrained to increase

$$T^{out} + \varepsilon^{p} \geq T^{in} \tag{5.38}$$

and $\varepsilon^p = 0.273$ K is used in the case studies. ε^p may be tuned to add frictional losses to the pump.

5.2.3 Deaerator Model

The primary purpose of the deaerator is to reduce O_2 concentrations in the feedwater to less than 5 ppb and remove virtually all CO_2 to reduce corrosion in the boiler (Advanced Manufacturing Office, 2012). This is accomplished by injecting a small out of extracted steam into the deareator. A majority of the steam heats the liquid water in the deaerator, while 5-15% is vented with the dissolved gases. Make-up water is added to offset the vented steam. For deaerator steam calculation, the feed water outlet of the deaerator is commonly assumed to be a saturated liquid (Energy Efficiency & Renewable Energy, 2012; Black, 2014). The secondary purpose of the deaerator is to provide water storage and ensure adequate water levels in the boiler during transient operation.

In this framework, make-up water is neglected. The outlet of the deaerator is specified as a saturated liquid, which allows for implicit calculation of the steam requirement using an energy balance. Thus, the deaerator is modeled in the framework as an adiabatic flash vessel. Furthermore, the outlet of the deaerator is bounded between 4.8-9.3 bar and 420-450 K, which is consistent with Black (2014).

5.2.4 Remaining Equipment Models

Models for the remaining equipment, specifically flash vessels and valves, are presented in Chapter 2. In summary, valves and flash vessels (which are equivalent to mixers in this framework) are modeled using isenthalpic flash calculations. Because the inlet and outlet phases for steam side equipment are specified *a priori*, (2.57) and (2.58) are not necessary. The amount of pressure drop for each unit is an optimization variable. Similarly, each half side of a heat exchanger (shown in Figures 5.12 and 5.15) is also modeled to allow for phase changes, where the heating or cooling load is an optimization variable. Cotton (1998) recommends a 7 - 10% pressure drop for reheaters and assosiated piping, with an additional 2% pressure drop for stop and intercept valves. Similarly, Babcock & Wilcox Co. (2005a) observes a pressure drop of 8 - 10% for reheat (including all piping, etc.) is typical. In this work, a steam side pressure drop of 8% is assumed for each reheater. Cotton (1998) recommends a pressure drop of 4% for the stop and control valves (wide-open) before the high pressure turbine section, and a pressure drop of 3% for the IP-LP crossover. A pressure drop of 2.5% is assumed for the primary superheater. For air heaters, the pressure drop is typically 0.5 to 1.7 kPa at full load (Babcock & Wilcox Co., 2005b). A value of 0.2 bar is assumed in this work. Consistent with Black (2014), 2% and 4% pressure drops are assumed for the gas and liquid sides of the remaining heat exchangers in the steam cycle.

Stand-alone Heat Exchanger Network Synthesis (HENS) methods seek a design with fixed stream data (flowrates and temperatures) that minimizes

a balance of capital (area and number of matches) and operating (utility) costs (Chapter 3). For the steam cycle design problem, this approach is restrictive as we seek to simultaneously adjust flowsheet operating conditions (i.e., stream data) while performing heat integration by calculating minimum utility demands. This is done by using the Duran-Grossmann formulation and extensions, which are presented in Chapter 3. Furthermore, it allows for heat exchanger halves for boiler feed water heats, economizers, reheaters, air heaters and condensers in the steam cycle (Figure 5.15) to be integrated together, without assuming exact pairing between hot and cold sides of heat exchanger halves *a priori*. This allows for other heat sources or sinks, such as coolers after compression stages in the ASU and CPU, to be easily heat integrated with steam cycle. In contrast to previous work (Fu and Gundersen, 2010; Fu, Anantharaman, and Gundersen, 2014; Soundararajan, Anantharaman, and Gundersen, 2014), this approach couples heat integration with optimization, and operating conditions in the steam cycle are allowed to change in response to the heat integration, which creates additional degrees of freedom for optimization and leads to more tightly integrated (and efficient) power plant designs. Furthermore, heat integration zones (Chapter 3) are used to restrict integration between heat exchanger halves and maintain some practical constraints and common pairings, as shown in Table 5.5.

Table 5.5: Minimum Approach Temperatures

	Zone	$\Delta\underline{T}_z$	Ref.
1	Boiler Feed Water Heaters and Condenser	10 K	a
2	Primary Superheater	25 K	a
3	Reheaters	25 K	a
4	Economizer	20 K	b
5	Air Heaters	25 K	a

a: Black (2014)
b: Babcock & Wilcox Co. (2005b)

5.3 Nonlinear Surfaces for Steam Properties

All of the equipment models presented in the previous section require an additional thermodynamics module to calculate the enthalpy, entropy and compressibility of steam as a function of temperature, pressure and phase. Previous mathematical programming based CHP studies rely on various regressed models to represent steam tables. For example, Mavromatis and Kokossis (1998a), Medina-Flores and Picón-Núñez (2010) and Luo et al. (2011) consider an approximation for isentropic change in enthalpy,

$$\Delta H_{is} = \frac{\Delta T^{sat}}{1854 - 1931(H_{in} - H_{in}^{liq})} \tag{5.39}$$

where H_{in} and H_{in}^{liq} are the enthalpies of the inlet steam and a saturated liquid, respectively. This model was originally suggested by Singh (1997) and has an error around 5 - 10%. In order to reduce this error, Luo et al. (2011) proposed an alternate set of linear relationships between ΔH_{is} and enthalpy of inlet steam for fixed inlet and outlet pressures. Similarly, Medina-Flores and Picón-Núñez (2010) and Luo et al. (2011) both proposed piecewise modeling strategies to calculate extraction temperature and enthalpy, and saturation temperature as a function of pressure. Finally, Bruno, Fernandez, and Grossmann (1998) and Li et al. (2014) both use polynomial models to calculate steam enthalpy and entropy as a function of temperature at fixed pressures. These approaches are undesirable for equation-based optimization for three reasons:

1. The piecewise models are non-smooth and possibly discontinuous at the transition points, which creates significant modeling and optimization challenges.

2. Many of the proposed models require fixed steam header pressures, which reduces the number of degrees of freedom.

3. All of the proposed regression-based models exhibit error.

The first two issues would be addressed by considering the cubic equation of state model for water proposed by Valderrama and Vargas (2003). Their model, however, has average errors of 1 - 2% for enthalpy, entropy and specific volume. In contrast, steam tables are considered the "gold standard" for industrial designs and performance calculations.

Embedding steam table lookups in an equation-based framework is far from trivial, as evident from review of the technical documentation for the IAPWS-97 steam table (IAPWS, 2007). First, the P-T space is divided into five regions, one of which is nonconvex. Each region has its own set of equations, which complicates implementation, especially if streams in the flowsheet are not constrained to one specific region. This is similar to the concern regarding piecewise alternates for (5.39). Furthermore, the equations in the IAPWS-97 steam table are ill-conditioned. For example, consider the formula for dimensionless Gibbs free energy in Region 1 (liquid with $T < 623.15$ K):

$$\frac{G(P,T)}{RT} = \sum_{i=1}^{34} n_i (7.1 - \pi)^{I_i} (\tau - 1.222)^{J_i} \tag{5.40a}$$

$$\pi = \frac{P}{16.53 \text{ MPa}} \tag{5.40b}$$

$$\tau = \frac{1386 \text{ K}}{T} \tag{5.40c}$$

where n_i, I_i and J_i are coefficients from a table with 34 entries (rows)! Worse, I_i has values from between 0 and 32, J_i has values between -41 and 10, and $|n_i|$

has values from $O(10^0)$ to $O(10^{-25})$. Thus the IAPWS-97 standard, if implemented in GAMS, would most likely result in very poorly scaled optimization problems. Significant reformulation would be required.

Instead, we seek to develop a highly accurate steam table model regression model in this section that has smooth (and differentiable) transitions between the vapor, supercritical and liquid regions. We refer to this as **Strategy A** for embedding steam table calculations in the equation-based process optimization framework. Ultimately we conclude the errors in this model (and perhaps most surrogate steam table models) result in unreasonable optimization results. In Section 5.5, an alternate approach, **Strategy B**, is presented to overcome this problem. For both of these strategies, steam thermodynamic property data are generated using X Steam (Homgren, 2006), a MATLAB implementation of the IAPWS-97 standard. This standard was chosen because the internal calculations are thoroughly documented and the X Steam package is open source (and free). However, the methodologies presented in this chapter are applicable to any steam table standard.

5.3.1 Steam Table Visualization

Visualization of enthalpy, entropy and compressibility factor for steam as a function of pressure and temperature (Figure 5.5) reveals three regions: vapor, liquid and supercritical. Below the critical pressure of water, the vapor and liquid regions are distinct and are separated by a "cliff". Above the critical pressure, these surfaces are blended together. The chosen algebraic form of the property models accommodate this shape. Furthermore, the vapor and liquid models must give distinct values for each property along the saturation curve for steam quality (i.e., equilibrium) calculations.

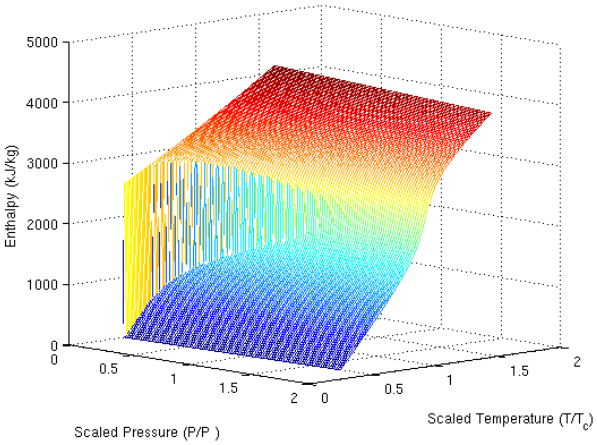

(a) Enthalpy

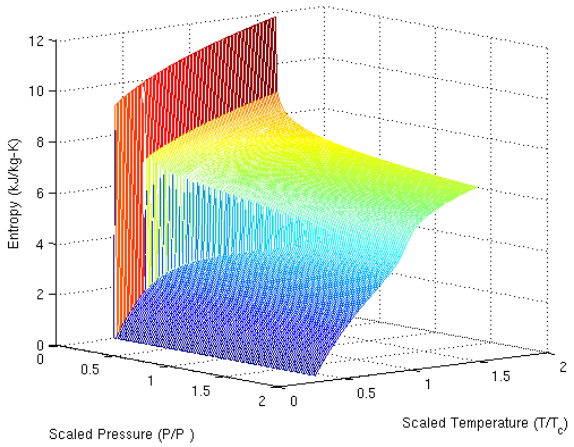

(b) Entropy

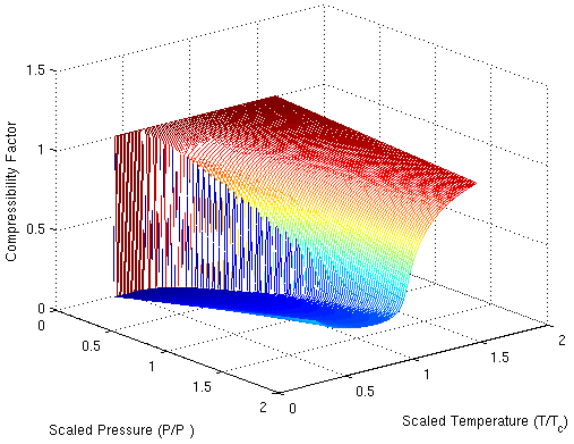

(c) Compressibility Factor

Figure 5.5: Visualization of Steam Thermodynamic Properties in PT Space

5.3.2 Saturation Curve

The first step in developing an algebraic steam table model is to fit a saturation curve correlation, which is required to determine the phase of water below the critical pressure and locate the ridge between the vapor and liquid surfaces in Figure 5.5. Iterative model refinement led to the following correlation for saturation temperature as a function of pressure:

$$\begin{aligned}\frac{T^{sat}}{T^{crit}} &= 0.574758933724728 + 0.001280225109360P \\ &+ 0.097270553837766\log_{10}(P) \\ &- 3.990655341783983\times10^{-4}P\log_{10}(P) \\ &+ 0.017246540714413[\log_{10}(P)]^2 \\ &+ 0.002044357202422[\log_{10}(P)]^3\end{aligned} \tag{5.41}$$

where T^{crit} is the critical temperature of water and P is pressure in bar. Figure 5.6 show an excellent fit, with relative errors less than 0.015%.

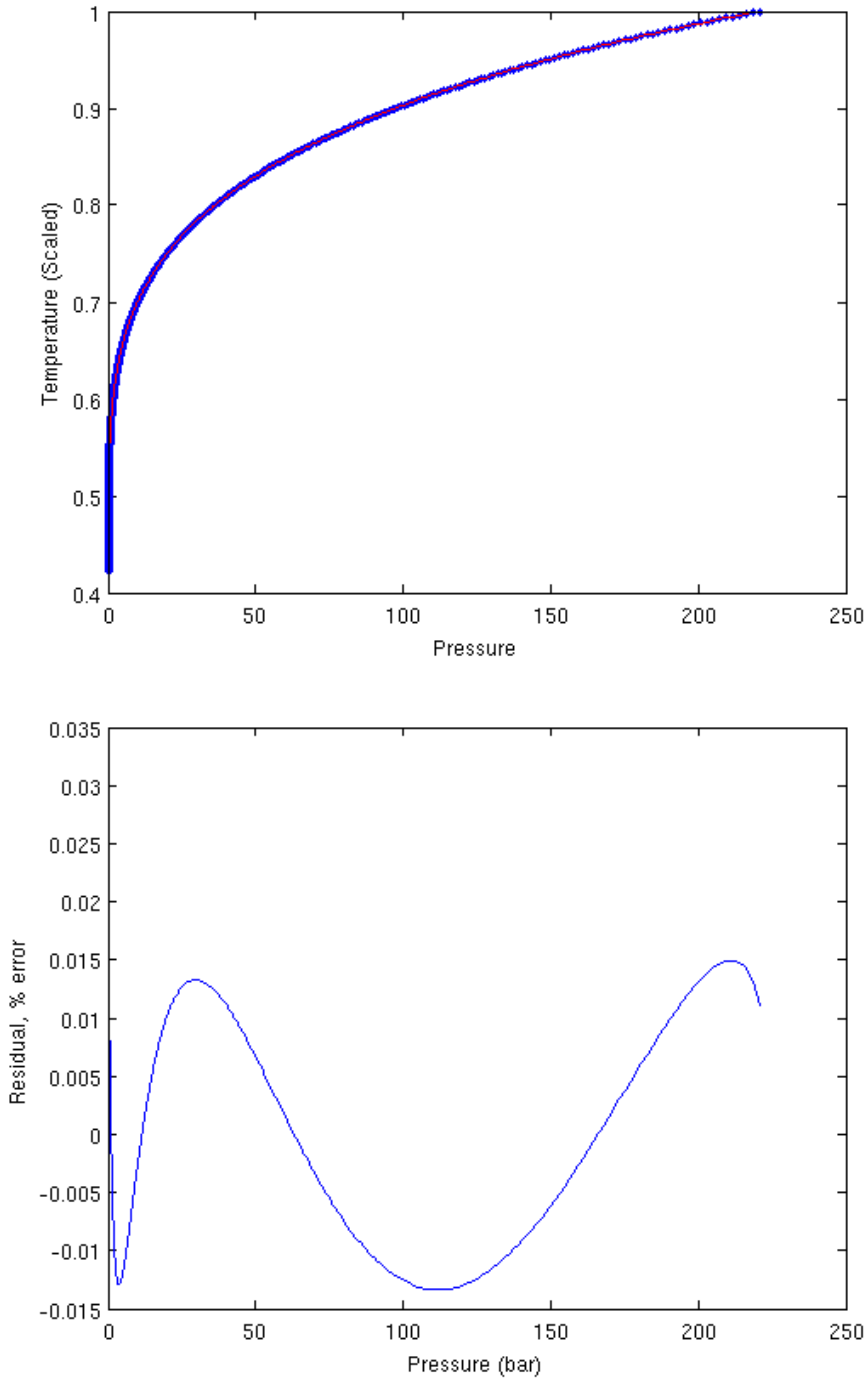

Figure 5.6: A Correlation for Saturation Temperature

5.3.3 Phase Specifications

The phase diagram for water is divided into four regions, vapor, supercritical, low pressure liquid and high pressure liquid, as shown in Figure 5.7. These regions are combined to form nine different phase groups (e.g., vapor or super-

critical), and each stream is specified *a priori* into one of groups. On account of the error in (5.41), constraints regarding temperature are backed off using $\varepsilon^{stm} = 0.01$ to restrict streams from operating too close to the saturation curve. This helps avoid numeric issues with X Steam, as there is a sharp difference in vapor and liquid properties, which is especially important for Strategy B (Section 5.5). The equation-based bounds for each of the nine cases (which are derived from different combinations of regions in Figure 5.7) are presented below. In addition to these constraints, all steam streams as also subject to global temperature and pressure bounds.

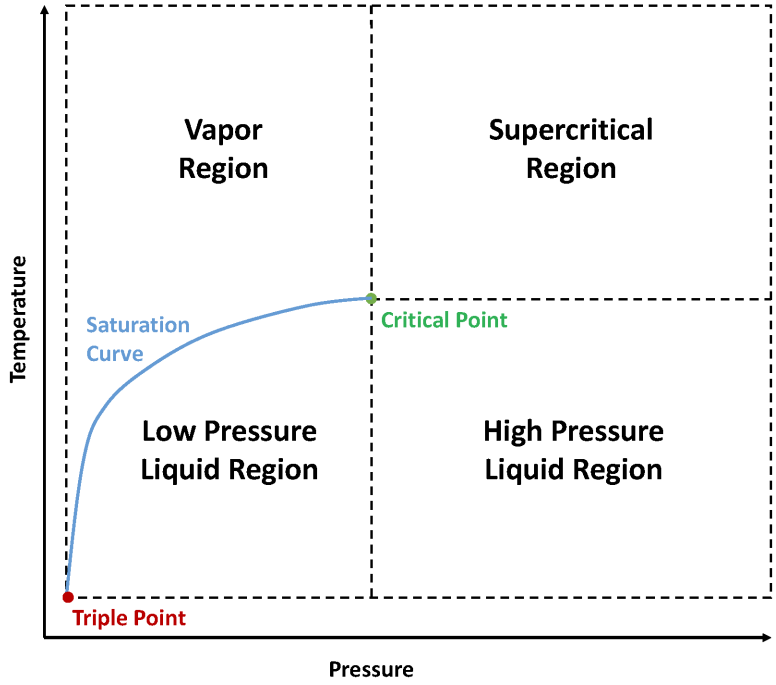

Figure 5.7: Phase diagram for water divided into four regions

Vapor

$$T_s \geq (1 + \varepsilon^{stm}) T_s^{sat}, \quad \forall s \in \{VapOnly\} \tag{5.42a}$$

$$P_s \leq P^{crit}, \quad \forall s \in \{VapOnly\} \tag{5.42b}$$

Low Pressure Liquid

$$T_s \leq (1 - \varepsilon^{stm}) T_s^{sat}, \quad \forall s \in \{LPLiqOnly\} \tag{5.43a}$$

$$P_s \leq P^{crit}, \quad \forall s \in \{LPLiqOnly\} \tag{5.43b}$$

High Pressure Liquid

$$T_s \leq T^{crit}, \quad \forall s \in \{HPLiqOnly\} \tag{5.44a}$$
$$P_s \geq P^{crit}, \quad \forall s \in \{HPLiqOnly\} \tag{5.44b}$$

Supercritical

$$T_s \geq T^{crit}, \quad \forall s \in \{SupOnly\} \tag{5.45a}$$
$$P_s \geq P^{crit}, \quad \forall s \in \{SupOnly\} \tag{5.45b}$$

High Pressure Liquid or Supercritical

$$P_s \geq P^{crit}, \quad \forall s \in \{HPLiqSup\} \tag{5.46}$$

Liquid Only

$$T_s \leq (1 - \varepsilon^{stm}) T_s^{sat}, \quad \forall s \in \{LiqOnly\} \tag{5.47a}$$
$$T_s \leq T^{crit}, \quad \forall s \in \{LiqOnly\} \tag{5.47b}$$

Liquid or Supercritical

$$T_s \leq (1 - \varepsilon^{stm}) T_s^{sat} \qquad \text{if } P < P^{crit}$$

$$T_s - \tau_s^T \leq (1 - \varepsilon^{stm}) T_s^{sat}, \quad \forall s \in \{LiqSup\} \tag{5.48a}$$
$$P + \tau_s^P \geq P^{crit}, \quad \forall s \in \{LiqSup\} \tag{5.48b}$$
$$0 \leq \tau_s^T \perp \tau_s^P \geq 0, \quad \forall s \in \{LiqSup\} \tag{5.48c}$$

Vapor or Supercritical

$$T_s \geq \min((1 + \varepsilon^{stm}) T_s^{sat}, T^{crit})$$

$$T_s \geq T^{crit} - \tau_s^{crit}, \quad \forall s \in \{VapSup\} \tag{5.49a}$$
$$T_s \geq (1 + \varepsilon^{stm}) T_s^{sat} - \tau_s^{sat}, \quad \forall s \in \{VapSup\} \tag{5.49b}$$
$$0 \leq \tau_s^{crit} \perp \tau_s^{sat} \geq 0, \quad \forall s \in \{VapSup\} \tag{5.49c}$$

Saturated

$$T_s = T_s^{sat}, \quad \forall s \in \{SatOnly\} \tag{5.50a}$$
$$P_s \leq P^{crit}, \quad \forall s \in \{SatOnly\} \tag{5.50b}$$

5.3.4 Property Models

Given the structure of the property surfaces, a two part modeling strategy is proposed. First, two polynomial surfaces are fit for the vapor + supercritical ($T \geq \min(T^{crit}, T^{sat})$) and liquid ($T \leq \min(T^{crit}, T^{sat})$) regions. Beyond the critical pressure ($P \geq P_c$), the two models are blended together using a sigmoidal function. Let $f_{VS}(T,P)$ and $f_L(T,P)$ be the fitted surfaces for a thermodynamic property F, and let $s(T,P)$ be a sigmoidal function that evaluates near unity far into the supercritical region and near zero far into the liquid region. Thus,

$$F(T,P) = \begin{cases} f_{VS}(T,P) & \text{if } T \geq T^{sat}(P),\ P < P_c \\ f_L(T,P) & \text{if } T \leq T^{sat}(P),\ P < P_c \\ s(T,P)f_{VS}(T,P) + (1 - s(T,P))f_L(T,P) & \text{if } P \geq P_c \end{cases}$$

where F is a thermodynamic property, such as enthalpy (H), entropy (S) and compressibility factor (V).

Sigmoidal Functions

Sigmoidal functions are algebraic, differentiable functions with an "S shape", such as

$$s_a(x) = \frac{1}{1 + e^{-\underline{\alpha}(x - x_0)}} \tag{5.51a}$$

$$s_b(x) = \frac{\underline{\alpha}(x - x_0)}{2\sqrt{1 + [\alpha(x - x_0)]^2}} + \frac{1}{2} \tag{5.51b}$$

$$s_c(x) = \frac{1}{2}\left[1 + \tanh \underline{\alpha}(x - x_0)\right] \tag{5.51c}$$

where x_0 is the switching point and $\underline{\alpha}$ acts as a slope, which adjusts the steepness of the "S curve". These three functions are shown in Figure 5.8.

For steam physical properties, the transition between regions is centered on the extrapolated saturated temperature curve, and thus we propose $x = T$ and $x_0 = T^{sat}(P)$ for the sigmoidal function, where $\underline{\alpha}$ is a fitted function (defined later).

"Polynomial Plus" Surfaces

As a starting point for the polynomial surface models, consider the behavior of an ideal gas. Enthalpy is calculated by integrating heat capacity (C_p) with respect to temperature,

$$H^{IG}(T) = \int_{T^\circ}^{T_f} C_p(T)dT \tag{5.52}$$

and C_p of an ideal gas is typically modeled as a polynomial with respect to temperature. Therefore, enthalpy may also be modeled as polynomial with

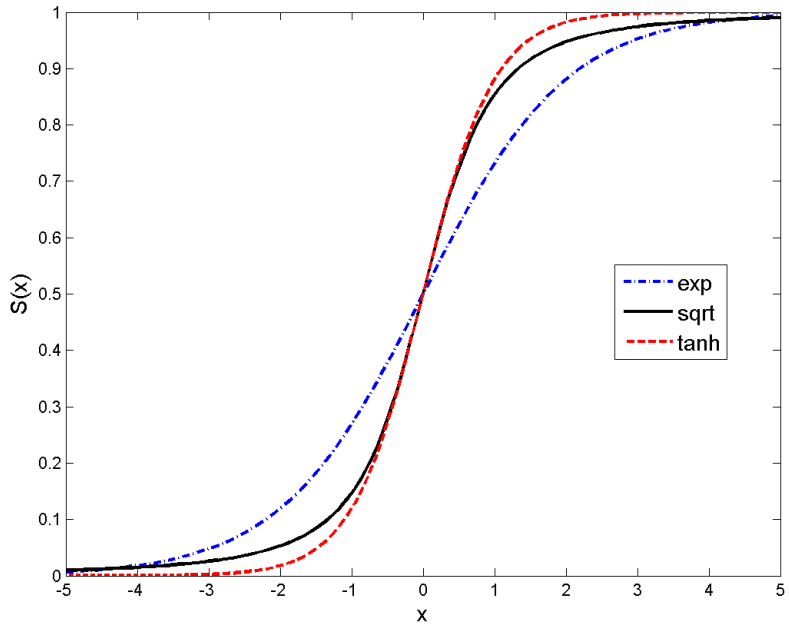

Figure 5.8: Visualization of sigmoidal functions (5.51) with $x_0 = 0$ and $\underline{\alpha} = 1$

respect to temperature. However, steam does not always behave as an ideal gas. As seen in Figure 5.5(a), the enthalpy of steam depends on pressure. Therefore, we also consider polynomial terms in pressure for the enthalpy model. A simple polynomial model, even with $T \cdot P$ interaction terms, is insufficient to capture nonlinearities in the entropy surface shown in Figure 5.5(b). Instead, consider the entropy of an ideal gas,

$$\begin{aligned} S^{IG}(T,P) &= \int_{T^\circ}^{T_f} \frac{C_v}{T} dT + \int_{V_{ref}}^{V_f} \frac{R}{V} dV \\ &= \int_{T^\circ}^{T_f} \frac{C_v}{T} dT + R \ln\left(\frac{T_f}{T^\circ}\right) - R \ln\left(\frac{P_f}{P^\circ}\right) \end{aligned} \tag{5.53}$$

where C_v is a polynomial function of temperature and pressure. The solution to the integral in (5.53) has $\ln P$, $\ln T$ and polynomial terms in T as basis functions. This provides motivations for the following "polynomial plus" surface for a generic thermodynamic property,

$$\begin{aligned} f(T,P) = {} & a_{00} + a_{10}T + a_{01}P + a_{20}T^2 + a_{11}TP + a_{02}P^2 \\ & + a_{30}T^3 + a_{21}T^2P + a_{12}TP^2 + a_{03}P^3 \\ & + (b_{00} + b_{10}T + b_{01}P + b_{20}T^2 + b_{11}TP + b_{02}P^2)\ln T \\ & + (c_{00} + c_{10}T + c_{01}P + c_{20}T^2 + c_{11}TP + c_{02}P^2)\ln P \end{aligned} \tag{5.54}$$

where a_{00} through c_{02} are fitted parameters.

Fitting Procedure

In order to ensure the best fit, the coefficients in the surfaces (a_{00} to c_{02}) and sigmoidal functions ($\underline{\alpha}$) are determined simultaneously. This results in a large, nonlinear regression problem which requires careful initialization. We found the following fitting produce to be very effective.

1. Sample enthalpy, entropy and compressibility factor from a steam table package at 10,000 points spaced in a grid (100 temperatures by 100 pressures)

2. Fit f_{VS} and f_L, which are instances for (5.54) for the vapor plus supercritical and liquid phase regions, for each property without the sigmoidal function. This is a standard linear regression problem.

3. Initialize the sigmodial function with $\underline{\alpha}$ decreasing linearly as a function of pressure

4. Simultaneously fit the surface coefficients (a_{00} to c_{02}) and $\underline{\alpha}_1$ to $\underline{\alpha}_n$, where each pressure level above P_c has its own $\underline{\alpha}_i$

5. Plot $\underline{\alpha}$ versus pressure and postulate algebraic functions for $\underline{\alpha}(P)$, such as (5.55). Fit one of these models, obtaining new values for $\underline{\alpha}_i$

6. Simultaneously fit the surface coefficients and coefficients in $\underline{\alpha}(P)$

7. Plot the fitted property model overlaid on real data (Figure 5.5). Examine residual plots and repeat the process with alternative forms for (5.54) and/or (5.55).

Fitted Models

Using the proposed procedure, we developed models for enthalpy, entropy and compressibility using

$$\underline{\alpha}(P) = -\underline{\beta}_1 \ln\left[\underline{\beta}_2(P + \underline{\beta}_3)\right] \tag{5.55}$$

as the function P, along with (5.51c) and (5.54). The fitted coefficients are shown in Tables 5.6 and 5.7. The fitted surfaces and residual plots are shown in Figures 5.9 - 5.11. For all three models, the maximum absolute errors occur near the transition between the liquid and vapor regions around the critical point.

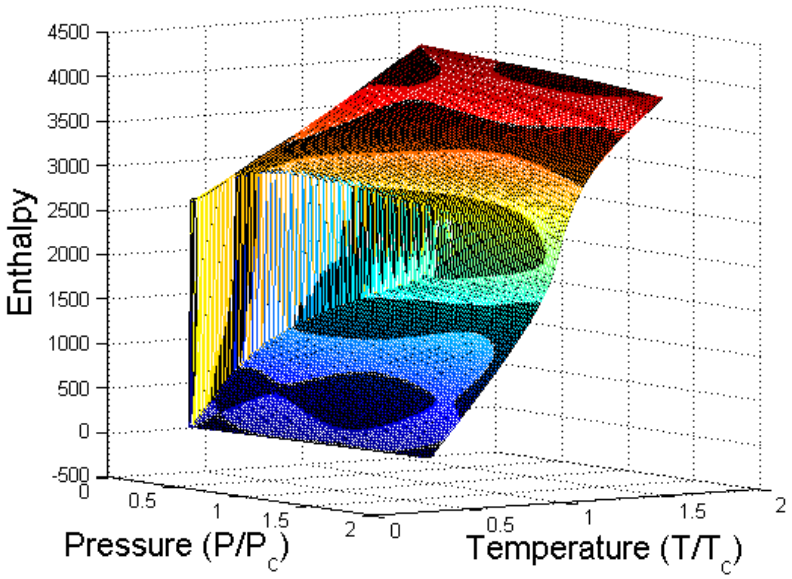

(a) Fitted Surface (dark)

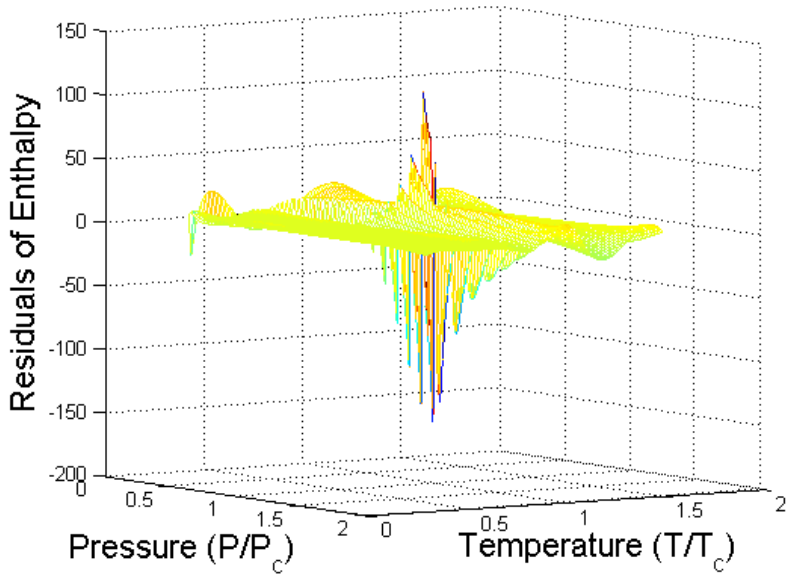

(b) Residual Plot

Figure 5.9: Enthalpy Model

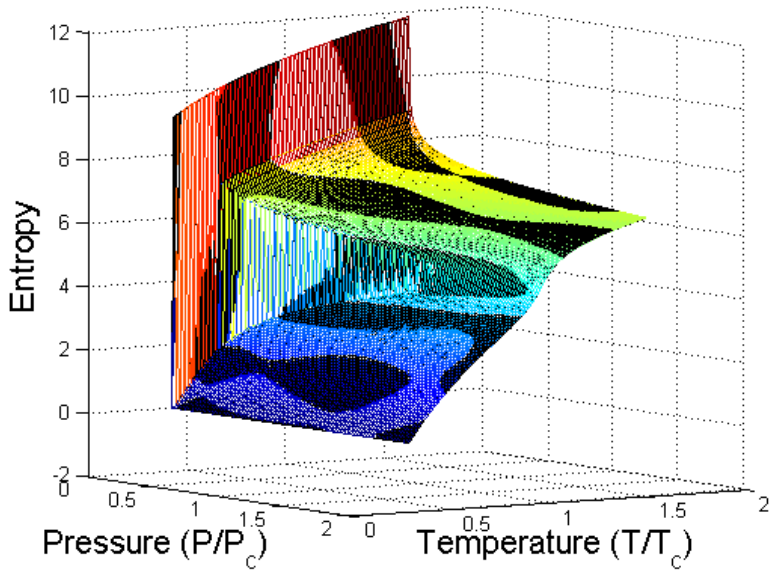

(a) Fitted Surface (dark)

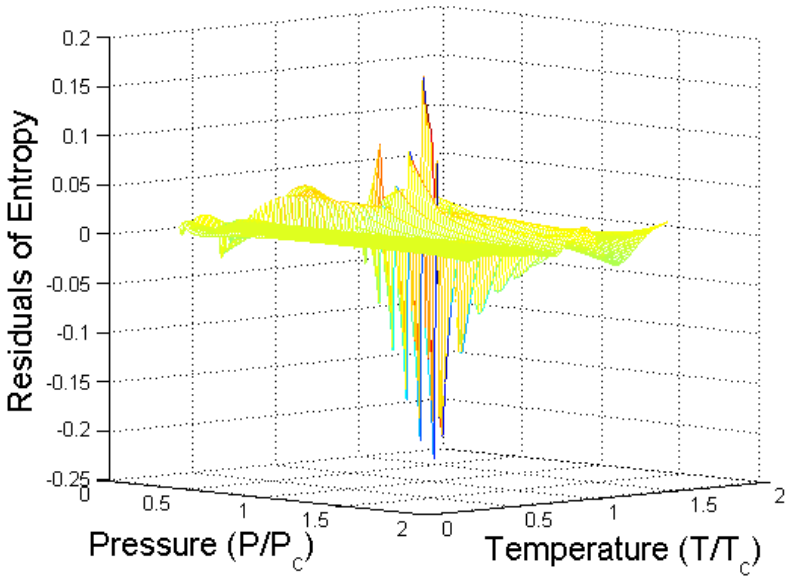

(b) Residual Plot

Figure 5.10: Entropy Model

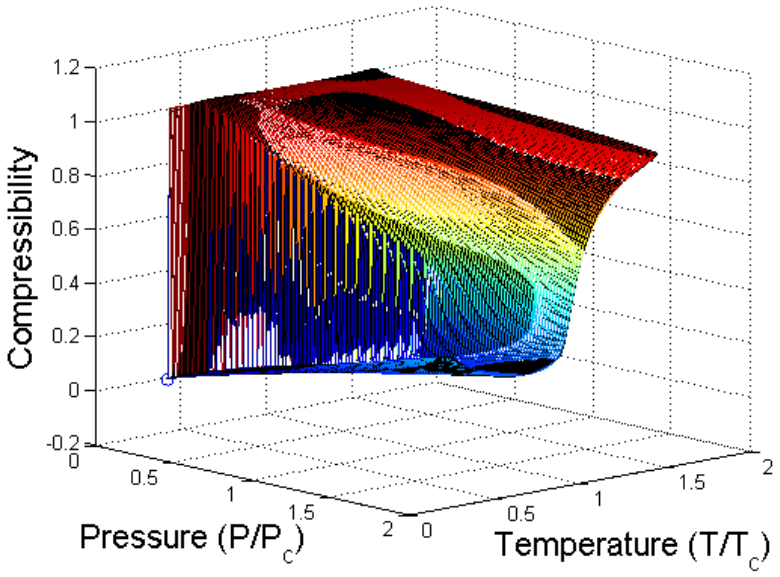

(a) Fitted Surface (dark)

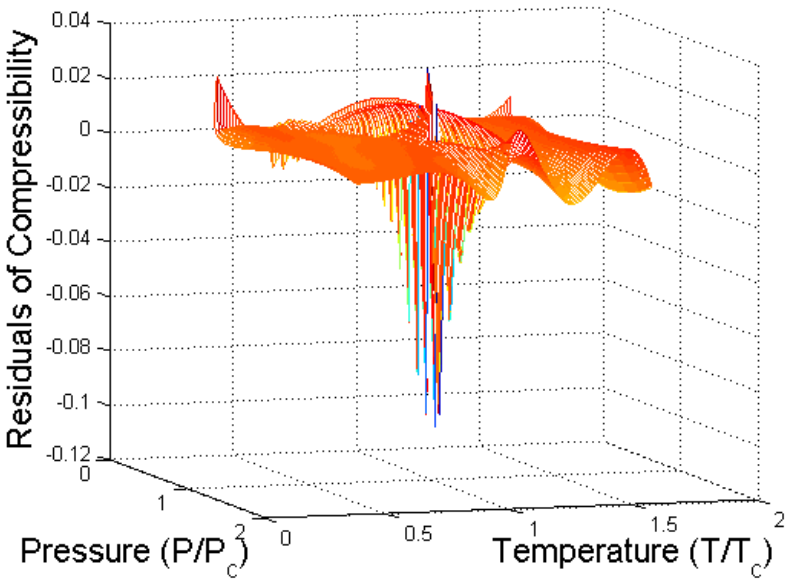

(b) Residual Plot

Figure 5.11: Compressibility Factor Model

Table 5.6: Fitted coefficients for (5.54) for enthalpy (H), entropy (S) and compressibility factor (Z) for steam (vapor and supercritical) and water (liquid)

	H		S		Z	
	Vapor & S. C.	Liquid	Vapor & S. C.	Liquid	Vapor & S. C.	Liquid
a_{00}	-100000	27827.530	460.596	12.496	-3.473	5.995×10^{-2}
a_{10}	100000	63281.167	765.491	-16.616	7.331	-0.189
a_{01}	95319.019	19610.310	382.054	35.969	4.371	-1.904
a_{11}	-100000	-9972.720	-358.732	-18.211	-14.163	0.203
a_{20}	17305.008	-100000	-1134.609	-26.424	-1.137	-3.026
a_{02}	2871.454	103.0402	4.283	0.111	0.973	-0.331
a_{30}	-14109.300	10732.655	-85.558	34.664	-1.742	3.293
a_{21}	4354.387	-10327.160	-23.788	-18.840	9.495	1.629
a_{12}	-3168.354	436.619	-4.593	0.666	-1.147	0.383
a_{03}	-17.973	94.131	-2.140×10^{-2}	0.135	-1.906×10^{-2}	8.407×10^{-3}
b_{00}	-35683.0437	6624.278	126.035	5.348	-1.405	-0.509
b_{10}	-90932.735	75834.605	1000.001	16.949	-3.573	2.446
b_{01}	60354.0178	6746.0365	198.315	12.217	14.540	-0.402
b_{20}	35533.062	27521.090	636.189	-47.971	5.132	-4.976
b_{02}	4094.394	-218.323	5.802	-0.334	1.237	-0.254
b_{11}	33665.353	22707.108	212.540	41.677	-16.797	-3.553
c_{00}	32.482	69.612	-0.386	0.100	1.392×10^{-2}	8.418×10^{-2}
c_{10}	-66.273	-250.851	-0.146	-0.361	-3.230×10^{-2}	-0.327
c_{01}	-652.359	-206.0781	-1.134	-0.294	-0.541	-8.415×10^{-2}
c_{20}	30.997	191.730	6.569×10^{-2}	0.277	1.643×10^{-2}	0.307
c_{02}	128.725	-419.192	0.142	-0.601	0.149	-3.542E-2
c_{11}	539.694	-142.117	0.890	-0.201	0.468	0.116

Table 5.7: Fitted coefficients for (5.55) for enthalpy (H), entropy (S) and compressibility factor (Z) for steam (vapor and supercritical) and water (liquid)

	H	S	Z
$\underline{\beta}_1$	24.690969	26.074744	107.457773
$\underline{\beta}_2$	0.506594	0.529757	0.330817
$\underline{\beta}_3$	-0.9999	-0.9999	0.617709

5.4 Demonstration Optimization

A single reheat regenerative Rankine cycle is considered as a demonstration system to benchmark the equipment and thermodynamic models discussed in this chapter.

5.4.1 Demonstration System

The steam and gas sides of the cycle are shown in Figure 5.12. Each turbine section is assigned a constant overall isentropic efficiency (HP 90%, IP 94%, LP 88.5%). Individual stages or stage groups are not considered in this system. The single reheat occurs between the high and intermediate pressure turbine sections. Uncontrolled steam extraction for feedwater heating is allowed between each turbine section. For simplicity, the boiler heat and flue gas outputs are fixed and taken from the PacificCorp Hunter 3 unit air-fired case discussed in Section 5.6. The remaining assumption and optimization bounds for this reference case are shown in Table 5.8. Using the thermodynamic models in Sections 5.3 and 5.5, the following optimization problem is solved:

$$\begin{aligned} \max \quad & \text{Thermal Efficiency} + \left(0.1 \tfrac{\%}{\text{kW}}\right) Q^s + \left(10^{-10} \tfrac{\%}{\text{kW}}\right) Q^w \\ & + \rho \text{ (Complementary Violations)} \end{aligned}$$

$$\text{s.t.} \quad \text{Thermal Efficiency} = \frac{\sum_{i=1}^{n_T} W_i^{turbine} - \sum_{j=1}^{n_p} W_j^{pump}}{\text{Fuel Heat Rate}}$$

Steam Turbine Model	(5.34) - (5.36)
Pump Model	(5.37) & (5.38)
Deaerator Model	Section 5.2.3
Heat Integration Model	(3.1) - (3.3), (3.5) - (3.6), (3.12) - (3.14)
Remaining Equipment Models	(2.55), (2.56), (2.58) - (2.60)
Steam Thermodynamics	Section 5.3 or 5.5
Thermodynamics (Flue Gas)	(2.21), (2.22), (2.23) - (2.25)
Fixed Parameters and Bounds	Table 5.8

5.4.2 Optimization Results

Using the proposed steam thermodynamics model, (5.51c), (5.54) and (5.55), thermal efficiency maximized for the single reheat regenerative Rankine cycle. Surprisingly, CONOPT finds a local maximum thermal efficiency of 81.5% ($\eta_{optimized}$). An upper bound for the Carnot efficiency of this system is

$$\eta_{Carnot} \leq 1 - \frac{\text{Condenser temperature}}{\text{Max steam temperature}} = 1 - \frac{289 \text{ K}}{867 \text{ K}} = 66.7\% \tag{5.56}$$

and the Carnot efficiency is an upper bound for efficiency of all heat engines. Therefore, $\eta_{optimized} > \eta_{Carnot}$ is the first indication of nonphysical results. Table 5.9 shows the properties for all streams in Figure 5.12. SStm1 - SStm3

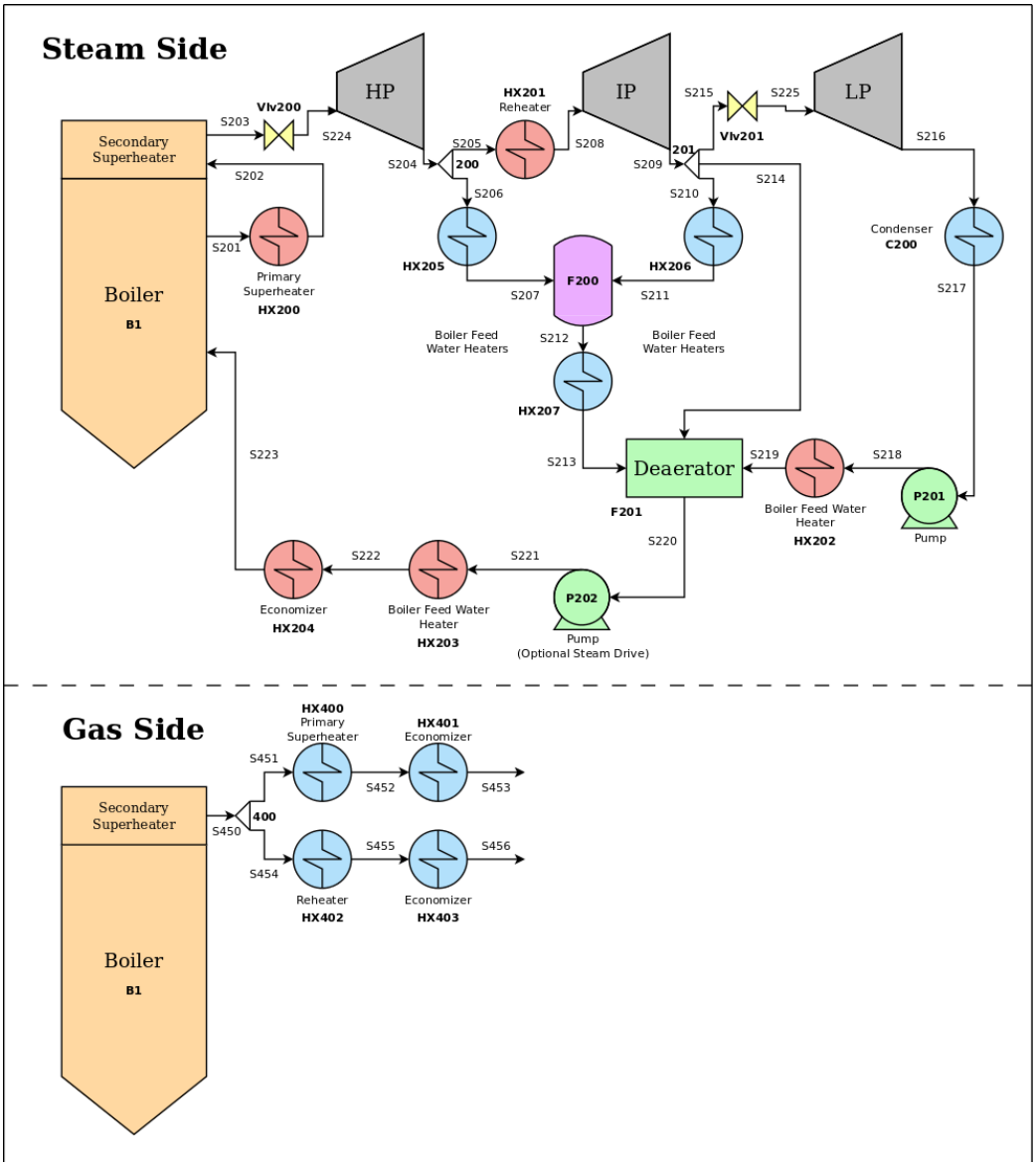

Figure 5.12: Single Reheat Regenerative Rankine Cycle

are the shadow streams for the turbine sections (HP - LP), which are used for isentropic efficiency calculations, (5.36). H^{actual} and S^{actual} are the actual enthalpy and entropy values, as calculated using X Steam. Table 5.10 shows the heat and work loads for various equipment in the steam cycle, which are calculated using an enthalpy balance and data in Table 5.9. The optimizer takes advantage of errors in the proposed nonlinear thermodynamics model, especially the low pressure region, and finds too-good-to-be-true designs that violate thermodynamics. For example, the proposed nonlinear model severely under-predicts the enthalpy of the LP turbine exhaust. As consequence, the LP section power output is over-predicted by 661 MW. Furthermore, examination of S and S^{actual} values in Table 5.9 reveals that entropy is actually destroyed in

Table 5.8: Assumptions and Bounds for Demonstration Rankine Cycle Efficiency Maximization

Steam Stream Classifications

Liquid Only	S217-S219
Vapor Only	S204-S215, S225
Saturated	S216, S220
Liquid or Supercrit.	S221 - S223
Vapor or Supercrit.	S201-S203, S224

Steam Side Pressure Drops

Prim. Super -heater (HX200)	2.5 %
Reheater (HX201)	8 %
Feed Water Heaters (HX202 & HX203)	4 %
Economizer (HX204)	4 %
Feed Water Heaters (HX205 - HX207)	2 %
Throttle Valve (Vlv200)	4 %
IP/LP Crossover (Vlv201)	3 %

Steam Side Bounds

All Steam Streams	$0.068 \leq P \leq 242.3$ bar $289 \text{ K} \leq T \leq 867$ K
Steam Extraction (S207 & S210)	$F \geq 10$ mol/s

Flue Gas Fixed Values (S450)

Flowrate	19,860 mol/s
Mole fractions	
CO	$O(10^{-6})$
CO_2	0.136
H_2	$O(10^{-6})$
H_2O	0.083
N_2	0.741
O_2	0.040
SO_2	$O(10^{-4})$
Pressure	
Temperature	1506 K

Boiler Fixed Values (B1)

Wall Duty	$Q^{wall} = 344.0$ MW
Wall Temp.	$T^{wall} = 623.2$ K
Sec. S.H. Duty	$Q^{ssh} = 83.6$ MW
Sec. S.H. Temp.	$T^{ssh} = 699.8$ K
Fuel Heat Rate	1325.5 MW (HHV)

Gas Side Bounds

Economizer Exit	$T \geq 320$ °C

the turbines sections, which is impossible. We postulate this happens because the regressed thermodynamics models lack certain consistency properties. For real steam, (5.34) and (5.36) guarantee $S^{out} > S^{in}$ when $\eta^{is} < 1$, because the enthalpy drop in the turbine is less than isentropic enthalpy drop. In the LP section, however, $S^{out} < S^{in}$. Similarly, errors in the proposed thermodynamic model allow the optimizer to find a solution with no heat rejected in the condenser and no pumping work, which do not agree with the steam table thermodynamics calculations. Thus, the solution detailed in Table 5.9 is not feasible considering the true thermodynamics of steam (modeled with the IAPWS IF-97 standard).

Table 5.9: Stream data for optimization of Figure 5.12 with nonlinear fitted thermodynamics model

Stream	F	T	P	H	H^{act}	S	S^{act}
S201	19912.4419	673.1500	220.6416	40.8443	49.2342	–	–
S202	19912.4419	677.6290	215.1255	50.0897	50.2482	–	–
S203	19912.4419	722.0050	215.1255	54.2895	54.4908	–	–
S204	19912.4419	589.9275	38.8037	54.2895	54.2481	0.1165	0.1164
S205	19902.4419	589.9275	38.8037	–	–	–	–
S206	10.0000	589.9275	38.8037	–	–	–	–
S207	10.0000	525.6547	38.0276	50.6202	50.8252	–	–
S208	19902.4419	867.0000	35.6994	65.9818	66.0119	0.1334	0.1335
S209	19902.4419	760.2610	4.9979	61.9509	62.2744	0.1446	0.1451
S210	42.5078	760.2610	4.9979	–	–	–	–
S211	42.5078	433.1307	4.8980	50.0158	49.8690	–	–
S212	52.5078	435.7870	4.8980	50.1309	49.9789	–	–
S213	52.5078	435.4097	4.8000	50.1309	49.9770	–	–
S214	3127.4450	760.2610	4.9979	–	–	–	–
S215	16732.4892	760.2610	4.9979	–	–	–	–
S216	16732.4892	312.8647	0.0727	2.1869	42.0181	0.1358	0.1350
S217	16732.4892	300.2060	0.0727	2.1869	2.0436	0.0073	0.0071
S218	16732.4892	302.7931	5.0000	2.1869	2.2466	0.0077	0.0078
S219	16732.4892	303.2337	4.8000	2.2194	2.2795	–	–
S220	19912.4419	423.5334	4.8000	11.7272	11.4139	0.0333	0.0332
S221	19912.4419	423.8066	239.4114	11.7272	11.7070	0.0329	0.0329
S222	19912.4419	423.9448	229.8350	11.7272	11.7065	–	–
S223	19912.4419	573.1500	220.6416	24.0690	24.0104	–	–
S224	19912.4419	657.4020	110.8677	54.2895	54.3999	0.1090	0.1091
S225	16732.4892	760.2149	4.8480	61.9509	62.2757	0.1448	0.1453
S450	19860.5038	1506.4190	1.0126	-30.828	–	–	–
S451	6167.5433	1506.4190	1.0126	–	–	–	–
S452	6167.5433	698.1500	1.0126	-60.6777	–	–	–
S453	6167.5433	593.1500	1.0126	-64.1888	–	–	–
S454	13692.9605	1506.4190	1.0126	–	–	–	–
S455	13692.9605	1060.6851	1.0126	-47.8226	–	–	–
S456	13692.9605	593.1500	1.0126	-64.1888	–	–	–
SStm1	0.0001	589.9275	38.8037	54.2895	54.2481	0.1165	0.1164
SStm2	0.0001	753.7422	4.9979	61.6936	62.0231	0.1442	0.1447
SStm3	0.0001	312.8647	0.0727	-5.57903	42.0181	0.1448	0.1350

Table 5.10: Overall heat balance for steam side of Figure 5.12 with nonlinear fitted thermodynamics model

	Nonlinear Thermo.	Steam Table
Work from Turbines (MW)	1080.2	416.4
HP	0	3.0
MP	80.2	74.4
LP	1000.0	339.0
Pumping Work (MW)	0.0	48.3
P200	0.0	3.4
P201	0.0	5.8
Heat from Boiler (MW)	417.7	274.0
Boiler Walls	334.0	189.3
Sec. Superheat.	83.6	84.7
Heat from Flue Gas (MW)	642.6	502.3
Prm. Superheat.	184.1	20.2
Reheater	232.7	234.1
Economizer	245.8	245.0
Heat Rejected (MW)	0	668.9
Flue Heat Rate (MW)	1325.5	1325.5

5.5 Adaptive Thermodynamic Models

The nonlinear models presented the previous section (Strategy A) suffer from inaccuracies, which the optimizer exploits and cheats thermodynamics to improve the objective function. Although alternate forms of the model should reduce these errors, it is difficult to produce a small set of models that are valid over the entire temperature and pressure range with insignificant error. Instead, we present and alternate adaptive model procedure this section (Strategy B). Simple models for steam thermodynamics are defined for each stream, which are sufficiently accurate on a small domain. The models are then updated during optimization using a trust region strategy.

5.5.1 Trust Region Adaptation/Optimization Strategy

The problem of obtaining derivatives for the steam thermodynamics and boiler model behavior is addressed using concepts of reduced or surrogate models and trust region algorithms. Reduced models are commonly used in the chemical engineering literature to provide a simpler representation of a system that is more suitable for optimization and analysis. For example, in the inside-out flash calculation proposed by Boston and Britt (1978), phase equilibrium is calculated in an inner problem using a reduced model for the phase equilibrium coefficient (K_c), and in the outer loop the reduced model is updated. Similarly, Caballero and Grossmann (2008) consider process optimization problems with Kriging surrogate models in place modular flowsheet equipment simulations. This approach features iterative model improvements, but does not guarantee convergence to optimal points due to noise in the original black box functions. As they note, inaccuracies in the reduced models tend to cause optimization algorithms to find suboptimal solutions with regards to the detailed original model. Trust region methods alleviate this difficulty by managing the reduced models in a manner that can guarantee convergence to the rigorous model optimum. The goal is to solve the following NLPs,

$$\text{ODM:} \quad \min_{x,y} f(x,y) \quad \text{s.t.} \quad g(x,y) \leq 0, \quad c(x,y) = 0, \quad y = d(x) \tag{5.57a}$$

$$\text{RM:} \quad \min_{x,y} f(x,y) \quad \text{s.t.} \quad g(x,y) \leq 0, \quad c(x,y) = 0, \quad y = r(x)\ , \tag{5.57b}$$

where $d(x)$ is the original detailed model (ODM), x are the independent variables, y are the dependent variables (i.e., ODM outputs), $f(x,y)$ is the objective function, and $g(x,y)$ and $c(x,y)$ are inequality and equality constraints. $r(x)$ is an algebraic reduced model (i.e., surrogate models). For an oxycombustion application, the ODM may be steam tables for calculating thermodynamic properties and/or CFD-based boiler simulations.

Trust algorithms for solving (5.57a) are classified based on the types of constraints and the availability of derivatives. For unconstrained problems with available first derivatives for the ODM, Alexandrov et al. (1998) introduced the ideas of zero-order and first-order corrections, where the reduced

model, $r(x)$, is constructed such that the function values and first derivatives match those of the ODM. Fahl and Sachs (2003) proved convergence with these consistency properties. Conn, Scheinberg, and Vicente (2009) consider the unconstrained derivative free case, and proved convergence as $\Delta_k \to 0$. Their analysis and proposed algorithm requires the *fully linear property* for reduced models, which imply that as the trust region shrinks, the derivatives of the reduced model approach those of the ODM. Agarwal and Biegler (2013) applied ideas to constrained optimization problem, and considered both penalty and filter algorithms to accommodate the constraints. More recently, Biegler, Lang, and Lin (2014) reviewed three trust region algorithms for optimization with reduced models and discussed their convergence properties. These algorithms are especially interesting for engineering applications, as they consider constrained problems.

Algorithm I of Biegler, Lang, and Lin (2014) considered the zero and first order corrections proposed from Alexandrov et al. (1998). Instead of solving (5.57), the reduced space problem is considered,

$$\min_{x,y} f(x) \qquad \text{s.t.} \quad g(x) \leq 0, \tag{5.58}$$

where $d(x)$ is implicitly considered in $f(x)$ and $g(x)$. For each trust region iteration k, the step s_k is calculated in the following subproblem:

$$s_k = \arg\min_s f_k^R(x_k + s) \qquad \text{s.t.} \quad g_k^R(x_k + s) \leq 0, \quad ||s_k||_\infty \leq \Delta_k, \tag{5.59}$$

where x_k and Δ_k are the center and radius of the trust region at iteration k, respectively. The reduced models (RM) for the objective and constraints, f_k^R and g_k^R, are constructed for each iteration using local additive corrections to ensure the objective and constraint function values and gradients are consistent with the ODM. The quality of step s_k is measured using the penalty functions

$$\psi(x) = f(x) + \nu \sum_{i \in I} \max(0, g_i(x)) \tag{5.60a}$$

$$\psi_k^R(x) = f_k^R(x) + \nu \sum_{i \in I} \max(0, g_{k,i}^R(x)) \tag{5.60b}$$

where ν is a sufficiently large constant. The ratio of actual to predicted improvement in ψ,

$$\rho_k = \frac{\text{ActualReduction}_k}{\text{PredictedReduction}_k} = \frac{\psi(x_k) - \psi(x_k + s_k)}{\psi^R(x_k) - \psi^R(x_k + s_k)} \tag{5.61}$$

is used to measure the quality of each step. If ρ_k is large, s_k is accepted. Otherwise, s_k is rejected and recomputed. Similarly, the value of ρ_k determines if the radius either expands, stays the same or contracts. Under the assumptions discussed in Biegler, Lang, and Lin (2014), this algorithm is shown to be convergent to a local solution of (5.58). This approach, however, requires accurate

first derivatives of the ODM, which are not always available. Furthermore the appropriate choice of ν is problem dependent and may require tuning. The algorithm was developed by Agarwal and Biegler (2013) and demonstrated in a pressure swing adsorption system optimization case study, where the partial differential algebraic equation (PDAE) bed models are replaced with proper orthogonal decomposition (POD) based reduced models.

Agarwal and Biegler (2013) also developed a derivative free version of the previous approach, which is Algorithm II in Biegler, Lang, and Lin (2014). Instead of accurate gradients, the algorithm requires the *fully linear property* and $\Delta_k \to 0$ for convergence (Conn, Scheinberg, and Vicente, 2009). Algorithms I and II share a similar structure, although Algorithm I tends to require fewer iterations due to the first derivatives from the ODM. Agarwal and Biegler (2013) also applied a hybrid approach to the PSA optimization case study. At the beginning of optimization, RM are constructed without derivative information (Algorithm II). Near the solution, derivative information is incorporated into the RM using a first order correction additive term (Algorithm I). Overall, the approach prevents both expensive ODM derivative calculations (e.g. finite difference perturbations, sensitivity equation integration) early in the optimization procedure and excessive iterations near the solution.

Finally, Algorithm III in Biegler, Lang, and Lin (2014) uses ϵ-exact models to reduce evaluations of the ODM during the trust region algorithm. Instead, significant effort is invested to construct accurate reduced models using a space-filling design of experiments and cross-validation to estimate the error of the models. Provided the RMs remain accurate during optimization, additional evaluations of the ODM are not required. Biegler, Lang, and Lin (2014) derive bounds relating the accuracy of the RMs and errors in the first order optimality conditions of (5.57a). Algorithm III is demonstrated with a polymerization reactor operation optimization case study.

The three algorithms summarized by Biegler, Lang, and Lin (2014) focus on inequality constrained nonlinear programs with embedded complex models (e.g., DAE or PDAE reactor simulations, etc.). Without modification, these algorithms may be applied in the reduced space of some equality constrained problems (with a constant reduced space dimension), i.e., the equality constraints are used to eliminate some variables from the optimization problem. For flowsheet optimization problems with recycle streams, this approach is problematic. Convergence of mass balances requires repeated evaluation of any ODMs for equipment inside the recycle loop, such as the boiler in an oxycombustion process. Instead, for oxycombustion design we seek to solve

$$\begin{aligned} \min_{x,y,z} \quad & f(x,y,z) \\ \text{s.t.} \quad & g(x,y,z) \le 0 \\ & h(x,y,z) = 0 \\ & y = d(x), \quad \text{[replaced with } y = r(x)\text{]} \end{aligned} \tag{5.62}$$

where $d(x)$ is the complex original detailed model, x and y are its inputs

and outputs, respectively, z are variables independent of the ODM, $f(x, y, z)$ is the objective function and $g(x, y, z)$ and $h(x, y, z)$ are nonlinear inequality and equality constraints, respectively. For problems with many equality constraints, the penalty approach described above has two significant drawbacks. First, performance of the trust region algorithm is sensitive to the selected weight for the penalty in the objective function, and extensive tuning is required for most problems. Second, penalized equality constraints typically lead to ill-conditioned NLPs.

As an alternative to the penalty approach, Agarwal and Biegler (2013) also consider a filter trust region algorithm. Borrowing ideas used in multi-objective optimization, filter methods balance two competing goals, i.e., improvement in the objective function value and improvement in a feasibility metric, e.g., (5.66), to determine if a step is acceptable. If shrinking the trust region does not result in a feasible step, the algorithm switches to restoration model, with the goal of minimizing infeasibilities. See below and Fletcher and Leyffer (2002) for additional details. This algorithm has been adapted by Eason and Biegler (2015) for application to flowsheet optimization problems without exact ODM derivatives. Some results for power plant design are shown in Dowling et al. (2014).

In the filter algorithms of Agarwal and Biegler (2013), Eason and Biegler (2015) and this work, proposed steps are calculated using a decomposition approach inspired by Omojokun (1990). First, the normal subproblem (this work),

$$\begin{aligned} \bar{\delta_k} = \min_{v,\delta} \quad & \sum_{i=1}^{N_y} \delta_i \\ \text{s.t.} \quad & -\delta_i \leq y_i + v_i^y - r_{k,i}(x + v^x) \leq \delta_i, \quad \forall i = 1, ..., N_y \\ & g(x + v^x, y + v^y, z + v^z) \leq 0 \\ & h(x + v^x, y + v^y, z + v^z) = 0 \\ & ||v^x||_\infty, ||v^y||_\infty \leq \xi_N \Delta_k, \end{aligned} \tag{5.63}$$

is solved to determine the minimum derivation between the reduced model output values, $r(x)$, and output variables, y, that ensures the remaining constraints, $g(\cdot) \leq 0$ and $h(\cdot) = 0$, are feasible. $v^T = [(v^x)^T, (v^y)^T, (v^z)^T]$ and $\xi_N \in (0, 1)$. The proposed step is then calculated in the tangential subproblem,

$$\begin{aligned} s_k = \arg\min_{s} \quad & f(x_k + s^x, y_k + s^y, z_k + s^z) \\ \text{s.t.} \quad & ||y_k + s^y - r_k(x_k + s^x)||_1 \leq \bar{\delta_k} \\ & g(x_k + s^x, y_k + s^y, z_k + s^z) \leq 0 \\ & h(x_k + s^x, y_k + s^y, z_k + s^z) = 0 \\ & ||s^x||_\infty, ||s^y||_\infty \leq \Delta_k, \end{aligned} \tag{5.64}$$

where $\bar{\delta_k}$ is the solution of (5.63). For each proposed step, the maximum deviation between the RMs and ODMs is calculated,

$$\theta(\chi_k + s_k) = ||y_k + s_k^y - d(x_k + s_k^x)||_\infty, \tag{5.65}$$

where $\chi^T = [x^T,\ y^T,\ z^T]$. If the filter condition,

$$\begin{gathered}\theta(\chi_k + s_k) \leq (1 - \gamma_\theta)\theta_j \quad \text{or} \quad f(\chi_k + s_k) \leq f_j - \gamma_f \theta_j, \\ \forall (\theta_j, f_j) \in \mathcal{F} \cup (\theta_k, f_k),\end{gathered} \tag{5.66}$$

holds, where $\mathcal{F}$ is the set of saved points for the filter, the step is accepted and $\chi_{k+1} = \chi_k + s_k$. If the switching condition,

$$f(\chi_k) - f(\chi_k + s_k) \geq \kappa_\theta \theta(\chi_k)^{\gamma_s}, \tag{5.67}$$

is true, iteration k is classified as a *f-type* step and the trust region expands. The filter is not updated in a *f-type* step, which helps to maintain a decent direction in f near feasibility (small θ). If (5.67) is false, the step is classified as a *θ-type* step, (θ_k,f_k) is added to the filter, and the trust region radius is unchanged. If (5.66) is false, the trial step is not accepted, the trust region shrinks and the step is recomputed. Finally, if a successful step is not found as the trust region shrinks over multiple iterations, the algorithm switches to a restoration phase procedure, which focuses solely on improving feasibility (θ). Additional details for the filter trust region algorithm used in this work are presented by Eason and Biegler (2015).

5.5.2 Adaptive Property Correlations

Steam enthalpies (H), entropies (S) and compressibility factors (Z) are calculated for streams in the steam cycle flowsheet based on the IAPWS IF-97 standard using X Steam, and are a function of temperature (T), pressure (P) and phase. The slope and intercept of

$$r_s(T_s, P_s) = a_s + b_s(\bar{T}_s - T_s) + c_s(\bar{P}_s - P_s) \tag{5.68}$$

are calculated from evaluations of the thermodynamic properties at three points: ($\bar{T}$,$\bar{P}$), (T_1,P_1) and (T_2,P_2). The the latter two points are slight perturbations from the original point. $\bar{T}_s$ and $\bar{P}_s$ are the initial temperature and pressure in stream s. Unlike the steam tables, the RM is differentiable. These linearized steam table models are updated throughout the optimization procedure by refitting at new ($\bar{T}_s, \bar{P}_s$) points as part of the trust region algorithm. Although it is possible to use high order polynomial RM, we empircally observed the best results with (5.68). Finally, the phase specification previously presented, (5.41) - (5.50), are used to restrict the temperature and pressure of each stream.

5.5.3 Optimization Results

Using (5.41) - (5.50) and (5.68), the thermal efficiency of the single reheat regenerative Rankine cycle is maximized. Unlike the results in Section 5.4.2 with Strategy A, the maximum cycle gross thermal efficiency of 34.4% is reasonable, despite being lower than the subcritical plant summarized in Table 5.1 (36.3%, net). Although the maximum steam temperature in this problem is higher (1100 versus 1050 °F), the average boiler wall and secondary superheater temperatures are fixed at 623.2 K (662.1 °F) and 699.8 K (800 °F), respectively. Thus the steam entering the high pressure turbine is substantially cooler with these results. Furthermore, the subcritical reference allow for steam extraction between stage groups on the turbines. For simplicity, however, steam extraction is only considered at two points in between sections of the turbine, HP - IP and IP - LP. Both these factors contribute to a lower thermal efficiency. The reference case, however, includes auxiliary power demands (mills, fans, etc.), which are not considered in this case study. The detailed stream table and loads of each unit are shown in Tables 5.11 and 5.12, respectively.

Table 5.11: Stream data for optimization of Figure 5.12 with linear thermodynamics models using trust region method

Stream	F	T	P	H	Hact	S	Sact
S201	17837.2137	630.0314	165.8278	47.7133	47.7133	–	–
S202	17837.2137	666.2972	161.6821	52.4326	52.4326	–	–
S203	17837.2137	733.3368	161.6821	57.1209	57.1209	–	–
S204	17837.2137	540.8669	38.8037	51.6930	51.6930	0.1119	0.1119
S205	17827.2137	540.8669	38.8037	–	–	–	–
S206	10.0000	540.8669	38.8037	–	–	–	–
S207	10.0000	525.6547	38.0276	50.8252	50.8252	–	–
S208	17827.2137	867.0000	35.6994	66.0119	66.0119	0.1335	0.1335
S209	17827.2137	577.2055	4.9979	55.3606	55.3606	0.1347	0.1347
S210	443.2357	577.2055	4.9979	–	–	–	–
S211	443.2357	428.5321	4.8980	49.6763	49.6763	–	–
S212	453.2357	429.1318	4.8980	49.7016	49.7016	–	–
S213	453.2357	428.7755	4.8000	49.7016	49.7016	–	–
S214	2674.3408	577.2055	4.9979	–	–	–	–
S215	14709.6372	577.2055	4.9979	–	–	–	–
S216	14709.6372	311.2490	0.0425	43.2384	43.2384	0.1430	0.1430
S217	14709.6372	300.2060	0.0425	2.0436	2.0436	0.0071	0.0071
S218	14709.6372	300.4792	5.0000	2.0724	2.0724	0.0072	0.0072
S219	14709.6372	302.7662	4.8000	2.2443	2.2443	–	–
S220	17837.2137	423.5334	4.8000	11.4139	11.4139	0.0332	0.0332
S221	17837.2137	425.3438	179.9347	11.7566	11.7566	0.0332	0.0332
S222	17837.2137	425.4502	172.7373	11.7566	11.7566	–	–
S223	17837.2137	616.2686	165.8278	28.9864	28.9864	–	–
S224	17837.2137	729.9143	155.2148	57.1209	57.1209	0.1108	0.1108
S225	14709.6372	577.0261	4.8480	55.3606	55.3606	0.1349	0.1349
S450	19860.5038	1506.4190	1.0126	-30.828	–	–	–
S451	8813.1104	1506.4190	1.0126	–	–	–	–
S452	8813.1104	1259.3492	1.0126	-40.3794	–	–	–
S453	8813.1104	593.1500	1.0126	-64.1888	–	–	–
S454	11047.3934	1506.4190	1.0126	–	–	–	–
S455	11047.3934	892.0000	1.0126	-53.9344	–	–	–
S456	11047.3934	636.2686	1.0126	-62.7598	–	–	–
SStm1	0.0001	530.9604	38.8037	51.0899	51.0899	0.1108	0.1108
SStm2	0.0001	558.9371	4.9979	54.6807	54.6807	0.1335	0.1335
SStm3	0.0001	312.8647	0.0425	41.6632	41.6632	0.1378	0.1378

Table 5.12: Overall heat balance for steam side of Figure 5.12 with linear thermodynamics models using trust region method

Work from Turbines (MW)	465.0
HP	96.8
MP	189.9
LP	178.3
Pumping Work (MW)	6.5
P200	0.4
P201	6.1
Heat from Boiler (MW)	417.7
Boiler Walls	334.0
Secondary Superheater	83.6
Heat from Flue Gas (MW)	646.8
Primary Superheater	84.2
Reheater	255.3
Economizer	307.3
Heat Rejected (MW)	606.0
Flue Heat Rate (MW)	1325.5

In summary, the adaptive reduced models and trust region approach (Strategy B) presented in this section ensured bounded errors between the reduced models and steam table thermodynamics package X Steam. In contrast with static surrogate models (Strategy A), the optimizer exploits model mismatch to artificially improve the objective function and terminates point infeasible with respect to true steam thermodynamics.

5.6 Hybrid 1D/3D Zonal Boiler Model

In this study a hybrid 1D/3D zonal model developed by Ma et al. (2014) is used for the coal boiler. It requires less than one minute to evaluate, providing a nice balance between speed and accuracy compared to over-simplified equilibrium reactors (inaccurate and computational cheaper) and detailed CFD (high fidelity but expensive). Furthermore, the low computational cost allows for more boiler design variables to be optimized, such as geometry, compared with using expensive CFD simulations given a fixed computational budget. Similarly, when simulating an oxy-fired flowsheet, multiple evaluations of the boiler may be required to converge the recycle loop, as the inlet conditions to the boiler implicitly depends on its outlet.

5.6.1 Surrogate Model

Low computational costs are important because this boiler model, along with CFD models in general, does not supply exact derivatives, which are required for efficient optimization. Instead of directly linking the boiler model to the steam cycle model, a surrogate model is used. The surrogate model is refit during the optimization procedure, as described in Section 5.5. Moderately low computational costs for the boiler model keep the overall costs of the optimization methodology reasonable. In contrast, Edge et al. (2012) construct a static surrogate boiler model from data generated using 3D CFD simulations using nonlinear regression, and do not update the CFD model with new data as part of the simulation methodology. As a result, there is a likely mismatch between their surrogate model and CFD simulations at the final solution. The update procedure used in our methodology avoids this mismatch while maintaining mathematically provable convergence.

Local, linear surrogate models are fit for each outlet of the boiler model, such that

$$y = A(x - x_0) + y_0 \tag{5.69}$$

where x is the vector of boiler inputs, y is the vector of boiler outputs and A contains the fitted coefficients, and x_0 and y_0 are the inlet and outlet values around which the surrogate model is constructed ("center of the trust region", see Section 5.5.1). The boiler model inputs includes the following variables: primary and secondary air temperature (T^p, T^s), flowrate (F^p, F^s) and composition (y^p, y^s); boiler height, width and other geometry measurements; and location of the primary and secondary air inlets. The outputs include the

following variables: heat lost to the wall (Q^{wall}); heat lost to the secondary superheater (Q^{super}); and flue gas temperature (T^f), flowrate (F^f) and composition (y^f).

5.6.2 Zonal Model Details and Validation

In the hybrid zonal mode, the boiler is discretized into N^z user specified vertical zones, as shown in Figure 5.14. Each zone is modeled as a well-stirred reactor and the gas phase is assumed to be in chemical equilibrium. Reaction kinetics are only considered for char oxidation and gasification. Uniform properties (velocity, temperature, etc.) are assumed in each zone, except for radiation intensity, which is calculated using a discrete ordinate method on a 3D mesh consisting of unstructured hexagonal cells (see Figure 5.14). Sample temperature profiles are shown in Figure 5.13. As expected, the gas temperature is uniform in each zone, but the wall temperature varies in multiple dimensions. This is because of the 3D radiative heat transfer calculations. The wall temperature profiles also includes radiant superheaters at the top of the boiler. Additional reheaters, convective superheaters and the economizer are modeled as (convective) heat exchangers (Section 5.2.4). Additional details for this hybrid boiler model are given by Ma et al. (2014).

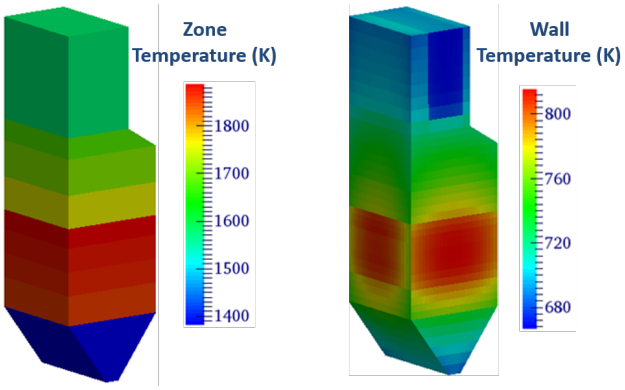

Figure 5.13: Zone and wall temperatures from hybrid boiler model

The hybrid boiler model was validated against air-fired and oxy-fired 3D simulations for an existing utility boiler (PacifiCorp's Hunter 3 unit). Details of the CFD simulations are available in an NETL/Reaction Engineering International (REI) technical report (Adams et al., 2013). Comparisons between this hybrid boiler model and the CFD simulations are summarized in Table 5.13. As expected, the hybrid boiler model's heat losses to the enclosures are less than with the reference CFD model. This occurs because the hybrid boiler model does not include the section beyond the vertical nose plane. This part of the boiler is modeled using convective heat exchange equations (Section 3).

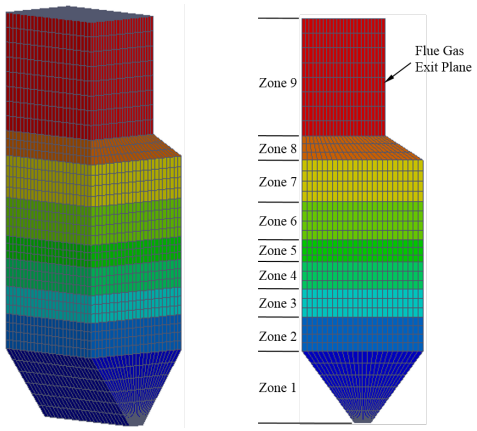

Figure 5.14: 1D zones and 3D mesh for hybrid boiler model

Table 5.13: Comparison between hybrid boiler model and CFD simulations (Ma et al., 2014)

	Air-fired	
	Hybrid Model	CFD Model
Horz. Nose Flue Gas Exit Temp.	1679 K	1674 K
Heat Loss to Wall (Q^{wall})	410.8 MW	436.0 MW
Heat Loss to Platen Superheater (Q^{sup})	101.8 MW	102.8 MW
	Oxy-fired	
	Hybrid Model	CFD Model
Horz. Nose Flue Gas Exit Temp.	1628 K	1656 K
Heat Loss to Wall (Q^{wall})	393 MW	403 MW
Heat Loss to Platen Superheater (Q^{sup})	98.9 MW	109 MW

5.7 Case Study: Air-Fired Steam Cycle

In the final case study, we consider optimization of a double reheat regenerative steam cycle, shown in Figure 5.15, which is more representative of a green-field oxycombustion or supercritical power plant than the demonstration system presented in Section 5.4.1. Consistent with the supercritical reference plant for the CCSI project (CCSI, 2013), nine uncontrolled steam extractions and ten turbine sections (two high pressure, four intermediate pressure and four low pressure) are included. Furthermore, air heaters are considered in this case study, unlike the demonstration system from Section 5.4.1. Using the models and methods presented in this chapter, the double reheat regenerative Rankine cycle is optimized with fixed boiler input/outputs. See Table 5.14 for a common set of assumptions.

5.7.1 Reference Case

As expected, the optimizer selects the highest possible temperature, 1100° F (upper bound), for the reheater steam outlets to maximize efficiency. Similarly,

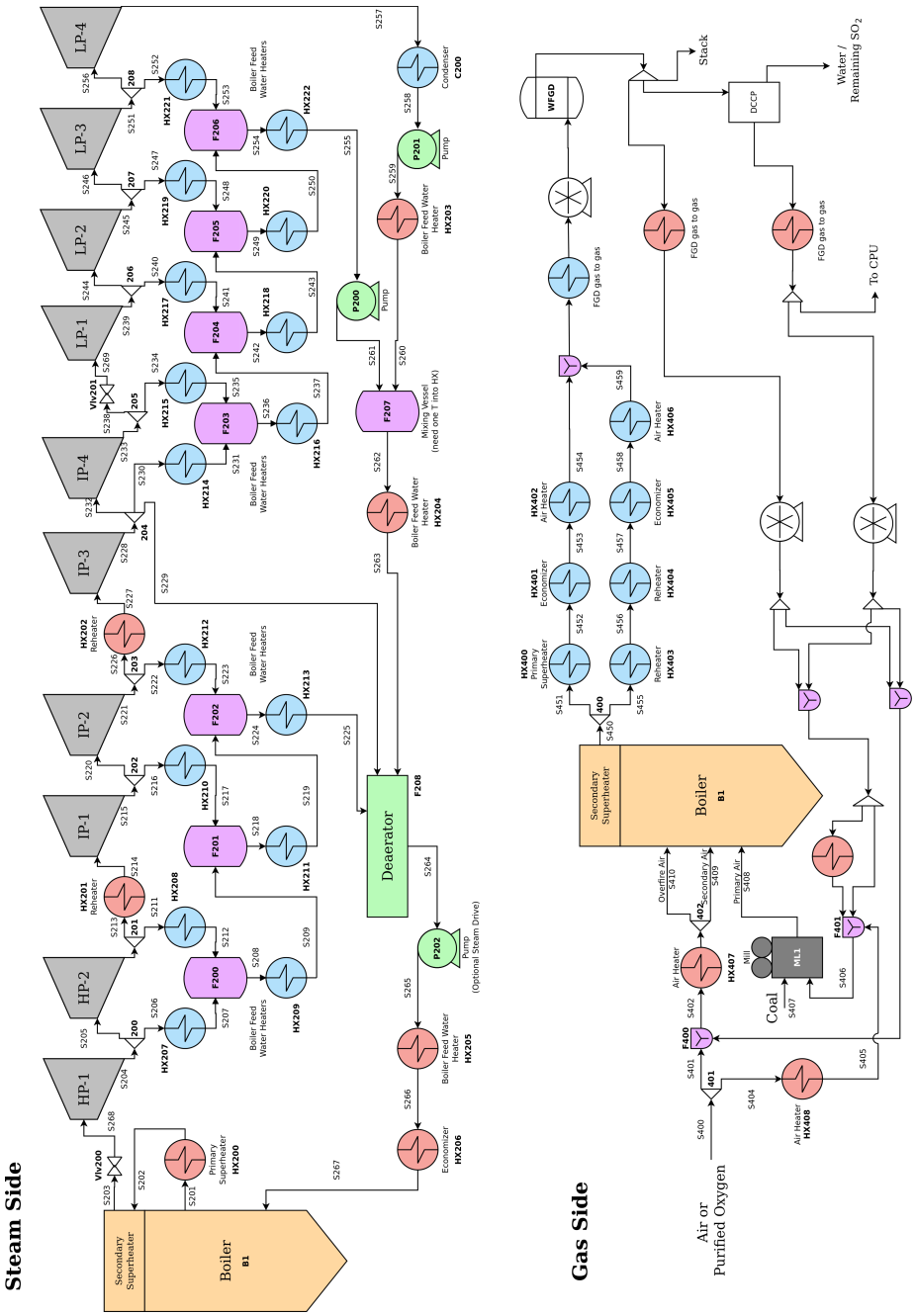

Figure 5.15: Steam Cycle Flowsheet. Streams and equipment without numbers/labels are excluded from the air-fired case studies, but will be considered for oxycombustion systems (future work).

a high steam pressure of 211.2 bar is selected in the boiler walls, which results in a gross thermal efficiency of 42.5% for the optimized cycle. This is significantly higher than the 39.3% net efficiency reported in Table 5.3 for the supercritical reference. One portion of the difference is related to gross versus net efficiency; the optimized steam cycle does not consider auxiliary power loads (e.g., fans,

Table 5.14: Assumptions and Bounds for Demonstration Rankine Cycle Efficiency Maximization

Steam Stream Classifications	
Liquid Only	S255, S258 - S263
Vapor Only	S215-S225, S226-S254 S256, S269
Saturated	S257, S264
Liquid or Supercrit.	S265 - S267
Vapor or Supercrit.	S201 - S214, S268

Gas Side Bounds	
Air Heater Exits (HX402 & HX406)	$T \geq 150$ °C

Steam Side Bounds	
All Steam Streams	$0.068 \leq P \leq 242.3$ bar 289 K $\leq T \leq$ 867 K
Steam Extraction	$F \geq 10$ mol/s

Steam Side Pressure Drops	
Prim. Super -heater (HX200)	2.5 %
Reheaters (HX201 & HX202)	8 %
Feed Water Heaters (HX203 - HX205)	4 %
Economizer (HX206)	4 %
Feed Water Heaters (HX207 - HX222)	2 %
Throttle Valve (Vlv200)	4 %
IP/LP Crossover (Vlv201)	3 %

mills, cooling water pumps, etc.). In the reference design (Table 5.1), 580.4 MWe (gross) are produced by the steam turbine, but 30.4 MWe are required run auxiliary systems (including 5.5 MWe for the condensate and circulating pumps). If 25 MWe is assumed for auxiliary loads in the optimized system, the net efficiency is 40.7%. The remaining 1.4 percentage point difference in net efficiency may be attributed to the additional reheat (double versus single), different turbine isentropic efficiencies, and additional steam extraction locations in the optimized system. The heat balance and detailed stream data for the optimized cycle are given in Tables 5.15 and 5.16. The composite curves for each heat integration zone (except the condenser) are shown in Figure 5.16. Each zone, except the condenser, is completely self integrated and requires no external utilities. The condenser zone, however, is specified to contain no cold streams (no heating units), and all cold utility is supplied by cooling water. This restriction does not miss any integration opportunities, as the condenser is both the coldest part of the steam cycle and has a large cooling demand, about 600 MWt.

Table 5.15: Overall heat balance for steam side of Figure 5.3

Work from Turbines (MW)	572.9
HP	78.0
IP	269.4
LP	225.6
Pumping Work (MW)	9.1
P200	0.2
P201	0.5
P202	8.3
Heat from Boiler (MW)	417.7
Boiler Walls	334.0
Sec. Superheat.	83.6
Heat from Flue Gas (MW)	663.0
Prm. Superheat.	86.6
Reheater (HX201)	233.8
Reheater (HX202)	192.0
Economizer	150.7
Heat Rejected (MW)	514.4
Flue Heat Rate (MW)	1325.5

Table 5.16: Stream data for optimization of Figure 5.3 with fixed boiler operating conditions

Stream	F	T	P	H	H^{act}	S	S^{act}
S201	17984.3734	629.3815	165.2875	47.6609	47.6609	–	–
S202	17984.3734	666.4665	161.1553	52.4773	52.4773	–	–
S203	17984.3734	733.1675	161.1553	57.1272	57.1272	–	–
S204	17984.3734	612.1755	69.6511	53.7474	53.7474	0.1113	0.1113
S205	17974.3734	612.1755	69.6511	–	–	–	–
S206	10.0000	612.1755	69.6511	–	–	–	–
S207	10.0000	610.8390	68.2581	53.7474	53.7474	–	–
S208	20.0000	548.0554	22.3009	53.2698	53.2698	–	–
S209	20.0000	547.4152	21.8549	53.2698	53.2698	–	–
S210	17974.3734	579.4998	54.1482	52.7922	52.7922	0.1115	0.1115
S211	10.0000	579.4998	54.1482	–	–	–	–
S212	10.0000	578.2503	53.0652	52.7922	52.7922	–	–
S213	17964.3734	579.4998	54.1482	–	–	–	–
S214	17964.3734	867.0000	49.8163	65.8043	65.8043	0.1305	0.1305
S215	17964.3734	704.0260	18.1041	59.7886	59.7886	0.1311	0.1311
S216	10.0000	704.0260	18.1041	–	–	–	–
S217	10.0000	703.7879	17.7421	59.7886	59.7886	–	–
S218	30.0000	582.8357	7.9197	55.4427	55.4427	–	–
S219	30.0000	582.6040	7.7613	55.4409	55.4409	–	–
S220	17954.3734	704.0260	18.1041	–	–	–	–
S221	17954.3734	590.3121	7.9197	55.7261	55.7261	0.1315	0.1315
S222	10.0000	590.3121	7.9197	–	–	–	–
S223	10.0000	575.7700	7.7613	55.1818	55.1818	–	–
S224	40.0000	580.8949	7.7613	55.3761	55.3761	–	–
S225	40.0000	541.6704	7.6060	53.8921	53.8921	–	–
S226	17944.3734	590.3121	7.9197	–	–	–	–
S227	17944.3734	867.0000	7.2861	66.4232	66.4232	0.1471	0.1471
S228	17944.3734	797.1057	4.8000	63.7069	63.7069	0.1473	0.1473
S229	10.0000	797.1057	4.8000	–	–	–	–
S230	254.9020	797.1057	4.8000	–	–	–	–
S231	254.9020	797.0616	4.7040	63.7069	63.7069	–	–
S232	17679.4714	797.1057	4.8000	–	–	–	–
S233	17679.4714	738.1888	3.2879	61.4629	61.4629	0.1475	0.1475
S234	77.5982	738.1888	3.2879	–	–	–	–
S235	77.5982	738.1511	3.2221	61.4629	61.4629	–	–
S236	332.5003	781.5018	0.3845	63.1832	63.1832	–	–
S237	332.5003	781.4981	0.3768	63.1832	63.1832	–	–
S238	17601.8732	738.1888	3.2879	–	–	–	–
S239	17601.8732	587.8956	1.0093	55.9238	55.9238	0.1489	0.1489
S240	3973.8402	587.8956	1.0093	–	–	–	–
S241	3973.8402	587.8729	0.9891	55.9238	55.9238	–	–
S242	4306.3405	602.6090	0.3768	56.4844	56.4844	–	–
S243	4306.3405	602.6012	0.3693	56.4844	56.4844	–	–
S244	13628.0330	587.8956	1.0093	–	–	–	–
S245	13628.0330	480.3554	0.3768	52.1078	52.1078	0.1499	0.1499
S246	13610.3163	480.3554	0.3768	–	–	–	–
S247	17.7167	480.3554	0.3768	–	–	–	–
S248	17.7167	480.3388	0.3693	52.1078	52.1078	–	–
S249	4324.0572	602.1088	0.3693	56.4664	56.4664	–	–
S250	4324.0572	602.1010	0.3619	56.4664	56.4664	–	–
S251	13610.3163	403.0911	0.1634	49.4345	49.4345	0.1508	0.1508
S252	1919.0673	403.0911	0.1634	–	–	–	–
S253	1919.0673	403.0764	0.1601	49.4345	49.4345	–	–
S254	6243.1244	541.9240	0.1601	54.3049	54.3049	–	–
S255	6243.1244	324.7141	0.1569	3.8891	3.8891	0.0130	0.0130
S256	11691.2490	403.0911	0.1634	–	–	–	–
S257	11691.2490	330.2060	0.0425	46.0405	46.0405	0.1523	0.1523
S258	11691.2490	300.2060	0.0425	2.0436	2.0436	0.0071	0.0071
S259	11691.2490	300.4792	5.5786	2.0733	2.0733	0.0072	0.0072
S260	11691.2490	300.4841	5.3554	2.0733	2.0733	–	–
S261	6243.1244	324.9872	5.3554	3.9177	3.9177	0.0131	0.0131

Continued on next page

Table 5.16: Stream data for optimization of Figure 5.3 with fixed boiler operating conditions

Stream	F	T	P	H	H^{act}	S	S^{act}
S262	17934.3734	309.0130	5.3554	2.7154	2.7154	–	–
S263	17934.3734	421.8535	5.1412	11.2900	11.2900	–	–
S264	17984.3734	424.5131	4.8000	11.4139	11.4139	0.0332	0.0332
S265	17984.3734	425.3376	179.3485	11.7554	11.7554	0.0332	0.0332
S266	17984.3734	536.4227	172.1745	20.7097	20.7097	–	–
S267	17984.3734	616.9185	165.2875	29.0872	29.0872	–	–
S268	17984.3734	729.7522	154.7091	57.1272	57.1272	0.1108	0.1108
S269	17601.8732	738.1322	3.1892	61.4629	61.4629	0.1477	0.1477
S400	17662.3265	298.1500	1.3000	-3.66185	–	–	–
S401	14242.9410	298.1500	1.3000	–	–	–	–
S402	14242.9410	298.1500	1.3000	-3.66185	–	–	–
S403	14242.9410	548.7060	1.3000	3.6325	–	–	–
S404	3419.3856	298.1500	1.3000	–	–	–	–
S405	3419.3856	338.7060	1.3000	-2.5191	–	–	–
S406	3419.3856	338.7060	1.3000	-2.5191	–	–	–
S408	3419.3856	338.7060	1.3000	0	–	–	–
S409	9998.0670	548.7060	1.3000	–	–	–	–
S410	4244.8740	548.7060	1.3000	–	–	–	–
S450	19860.5038	1506.4190	1.0126	-30.828	–	–	–
S451	3330.5448	1506.4190	1.0126	–	–	–	–
S452	3330.5448	809.7225	1.0126	-56.8357	–	–	–
S453	3330.5448	646.7770	1.0126	-62.4088	–	–	–
S454	3330.5448	423.1500	1.0126	-69.6382	–	–	–
S455	16529.9590	1506.4190	1.0126	–	–	–	–
S456	16529.9590	1506.4190	1.0126	-30.828	–	–	–
S457	16529.9590	816.9928	1.0126	-56.5816	–	–	–
S458	16529.9590	581.4540	1.0126	-64.5733	–	–	–
S459	16529.9590	423.1500	1.0126	-69.6382	–	–	–
SStm1	0.0001	606.8166	69.6511	53.4335	53.4335	0.1108	0.1108
SStm2	0.0001	577.7825	54.1482	52.6919	52.6919	0.1113	0.1113
SStm3	0.0001	694.2670	18.1041	59.4046	59.4046	0.1305	0.1305
SStm4	0.0001	583.2696	7.9197	55.4592	55.4592	0.1311	0.1311
SStm5	0.0001	793.1768	4.8000	63.5539	63.5539	0.1471	0.1471
SStm6	0.0001	734.1046	3.2879	61.3069	61.3069	0.1473	0.1473
SStm7	0.0001	569.4213	1.0093	55.2532	55.2532	0.1477	0.1477
SStm8	0.0001	466.7703	0.3768	51.6297	51.6297	0.1489	0.1489
SStm9	0.0001	393.0701	0.1634	49.0883	49.0883	0.1499	0.1499
SStm10	0.0001	310.0000	0.0425	45.5864	45.5864	0.1508	0.1508

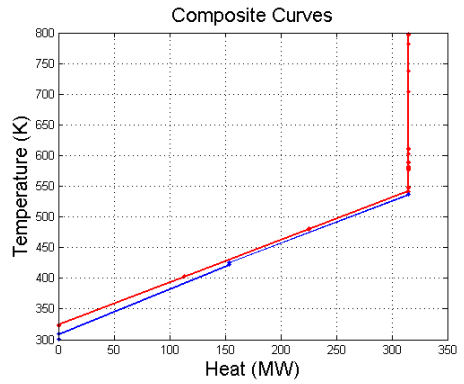

(a) Zone 1: Feed Water Heaters

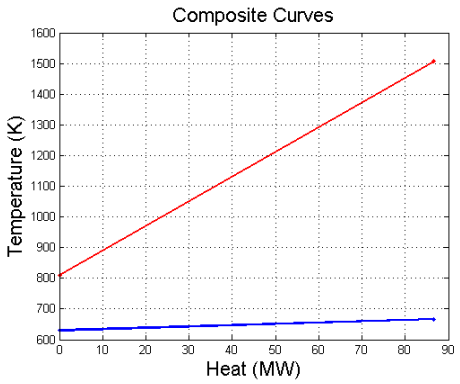

(b) Zone 3: Primary Superheater

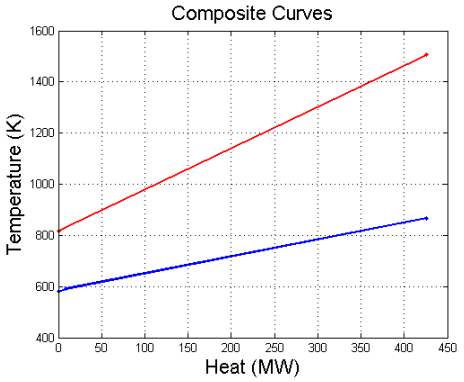

(c) Zone 4: Reheaters

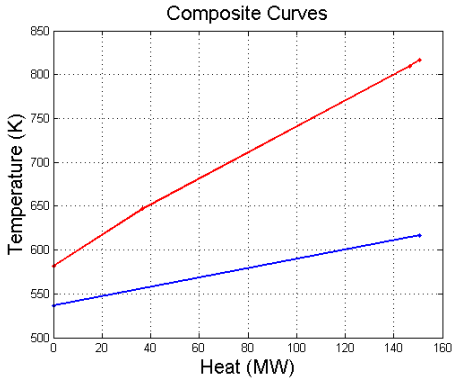

(d) Zone 5: Economizer

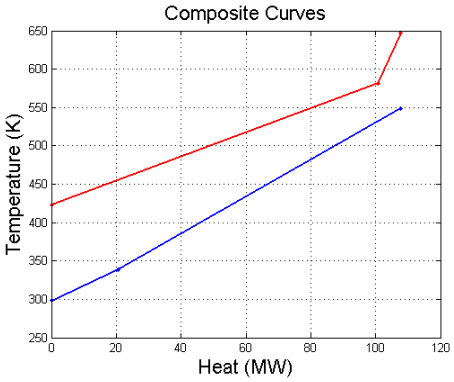

(e) Zone 6: Air Heater

Figure 5.16: Composite Curves for Each Heat Integration Zone

5.7.2 Utilization of Waste Heat

Using methods developed in this chapter, the double reheat regenerative Rankine cycle (Figure 5.15) is reoptimized with 2.5 to 12.5 MWt of waste heat at 50 °C, which results in cycle designs with increased net power outputs (0.28 to 0.88 MWe, respectively). The composite curves in Figure 5.16 show that this low grade heat may only be used with some feedwater heaters, and as consequence, at most 11.3% of the waste heat is converted into useful shaft work. As expected, the optimizer uses the low grade heat to reduce the amount

of extracted steam in the low pressure section (S230, S234, S240, S247 and S252) from 34.8% to 33.6% of the total steam flowrate, as shown in Figure 5.17. Thus, 71 - 78% of the additional power output comes from turbine stage groups IP4 through LP4. For all of the waste heat cases, the optimizer selected the same steam overall steam flowrate and maximum pressure (see Table 5.16). Furthermore, Figure 5.18 shows diminishing returns for utilization of 50 °C beyond 7.5 MWt. For this systems, no more than 10 MWt of 50 °C waste heat may be converted into useful shaft work.

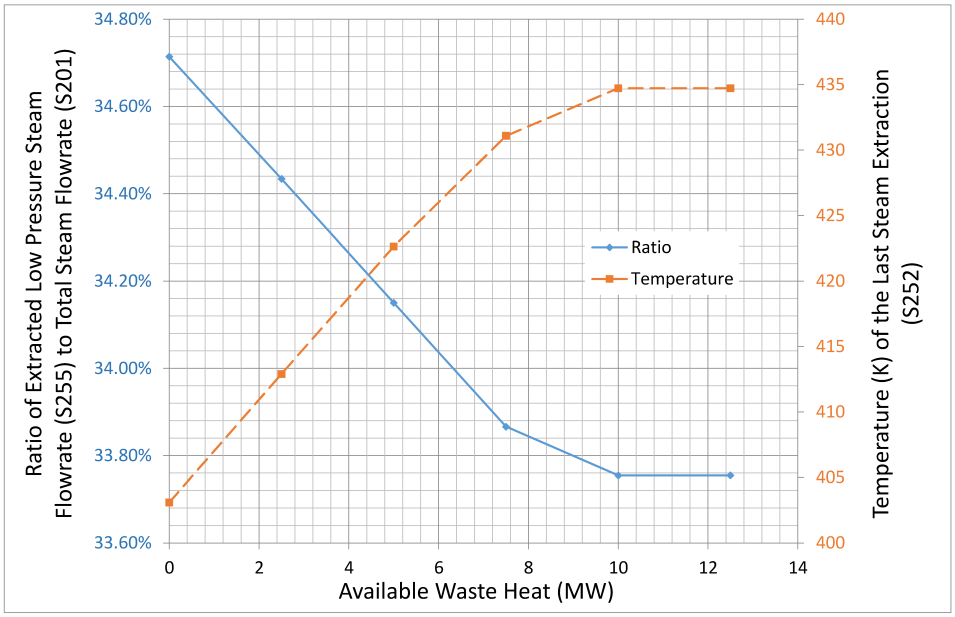

Figure 5.17: Impact of waste heat integration on the low pressure steam extraction

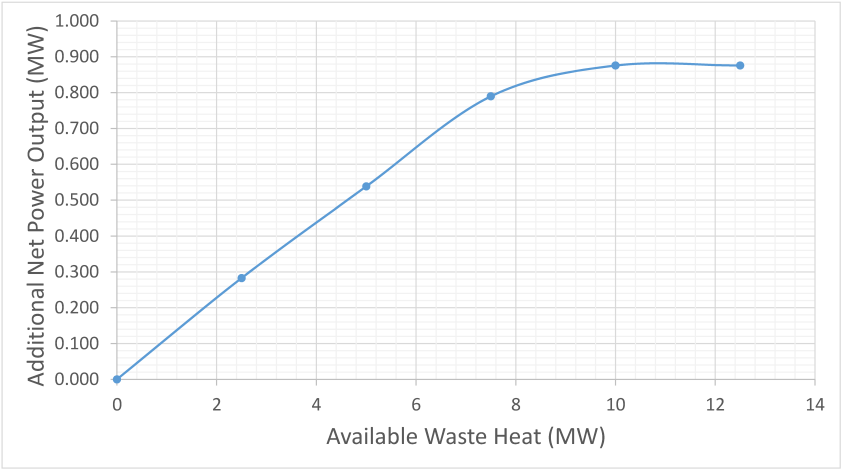

Figure 5.18: Additional power production as a function of available low grade (50 ° C) waste heat

The low utilization of waste heat is in part due to the fixed temperature assumptions for the boiler walls and secondary superheater. If the boiler operating conditions are considered as additional degrees of freedom, it is likely the maximum amount and efficiency of waste heat utilization will increase. Nevertheless, this case study demonstrates the flexibility of the models and methods to systematically redesign a steam cycle that optimally utilizes waste heat. It serves as a precursor to optimization of an integrated oxycombustion system in which waste heat from inter-stage cooling of compressors for the air separation unit (ASU) and CO_2 processing unit (CPU) is utilized in the steam cycle.

5.8 Conclusions and Future Directions

In this chapter, extensions of the equation-based flowsheet optimization framework for steam cycle design are proposed and demonstrated. Unlike the previous systems considered, analytic derivatives are not available for two crucial elements of high-fidelity steam cycle models: steam table thermodynamic lookups and computational fluid dynamics based furnace simulations. Two strategies to embed these types of models are examined. In Strategy A, nonlinear surfaces are proposed and fit for steam enthalpy, entropy and compressibility as a function of temperature and pressure. This approach is inspired previous CHP design studies that use approximate regression based thermodynamics models. Sigmodial functions are used to model the sharp transition from vapor to liquid properties along the saturation curve, which avoids piecewise models. The maximum errors for physical property predictions are approximately 10% and occur near the saturation curve. In a small single reheat regenerative Rankine cycle, the optimization routine exploits these physical property model errors to design a system with a predicted thermal efficiency above 80%. These results are nonphysical and infeasible regarding the original steam table model. For example, entropy, as calculated using steam table lookups, is destroyed in some of the turbine sections.

This case study highlights a major concern with data driven algebraic surrogate models, namely that the optimization routine exploits model inaccuracies, and motivates Strategy B. Instead of considering static surrogate models that are fit over a large P-T space, local linear adaptive models are fit for the physical properties of each steam stream. These models are then updated during optimization with a trust region algorithm. Unlike Strategy A, this approach ensures accuracy of the fit reduced models within a specified tolerance. A filter method is used to incorporate the equation-based equipment models (e.g., mass and energy balances, efficiency calculations, etc.), which maintains the computational efficiency provided by accurate derivative information for these constraints. Both single and double reheat regenerative Rankine cycle are optimized with Strategy B, which produces physically realistic steam cycle designs with gross electrical efficiencies of 34.4% and 42.5%, respectively. Finally, the flexibility of the methodology is demonstrated by reoptimizing

the double reheat system with varying amounts of waste reheat, which is substituted for low grade waste heat for extracted steam used in the feedwater preheaters, and boosts the low pressure turbine section power output and cycle efficiency.

The methods in this chapter lay the foundation for optimization of the steam cycle in an oxycombustion power generation systems. Ongoing work includes extension of the trust region algorithm to consider optimization of a steam cycle with boiler operating conditions (temperature, pressure and inlet air composition, etc.) considered as additional degrees of freedom. In place of a full-scale CFD, the hybrid 1D/3D zonal boiler model (Section 5.6) will be considered. This will allow several key design variables, include flue gas recycle rate and composition, ASU product O_2 purity and CPU inlet CO_2 purity to be optimized. Finally, integration of waste heat from compressor inter-stage cooling into the steam cycle will be considered, similar to Section 5.7.2.

One downside of Strategy B is the significant number of trust region iterations required to converge steam thermodynamics for some systems. Furthermore, for the waste reheat integration problem discussed in Section 5.7.2, the optimization results are heavily dependent on the initial point, thus the thermal efficiency maximization was resolved from several starting points. These two factors, high iteration counts and local solutions, may be problematic for optimization of oxy-fired systems with expensive boiler model evaluations. Instead, it may be beneficial to revisit Strategy A with alternate steam thermodynamics models that exhibit thermodynamic consistency properties, such as $\left(\frac{\partial H}{\partial T}\right)_P \geq 0$. Similarly, although the cubic equation of state model for water proposed by Valderrama and Vargas (2003) exhibit average property prediction errors of 2%, it may possess necessary consistency properties to prevent entropy destruction in turbines and other nonphysical features cycle designs from Section 5.3. Accuracy concerns can be further mitigated using a two step process, where the flowsheet is first optimized with the water cubic EoS thermodynamics model. Next, the solution would be refined using the trust region algorithm and steam table lookups. Ultimately, using a static model for steam thermodynamics should drastically reduce the computational expense of converging the steam cycle optimization problems compared to the trust region filter method. Such a model needs to be carefully chosen, otherwise the optimizer will exploit thermodynamic model errors and find too-good-to-be-true solutions that violate physics.

Finally, this chapter is limited to on-design (i.e., full capacity) operation, and both off-design and dynamics are left as future work. In principle, flexible operation may be considered by formulating a two-stage stochastic programming problem. Scenarios would be associated with different operating conditions, such as power output capacity (for load following) or fuel type. Such a formulation would optimize both design point (i.e., turbine full capacity) and off-design operations, thus ensuring sufficient flexibility for the anticipated operating scenarios. This requires a sufficiently detailed model for off-design

turbine performance, such as the Turbine Hardware Model (Mavromatis and Kokossis, 1998a,b) or correlations of Spencer, Cotton, and Cannon (1963), which are reviewed in Sections 5.2.1.1 and 5.2.1.2. Neither of these models are ideal, however, as the THM is intended for combined heat and power systems, and the SCC model is based on power plant turbine efficiency data from the 1960s.

Future work should also consider additional design trade-offs. For example, in combined heat and power systems, steam is required at specified pressures to supply heat for separations and chemical reactors. Governing stages are used to ensure constant pressure of this extracted steam under load (and steam flowrate) variations, but with a penalty to turbine efficiency. In contrast, steam extractions for feedwater preheating in power systems are uncontrolled, and the pressure varies for off-design operation. Thus there is a trade-off between constant pressure extracted steam and turbine efficiency. For most CHP systems, such as large integrated chemical manufacturing facilities and oil refineries, controlled extractions are the correct design choice. Requiring all steam consuming unit operations to acceptable variable steam pressure (and temperature) utilities involves too many design and control challenges. However, for Integrated Gasification Combined Cycle (IGCC) power plants with carbon capture and other systems with only several steam consuming unit operations, it may be beneficial to consider some uncontrolled extractions for steam utility levels in exchange for increased turbine section efficiencies. Mathematically, this design decision may be formulated as an integer program with binary variables for the selection of governing stages (controlled versus uncontrolled extraction). Such an endeavor, however, requires detailed models for governing stage performance.

Chapter 6

Initialization and Other Implementation Details

Key Contributions and Results:

- Present detailed formulations for the NLPs solved in each step of the initialization procedure
- Demonstrate the efficacy of the multi-start approach with the ASU optimization case study
- Introduce *Degeneracy Hunter*, a diagnostic tool to identify irreducible sets of linearly dependent constraints
- Show the benefits *Degeneracy Hunter* in a case study where degenerate equations are identified and removed from the ASU models

For many optimization problems, formulation is as or more important than the algorithms used to solve them, and for most complex nonlinear programs, careful initialization is essential. This chapter focuses on three areas of implementation crucial to the proposed framework for flowsheet optimization:

1. Development of a systemic initialization routine
2. Use of multi-start strategies to identify multiple locally optimal solutions
3. Refinement of the models to avoid degenerate equations, which severely degrade solver performance

These elements transform the mathematical models presented in Chapters 2 to 5 into a useful tool for process design and optimization.

6.1 Systematic Initialization Strategy

Model refinement is used to initialize highly nonlinear parts of the flowsheet model, as shown in Figure 6.1. The flowsheet is first optimized with simpler, less nonlinear models (cascade approximation, ideal gas/liquid thermodynamics). Model complexity is increased in subsequent NLP problems with

the eventual optimization of the flowsheet with cubic EoS thermodynamics, MESH cascade models and many heat exchange subunits. Six detailed initialization steps used for the framework are introduced in Chapter 1. This idea of model refined is similar to the procedures employed by Kossack, Kraemer, and Marquardt (2006) and others.

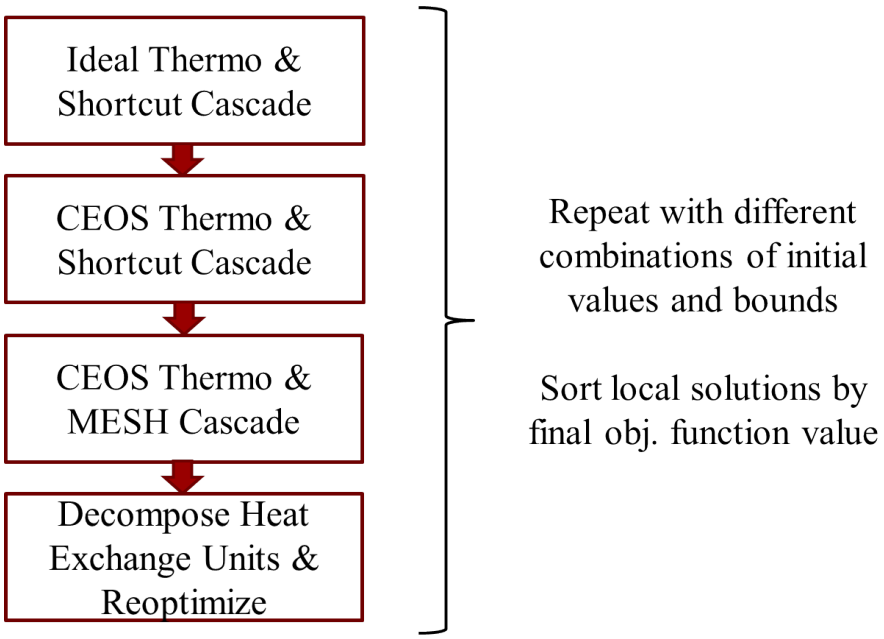

Figure 6.1: Initialization Procedure

In the remainder of this section, the NLPs from each step of the initialization procedure are documented, and best practices are shared. $\tilde{f}$, $\tilde{x}$, $\tilde{T}$ and $\tilde{P}$ represent target values (constants) used in some of the initialization NLPs.

Step 0: Load Point and Stream Initialization

The first step is to initialize the essential stream properties: flowrate, mole fraction, temperature and pressure. The preferred option is to load these values from a stored solution, either generated from earlier optimization runs, intuition or a commercial flowsheet simulator[1]. An optional mass balance NLP, shown below, may be solved to initialize flowrates and compositions. The goal of this problem is to ensure feasibility of the material balances while maintaining non-zero flow in all streams. If no guess for stream properties are provided, the flowrate and composition targets, $\tilde{f}_{s,c}$ and $\tilde{x}_{s,c}$, are set to the feed specification for all streams in the flowsheet. If an initial point is provided, $\tilde{f}_{s,c}$ and $\tilde{x}_{s,c}$ are set to the values in the initial point.

[1]The GAMS code includes the ability to load these stream values (indirectly) from a text file, which can be assembled in a spreadsheet computer program.

$$\min \quad \sum_{c\in\mathcal{C}}\sum_{s\in\mathcal{S}} \left(f_{s,c} - \tilde{f}_{s,c}\right)^2 + 10\left(x_{s,c} - \tilde{x}_{s,c}\right)^2$$

s.t. Flowsheet Connectivity
Stream Models (2.21)
Mole Balances (2.55a) & (4.1a)
Product Recovery and/or Purity Calculations

Experience has shown it is effective to use this mass balance NLP and the subsequent steps to generate initial flowsheet optimization results. In subsequent solves these results should be loaded, bypassing the mass balance NLP and skipping this step. The mass balance NLP is also useful when streams and/or units are added to the flowsheet, and only a partial initial point is available.

Step 1, Part A: Initialization of Cascade Variables with Simple Thermodynamics

In Step 1, the system is optimized with the shortcut cascade model (if it contains any cascade sections) and ideal gas thermodynamics. Before this, an optional NLP may be solved to initialize only the shortcut cascade variables, which are some of the most nonlinear aspects of the simple flowsheet models. This step helps find cascade variable values (such as number of trays) that match the inlet and outlet stream properties.

$$\mathcal{E}_S := \{s|(s,e) \in \mathcal{E}_{in}^V \cup \mathcal{E}_{in}^L \cup \mathcal{E}_{out}^V \cup \mathcal{E}_{out}^L \ \forall e \in \mathcal{E}\}$$

$$\min \quad \sum_{s\in\mathcal{E}_S}\left[\sigma_s^V + \sigma_s^L + 0.1\left(T_s - \tilde{T}_s\right)^2 + 0.1\left(P_s - \tilde{P}_s\right)^2 + 0.1\sum_{c\in\mathcal{C}}\left(f_{s,c} - \tilde{f}_{s,c}\right)^2\right]$$

s.t. Flowsheet Connectivity
Stream Models (2.21)
Simple Thermodynamics (2.23) - (2.25)
Shortcut Cascade Model (4.1) - (4.4)

Step 1, Part B: Flowsheet Optimization with Simple Thermodynamics and Cascade Shortcut Model

The flowsheet is then optimized with the simple thermodynamic model, cascade shortcut model and constant heat capacity heat exchange units. The solution of this problem provides reasonable temperatures, pressures, composition and flowrates used to initialize variables in the highly nonlinear cubic EoS model. Optionally, this step may be skipped (which was preferred for the CPU case study).

min or max flowsheet objective function
s.t. Flowsheet Connectivity
Stream Models (2.21) & (2.22)
Thermodynamics Models (2.23) - (2.25)
Equipment Models (2.55), (2.56), (2.58) - (2.60)
Heat Integration Models (3.1) - (3.3), (3.5) - (3.8)
Distillation Cascade Models (4.1) - (4.4)
Purity and/or Recovery Constraints
Additional Problem Specific Constraints

Step 2: Initialization of Cubic EOS Variables

Initialization of cubic EoS variables is essential for robust flowsheet convergence. For example, initializing Z with the incorrect phase typically leads to infeasible solutions or violations of the complementarity constraints (2.22)[2]. Reliable initialization is done with logic for phase detection, analytic calculation of Z (Adewumi, 2014) and two optimization problems. $\tilde{F}$, $\tilde{x}$, $\tilde{T}$ and $\tilde{P}$ are initialized using the solution from Step 1 (or initial point is Step 1 is skipped). The first NLP,

$$\mathcal{S}_\sigma := \{s \in \left(\mathcal{S}_{Vap}^{Flash} \cup \mathcal{S}_{Liq}^{Flash}\right) \setminus \left(\mathcal{S}_{shdw}^{V} \cup \mathcal{S}_{shdw}^{L}\right) | \tilde{F}_s > 0\}$$

$$\min \quad \sum_{s \in \mathcal{S}_\sigma} \left[\sigma_s^V + \sigma_s^L + 100\left(T_s - \tilde{T}_s\right)^2 + 10\left(P_s - \tilde{P}_s\right)^2 + 10\sum_{c \in \mathcal{C}} (x_{s,c} - \tilde{x}_{s,c})^2\right]$$

s.t. Stream Models (2.21)
Cubic EoS Thermo. Model (2.26) - (2.29)
"Lite" Equipment Model (2.56), (2.59a), (2.60a) - (2.60d), (2.61d), (2.61e), (2.66b), (2.66c)

ensures feasibility of the base cubic EoS models. Next, T is initialized for streams in $\mathcal{S}_{shdw}^V$ and $\mathcal{S}_{shdw}^L$ using twenty iterations of Newton's method (manually programmed in GAMS) to converge Antoine's equation for bubble and dew point calculations. An optional NLP (not shown) may then be solved to converge only the bubble and dew point calculations and shadow stream equations with the cubic EoS model: (2.37), (2.38), (2.50), (2.51), (2.52d) and (2.52e). The second major NLP for Step 2,

[2]Initializing Z such that $Z > \bar{Z}$ for liquid streams or $Z < \bar{Z}$ for vapor streams where $F > 0$ typically leads to complementarity violations. However, such an initialization for Z may be required in the single root region to find feasible solutions.

$$\min \quad \sum_{s \in \mathcal{S}_\sigma} \left[\sigma_s^V + \sigma_s^L + 100 \left(T_s - \tilde{T}_s \right)^2 + 10 \left(P_s - \tilde{P}_s \right)^2 + 10 \sum_{c \in \mathcal{C}} \left(x_{s,c} - \tilde{x}_{s,c} \right)^2 \right]$$

s.t. Stream Models (2.21)
Cubic EoS Thermo. Model (2.26) - (2.40), (2.43) (2.46), (2.49) - (2.52e)
"Lite" Equipment Model (2.56), (2.59a), (2.60a) - (2.60d), (2.61d), (2.61e), (2.66)
Splitter Model, i.e., copy intrinsic props. from inlet to outlet streams

is solved to initialize property calculations with the cubic EoS model. Optionally, vapor-liquid equilibrium calculations, i.e., (2.57) or (2.58), are included in the second NLP (above). CONOPT is used first to solve both NLPs. If CONOPT terminates at either an infeasible point or solution with an objective function greater than a tolerance (e.g., $O(10^{-10})$), the NLPs are resolved with IPOPT. Experience shows IPOPT tends to find better solutions than CONOPT if started from good initial point (near feasible constraints). Overall, Step 2 of the initialization procedure is very important to ensure success with the additional steps.

Step 3: Reoptimization with cubic EoS thermodynamics and cascade shortcut model

After initialization of the cubic EoS variables, the flowsheet is reoptimized using cubic EoS thermodynamics and the cascade shortcut model:

min or max flowsheet objective function
s.t. Flowsheet Connectivity
Stream Models (2.21) & (2.22)
Cubic EoS Thermo. Models (2.26) - (2.46), (2.49) - (2.52)
Equipment Models (2.55) - (2.57), (2.59), (2.60)
Compressor and Pump Models (2.61) - (2.67)
Heat Integration Models (3.1) - (3.3), (3.5) - (3.8)
Distillation Cascade Models (4.1), (4.2), (4.5)
Purity and/or Recovery Constraints
Additional Problem Specific Constraints

Optionally, (2.57) may be replaced with (2.58).

Step 4: Initialization of MESH Cascade Variables and Flowsheet Reoptimization

Next, the MESH cascade variables are initialized using results from the shortcut model and linear interpolation. The cubic EoS variables for the cascade streams are then initialized by solving an optimization problem similar to Step 2. Finally the flowsheet is reoptimized:

min or max flowsheet objective function
s.t. Flowsheet Connectivity

Stream Models	(2.21) & (2.22)
Cubic EoS Thermo. Models	(2.26) - (2.46), (2.49) - (2.52)
Equipment Models	(2.55) - (2.57), (2.59), (2.60)
Compressor and Pump Models	(2.61) - (2.67)
Heat Integration Models	(3.1) - (3.3), (3.5) - (3.8)
Distillation Cascade Models	(4.10) - (4.14)
Purity and/or Recovery Constraints	
Additional Problem Specific Constraints	

The NLP for Step 5 (above) is resolved, typically two to four times (user specified), and ε^s is shrunk by an order of magnitude between each solve. Furthermore, the MESH superstructure is adjusted and resized, as described in Section 4.4.2.

Step 5: Initialization of Subheat Exchange Units

Step 5 is the most complex of the initialization routine. Each heat exchange unit is decomposed into a series of N^{sub} subunits (where N^{sub} is a user-specified constant, typically four to ten). Equations indexed over the original/large heat exchange units are deactivated, and instead evaluated for subunits. New substreams are automatically assigned and properties are initialized using interpolation and/or analytic formulas. Pressure drop coefficients are propagated from the original units to their subunits. Finally, temperatures for each substream are fixed (for now) to ensure equal temperature spacing of subunit outlets in each series. Then, the following procedure is used to initialize vapor-liquid equilibrium for the subunits' outlets:

1. Set $n = 1$, where n is a counter. Fix the pressure of the inlet and outlet streams for the large units
2. Fix the component flowrates for the inlet streams of the n^{th} subunit in each series
3. Place the inlet and outlet streams for the n^{th} subunit in each series in $\mathcal{S}^{act}$, and disable all other streams and units. Set $i = 1$ and select CONOPT as the solver
4. Solve the NLP below to initialize vapor liquid equilibrium for the "active" outlet streams
5. If $\psi < \varepsilon$ in (6.2) and the NLP is feasible, go to step 10
6. Otherwise, if $i > N^{try}$ goto step 9 (N^{try} is typically set to 4)
7. If the presolve routine in CONOPT failed, select SNOPT (Gill, Murray, and Saunders, 2002) as the solver, and resolve the NLP

8. Analyze any complementarity violations involving σ^V or σ^L, and reinitialize F and/or Z for the offending stream(s) (e.g., move all flow to the vapor phase, move all flow to the liquid phase, etc.). Increment i by 1 and go to step 4

9. Select IPOPT as the solver and resolve the NLP

10. If $n = N^{sub} - 1$, STOP. Otherwise, increment n by 1 and goto step 2

$$\begin{aligned} &P_{s^{in}} \geq P_{s^{out}}, \\ &\forall (s^{in}, s^{out}) \in \{(s^1, s^2) | (s^1, g) \in \mathcal{G}^1_{in}, (s^2, x) \in \mathcal{G}^1_{out}, \\ &\forall (g, x) \in \mathcal{G}^{sub}_{map} | x \in \mathcal{X}^{sub} \cap \mathcal{G}^{PD}\} \end{aligned} \tag{6.1}$$

$$S1 := \mathcal{S}^{act} \cap \mathcal{S}_{sup} \cap \left(\mathcal{S}^{Flash}_{Vap} \cup \mathcal{S}_{Vap}\right)$$

$$S2 := \mathcal{S}^{act} \cap \mathcal{S}_{sup}$$

$$\begin{aligned} \min \quad \psi =& 100 \sum_{s \in \mathcal{S}^{act}} \left[F_s \sigma^V_s + F_s \sigma^L_s\right] + 100 \sum_{s \in S2} \left[\sigma^P_s \xi_s\right] \\ &+ 100 \sum_{s \in S1} \left[F_s \sigma^{2b}_s + \sigma^{2a}_s \sigma^{2b}_s\right] \\ &+ 100 \sum_{s \in S1} \left[\left(\Omega_s - (\bar{P}_s - P_s)\right)\left(\Omega_s - (T_s - \bar{T}_s)\right)\right] \end{aligned} \tag{6.2}$$

s.t. Updated Flowsheet Connectivity with Subunits

Stream Models	(2.21)
Cubic EoS Thermo. Model	(2.26) - (2.40), (2.43), (2.46), (2.49) - (2.52e)
Equipment Models	(2.55), (2.56b), (2.57), (2.60c) - (2.60f) (3.10b), (3.10d), (6.1)
Fixed T and P for Select Streams	

Although complex, experience has shown this procedure to be fairly reliable. If $\psi >> 0$ even after IPOPT is selected as the solver, there is an increased chance that the subsequent steps of the initialization procedure will get stuck at infeasible points.

In the final part of Step 5, all of the inlet and outlet streams for all subunits are activated, and added to $\mathcal{S}^{act}$. Component flowrates are unfixed. Temperatures and pressures are unfixed, but bounded near the nominal values. Predicted values from the previous NLPs are stored in $\tilde{F}$, $\tilde{x}$, $\tilde{T}$ and $\tilde{P}$, and the following NLP is solved:

$$\begin{aligned}\min \quad & \sum_{s\in\mathcal{S}^{act}}\left[F_s^+ + F_s^- + 10\sum_{c\in\mathcal{C}}\left(x_{s,c}-\tilde{x}_{s,c}\right)^2 + 0.1\left(P_s-\tilde{P}_s\right)^2 + \left(T_s-\tilde{T}_s\right)^2\right] \\ & +100\sum_{s\in\mathcal{S}^{act}}\left[F_s\sigma_s^V + F_s\sigma_s^L\right] + 100\sum_{s\in S2}\sigma_s^P\xi_s \\ & +100\sum_{s\in S1}\left[F_s\sigma_s^{2b} + \sigma_s^{2a}\sigma_s^{2b} + \left(\Omega_s-(\bar{P}_s-P_s)\right)\left(\Omega_s-(T_s-\bar{T}_s)\right)\right]\end{aligned}$$

s.t. $F_s - \tilde{F}_s = F_s^+ + F_s^-, \quad \forall s \in \mathcal{S}^{act}$

Updated Flowsheet Connectivity with Subunits

Stream Model	(2.21)
Cubic EoS Thermo. Model	(2.26) - (2.40), (2.43), (2.46), (2.49) - (2.52e)
Equipment Models	(2.55), (2.56b), (2.57), (2.60) (3.10)

The initialization procedure has been tuned for the case studies and reliably finds objective function values O(10^{-10}) or less for the NLP, which indicates all of the "large" heat integration units have been successfully decomposed. Furthermore, it is important to remember these large units are disabled for Steps 5 and 6, and are instead replaced with the subunits. At this point, it is possible to calculate new $\Delta\underline{T}_z$ values using the initialization procedure for the heat integration model. In principle, if there is a negligible change in $\Delta\underline{T}_z$ from before and after decomposition, reoptimization is not necessary and the optimization procedure can terminate here. This typically isn't the case, and the framework is set up to always consider Step 6.

Step 6: Final Reoptimization of the Flowsheet

Finally, in Step 6 the flowsheet is reoptimized with the MESH distillation model and decomposed heat exchangers by solving the following NLP:

min or max flowsheet objective function

s.t. Flowsheet Connectivity

Stream Models	(2.21) & (2.22)
Cubic EoS Thermo. Models	(2.26) - (2.46), (2.49) - (2.52)
Equipment Models	(2.55) - (2.57), (2.59), (2.60), (3.10)
Compressor and Pump Models	(2.61) - (2.67)
Heat Integration Models	(3.1) - (3.3), (3.5) - (3.8)
Distillation Cascade Models	(4.10) - (4.14)
Purity and/or Recovery Constraints	
Additional Problem Specific Constraints	

As a reminder, the complementary constraints in the flowsheet optimization NLPs (Steps 1, 3, 4 and 6) are accommodated with the penalty formulation (1.2e). Furthermore, the flowsheet optimization NLPs are solved repeatedly (e.g., two to four times) in each section with ρ (the complementarity penalty) increasing and ε^s decreasing.

6.2 Multi-start Initialization

Another case study is performed with the ASU system (Chapter 4) to further explain and demonstrate the multi-start procedure. Despite the highly nonlinear models and complementarity conditions, the initialization procedure and CONOPT lead to locally optimal solutions most of the time. Table 6.1 shows the various initialization parameter level values considered for this demonstration of the multi-start algorithm. There are 288 different combinations of parameter values shown Table 6.1. A summary of optimization with these 288 initialization points (95% O_2 purity) is shown in Table 6.2. For 69% of these cases CONOPT found a locally optimal solution to the final, full flowsheet NLP with negligible complementarity violations, i.e., less than 10^{-5} for (2.22). For all but one of these solutions, negligible external utilities are required ($Q^s + Q^w < 10^{-3}$). In 74% of the cases considered, CONOPT found at least a feasible solution with negligible complementarity violations. In 6% of the cases, CONOPT terminated at an infeasible solution for the final flowsheet NLP. In 5% of the cases, the initialization procedure was terminated in a previous step due to an infeasibility.

Table 6.1: Sample Initialization Parameters for ASU Case Study

Parameters	**Level Values**
Number of initial stages for simple cascade model (N_e) in Step 1	15, 25
Lower bound for φ_e^A & φ_e^S in Step 3	10^{-6}, 10^{-7}, 10^{-8}
Use flowsheet pruning?	Yes/No
Start with condenser 2 removed from flowsheet?	Yes/No
Initial temperature bump in heat integration model (α)	0.1, 0.15 K
ΔT for Step 1	4, 6 K
O_2 recovery lower bound for Steps 1 - 4	55 mol%
ε^{CEOS}, which is used to tighten (2.40)	10^{-5}, 10^{-6}, 10^{-7}
Lowerbound for $Z - B$ intermediate term in cubic EoS departure functions	10^{-7}
Initial lowerbound for $I_{ed,c}^A$ & $I_{ed,c}^B$	10^{-6}
N^+ in MESH initialization/adjustment procedure	10

Figure 6.2 shows the 200 "quality" optimal solutions (complementarity violations $< 10^{-5}$, $Q^s + Q^w < 10^{-3}$) sorted by objective function value. From the left graph, it is clear the top 20 optimal solutions' objective function values are within 1% of the best solution. Similarly, the top 50 solutions are within 5% of the best objective function value (out of the 288 points considered).

After work with the ASU system was complete, the six step initialization procedure was further refined for the CPU system. When Steps 1, 3 and 4 are skipped, and Z values are loaded from the initial point in Step 2, the ini-

Table 6.2: Breakdown of Solutions from Multi-start Initialization

	Locally Optimal	Only Feasible
Neg. $\perp$ violation	201 (69.8%)	13 (4.5%)
$\perp$ violation	26 (9.0%)	15 (5.2%)
	Locally Infeasible	Terminated in Previous Step
Neg. $\perp$ violation $\perp$ violation	18 (6.2%)	15 (5.2%)

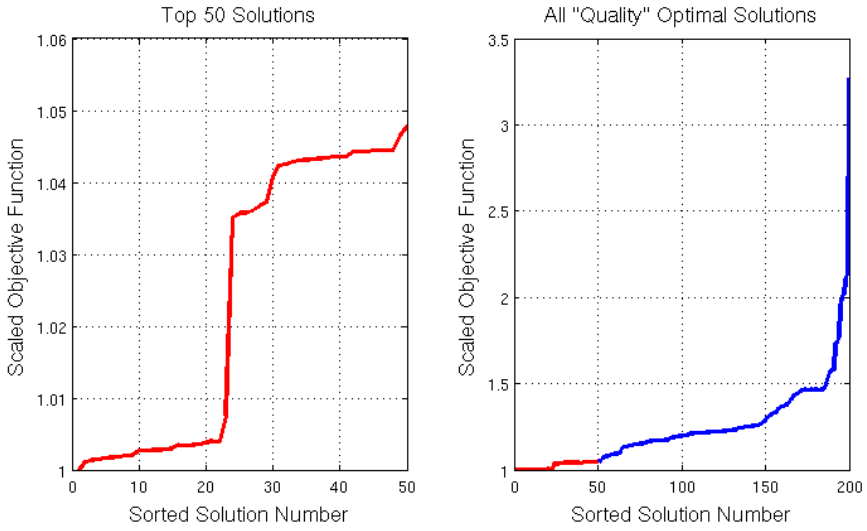

Figure 6.2: Optimal solutions sorted by objective function value

tialization and multi-start procedures perform phenomenally well for the CPU system. When 48 initialization parameter combinations were considered for the modified Duran-Grossmann heat integration model, all but two solutions (96%) met the "quality" criteria discussed above. See Section 3.4.4 for the detailed results.

6.3 Degenerate Constraints

Degenerate constraints, i.e. constraints that violate the Linearly Independent Constraint Qualification (LICQ), are prevalent in many process optimization problems. They are consequence of poor model formulations (typically human error) and overspecifications, zero flowrates and disappearing units, and recycle loops. Because degenerate constraints lead to singular Karush-Kuhn-Tucker (KKT) systems and significant challenges for numeric solvers, these constraints complicate the solution procedure for nonlinear programs. Although most modern NLP solvers implement counter-measures to detect and eliminate degeneracies, increased computational effort and convergence failures may still result. Instead, the best approach is to reformulate the original NLP model. Unfortunately, this is difficult for complex models with thousands

of equations. This section describes the *Degeneracy Hunter*, an algorithm that systematically analyzes any iteration from a continuous mathematical program solver and determines irreducible sets of degenerate constraints. This tool allows the expert modeler to focus on only a handful of equations, instead of the thousands that make up a typical process optimization problem. The algorithm has been prototyped in MATLAB and analyzes derivative information exported from GAMS. Calculation of irreducible sets of degenerate equations is formulated as a mixed integer linear program. The algorithm has been applied to a nonconvex, highly nonlinear Air Separation Unit (ASU) design problem, which identified three sources of degenerate equations. Straightforward revisions of the model to remove these degenerate constraints resulted in a 16% decrease in average CPU time and less frequent termination at infeasible points. Identification of these degeneracies would have been virtually impossible without a systematic approach.

6.3.1 Introduction and Motivating Examples

Two classes of degenerate constraints are considered: local and global. Local (or point) degeneracies occur only at specific values for variables in the mathematical program. For example, mass balance equations, shown in (6.3), become degenerate when flowrates go to zero ($F = L = V = 0$). The Jacobian of the equations is shown in (6.4), with F and z fixed. At the zero flowrate point, pivoting on the first two columns in (6.4b) shows that the Jacobian matrix is rank deficient.

$$F = V + L \tag{6.3a}$$

$$Fz_i = x_i L + y_i V, \quad \forall i \in \mathcal{C} \tag{6.3b}$$

$$\sum_{i \in \mathcal{C}} (x_i - y_i) = 0 \tag{6.3c}$$

$$A = \begin{array}{l} \\ \text{Overall MB} \\ \text{MB} \quad i = 1 \\ \vdots \\ \text{MB} \quad i = n \\ \sum \end{array} \begin{array}{c} \begin{array}{cccccccc} L & V & x_1 & \cdots & x_n & y_1 & \cdots & y_n \end{array} \\ \begin{pmatrix} -1 & -1 & 0 & \cdots & 0 & 0 & \cdots & 0 \\ -x_1 & -y_1 & -L & \cdots & 0 & -V & \cdots & 0 \\ \vdots & \vdots & \vdots & \ddots & \vdots & \vdots & \ddots & \vdots \\ -x_n & -y_n & 0 & \cdots & -L & 0 & \cdots & -V \\ 0 & 0 & 1 & \cdots & 1 & -1 & \cdots & -1 \end{pmatrix} \end{array} \tag{6.4a}$$

$$A(F = L = V = 0) = \begin{pmatrix} -1 & -1 & 0 & \cdots & 0 & 0 & \cdots & 0 \\ -x_1 & -y_1 & 0 & \cdots & 0 & 0 & \cdots & 0 \\ \vdots & \vdots & \vdots & \ddots & \vdots & \vdots & \ddots & \vdots \\ -x_n & -y_n & 0 & \cdots & 0 & 0 & \cdots & 0 \\ 0 & 0 & 1 & \cdots & 1 & -1 & \cdots & -1 \end{pmatrix} \tag{6.4b}$$

In contrast, global degeneracies always lead to rank deficient Jacobians, regardless of the value of the variables. These most commonly are a consequence of overspecifications. For example, if $\sum_i y_i = 1$ and $y_i = K_i x_i \ \forall i$ are added to (6.3), the system is always overspecified ($2+2n$ variables and $3+2n$ equations when F, z and K are specified) and the Jacobian is rank deficient.

As another example, consider the system shown in Figure 6.3, comprising two vessels, a splitter and seven streams. Stream 1 is fed into the first vessel, which has two outlets: streams 2 and 3. Without loss of generality, let streams 2 and 3 represent two different phases in equilibrium. These streams are fed into the second vessel, producing effluent streams 4 and 5. Stream 5 is split into streams 6 and 7, and the latter is recycled into the first vessel. Pressure relationships for these streams are shown in (6.5). The equations are derived from two simple rules: streams leaving a vessel are in pressure equilibrium, and pressure cannot increase across vessels and is constant across a splitter. This constraint system is overspecified (and degenerate), as there are seven constraints and seven variables, but there should be one degree of freedom (e.g. P_1 should be free). If P_2, P_4, P_6 and P_5 are removed using substitution with the equality constraints, $P_1 \geq P_3 \geq P_7 \geq P_3$ remains. As consequence, all of the inequality constraints are active at the solution, and two of them imply $P_3 = P_7$ and $P_7 = P_3$, hence the redundancy. This overspecification involves inequality constraints and MFCQ holds (although LICQ does not). For overspecifications with only equality constraints, typically no constraint qualifications hold, which is very problematic for NLP solvers.

$$P_2 = P_3 \tag{6.5a}$$
$$P_4 = P_5 \tag{6.5b}$$
$$P_6 = P_7 \tag{6.5c}$$
$$P_5 = P_7 \tag{6.5d}$$
$$P_1 \geq P_3 \tag{6.5e}$$
$$P_2 \geq P_5 \tag{6.5f}$$
$$P_7 \geq P_3 \tag{6.5g}$$

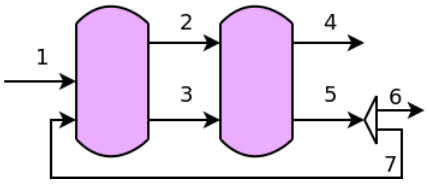

Figure 6.3: Pressure recycle degeneracy example

Many nonlinear programming (NLP) solvers implement safeguards to mitigate degenerate constraints. For example, CONOPT (Drud, 1994), a large-scale active-set generalized reduced gradient (GRG) optimization solver, removes degenerate constraints from the active set, effectively ignoring these

constraints. However, determining the active set for inequality (and degenerate constraints) is an NP-hard task. Moreover, interior point methods avoid the computational complexity of active set determination by penalizing inequality constraints with a barrier term. As a consequence, degenerate constraints cannot easily be removed from the active set. In IPOPT (Wächter and Biegler, 2006), a large-scale interior point method, degenerate constraints are instead dealt with using regularization techniques (Wang et al., 2013; Chiang and Zavala, 2014). However, neither of these general purpose strategies are fully effective, as shown in the case study (Section 6.3.3).

With global degeneracies, the best option is model reformulation. For example, consider the system in Figure 6.3. Either the recycle pressure constraint, (6.5g), should be removed and all of the inequality constraints converted to equality constraints, or a pump should be added to the recycle loop. Identifying the cause of degenerate constraints such as these, however, is difficult in large problems with thousands of constraints.

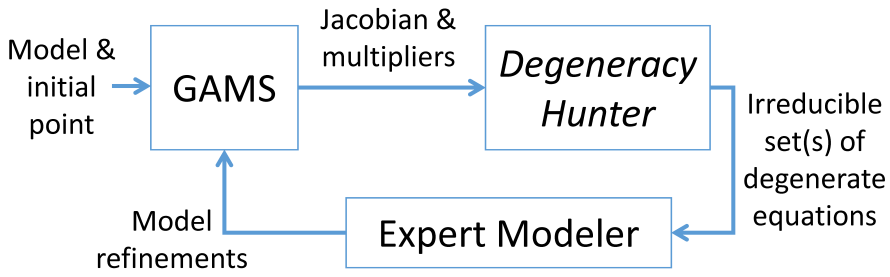

Figure 6.4: Recommend workflow with *Degeneracy Hunter*

Although factorization of the active Jacobian is sufficient for the identification of individual degenerate equations, it is still difficult to debug large models. Furthermore, blindly removing degenerate equation permanently from a model may be dangerous. For example, if a constraint is deleted from (6.3), there is no guarantee mass balances will hold with non-zero flowrates. Instead *Degeneracy Hunter* aims to help expert modelers uncover the cause of degeneracies by finding the smallest sets of degenerate equations, i.e. **irreducible degenerate sets**. This allows the modeler to focus on a handful of equations instead of thousands (in large problems). Thus, the algorithms in *Degeneracy Hunter* are intended for post optimization analysis and not realtime use embedded in a NLP solver. The envisioned workflow with *Degeneracy Hunter* is shown in Figure 6.4.

6.3.2 The *Degeneracy Hunter* Algorithm

The *Degeneracy Hunter* algorithm is divided into four steps, and is summarized in Algorithm 1. First, in the **processing step**, the Jacobian and KKT

(Karush-Kuhn-Tucker) multipliers are extracted from GAMS (or a similar environment), and the constraints are classified into four categories: equality, inactive inequality, strongly active inequality (non-zero multipliers) and weakly active inequality (zero multipliers). The *active Jacobian* (A_{dh}) is then assembled. It contains only the equality, strongly active inequality and optionally weakly active inequality constraints.[3]

Next, in the **factorization step**, non-pivot rows of the active Jacobian are identified using either sparse or dense QR factorization (or LU decomposition). These rows are candidate degenerate equations, and added to $\mathcal{R}_{cand}$. If the active Jacobian is not degenerate, there are no candidates and the algorithm terminates in this step.

In the **analysis step**, irreducible degenerate sets are calculated by solving a sequence of mixed integer linear programs (MILP), shown in (6.6), in order to minimize the number of non-zero elements in the adjoint vector λ. Integer variables y are used to count the number of non-zero elements. In order to avoid the trivial solution, $\|\lambda\| = 0$, the problem is resolved repeatedly with $\lambda_j = 1$ where $j = 1, 2, \ldots, |\mathcal{R}_{cand}|$ are the indices of the candidate degenerate equations. Thus, this procedure may identify several irreducible degenerate sets instead of simply the smallest set. This is desirable, as there may be several independent sources of degeneracies in a large problem. Furthermore, because (6.6) is an MILP, its solution has the lowest possible cardinality. Through careful integration with mixed integer programming solvers, it would be possible to recover several irreducible degenerate sets containing candidate j with equal cardinality. Alternatively, it is also common for (6.6) to be infeasible. This indicates that candidate equation j does not significantly contribute to any degenerate set. Its original identification may have resulted from numerical noise in the factorization step. In the current implementation, the MILP is solved in GAMS with CPLEX or a similar solver. For the test problems, including the case study with 15,000+ variables, the MILPs solve in (typically far) less than 1 CPU minute each. This is due both to the efficiency of commercial MILP solvers and the sparsity of the Jacobian for many chemical engineering problems.

$$\min \quad \sum_{i \in \mathcal{R}_{all}} y_i \tag{6.6a}$$

$$\text{s.t.} \quad A_{dh}^T \lambda = 0 \tag{6.6b}$$

$$-My_i \leq \lambda_i \leq My_i \ , \quad \forall i \in \{\mathcal{R}_{all} | i \neq j\} \tag{6.6c}$$

$$\lambda_j = 1, \quad y_j = 1 \tag{6.6d}$$

Finally, in the **display step**, each irreducible degenerate set is reported (with the equation names from GAMS) along with the adjoint vector elements, λ, for these equations. This information allows the modeler to understand how

[3] If bounds are included in the analysis (user specified option), they are treated as inequality constraints.

a small number of equations interact to form degeneracies.

Data: Jacobian A, KKT multipliers m, constraint values c
Step 1: Assemble active Jacobian A_{dh} using A, m, c and user specified options ;
Step 2: Factorize A_{dh} and identify set of candidate degenerate equations $\mathcal{R}_{cand}$;
foreach $j \in \mathcal{R}_{cand}$ **do**
  Step 3: Solve (6.6) ;
  if *(6.6) is feasible* **then**
    Step 4: Display non-zero elements of λ (i.e. $y_i = 1$) and associated equation names ;
  else
    Step 4: Display equation j's name and "is not part of a degenerate set"
  end
end

Algorithm 1: Pseudo-code for *Degeneracy Hunter*

6.3.3 Air Separation Unit Design Revisted

Degeneracy Hunter was applied throughout the development of the mathematical models proposed in this thesis to improve optimization performance. When applied to the ASU case study (Chapter 4), *Degeneracy Hunter* led to the discovery (and correction) instances of overspecification in the models, which are described below.

6.3.3.1 Overspecification 1: Pressure Loops

The first overspecification was a pressure loop, similar to Figure 6.3, with a cascade and reboiler in the ASU. For the aggregate cascade model, there are no pressure drops per (4.1e). However, no pressure drop also specified for the reboiler, (2.60a), which creates a recycle loop and pressure overspecification. Similarly, the pressure drop equations in the MESH model, (4.7d) - (4.9), and no pressure drop specification for the reboiler, (2.60a), are together degenerate. This degeneracy was eliminated in the ASU case study by removing (2.60a) from the optimization problem.

6.3.3.2 Overspecification 2: Equal Temperature Differences

The second overspecification relates to the equal temperature spacing constraint for heat exchange subunits, (3.10a), which is shown below for clarity:

$$T_{s^{in}} - T_{s^{out}} = \delta T_g / N^{sub},$$
$$\forall (s^{in}, s^{out}, x, g) \in \{(s^1, s^2, x, g) | (s^1, x) \in \mathcal{G}^1_{in}, (s^2, x) \in \mathcal{G}^1_{out},$$
$$x \in \mathcal{X}^{sub}, (g, x) \in \mathcal{G}^{sub}_{map}\}$$

In addition to (3.10a),

$$T_{s^{in}} - T_{s^{out}} = \delta T_g,$$
$$\forall (s^{in}, s^{out}, x, g) \in \{(s^1, s^2, g) | (s^1, g) \in \mathcal{G}^1_{in}, (s^2, g) \in \mathcal{G}^1_{out}, g \notin \mathcal{X}^{sub}\} \tag{6.7}$$

was also included in the original model, which is redundant.

6.3.3.3 Overspecification 3: Inactive Heat Exchange Units

The final overspecification identified by *Degeneracy Hunter* relates to specifications for heat exchange units. $Q^{in} \geq 0$ and $T^{out} \geq T^{in}$ are required for all heating units, whereas $Q^{out} \geq 0$ and $T^{in} \geq T^{out}$ is required for cooling units per (2.60c) - (2.60f). However, when $Q^{in} = Q^{out} = 0$ and $T^{in} = T^{out}$, these specifications are redundant due to the thermodynamic model which requires $\Delta P = 0$ and $\Delta T = 0 \Leftrightarrow Q = 0$. This problem isn't as hazardous as the other overspecifications, as this only involves inequality constraints (or bounds), and the Mangasarian-Fromovitz constraint qualification (MFCQ) should still hold. Nevertheless, CONOPT may cycle and experience trouble deciding which constraints to include in the active set. Furthermore, (2.60c) - (2.60f) were found to be important to discourage certain complementarity violations in Step 5 of the initialization procedure with the CPU case study. Thus, (2.60c) - (2.60f) are retained in the final version of the framework.

6.3.3.4 Computational Results

The ASU design optimization problem (Chapter 4) was resolved for several different combinations of overspecifications 1 through 3 being included or removed. The same 288 initial points generated from the parameters in Table 6.1 were considered for each trial. All instances were solved on the same desktop computer, running Ubuntu Linux and GAMS 24.3.1 with a quad-core 2.8 GHz Intel i7 processor. In order to quantify variations in timings due to background jobs, GAMS overhead, disk access, etc., several of the trials were repeated. The timings are consistent within a few seconds. The average CPU time for all 288 instances of the optimization problem are reported in Table 6.3 for each trial. These CPU times include the entire initialization procedure described in Section 6.1.

The best performance was obtained with all three sources of degeneracy removed (753.9 s) and the worst performance occurred with all three sources of degeneracies remaining in the optimization formulation (896.4 s). Thus with this case study, removing the degenerate equations decreased CPU time by 16%. Furthermore, the presence of degenerate constraints also impacted the termination status with CONOPT. The last two columns of Table 6.3 show the number optimal and only feasible solution points, as classified by CONOPT, for each trial. "High quality" solutions are defined as completely heat integrated with no complementarity violations. CONOPT terminated at locally optimal points 214 times in trial six (all degeneracies removed). In contrast, with some degeneracies present in trial five, CONOPT terminated at locally optimal solutions only 204 times. This performance difference is expected, as

Table 6.3: Comparison of CPU times for the ASU design optimization problem with various degenerate constraints removed.

Trial	O1 removed?	O2 removed?	O3 removed?	Average CPU time	"High Quality" Optimal	"High Quality" Only Feasible
1	No	No	No	896.4 s	210	14
2	No	Yes	Yes	863.6 s	204	17
3a	Yes	No	No	791.2 s	215	20
3b	Yes	No	No	788.7 s	215	20
4a	Yes	Yes	No	817.5 s	205	13
4b	Yes	Yes	No	818.4 s	205	13
5a	Yes	No	Yes	858.0 s	204	23
5b	Yes	No	Yes	859.8 s	204	23
6a	Yes	Yes	Yes	753.3 s	214	18
6b	Yes	Yes	Yes	754.1 s	214	18
6c	Yes	Yes	Yes	754.4 s	214	18

the KKT multipliers are not unique in the presence of degeneracies. For the feasible only points, the active-set strategy may have not removed all of the degenerate constraints. Furthermore, in trial four (218), CONOPT terminated at 17 more infeasible and/or not high quality points than trial three (235). This speaks to the complexity of NLP solution techniques and the initialization procedure used in the framework. It is likely the presence of degeneracies (especially the pressure recycle loop) causes the NLP solver, CONOPT, to take different convergence paths early in the initialization procedure. This can result in very different solutions for each initial point considered.

6.3.4 Flowsheet Pruning

Although *Degeneracy Hunter* is an effective tool for identifying irreducible sets of linearly dependent constraints, model reformulation is only effective for global degeneracies. As shown in the first motivating of Section 6.3.1, mass balance constraints are generate when flowrates go to zero, which occurs frequently the process design superstructures when equipment are deactivated. One option is to use disjunctive programming with a master integer program and pure continuous nonlinear subproblem, as Yeomans and Grossmann (2000b) did for distillation column design. Equipment (or trays) are selected in the master problem, and the inner problem is formulated to only include equations for the selected equipment (or trays). This approach requires custom implementation and may be too computationally expensive with severely nonlinear thermodynamics models. In contrast, integer variables are avoided in this framework, and instead an optional pruning step is considered at various parts of the initialization procedure. When the pruning step is activated, any equipment with zero inlet and outlet flowrates are removed. This mechanism may also be used to remove liquid or vapor inlet/outlet streams for compressors and pumps before optimization, as discussed in Section 2.8.

6.4 Conclusions and Future Directions

Implementation details including initialization and careful model formulation are essential for successful optimization with the equation-based mathematical models presented in this thesis. Regarding initialization, a successive model refinement strategy is developed and used in the framework. The process design problem is first optimized with shortcut models and simple thermodynamics. The results are then used to initialize the more complex and nonlinear models. Details for the six step initialization procedure are documented in this chapter, including the NLPs solved in each step. Without a systematic initialization routine, it is very difficult to solve optimization problem with the mathematical models presented in Chapters 2 through 5.

Furthermore, because the models are nonconvex, multiple local solutions are expected and observed. A multi-start procedure is used to resolve the flowsheet optimization problem with different combinations of key initialization parameters, including bounds for certain variables, alternate model formulation (e.g., different heat integration models), variations on the initialization and different initial values for other variables. This procedure is demonstrated for both the CPU system in Section 3.4.4 and for the ASU system in this chapter. Overall, the multi-start and initialization procedures have been tuned to be high effective, and find locally optimal solutions with negligible complementarity violations 70% of the time for the ASU system. After additional refinement, the success rate increased to 96% for the CPU case study. Thus, multi-start optimization is a practical alternative to deterministic global optimization methods for these highly nonlinear and nonconvex models.

Finally, the impact of degenerate constraints, i.e. constraints with rank deficient Jacobians, is discussed. In summary, degenerate models do not satisfy constraint qualifications and have singular KKT systems, which frustrates the calculation of Newton steps. As a consequence, many NLP solvers experience degraded performance in the presence of linearly dependent constraints. This motivated development of *Degeneracy Hunter*, a model diagnostic tool to find irreducible sets of degenerate constraints, which allows an expert modeler to focus on only a small subset of the model for refinements. *Degeneracy Hunter* was applied to the original ASU model, which led to the identification of three instances of overspecification. Computational studies were performed with various version of the ASU model with different combinations of the degenerate constraints removed, ultimately resulting in a 16% decrease in CPU time for the entire initialization procedure and an increase in the frequency of locally optimal solutions without complementarity violations from 73% to 75%.

By design, *Degeneracy Hunter* requires expert user intervention to analyze the results and propose alternate model formulations. Similarly, reformulation is typically only applicable to globally degenerate constraints, and not pointwise (or local) degeneracies. In contrast, several researchers are investigating improved algorithms in NLP solvers in order to handle degenerate constraints on-the-fly. For example, Wang et al. (2013) and Chiang and Zavala (2014) have

explored structural regularization techniques for IPOPT. Another possibility is to exploit problem specific information in flowsheet optimization problems. For example, if inlet flowrates go to zero, the mass balance can be removed to handle the degenerate equation. Furthermore, it may be advantageous to add slack variables to the mass balance equations, as the extra slack variables, τ, would prevent the constraint Jacobian from becoming singular. For example, if (6.3) is replaced with

$$F = V + L + \tau \tag{6.8a}$$

$$Fz_i = x_i L + y_i V, \quad \forall i \in \mathcal{C} \tag{6.8b}$$

$$\sum_{i \in \mathcal{C}} (x_i - y_i) = 0 \tag{6.8c}$$

$$\tau \geq 0 \ , \tag{6.8d}$$

and τ is sufficiently penalized in the objective function, the mass balance equations should no longer be degenerate. This strategy is similar to phase 1 in an LP solver or restoration phase in IPOPT where constraints are slacked and infeasibilities are minimized.

Chapter 7

Thesis Conclusions and Recommended Future Work

The primary goal of this thesis is to advance equation-oriented flowsheet design and optimization methods by leveraging exact first and second derivatives and state-of-the-art nonlinear programming algorithms. Compared to commercially available flowsheet optimization methods, this approach requires process models to be "opened-up" and completely exposed to the optimizer. Thus, "gray box" thermodynamic packages and other models that only provide function values and first derivative information are not preferred. Instead, a new framework for advanced flowsheet optimization is developed in this thesis. The framework is organized into five parts:

1. Embedded ideal gas and cubic equation of state thermodynamic models with complementarity constraints to accommodate vanishing and reappearing phases.

2. Simultaneous heat integration and process optimization using variations of the pinch-location method.

3. Distillation column size optimization using either and aggregate shortcut model or a novel, rigorous MESH with tray bypass model.

4. Equation-based steam turbine models and a hybrid 1D/3D zonal computational fluid dynamics (CFD) coal boiler model.

5. Trust region optimization strategy to incorporate complex models (e.g., CFD reactor) without exact derivatives using surrogate models while maintaining the computational benefits of an equation-oriented approach for the remainder of the flowsheet.

Three themes are incorporated throughout the framework. First, the models are organized in a modular fashion. For example, unit operations (equipment) are organized in a hierarchy, with balance and heat integration equations implemented for the most generic *general equipment* type. This structure

makes the framework compact, flexible and extensible. Second, a systematic model refinement procedure is used to initialize the highly nonlinear process models. The flowsheet is first optimized with simple ideal gas thermodynamics and aggregate distillation cascade models. The results are then used to initialize the cubic EoS and tray-by-tray distillation column models. Finally, complementarity constraints are used in various models as an alternate to integer variables to model switches, such as a change in the number of predicted phases at equilibrium. This is done to avoid mixed integer programs with highly nonlinear and nonconvex thermodynamics models.

Furthermore, the models in the framework are carefully reformulated to avoid linearly dependent constraint Jacobians, i.e., degeneracies, which cause degraded NLP solver performance. Arising from a practical need, the *Degeneracy Hunter* algorithm was created to calculate irreducible sets of degenerate constraints. This tool allows a modeler to focus on a handful of equations instead of thousands to identify problematic formulations and remove degenerate constraints. *Degeneracy Hunter* was used to identify three instances of overspecification in Air Separation Unit (ASU) optimization case study. Reformulation of the models led to a 16% improvement in average computation time and increased success in finding locally optimal solutions with the multi-start routine.

Finally, the models and methods developed in this thesis are applied to design coal-fired oxycombustion power systems with CO_2 capture. In contrast, most previous studies focused on individual subsystems in oxycombustion plants and/or did not consider multi-variable optimization. Instead, the proposed framework is used to rigorously optimize subsystems in the process and consider integration opportunities. The traditional oxycombustion system includes two sub-ambient/cryogenic gas separation systems: an Air Separation Unit (ASU) and CO_2 Processing Unit (CPU). Both of these systems and their accompanying multistream heat exchangers are optimized to minimize specific separation energy, and possible heat integration between the systems is investigated. The steam cycle side of the oxycombustion process is optimized using the trust region strategy, which incorporates steam table thermodynamic lookups into the optimization problem using surrogate models. The steam cycle is then reoptimized with varying quantities of available low-grade waste heat. As expected, the amount of extracted steam in the last sections of the low pressure steam turbine decreased and power output (shaft work) increased. This demonstrates the capability to consider optimal integration of interstage coolers from compressors in the ASU and CPU into the steam cycle. This is fundamentally different that most other studies, which do not consider adjustment of steam extraction rates for boiler feedwater with additional waste heat.

7.1 Contributions of the Thesis

The main contributions of this thesis are as follows:

1. Creation of a five part equation-based framework for flowsheet optimization that leverages state-of-the-art nonlinear programming solvers and considers rigorous models

2. Development of three new equation-based process models, or novel extensions of existing models:

   - Refinement of the embedded cubic EoS model to correct phase identification in the supercritical region and to prevent a flash of nonphysical (e.g., trivial) phase equilibrium solutions
   - Reformulation of the Duran-Grossmann heat integration model to avoid instances of the smoothed max operator (and associated errors)
   - Creation of a new MESH with tray bypass distillation model that allows for optimization of the new of trays and feed location without integer variables

3. Further demonstration of the efficacy of complementarity constraints to accommodate certain types of nonsmooth features (i.e., switches) in process models.

4. Discussion of initialization procedures based on model refinement and multi-start for flowsheet optimization applications.

5. Development of *Degeneracy Hunter*, a diagnostic tool to help detect the source of degenerate constraints in mathematical programs.

6. Demonstration of the proposed methods in oxycombustion power system design case studies. This approach is fundamentally different than previous oxycombustion studies as it allows for true system-wide optimization using non-proprietary models.

7.2 Recommendations for Future Work

This thesis focuses on early development of equation-oriented strategies for flowsheet optimization with completely open process models. The proposed framework should be expanded in several directions. New thermodynamics modules should be developed for the framework to include popular models such as Wilson, NRTL and UNIQFAC that are commonly used in commercial process simulators. This may be a very complex endeavour, especially for liquid-liquid-vapor and electrolyte systems. But it is important, given the necessity of advanced thermodynamic models for industrial applications. This framework should also be extended to consider decomposition methods (e.g., Schur complements, augmented Lagrangian decomposition, etc.) for large scale problems, which would enable parallelization. Automated strategies to decompose flowsheets into multiple blocks (similar to flowsheet zones discussed

in Chapter 2), with a minimal number of linking variables between each block, should also be pursued. Furthermore, design under uncertainty capabilities using a two stage stochastic programming approach should be added to the framework, which would also benefit from decomposition methods. On a more practical note, a more advanced programming environment with debugger features, native plotting support, unit tests, etc. should be considered instead of GAMS. This would greatly facilitate adding a user interface to the framework and decrease model development time.

Despite the use of *Degeneracy Hunter* and extensive model refinement, degenerate equations due to zero flowrates remain problematic (as they are locally degenerate). Alternate formulations of the mass balance model, such as (6.8), should be investigated. Currently only active set solvers, such as CONOPT, reliably solve each step of the initialization procedure. IPOPT can experience significant difficulties on converging these models, which is likely due to degenerate constraints. However, interior point methods like IPOPT are often preferred for very large problems. With the alternate heat integration formulations discussed in Chapter 3, CONOPT experienced severely degraded performance with larger models, despite most of the additional equations being linear.

The new process models presented in this thesis should be benchmarked with other systems beyond oxycombustion, and compared to alternate models. For example, the new MESH with tray bypass model should be directly compared to the MINLP distillation model of Viswanathan and Grossmann (1990). Computational experiments should be conducted compare the performance of the log-transformed (2.57) versus original (2.58) phase equilibrium models. Similarly, the phase constraints to toggle "on" and "off" pressure changers, (2.68), should be thoroughly tested.

Several modifications of the heat integration model should be considered as future work. Poor computational performance of the two alternate models that use inequality and/or complementarity constraints should be investigated using *Degeneracy Hunter* and other tools. Similarly, these models should be tested with IPOPT once the point-wise degeneracy for zero flowrates is resolved. Ongoing work to extend the Duran-Grossmann approach to include approximate area targeting should be completed and tested. This would allow for heat exchanger capital costs to be accounted for in a net present value objective function, and furthermore, would allow for ΔT to be considered as a optimization variable. The heat integration models also needs to be extended if two-stage design under uncertainty is considered. Finally, possible synergies between the disjunctive model of Kamath, Biegler, and Grossmann (2012) for phase change detection and the proposed bubble and dew point calculations to avoid nonphysical phase equilibrium predictions (in the cubic EoS thermodynamics module) should be investigated.

Ongoing work with collaborators is focused on extending the case studies in this thesis to consider simultaneous optimization of an entire oxycombustion power system. Planned work includes the following:

1. Investigation of ASU-CPU heat integration opportunities, including a new design where the ASU produces liquid N_2, which is vaporized to drive the refrigeration cycle in the CPU, allowing for CO_2 to be pumped (instead of compressed)

2. Optimization of ASU designs with recuperative vapor recompression heat pumps to further reduce energy requirements

3. Optimization of an oxycombustion steam cycle with boiler input variables manipulated in the optimization problem, and outputs calculated using the zonal 1D/3D hybrid CFD boiler model

4. Simultaneous optimization of the entire oxycombustion process to study

    - Optimal heat integration strategies for waste heat utilization (from compression) in the steam cycle
    - Optimal sizing of the ASU and CPU
    - Optimal flue gas recycle rates and strategies
    - Impact of key assumptions including steam temperature and pressure bounds (materials constraints) and air ingress rates on the optimal system design

Furthermore, this thesis (and proposed future work) focuses on steady-state flowsheet optimization. For power systems applications, however, dynamic operation and load following are important. As an intermediate, the models should be extended to consider two stage optimization, with scenarios corresponding to different power demands. Optimization variables would be partitioned into design (same for each scenario) and operational (optimized for each scenario) classifications, which would allow for recourse to be considered. This approach would add a flexibility requirement to the design problem, and facilitate load following (i.e., non-base load operation). From a model perspective, this will require implementation of the Spencer-Cotton-Cannon model to calculate off-design turbine efficiency, and extension of the trust region algorithm to efficiently manage multiple scenarios.

Bibliography

Adams, B. R.; David, K.; Senior, C.; Shim, H. S.; Otten, B. V.; Fry, A.; Wendt, J.; Eddings, E.; Paschedag, A.; Zurek, S.; Shaddix, C.; and Cox, W. 2013. Characterizaton of oxy-combustion impacts in existing coal-fired boilers. Technical report, National Energy Technology Labratory. NT0005288.

Adewumi, M. 2014. Solution techniques for cubic expressions and root finding.

Advanced Manufacturing Office. 2012. Deaerators in Industrial Steam Systems. Technical report, U.S. Department of Energy. DOE/GO-102012-3399.

Agarwal, A., and Biegler, L. T. 2013. A trust-region framework for constrained optimization using reduced order modeling. *Optimization and Engineering* 14(1):3–35.

Aguilar, O.; Perry, S. J.; Kim, J.-K.; and Smith, R. 2007a. Design and Optimization of Flexible Utility Systems Subject to Variable Conditions. Part 1: Modelling Framework. *Trans IChemE* 85(A8):1136–1148.

Aguilar, O.; Perry, S.; Kim, J.-K.; and Smith, R. 2007b. Design and Optimization of Flexible Utility Systems Subject to Variable Conditions. Part 2: Methodology and Applications. *Trans IChemE* 85(A8):1149–1168.

Aguilar, O.; Kim, J.-k.; Perry, S.; and Smith, R. 2008. Availability and reliability considerations in the design and optimisation of flexible utility systems. *Chemical Engineering Science* 63:3569–3584.

Ahmad, S.; Linnhoff, B.; and Smith, R. 1990. Cost Optimum Heat Exchanger Networks - 2. Targets and Design for Detailed Capital Cost Models. *Computers & Chemical Engineering* 14(7):751–767.

Alexandrov, N. M.; Dennis, J. E.; Lewis, R. M.; and Torczon, V. 1998. A Trust Region Framework for Managing the Use of Approximation Models in Optimization. *Structural Optimization* 15:16–23.

Andrecovich, M. J., and Westerberg, A. W. 1985. An MILP formulation for heat-integrated distillation sequence synthesis. *AIChE Journal* 31(9):1461–1474.

Babcock & Wilcox Co. 2005a. Boilers, Superheaters and Reheaters. In *Steam: its generation and use*. The Babcock & Wilcox Company, 41 edition. chapter 19, 19:1–19:22.

Babcock & Wilcox Co. 2005b. Economizers and Air Heaters. In *Steam: its generation and use*. The Babcock & Wilcox Company, 41 edition. chapter 20, 20:1–20:18.

Babcock & Wilcox Co. 2005c. Nitrogen Oxides Control. In *Steam: its generation and use*. The Babcock & Wilcox Company, 41 edition. chapter 34.

Babcock & Wilcox Co. 2005d. Sulfur Dioxide Control. In *Steam: its generation and use*. The Babcock & Wilcox Company, 41 edition. chapter 35.

Balakrishna, S., and Biegler, L. T. 1992. Targeting strategies for the synthesis and energy integration of nonisothermal reactor networks. *Industrial & Engineering Chemistry Research* 31(9):2152–2164.

Baliban, R. C.; Elia, J. A.; and Floudas, C. A. 2013. Novel natural gas to liquids processes: Process synthesis and global optimization strategies. *AIChE Journal* 59(2):505–531.

Bandyopadhyay, S.; Varghese, J.; and Bansal, V. 2010. Targeting for cogeneration potential through total site integration. *Applied Thermal Engineering* 30(1):6–14.

Baumrucker, B. T.; Renfro, J.; and Biegler, L. T. 2008. MPEC problem formulations and solution strategies with chemical engineering applications. *Computers & Chemical Engineering* 32(12):2903 – 2913.

Besong, M. T.; Maroto-Valer, M. M.; and Finn, A. J. 2013. Study of design parameters affecting the performance of co_2 purification units in oxy-fuel combustion. *International Journal of Greenhouse Gas Control* 12(0):441 – 449.

Biegler, L. T.; Grossmann, I. E.; and Westerberg, A. W. 1997. *Systematic Methods of Chemical Process Design*. Upper Saddle River, New Jersey, USA: Prentice Hall PTR.

Biegler, L. T.; Lang, Y.-d.; and Lin, W. 2014. Multi-scale Optimization for Process Systems Engineering. *Computers & Chemical Engineering* 60:17–30.

Biegler, L. T. 2010. *Nonlinear Programming: Concepts, Algorithms, and Applications to Chemical Processes*. Society of Industrial and Applied Mathematics.

Black, J. 2010. Cost and Performance Baseline for Fossil Energy Plants Volume 1: Bituminous Coal and Natural Gas to Electricity. Technical report, National Energy Technology Labratory. DOE/NETL-2010/1397, Rev. 2.

Black, J. 2014. Quality Guidelines for Energy Systems Studies: Process Modeling Design Parameters. Technical report, National Energy Technology Labratory. DOE/NETL-341/051314.

Boston, J. F., and Britt, H. I. 1978. A Radically Different Formulation and Solution of the Single-Stage Flash Problem. *Computers & Chemical Engineering* 2:109–122.

Boston, J., and Mathias, P. 1980. Phase equilibria in a third-generation process simulator. In *Proceedings of the 2nd International Conference on Phase Equilibria and Fluid Properties in the Chemical Process Industries, West Berlin*, 17–21.

Botros, B. B., and Brisson, J. G. 2011. Targeting the optimum steam system for power generation with increased flexibility in the steam power island design. *Energy* 36(8):4625–4632.

Bruno, J. C.; Fernandez, F.; and Grossmann, I. E. 1998. A rigorous MINLP model for the optimal synthesis and operation of utility plants. *Trans IChemE* 76(Part A).

Byrd, R. H.; Nocedal, J.; and Waltz, R. A. 2006. Knitro: An integrated package for nonlinear optimization. In Di Pillo, G., and Roma, M., eds., *Large-Scale Nonlinear Optimization*, volume 83 of *Nonconvex Optimization and Its Applications*. Springer US. 35–59.

Caballero, J. A., and Grossmann, I. E. 2001. Generalized disjunctive programming model for the optimal synthesis of thermally linked distillation columns. *Industrial & Engineering Chemistry Research* 40(10):2260–2274.

Caballero, J. A., and Grossmann, I. E. 2008. An Algorithm for the Use of Surrogate Models in Modular Flowsheet Optimization. *AIChE Journal* 54(10):2633–2650.

Castle, W. F. 2002. Air separation and liquefaction: recent developments and prospects for the beginning of the new millennium. *International Journal of Refrigeration* 25:158–172.

CCSI. 2013. Reference power plant model user manual. Technical report, Carbon Capture Simulation Initiative.

Cerda, J., and Westerburg, A. W. 1983. Synthesizing heat exchanger networks having restricted stream/stream matches using transportation problem formulations. *Chemical Engineering Science* 38(10):1723–1740.

Cerda, J.; Westerburg, A. W.; Mason, D.; and Linnhoffb, B. 1983. Minimum Utility Usage in Heat Exchanger Network Synthesis. *Chemical Engineering Science* 38(3):373–387.

Chacartegui, R.; Sanchez, D.; Becerra, J.; Munoz, A.; and Sanchez, T. 2011. Performance Analysis of a 565 MW Steam Power Plant. In *ASME 2011 Turbo Expo: Turbine Technical Conference and Exposition*, 2427–2436. American Society of Mechanical Engineers.

Chen, J.-S., and Pan, S. 2008. A family of NCP functions and a descent method for the nonlinear complementarity problem. *Computational Optimization and Applications* 40(3):389–404.

Chen, L.; Yong, S. Z.; and Ghoniem, A. F. 2012. Oxy-fuel combustion of pulverized coal: Characterization, fundamentals, stabilization and CFD modeling. *Progress in Energy and Combustion Science* 38(2):156–214.

Chi, J.; Wang, B.; Zhang, S.; and Xiao, Y. 2010. Off-design performance of a chemical looping combustion (CLC) combined cycle: Effects of ambient temperature. *Journal of Thermal Science* 19(1):87–96.

Chiang, N., and Zavala, V. M. 2014. An inertia-free filter line-search algorithm for large-scale nonlinear programming. Preprint ANL/MCS-P5197-0914.

Chou, C.-C., and Shih, Y.-S. 1987. A thermodynamic approach to the design and synthesis of plant utility systems. *Industrial & Engineering Chemistry Research* 26(6):1100–1108.

Ciric, A. R., and Floudas, C. A. 1989. A retrofit approach for heat exchanger networks. *Computers & Chemical Engineering* 13(6):703–715.

Ciric, A. R., and Floudas, C. A. 1990. Application of the simultaneous match-network optimization approach to the pseudo-pinch problem. *Computers & Chemical Engineering* 14(3):241–250.

Ciric, A. R., and Floudas, C. A. 1991. Heat exchanger network synthesis without decomposition. *Computers & Chemical Engineering* 15(6):385–396.

Colberg, R. D.; Morari, M.; and Townsend, D. W. 1989. A Resilience Target Network for Heat Synthesis. *Computers & Chemical Engineering* 13(7):821–837.

Colbert, R. 1982. Heat-transfer in action: Industrial heat-exchange networks. *Chemical Engineering Progress* 78(7):47–54.

Colmenares, T. R., and Seider, W. D. 1989. Synthesis of Utility Systems Integrated with Chemical Processes. *Industrial & Engineering Chemistry Research* 28:84–93.

Conn, A. R.; Scheinberg, K.; and Vicente, L. N. 2009. *Introduction to Derivative-Free Optimization*. SIAM and MPS.

Cooke, D. H. 1985. On Prediction of Off-Design Multistage Turbine Pressures by Stodola's Ellipse. *Journal of Engineering for Gas Turbines and Power* 107:596–606.

Cotton, K. 1998. *Evaluating and Improving Steam Turbine Performance*. Cotton Fact Inc.

Cozad, A.; Sahinidis, N. V.; and Miller, D. C. 2014. Learning surrogate models for simulation-based optimization. *AIChE Journal* 60(6):2211–2227.

Darde, A.; Prabhakar, R.; Tranier, J.-P.; and Perrin, N. 2009. Air separation and flue gas compression and purification units for oxy-coal combustion systems. *Energy Procedia* 1(1):527–534.

Del Nogal, F.; Kim, J.-K.; Perry, S.; and Smith, R. 2008. Optimal Design of Mixed Refrigerant Cycles. *Industrial & Engineering Chemistry Research* 47:8724–8740.

Dhole, V. R., and Linnhoff, B. 1993. Total site targets for fuel co-generation, emissions, and cooling. *Computers & Chemical Engineering* 17(Suppl-H):S101–S109.

Dowling, A. W., and Biegler, L. T. 2013. Optimization-based Process Synthesis for Sustainable Power Generation. *Chemical Engineering Transactions* 35:1–12.

Dowling, A. W.; Eason, J. P.; Ma, J.; Miller, D. C.; and Biegler, L. T. 2014. Coal Oxycombustion Power Plant Optimization using First Principles and Surrogate Boiler Models. *Energy Procedia* 63:352–361.

Dowling, A. W.; Vetukuri, S. R. R.; and Biegler, L. T. 2012. Large-Scale Optimization Strategies for Pressure Swing Adsorption Cycle Synthesis. *AIChE Journal* 58(12):3777–3791.

Drud, A. S. 1994. CONOPT – a large-scale GRG code. *ORSA Journal on Computing* 6(2):207–216.

Duran, M. A., and Grossmann, I. E. 1986. Simultaneous optimization and heat integration of chemical processes. *AIChE Journal* 32(1):123–138.

Eason, J. P., and Biegler, L. T. 2015. Reduced model trust region methods for embedding complex simulations in optimization problems. In *12th International Symposium on Process Systems Engineering and 25th European Symposium on Computer Aided Process Engineering*.

Edge, P.; Heggs, P.; Pourkashanian, M.; Stephenson, P.; and Williams, A. 2012. A reduced order full plant model for oxyfuel combustion. *Fuel* 101:234–243.

Edge, P.; Heggs, P.; Pourkashanian, M.; and Stephenson, P. 2013. Integrated fluid dynamics-process modelling of a coal-fired power plant with carbon capture. *Applied Thermal Engineering* 60(1-2):242–250.

Edmister, W. C. 1957. Absorption and stripping-factor functions for distillation calculation by manual- and digital-computer methods. *AIChE Journal* 3(2):165–171.

Energy Efficiency & Renewable Energy. 2012. Steam calculators: Deaerator calculator.

Erbar, J., and Maddox, R. 1961. Latest score: reflux vs. trays. *Petroleum Refiner* 40(5):183–188.

Fahl, M., and Sachs, E. W. 2003. Reduced order modelling approaches to pde-constrained optimization based on proper orthogonal decomposition. In *Large-scale PDE-constrained optimization*. Springer. 268–280.

Fan, Z.; Seltzer, A.; and Hack, H. 2011. Oxyfuel Power Generation with Closed-Loop to Reach Zero Emission. In *10th Annual Conference on Carbon Capture and Sequestration*.

Fenske, M. R. 1932. Fractionation of Straight-Run Pennsylvania Gasoline. *Industrial & Engineering Chemistry* 24(5):482–485.

Ferris, M., and GAMS Development. 2015. NLPEC user manual.

Fletcher, R., and Leyffer, S. 2002. Nonlinear programming without a penalty function. *Mathematical Programming* 91:239–269.

Floudas, C. A., and Ciric, A. R. 1989. Strategies for overcoming uncertainties in heat exchanger network synthesis. *Computers & Chemical Engineering* 13(10):1133–1152.

Floudas, C., and Ciric, A. 1990. Corrigendum - strategies for overcoming uncertainties in heat exchanger network synthesis. *Comput. Chem. Eng* 14(8).

Floudas, C. A., and Grossmann, I. E. 1986. Synthesis of flexible heat exchanger networks for multiperiod operation. *Computers & Chemical Engineering* 10(2):153–168.

Floudas, C. A., and Grossmann, I. E. 1987a. Synthesis of flexible heat exchanger networks with uncertain flowrates and temperatures. *Computers & Chemical Engineering* 11(4):319–336.

Floudas, C. A., and Grossmann, I. E. 1987b. Automatic generation of multiperiod heat exchanger network configurations. *Computers & Chemical Engineering* 11(2):123–142.

Floudas, C. A.; Ciric, A. R.; and Grossmann, I. E. 1986. Automatic Synthesis of Optimum Heat Exchanger Network Configurations. *AIChE Journal* 32(2):276–290.

Foerg, W. 2002. History of cryogenics: the epoch of the pioneers from the beginning to the year 1911. *International Journal of Refrigeration* 25:283–292.

Fu, C.; Anantharaman, R.; and Gundersen, T. 2014. Optimal integration of compression heat with regenerative steam Rankine cycles. In Eden, M. R.; Siirola, J. D.; and Towler, G. P., eds., *Proceedings of the 8th International Conference on Foundations of Computer-Aided Process Design*, volume 34 of *Computer Aided Chemical Engineering*. Elsevier. 519–524.

Fu, C., and Gundersen, T. 2010. Heat Integration of an Oxy-Combustion Process for Coal- Fired Power Plants with CO_2 Capture by Pinch Analysis. *Chemical Engineering Transactions* 21(2008):181–186.

Fu, C., and Gundersen, T. 2012. Using exergy analysis to reduce power consumption in air separation units for oxy-combustion processes. *Energy* 44:60–68.

Fu, C., and Gundersen, T. 2013. Recuperative vapor recompression heat pumps in cryogenic air separation processes. *Energy* 59:708–718.

Fu, C., and Gunderson, T. 2012. Techno-economic Analysis of Co_2 Conditioning Processes in a Coal Based Oxy-combustion Power Plant. *International Journal of Greenhouse Gas Control* 9:419–427.

Furman, K. C., and Sahinidis, N. V. 2001. Computational complexity of heat exchanger network synthesis. *Computers & Chemical Engineering* 25:1371–1390.

Furman, K. C., and Sahinidis, N. V. 2002. A Critical Review and Annotated Bibliography for Heat Exchanger Network Synthesis in the 20th Century. *Industrial & Engineering Chemistry Research* 41:2335–2370.

Gill, P. E.; Murray, W.; and Saunders, M. A. 2002. SNOPT: An SQP Algorithm for Large-Scale Constrained Optimization. *SIAM Journal on Optimization* 12(4):979–1006.

Gilliland, E. 1940. Multicomponent rectification estimation of the number of theoretical plates as a function of the reflux ratio. *Industrial & Engineering Chemistry* 32(9):1220–1223.

Gomez Giammattei, J. A. 1994. *Simultaneous Optimization of a Chemical Process, Its Heat Exchange Network, and the Utility System Using a Process Simulator*. Ph.D. Dissertation, Massachusetts Institute of Technology.

Gong, J., and You, F. 2014. Optimal design and synthesis of algal biorefinery processes for biological carbon sequestration and utilization with zero direct greenhouse gas emissions: Minlp model and global optimization algorithm. *Industrial & Engineering Chemistry Research* 53(4):1563–1579.

Gopal, V., and Biegler, L. T. 1999. Smoothing methods for complementarity problems in process engineering. *AIChE Journal* 45(7):1535–1547.

Grossmann, I. E., and Daichendt, M. M. 1996. New trends in optimization-based approaches to process synthesis. *Computers & Chemical Engineering* 20(6 – 7):665 – 683. Fifth International Symposium on Process Systems Engineering.

Grossmann, I. E., and Santibanez, J. 1980. Applications of mixed-integer linear programming in process synthesis. *Computers & Chemical Engineering* 4(4):205 – 214.

Grossmann, I. E.; Yeomans, H.; and Kravanja, Z. 1998. A Rigorous Disjunctive Optimization Model for Simultaneous Flowsheet Optimization and Heat Integration. *Computers & Chemical Engineering* 22(Supplemental):S157–S164.

Grossmann, I. E. 1985. Mixed-integer programming approach for the synthesis of integrated process flowsheets. *Computers & Chemical Engineering* 9(5):463–482.

Gundersen, T., and Naess, L. 1988. The synthesis of cost optimal heat exchanger networks: an industrial review of the state of the art. *Computers & Chemical Engineering* 12(6):503–530.

Gundersen, T. 1982. Numerical aspects of the implementation of cubic equations of state in flash calculation routines. *Computers & Chemical Engineering* 6(3):245–255.

Hack, H.; Fan, Z.; and Seltzer, A. 2010. Advanced Oxyfuel Combustion Leading to Zero Emission Power Generation. In *The 35th International Technical Conference on Clean Coal & Fuel Systems*.

Hagi, H.; Nemer, M.; Le Moullec, Y.; and Bouallou, C. 2013. Assessment of the Flue Gas Recycle Strategies on Oxy- Coal Power Plants using an Exergy-based Methodology. *Chemical Engineering Transactions* 35:343–348.

Harding, S. T., and Floudas, C. A. 2000. Phase stability with cubic equations of state: Global optimization approach. *AIChE Journal* 46(7):1422–1440.

Hasan, M. M. F.; Baliban, R. C.; Elia, J. A.; and Floudas, C. A. 2012. Modeling, simulation, and optimization of postcombustion CO_2 capture for variable feed concentration and flow rate. 2. pressure swing adsorption and

vacuum swing adsorption processes. *Industrial & Engineering Chemistry Research* 51(48):15665–15682.

Hegetschweiler, H., and Bartlett, R. 1957. Predicting performance of large steam turbine-generator units for central stations. *ASME Paper* (56-SA):52.

Homgren, M. 2006. X Steam, Thermodynamic properties of water and steam.

Hua, J. Z.; Brennecke, J. F.; and Stadtherr, M. A. 1998. Enhanced Interval Analysis for Phase Stability: Cubic Equation of State Models. *Industrial & Engineering Chemistry Research* 37:1519–1527.

Hui, C. W., and Ahmad, S. 1994. Total heat integration using the utility system. *Computers & Chemical Engineering* 18(8):729–742.

Humphrey, J. L. 1995. Separation processes: playing a critical role. *Chemical Engineering Progress* 91(10).

IAPWS. 2007. Revised release on the iapws industrial formulation 1997 for the thermodynamic properties of water and steam. Technical report, International Association for the Properties of Water and Steam, Lucerne, Switzerland.

Ito, K.; Horii, S.; Matsumoto, Y.; and Akagi, S. 1987. An optimal operation planning model for gas turbine cogeneration. In *Tokyo Internation Gas Turbine Congress*.

Iyer, R. R., and Grossmann, I. E. 1997. Optimal multiperiod operational planning for utility systems. *Computers & Chemical Engineering* 21(8):787–800.

Iyer, R., and Grossmann, I. 1998. Synthesis and operational planning of utility systems for multiperiod operation. *Computers & Chemical Engineering* 22(7):979–993.

Jones, D.; Bhattacharyya, D.; Turton, R.; and Zitney, S. E. 2011. Optimal design and integration of an air separation unit (ASU) for an integrated gasification combined cycle (IGCC) power plant with CO_2 capture. *Fuel Processing Technology* 92(9):1685–1695.

Jordal, K.; Yan, J.; and Strömberg, L. 2004. Oxyfuel Combustion for Coal-Fired Power Generation with CO_2 Capture – Opportunities and Challenges. In *7th International Conference on Greenhouse Gas Technologies*.

Kalitventzeff, B. 1991. Mixed integer non-linear programming and its applications to the management of utility networks. *Engineering Optimization* 18:183–207.

Kallrath, J. 2000. Mixed integer optimization in the chemical process industry: Experience, potential and future perspectives. *Chemical Engineering Research and Design* 78(6):809 – 822. Process Design.

Kamath, R. S.; Biegler, L. T.; and Grossmann, I. E. 2010. An equation-oriented approach for handling thermodynamics based on cubic equation of state in process optimization. *Computers & Chemical Engineering* 34(12):2085–2096.

Kamath, R. S.; Biegler, L. T.; and Grossmann, I. E. 2012. Modeling Multistream Heat Exchangers with and without Phase Changes for Simultaneous Optimization and Heat Integration. *AIChE Journal* 58(1):190–204.

Kamath, R. S.; Grossmann, I. E.; and Biegler, L. T. 2010. Aggregate models based on improved group methods for simulation and optimization of distillation systems. *Computers & Chemical Engineering* 34(8):1312–1319.

Klemes, J.; Dhole, V. R.; Raissi, K.; Perry, S. J.; and Puigjaner, L. 1997. Targeting and Design Methodology for Reduction of Fuel, Power and CO_2 on Total Sites. *Applied Thermal Engineering* 17(8-10):993–1003.

Klemeš, J. J., and Kravanja, Z. 2013. Forty years of Heat Integration: Pinch Analysis (PA) and Mathematical Programming (MP). *Current Opinion in Chemical Engineering* 2(4):461–474.

Knapp, H.; Doring, R.; Oellrich, L.; Plocker, U.; Prausnitz, J. M.; and Langhorst, S. Z. 1982. *Vapor-Liquid Equilibria for Mixtures of Low Boiling Substances, Vol. VI.* DECHEMA.

Kossack, S.; Kraemer, K.; and Marquardt, W. 2006. Efficient Optimization-Based Design of Distillation Columns for Homogenous Azeotropic Mixtures. *Industrial & Engineering Chemistry Research* 45(25):8492–8502.

Kraemer, K.; Kossack, S.; and Marquardt, W. 2009. Efficient Optimization-Based Design of Distillation Processes for Homogeneous Azeotropic Mixtures. *Industrial & Engineering Chemistry Research* 48(14):6749–6764.

Lang, Y.-D., and Biegler, L. T. 1987. A unified algorithm for flowsheet optimization. *Computers & Chemical Engineering* 11(2):143–158.

Lang, Y.-D., and Biegler, L. 2002. Distributed Stream Method for Tray Optimization. *AIChE Journal* 48(3):582–595.

Lang, Y.-d.; Biegler, L. T.; and Grossmann, I. E. 1988. Simultaneous Optimization and Heat Integration with Process Simulators. *Computers & Chemical Engineering* 12(4):311–327.

Lee, S., and Grossmann, I. E. 2001. A global optimization algorithm for nonconvex generalized disjunctive programming and applications to process systems. *Computers & Chemical Engineering* 25(11-12):1675 – 1697.

Lee, S., and Grossmann, I. E. 2003. Global optimization of nonlinear generalized disjunctive programming with bilinear equality constraints: applications to process networks. *Computers & Chemical Engineering* 27(11):1557 – 1575.

Leyffer, S.; López-Calva, G.; and Nocedal, J. 2006. Interior methods for mathematical programs with complementarity constraints. *SIAM Journal on Optimization* 17(1):52–77.

Li, H.; Hu, Y.; Ditaranto, M.; Willson, D.; and Yan, J. 2013. Optimization of Cryogenic CO_2 Purification for Oxy-coal Combustion. *Energy Procedia* 37:1341–1347.

Li, Z.; Du, W.; Zhao, L.; and Qian, F. 2014. Modeling and Optimization of a Steam System in a Chemical Plant Containing Multiple Direct Drive Steam Turbines. *Industrial & Engineering Chemistry Research* 53:11021–11032.

Linnhoff, B., and Ahmad, S. 1989a. Supertargeting: Optimum synthesis of energy management systems. *J. Energy Resour. Technol.* 111(3):121–130.

Linnhoff, B., and Ahmad, S. 1989b. Supertargeting: Optimum synthesis of energy management systems. *J. Energy Resour. Technol.* 113(3):121 – 130.

Linnhoff, B., and Ahmad, S. 1990. Cost Optimum Heat Exchanger Networks - 1. Minimium Energy and Capital Using Simple Models for Capital Cost. *Computers & Chemical Engineering* 14(7):729–750.

Linnhoff, B., and Flower, J. R. 1978a. Synthesis of heat exchanger networks: I. systematic generation of energy optimal networks. *AIChE Journal* 24(4):633–642.

Linnhoff, B., and Flower, J. R. 1978b. Synthesis of heat exchanger networks: Ii. evolutionary generation of networks with various criteria of optimality. *AIChE Journal* 24(4):642–654.

Linnhoff, B., and Hindmarsh, E. 1983. The Pinch Design Method for Heat Exchanger Networks. *Chemical Engineering Science* 38(5):745–763.

Linnhoff, B., and Smith, R. 1989. Design of flexible plant - how much capital for how much flexibility? *Chemie Ingenieur Technik* 59:166–167.

Linnhoff, B., and Turner, J. 1981. Heat-recovery networks: new insights yield big savings. *Chem. Eng.* 88(22).

Linnhoff, B. 1989. Pinch technology for the synthesis of optimal heat and power systems. *J. Energy Resour. Technol.* 113(3):137 – 147.

Linnhoff, B. 1993. Pinch analysis - a state-of-the-art overview. *Trans. IChemE.* 71(A).

Luo, X.; Zhang, B.; Chen, Y.; and Mo, S. 2011. Modeling and optimization of a utility system containing multiple extractions steam turbines. *Energy* 36(5):3501–3512.

Luo, X.; Zhang, B.; Chen, Y.; and Mo, S. 2012. Heat integration of regenerative Rankine cycle and process surplus heat through graphical targeting and mathematical modeling technique. *Energy* 45(1):556–569.

Ma, J.; Dowling, A.; Eason, J.; Biegler, L.; and Miller, D. 2014. Development of First Principle Boiler Model and Its Reduced Order Model for the Optimization of Oxy-combustion Power Generation System. In *39th International Technical Conference on Clean Coal & Fuel Systems*.

Marechal, F., and Kalitventzeff, B. 1996. Targeting the minimum cost of energy requirements: A new graphical technique for evaluating the integration of utility systems. *Computers & Chemical Engineering* 20(Suppl.):S225–S230.

Maréchal, F., and Kalitventzeff, B. 1997. Identification of the optimal pressure levels in steam networks using integrated combined heat and power method. *Chemical Engineering Science* 52(17):2977–2989.

Martín, M., and Grossmann, I. E. 2015. Optimal simultaneous production of biodiesel (faee) and bioethanol from switchgrass. *Industrial & Engineering Chemistry Research* 0(0).

Masso, A., and Rudd, D. 1969. The synthesis of system designs. ii. heuristic structuring. *AIChE Journal* 15(1):10–17.

Matuszewski, M. 2010. Cost and Performance for Low-Rank Pulverized Coal Oxycombustion Energy Plants. Technical Report DOE/NETL-401/093010, National Energy Technology Labratory.

Mavromatis, S. P., and Kokossis, A. C. 1998a. Conceptual optimisation of utility networks for operational variations - I. Targets and level optimisation. *Chemical Engineering Science* 53(8):1585–1608.

Mavromatis, S. P., and Kokossis, A. C. 1998b. Conceptual optimisation of utility networks for operational variations - II. Network development and optimisation. *Chemical Engineering Science* 53(8):1609–1630.

McDonald, C. M., and Floudas, C. A. 1995. Global optimization for the phase stability problem. *AIChE Journal* 41(7):1798–1814.

Medina-Flores, J. M., and Picón-Núñez, M. 2010. Modelling the power production of single and multiple extraction steam turbines. *Chemical Engineering Science* 65(9):2811–2820.

Michelsen, M. L. 1980. Calculation of phase envelopes and critical multicomponent mixtures points for. *Fluid Phase Equilibria* 4:1–10.

Michelsen, M. L. 1982a. The Isothermal Flash Problem. Part I. Stability. *Fluid Phase Equilibria* 9:1–19.

Michelsen, M. L. 1982b. The Isothermal Flash Problem. Part II. Phase-Split Calculation. *Fluid Phase Equilibria* 9:21–40.

Michelsen, M. L. 1993. Phase Equilibrium Calculations. What is easy and what is difficult? *Computers & Chemical Engineering* 17:431–439.

Mitsos, A., and Barton, P. I. 2007. A Dual Extremum Principle in Thermodynamics. *AIChE Journal* 53(8):2131–2147.

Morton, R. J., and Linnhoff, B. 1984. Individual process improvements in the context of site-wide interactions. In *IChemE 11th Annual Res. Meeting*.

Mussati, S.; Barttfeld, M.; Aguirre, P.; and Scenna, N. 2008. A disjunctive programming model for superstructure optimization of power and desalting plants. *Desalination* 222(1-3):457 – 465.

Nath, R., and Holliday, J. F. 1985. Optimizing a process plant utility system. *Mechanical Engineering* 40–50.

Navarro-Amorós, M. A.; Caballero, J. A.; Ruiz-Femenia, R.; and Grossmann, I. E. 2013. An alternative disjunctive optimization model for heat integration with variable temperatures. *Computers & Chemical Engineering* 56:12–26.

Nichita, D. V., and Gomez, S. 2009. Efficient location of multiple global minima for the phase stability problem. *Chemical Engineering Journal* 152(1):251–263.

Nichita, D. V.; Gomez, S.; and Luna, E. 2002a. Multiphase equilibria calculation by direct minimization of Gibbs free energy with a global optimization method. *Computers & Chemical Engineering* 26(12):1703–1724.

Nichita, D. V.; Gomez, S.; and Luna, E. 2002b. Phase stability analysis with cubic equations of state by using a global optimization method. *Fluid Phase Equilibria* 194-197:411–437.

Oliveira Francisco, A. P., and Matos, H. A. 2004. Multiperiod synthesis and operational planning of utility systems with environmental concerns. *Computers & Chemical Engineering* 28:745–753.

Omojokun, E. O. 1990. *Trust region algorithms for optimization with nonlinear equality and inequality constraints*. Ph.D. Dissertation, University of Colorado at Boulder.

Papoulias, S. A., and Grossmann, I. E. 1983a. A Structural Optimization Approach in Process Synthesis–I: Utility Systems. *Computers & Chemical Engineering* 7(6):695–706.

Papoulias, S. A., and Grossmann, I. E. 1983b. A structural optimization approach in process synthesis–III: Total processing systems. *Computers & Chemical Engineering* 7(6):723–734.

Papoulias, S. A., and Grossmann, I. E. 1983c. A structural optimization approach process synthesis–II: Heat Recovery Networks. *Computers & Chemical Engineering* 7(6):707–721.

Pattison, R., and Baldea, M. 2014. Equation-Oriented Flowsheet Simulation and Optimization Using Pseudo-Transient Models. *AIChE Journal* 60(12):4104–4123.

Pattison, R. C., and Baldea, M. 2015. Multistream Heat Exchangers: Equation-Oriented Modeling and Flowsheet Optimization. *AIChE Journal*.

Peterson, J., and Mann, W. L. 1985. Steam system design: how it evolves. *Chem Eng* 92(21).

Petroulas, T., and Reklaitis, G. V. 1984. Computer-aided synthesis and design of plant utility systems. *AIChE Journal* 30(1):69–78.

Pipitone, G., and Bolland, O. 2009. Power generation with CO_2 Capture: Technology for CO_2 purification. *International Journal of Greenhouse Gas Control* 3(5):528–534.

Poling, B. E.; Grens, E. A.; and Prausnitz, J. M. 1981. Thermodynamic properties from a cubic equation of state: avoiding trivial roots and spurious derivatives. *Industrial & Engineering Chemistry Process Design and Development* 20(1):127–130.

Praxair. 2009. Safety precautions for carbon dioxide. Technical report.

Raghunathan, A. U., and Biegler, L. T. 2003. Mathematical programs with equilibrium constraints (MPECs) in process engineering. *Computers & Chemical Engineering* 27(10):1381–1392.

Raghunathan, A., and Biegler, L. 2005. An interior point method for mathematical programs with complementarity constraints (MPCCs). *SIAM Journal on Optimization* 15(3):720–750.

Raghunathan, A. U.; Diaz, M. S.; and Biegler, L. T. 2004. An MPEC formulation for dynamic optimization of distillation operations. *Computers & Chemical Engineering* 28(10):2037 – 2052.

Ralph, D., and Wright, S. J. 2004. Some properties of regularization and penalization schemes for MPECs. *Optimization Methods and Software* 19(5):527–556.

Reid, R. C.; Prausnitz, J. M.; and Poling, B. E. 1987. *The Properties of Gases and Liquids*. McGraw-Hill Book Company, 4th edition.

Rév, E., and Fonyó, Z. 1986. Short Note Hidden and Pseudo Pinch Phenomena Relaxation Heat-Exchange Networks. *Computers & Chemical Engineering* 10(6):601–607.

Sargent, R., and Gaminibandara, K. 1976. Introduction: approaches to chemical process synthesis. *Optimization in Action*.

Scheffknecht, G.; Al-Makhadmeh, L.; Schnell, U.; and Maier, J. 2011. Oxy-fuel coal combustion âĂŤ A review of the current state-of-the-art. *International Journal of Greenhouse Gas Control* 5:S16–S35.

Seltzer, A.; Fan, Z.; Hack, H.; and Shah, M. 2010. Simulation and Prediction of Pollutants in a Flexi-Burn Oxyfuel Pulverized Coal Power Plant. In *35th International Technical Conference on Coal Utilization & Fuel Systems*.

Shah, M.; Degenstein, N.; Zanfir, M.; Solunke, R.; Kumar, R.; Bugayong, J.; and Burgers, K. 2011. Near Zero Emissions Oxy-Combustion Flue Gas Purification. In *2011 NETL CO_2 Capture Technology Meeting*. Pittsburgh, PA, USA: NETL CO_2 Capture Technology Meeting.

Shang, Z., and Kokossis, A. 2005. A systematic approach to the synthesis and design of flexible site utility systems. *Chemical Engineering Science* 60:4431–4451.

Shang, Z. 2000. *Analysis and Optimisation of Total Site Utility Systems*. Ph.D. Dissertation, University of Manchester Institute of Science and Technology.

Singh, H. 1997. *Strategies for emissions minimisation in chemical process industries*. Ph.D. Dissertation, UMIST, Manchester, UK. Department of Process Integration.

Soave, G., and Feliu, J. A. 2002. Saving energy in distillation towers by feed splitting. *Applied Thermal Engineering* 22(8):889 – 896.

Songolzadeh, M.; Soleimani, M.; Ravanchi, M. T.; and Songolzadeh, R. 2014. *Carbon Dioxide Separation from Flue Gases: A Technological Review Emphasizing Reduction in Greenhouse Gas Emissions*. 2014.

Soundararajan, R.; Anantharaman, R.; and Gundersen, T. 2014. Design of Steam Cycles for Oxy-combustion Coal based Power Plants with Emphasis on Heat Integration. *Energy Procedia* 51(1876):119–126.

Soundararajan, R.; Gundersen, T.; and Ditaranto, M. 2014. Oxy-Combustion Coal Based Power Plants: Study of Operating Pressure, Oxygen Purity and Downstream Purification Parameters. *Chemical Engineering Transactions* 39:229–234.

Spencer, R.; Cotton, K.; and Cannon, C. 1963. A Method for Predicting the Performance of Steam Turbine Generators: 16,500 kW and Larger. *Journal of Engineering for Power* 85(4):249–301.

Stein, O.; Oldenburg, J.; and Marquardt, W. 2004. Continuous reformulations of discrete-continuous optimization problems. *Computers & Chemical Engineering* 28(10):1951–1966.

Sun, L., and Smith, R. 2015. Performance Modeling of New and Existing Steam Turbines. *Industrial & Engineering Chemistry Research* 54:1908–1915.

Tawarmalani, M., and Sahinidis, N. V. 2005. A polyhedral branch-and-cut approach to global optimization. *Mathematical Programming* 103:225–249.

Toftegaard, M. B.; Brix, J.; Jensen, P. A.; Glarborg, P.; and Jensen, A. D. 2010. *Oxy-fuel Combustion of Solid Fuels. Progress in Energy and Combustion Science* 36:581–625.

Townsend, D., and Linnhoff, B. 1983a. Heat and Power Networks in Process Design. Part I: Criteria for Placement of Heat Engines and Heat Pumps in Process Networks. *AIChE Journal* 29(5):742–748.

Townsend, D., and Linnhoff, B. 1983b. Heat and Power Networks in Process Design. Part II: Design Procedure for Equipment Selection and Process Matching. *AIChE Journal* 29(5):748–771.

Trespalacios, F., and Grossmann, I. 2014. Review of mixed-integer nonlinear and generalized disjunctive programming methods. *Chemie Ingenieur Technik* 86(7):991–1012.

Trivedi, K. K.; O'Neill, B. K.; Roach, J. R.; and Wood, R. M. 1989. A new dual-temperature design method for the synthesis of heat exchanger networks. *Computers & Chemical Engineering* 13(6):667–685.

Trivedi, K.; O'Neill, B.; and Roach, J. 1989. Synthesis of heat exchanger networks featuring multiple pinch points. *Computers & Chemical Engineering* 13(3):291–294.

Umeda, T.; Itoh, J.; and Shiroko, K. 1978. Heat-exchange system synthesis. *Chemical Engineering Progress* 74(7):70–76.

Underwood, A. J. V. 1949. Fractional Distillation of Multicomponent Mixtures. *Industrial & Engineering Chemistry* 41(12):2844–2847.

Valderrama, J. O., and Vargas, D. A. 2003. A cubic equation of state for water and its application to power cycle calculations. *Applied Thermal Engineering* 23:1417–1425.

Varbanov, P.; Doyle, S.; and Smith, R. 2004. Modelling and Optimization of Utility Systems. *Chemical Engineering Research and Design* 82(A5):561–578.

Viswanathan, J., and Grossmann, I. E. 1990. A Combined Penalty Function and Outer-Approximation Method for MINLP Optimization. *Computers & Chemical Engineering* 14(7):769–782.

Viswanathan, J., and Grossmann, I. E. 1993a. An Alternate MINLP Model for Finding the Number of Trays Required for a Specified Separation Objective. *Computers & Chemical Engineering* 17(9):949–955.

Viswanathan, J., and Grossmann, I. E. 1993b. Optimal Feed Locations and Number of Trays for Distillation Columns with Multiple Feeds. *Industrial & Engineering Chemistry Research* 32:2942–2949.

Wächter, A., and Biegler, L. T. 2006. On the implementation of an interior-point filter line-search algorithm for large-scale nonlinear programming. *Mathematical programming* 106(1):25–57.

Wang, K.; Shao, Z.; Lang, Y.; Qian, J.; and Biegler, L. T. 2013. Barrier NLP methods with structured regularization for optimization of degenerate optimization problems. *Computers & Chemical Engineering* 57:24–29.

Wang, Y.; Dowling, A. W.; Krieft, C.; Walther, A.; and Biegler, L. T. 2015. Pressure Swing Adsorption Optimization Strategies for CO_2 Capture. In You, F., ed., *Sustainability of Products, Processes and Supply Chains: Theory and Applications*, Computer-Aided Chemical Engineering, 36. Amsterdam: Elsevier. 197–223.

Xiong, J.; Zhao, H.; Chen, M.; and Zheng, C. 2011. Simulation Study of an 800 MWe Oxy-combustion Pulverized-Coal- Fired Power Plant. *Energy & Fuels* 25:2405–2415.

Yee, T. F., and Grossmann, I. E. 1990. Simultaneous Optimization Models for Heat Integration - II. Heat Exchanger Network Synthesis. *Computers & Chemical Engineering* 14(10):1165–1184.

Yee, T. F.; Grossmann, I. E.; and Kravanja, Z. 1990a. Simultaneous Optimizaiton Models for Heat Integration - I. Area and Energy Targeting and Modeling of Multi-Stream Exchangers. *Computers & Chemical Engineering* 14(10):1151–1164.

Yee, T. F.; Grossmann, I. E.; and Kravanja, Z. 1990b. Simultaneous Optimization Models for Heat Integration - III. Process and Heat Exchanger Network Optimization. *Computers & Chemical Engineering* 14(11):1185–1200.

Yeomans, H., and Grossmann, I. E. 2000a. Disjunctive Programming Models for the Optimal Design of Distillation Columns and Separation Sequences. *Industrial & Engineering Chemistry Research* 39(6):1637–1648.

Yeomans, H., and Grossmann, I. E. 2000b. Disjunctive Programming Models for the Optimal Design of Distillation Columns and Separation Sequences. *Industrial & Engineering Chemistry Research* 39(6):1637–1648.

Yeomans, H., and Grossmann, I. E. 2000c. Optimal Design of Complex Distillation Columns Using Rigorous Tray-by-Tray Disjunctive Programming Models. *Industrial & Engineering Chemistry Research* 39(11):4326–4335.

Zanganeh, K. E.; Shafeen, A.; and Salvador, C. 2009. *CO_2 Capture and Developement of an Advanced Pilot-Scale Cryogenic Separation and Compression Unit*. volume 1 of *Energy Procedia*, 247–252. Elsevier.

Zebian, H.; Rossi, N.; Gazzino, M.; Cumbo, D.; and Mitsos, A. 2013. Optimal design and operation of pressurized oxy-coal combustion with a direct contact separation column. *Energy* 49:268–278.

Zebian, H.; Gazzino, M.; and Mitsos, A. 2012. Multi-variable optimization of pressurized oxy-coal combustion. *Energy* 38(1):37–57.

Zhang, Y., and Sahinidis, N. V. 2015. Global optimization of mathematical programs with complementarity constraints and application to clean energy deployment. *Optimization Letters* 1–16.

Zhu, Y.; Legg, S.; and Laird, C. D. 2010. Optimal design of cryogenic air separation columns under uncertainty. *Computers & Chemical Engineering* 34(9):1377–1384.

Zhu, Y.; Legg, S.; and Laird, C. D. 2011. Optimal operation of cryogenic air separation systems with demand uncertainty and contractual obligations. *Chemical Engineering Science* 66(5):953–963.

Appendix A

$f'(Z) = 0$ as the boundary between the single and three root regions

Using similar graphical arguments as Kamath, Biegler, and Grossmann (2010), we present a conjecture that the curve $f'(Z) = 0$ corresponds with the boundary between the one and three root regions. In the interior of the three root region, there are three distinct roots for Z, as shown in Figure A.1(a), and $f'(Z) \geq 0$ for the liquid and vapor roots. As mixture temperature, pressure and/or composition changes, the curve for $f(Z)$ shifts and the liquid and middle or vapor and middle roots move closer. At the boundary of the three root region, either the liquid or vapor root coincides with the middle root, as shown in Figure A.1(b). These double roots have no imaginary components. As evident from the cartoon, $f'(Z) = 0$ for the coinciding roots at this transition point. If the mixture properties are further perturbed, these roots become complex and there is only one real root, as shown in Figure A.1(c). Thus, if the transition between three and one reals roots for (2.26) is smooth, then $f'(Z) = 0$ at the boundary between these regions.

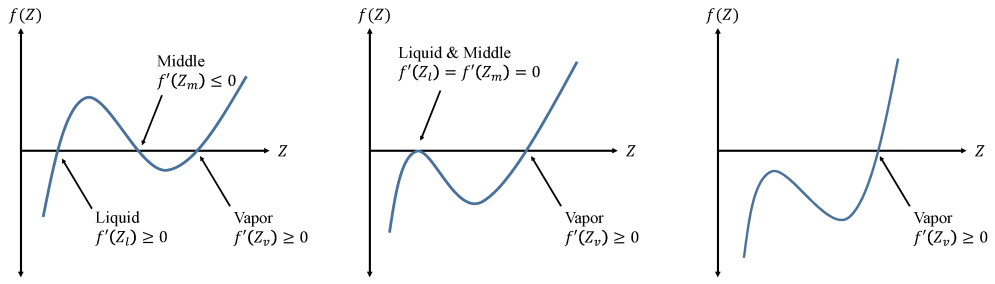

(a) Inside the three root region (b) Boundary between the regions (c) Insider the single root region

Figure A.1: Cartoon of $f(Z)$ and the location of its root(s)

This conjecture has been empirically verified by calculating all of the real

roots for (2.26) at a variety of temperatures and pressures using an analytic procedure (Adewumi, 2014). Plotting the number of real roots matches the results shown in Figure 2.1. The shape of the curve $f'(Z) = 0$ is also consistent with the three root region shown in Figure 8-17 of Reid, Prausnitz, and Poling (1987). Furthermore, Poling, Grens, and Prausnitz (1981) notes $f'(Z)$ goes to zero as a mixture transitions from the three-root to one-root region.

Appendix B

Nomenclature

Set	Description
$\mathcal{C}$	Components (for a specific flowsheet zone)
$\mathcal{C}_{All}$	All components in a system
$\mathcal{D}$	Distillation trays
$\mathcal{D}^{E}$	Distillation tray-cascade mapping
$\mathcal{D}_{b}^{L}$	Bypass liquid stream-tray mapping
$\mathcal{D}_{b}^{V}$	Bypass vapor stream-tray mapping
$\mathcal{D}_{e}^{L}$	Equilibrium liquid stream-tray mapping
$\mathcal{D}_{e}^{V}$	Equilibrium vapor stream-tray mapping
$\mathcal{D}_{in}^{L}$	Inlet liquid stream-tray mapping
$\mathcal{D}_{in}^{V}$	Inlet vapor stream-tray mapping
$\mathcal{D}_{out}^{L}$	Outlet liquid stream-tray mapping
$\mathcal{D}_{out}^{V}$	Outlet vapor stream-tray mapping
$\mathcal{E}$	(Edmister) column sections/cascades
$\mathcal{E}_{in}^{L}$	Inlet liquid stream-cascade mapping
$\mathcal{E}_{in}^{V}$	Inlet vapor stream-cascade mapping
$\mathcal{E}_{out}^{L}$	Outlet liquid stream-cascade mapping
$\mathcal{E}_{out}^{V}$	Outlet vapor stream-cascade mapping
$\mathcal{F}$	Flash vessels
$\mathcal{F}$	Set of points in filter (Section 5.5)
$\mathcal{G}$	General equipment
$\mathcal{G}^{PD}$	General equipment with specificied pressure drop
$\mathcal{G}_{cool}$	Cooling units (provide heat to HEN)
$\mathcal{G}_{cool}^{P}$	Pinch candidate stream-cooling heat exchange unit-heat integration zone mapping
$\mathcal{G}_{heat}$	Heating units (provide cold to HEN)
$\mathcal{G}_{heat}^{P}$	Pinch candidate stream-heating heat exchange unit-heat integration zone mapping
$\mathcal{G}_{in}^{1}$	Single inlet stream-general equipment mapping
$\mathcal{G}_{in}^{V}$	Outlet liquid stream-general equipment mapping
$\mathcal{G}_{map}^{sub}$	General (large) heat exchanger unit-subunit (small) mapping
$\mathcal{G}_{out}$	Outlet streams-general equipment mapping
$\mathcal{G}_{out}^{1}$	Single outlet stream-general equipment mapping
$\mathcal{G}_{out}^{V}$	Outlet vapor stream-general equipment mapping
$\mathcal{G}_{zones}^{HI}$	Mapping between heat exchange units and heat integration zones
$\mathcal{N}$	Condensers
$\mathcal{N}^{p}$	Partial condensers
$\mathcal{N}^{t}$	Total condensers
$\mathcal{P}$	Pressure change equipment (compressors and pumps)
$\mathcal{P}^{c}$	Compressors

$\mathcal{P}^p$	Pumps
$\mathcal{P}_{in}$	Inlet streams-pressure changer mapping
$\mathcal{P}^1_{in}$	Single inlet stream-pressure changer mapping
$\mathcal{P}^1_{out}$	Single outlet stream-pressure changer mapping
$\mathcal{P}^L_{out}$	Outlet liquid stream-pressure changer mapping
$\mathcal{P}^V_{out}$	Outlet vapor stream-pressure changer mapping
$\mathcal{R}$	Reboilers
$\mathcal{R}^p$	Partial reboilers
$\mathcal{R}^t$	Total reboilers
$\mathcal{R}_{cand}$	Candidate degenerate equations
$\mathcal{S}$	All streams
$\mathcal{S}^L_{2p}$	Liquid outlet streams of units operating in the two phase region
$\mathcal{S}^V_{2p}$	Vapor outlet streams of units operating in the two phase region
$\mathcal{S}_{bub}$	Streams constraints to be at their bubble point
$\mathcal{S}^L_{bub}$	Liquid outlet streams of units operating at the bubble point
$\mathcal{S}^V_{bub}$	Vapor outlet streams of units operating at the bubble point
$\mathcal{S}_{check}$	Streams for which a bubble or dew point is calculated to prevent nonphysical equilibrium solutions
$\mathcal{S}^H_{Calc}$	Stream for which enthalpy is calculated
$\mathcal{S}^S_{Calc}$	Stream for which entropy is calculated
$\mathcal{S}^\phi_{Calc}$	Stream for which fugacity is calculated
$\mathcal{S}^V_{Calc}$	Stream for which specific volume is calculated
$\mathcal{S}_{CO_2}$	Streams containing CO_2
$\mathcal{S}_{dew}$	Streams constraints to be at their dew point
$\mathcal{S}^L_{dew}$	Liquid outlet streams of units operating at the dew point
$\mathcal{S}^V_{dew}$	Vapor outlet streams of units operating at the dew point
$\mathcal{S}_{feed}$	Flowsheet feed streams
S^{in}_d	Inlet streams for distillation tray d
S^{out}_d	Outlet streams for distillation tray d
$\mathcal{S}_{Liq}$	Liquid streams that may not disappear
$\mathcal{S}^{Flash}_{Liq}$	Liquid streams that may disappear
$\mathcal{S}^L_{shdw}$	Liquid shadow streams
$\mathcal{S}^P$	Pinch candidate stream-heat integration zone mapping
$\mathcal{S}^{map}_{shdw}$	Process stream - vapor shadow stream - liquid shadow stream mapping
$\mathcal{S}_{sup}$	Streams that may be supercritical (in quadrants I or II of Figure 2.2)
$\mathcal{S}_{Vap}$	Liquid streams that may not disappear
$\mathcal{S}^{Flash}_{Vap}$	Vapor streams that may disappear
$\mathcal{S}^V_{shdw}$	Liquid shadow streams
$\mathcal{T}$	Thermodynamic equipment
$\mathcal{T}^*$	Outlet liquid - outlet vapor-thermodynamic equipment mapping defined for (2.57)
$\mathcal{T}^{dew}$	Thermodynamic equipment whose outlet is at its bubble point
$\mathcal{T}^{dew}$	Thermodynamic equipment whose outlet is at its dew point
$\mathcal{T}^{2p}$	Thermodynamic equipment whose outlet is in the two phase region
$\mathcal{V}$	Throttle valves
$\mathcal{X}$	Heat exchangers
$\mathcal{X}^{sub}$	Heat exchanger subunits
$\mathcal{Z}^{HI}$	Heat integration zones

Variable	Description	Units
$a_{s,c}$	Component specific cubic EoS variable	
a^m_s	a for mixture	
a^{DI}_s	Intermediate used in (2.53)	
A	Coefficient in THM (Chapter 5)	

A_{dh}	Jacobian of active constraints analyzed by *Degeneracy Hunter*	
A_s	Dimensionless version of a	
$\bar{A}_s$	A_s at the critical point	
$A^1_{e,c}$	Absorption coefficient for component c at the top of cascade e	
$A^E_{e,c}$	Average absorption coefficient for component c in cascade e	
A^L	KKT multiplier for $L \geq 0$	
$A^N_{e,c}$	Absorption coefficient for component c at the bottom of cascade e	
A^V	KKT multiplier for $V \geq 0$	
b_c	Component specific cubic EoS constant	
b^m_s	b for mixture	
b^{DI}_s	Intermediate used in (2.53)	
B	Coefficient in THM (Chapter 5)	
B_i	Backpressure at the end of stage i (Chapter 5)	
B^D_i	Design point backpressure at the end of stage i (Chapter 5)	
B_s	Dimensionless version of b	
$\bar{B}_s$	B at the critical point	
C_p	Constant pressure heat capacity	
C_v	Constant volume heat capacity	
$d(\cdot)$	Original detailed model	
E^{cmpr}	Compression energy (ASU case study)	
F_s	Total molar flowrate in stream s	mol/time
$f_{s,c}$	Molar flowrate of component c in stream s	mol/time
f^p_c	Pure component fugacity of component c in phase p	
f°_c	Pure component fugacity of component c at reference state	
f^L_c	Pure component fugacity of component c in liquid phase	
f^R_k	Reduced model for function f at iteration k (Section 5.5)	
f^V_c	Pure component fugacity of component c in vapor phase	
f_L	Function for steam properties in liquid region	
f_{VS}	Function for steam properties in vapor + supercritical region	
g^R_k	Reduced model for function g at iteration k (Section 5.5)	
G	Total Gibbs free energy	kJ/mol
G^p	Total Gibbs free energy of phase p	
$\bar{G}^p_c$	Partial molar Gibbs free energy for component c in phase p	
H_s	Specific enthalpy of stream s	kJ/mol
Δh^{act}_p	Actual enthalpy change in compressor p	kJ/mol
Δh^{isn}_p	Isentropic enthalpy change for compressor p	kJ/mol
ΔH_{is}	Isentropic enthalpy change in a turbine	
$K_{d,c}$	Phase equilibrium coefficient for dist. tray d and component c	
K_i	Stodola's constant (Chapter 5)	
$K_{g,c}$	Phase equilibrium coefficient for unit g and component c	
$I^A_{e,c}$	Intermediate variable in (4.2)	
$I^S_{e,c}$	Intermediate variable in (4.2)	
l_c	Molar flowrate on component c (liquid phase)	mol/time
L	Liquid flowrate	mol/time
L	Loss coefficient for Willans line intercept (Chapter 5)	
$\mathcal{L}$	Lagrange function	
L^1_e	Liquid flowrate leaving the top tray in cascade e	
m_c	Molar flowrate of component c in feed stream (typically fixed)	mol/time
m_i	Steam mass flowrate into stage i of a steam turbine (Chapter 5)	
M	Steam flowrate in a turbine (Chapter 5)	
M^{max}	Max steam flowrate for a turbine (Chapter 5)	
n	Willans line slope (Chapter 5)	
n_c	Molar flowrate of component c (Section (2.2))	

N_e	Number of stages in cascade e	
P_i	Steam pressure into stage i of a steam turbine (Chapter 5)	
P_i^D	Design point steam pressure into stage i of a turbine (Chapter 5)	
P_s	Pressure of stream s	bar
$\bar{P}_s$	Supercritical pressure of stream s	bar
$\bar{P}_s$	Trust region center for stream s (Section 5.5)	bar
$\tilde{P}_s$	Pressure of shadow stream s	bar
P^{in}	Pressure of turbine inlet stream	
P^u	Uncontrolled steam extraction pressure	
$\bar{P}^u$	Uncontrolled steam extraction pressure (design point)	
P^{out}	Outlet pressure of steam turbine	
$\bar{P}^{out}$	Outlet pressure of steam turbine	
P_s^{vap}	Vapor pressure of stream s	bar
ΔP_e	Pressure drop per tray in cascade e	bar
ΔP_p	Change in pressure in pressure changer p	bar
$Q_{s,z}^{Ac}$	Cold exchanged above the temperature of stream s in zone z	
$q_{s,g,z}^{Ac}$	Contribution of unit g to $Q_{s,z}^{Ac}$	kJ/time
$Q_{s,z}^{Ah}$	Heat exchanged above the temperature of stream s in zone z	
$q_{s,g,z}^{Ah}$	Contribution of unit g to $Q_{s,z}^{Ah}$	kJ/time
Q_g^{in}	Heat required by unit g	kJ/time
Q_g^{out}	Heat supplied by unit g	kJ/time
Q^s	Total hot utility demand	kJ/time
$\bar{Q}_z^s$	Hot utility demand for zone z	kJ/time
Q_{stage}	Heat removed from turbine stage (Chapter 5)	
Q^w	Cold cold utility demand	kJ/time
Q_1^w	Cold utility demand for zone 1	kJ/time
Q_2^w	Cold water utility for zone 2	kJ/time
$\bar{Q}_z^s$	Cold utility demand for zone z	kJ/time
$r(\cdot)$	Reduced (e.g., surrogate) model	
R_x	Fraction reaction for an ideal turbine stage (Chapter 5)	
s	Sigmoidal function output (Chapter 5)	
s_k	Proposed step for trust region iteration k	
S^s	Entropy for stream s	J/(mole-K)
$S_{e,c}^1$	Stripping coefficient for component c at the top of cascade e	
$S_{e,c}^E$	Average stripping coefficient for component c in cascade e	
$S_{e,c}^N$	Stripping coefficient for component c at the bottom of cascade e	
T_s	Temperature for stream s	K
$\tilde{T}_s$	Temperature of shadow stream s	
$\bar{T}_s$	Critical point temperature for stream s	
$\bar{T}_s$	Trust region center for stream s (Section 5.5)	
ΔT_p	Change in temperature in pressure changer p	K
T_s^{bub}	Bubble point temperature for stream s	
T_s^{dew}	Bubble point temperature for stream s	
T_g^{in}	Inlet temperature for heat exchange unit g	
T_g^{out}	Outlet temperature for heat exchange unit g	
T_s^{sat}	Saturation temperature of water stream s	
T_{in}^{sat}	Saturations temperature of steam into a turbine (Chapter 5)	
ΔT^{sat}	Difference in saturation temperature for turbine inlet and outlets	
v	Steam velocity (Chapter 5)	
v	Normal step computed in (5.63)	
V_c	Component specific volume of the fluid (optionally fixed)	m^3/kmol
v_c	Molar flowrate of component c (vapor phase)	mol/s
V	Vapor flowrate	mol/time

V^{in}	Vapor flow rate of fluid entering the unit	mol/time
V^{out}	Vapor flow rate of fluid leaving the unit	mol/time
V_e^N	Vapor flowrate leaving the bottom tray in cascade e	
V_i	Steam specific volume into stage i of a steam turbine (Chapter 5)	
w	Blade velocity in a steam turbine (Chapter 5)	
W	Work from a turbine (Chapter 5)	
W^{loss}	Linear intercept in Willans line (Chapter 5)	
W^{max}	Maximum work from a turbine (Chapter 5)	
W^{pump}	Work for a pump (steam cycle, Chapter 5)	
W^{total}	Work removed from steam in turbine (Chapter 5)	
W_p	Work required for pressure changer p	kJ/time
W_{stage}	Work from a single turbine stage (Chapter 5)	
x_c	Component mole fraction of the fluid (or specifically liquid phase)	
$\hat{x}_c$	Log-transform of x_c	
$\tilde{x}_c$	Component mole fraction of liquid shadow stream	
y_c	Component mole fraction of the vapor phase	
$\hat{y}_c$	Log-transform of y_c	
$\tilde{y}_c$	Component mole fraction for vapor shadow stream	
y_c^{out}	Vapor phase mole fraction for component c for a compressor outlet	
y_c^{shdw}	Vapor phase mole fraction for component c for a compressor shadow stream	
Z	compressibility factor	
Z_L	compressibility factor for liquid	
Z_V	compressibility factor for vapor	
$\bar{Z}$	Compressibility factor at the critical point	
$\mathbf{z}$	Mixture composition for tangent plane criteria	
$\tilde{\mathbf{z}}$	Trial composition for tangent plane criteria	

Variable	**Description**	**Units**
$\hat{\alpha}_{s,c}$	Nonlinear function for cubic EoS model, (2.28b)	
$\bar{\alpha}_g$	Pressure drop coefficient for unit g	
$\tilde{\alpha}$	Coefficient in alternate Willans line formula (5.32)	
$\underline{\alpha}$	"Slope" in sigmoidal function (Chapter 5)	
α_c^L	KKT multiplier for component c in liquid stream, (2.2c)	
α_c^V	KKT multiplier for component c in vapor stream, (2.2c)	
β	Slack variable for equilibrium calculations	
$\hat{\beta}$	Log-transformed version of β	
$\bar{\beta}_g$	Pressure drop coefficient for unit g	
$\tilde{\beta}$	Coefficient in alternate Willans line formula (5.32)	
$\underline{\beta}$	Coefficients in (5.55)	
γ_c	Slack variable for component c in equilibrium calculations	
δ_k	L1 norm of slacks for reduce model outputs (Section 5.5)	
Δ_k	Trust region radius for iteration k (Section 5.5)	
$\delta_{s,c}$	Intermediate variable for cubic EoS	
δT_g	Temperature change in large heat exchange unit g	K
ε^s	Small number used in the smoothed max operation	
ε_d, ε_n	Bypass efficiency for tray d (or n)	
ζ	Surrogate objective function for Gibbs free energy minimization	
η_{ideal}	Ideal stage efficiency (Chapter 5)	
η_{is}^{max}	Isentropic efficiency for a turbine at max load (Chapter 5)	
θ_k	Maximum derivation between ODM and RM outputs at iteration k	
Θ_g	Flowrate times heat capacity for unit g	
λ	Adjoint vector in *Degeneracy Hunter*	
λ_c	KKT multipliers for (2.2b)	

μ_c^p	Chemical potential of component c is phase p	
μ_c°	Chemical potential of component c at reference state	
μ_i	Chemical potential of component i (Section 2.5.5)	
ξ_s	Slack variable for supercritical phase relaxation	
$\pi_{s,c}$	Slack variable for bubble and dew point calculations	
ρ_k	Ration of actual and predicted reductions (Section 5.5)	
σ^L	Slack variable for vanishing liquid streams	
σ^P	Slack variable for detection of quad. I and II	
σ^V	Slack variable for vanishing vapor streams	
σ^{2a}, σ^{2b}	Slack variables for detection of quad. II	
$\sigma^{c1}_{s,g,z}$, $\sigma^{c2}_{s,g,z}$,	Slack variables in (3.15)	
$\sigma^{h1}_{s,g,z}$, $\sigma^{h2}_{s,g,z}$,	Slack variables in (3.16)	
ρ	Complementarity penalty (large number)	
$\tau_{s,z}$	Temperature for pinch candidate stream s in zone z	K
$\phi_{s,c}$	Fugacity of component c in stream s	
$\phi^L_{s,c}$	Fugacity of component c in liquid stream s	
$\phi^V_{s,c}$	Fugacity of component c in vapor stream s	
ϕ_i	Flow coefficient in turbine stage i (Chapter 5)	
ϕ^D_i	Design point flow coefficient in turbine stage i (Chapter 5)	
$\varphi^A_{e,c}$	Absorption factor for component c in cascade e	
$\varphi^S_{e,c}$	Stripping factor for component c in cascade e	
$\tilde{\varphi}^L_{s,c}$	Fugacity of component c in liquid shadow stream s	
$\tilde{\varphi}^V_{s,c}$	Fugacity of component c in vapor shadow stream s	
χ	Vector of variables for in trust region problems (Section 5.5)	
ψ	Obj. function for Gibbs tangent plane test (Section 2.5.5)	
ψ	Combined obj. func. and constraints (Section 5.5)	
ψ	Obj. function in initialization step (Chapter 6)	
ψ^R	Combined obj. func. and constraints for reduced models (Section 5.5)	
Ω_s	Slack variable for quadrant II detection (Section 2.5.4.2)	

Constant/ Parameter	Description	Value
α	Temperature bump (Chapter 3)	0.1 - 0.2 K
γ	Polytropic index	1.4
γ_θ	Constant in filter condition (5.66)	
γ_f	Constant in filter condition (5.66)	
γ_s	Exponent in switching condition (5.67)	
η_{pump}	Pump efficiency	0.736
η_{motor}	Motor (pump) efficiency	1
η^{isn}_{cmpr}	Isentropic efficiency of a compressor	0.82
η_{is}	Isentropic efficiency (turbine section/stage group)	
η^{mech}_{cmpr}	Mechanical efficiency of a compressor	0.97
η_{mech}	Mechanical efficiency (turbine section/stage group)	
ϵ	A small number	10^{-3} to 10^{-6} (typical)
ε^p	Small number in (5.38)	
ε^{stm}	Small number for backup away from the saturation curve	
κ_θ	Constant in switching condition (5.67)	
ρ	Weight for complementarity penalty in obj. func.	10^0 to 10^3 (typical)
ω_i	Cubic EoS specific acentric factor for species i	
$\underline{a}$	Cubic EoS specific constant	
a^{total}	Fitted coefficient for (5.30)	
$\mathcal{A}^a_c - \mathcal{A}^c_c$	Antoine eqn coefficients for component c	
$\bar{A}$	A for mixture at its critical point	Table 2.2

a_1 - b_2	Coefficients for THM	
a_1^c - b_2^c	Coefficients for CTHM	
$\hat{a}c_1$ - $\hat{b}_2$	Alternate THM coefficients	
$\underline{b}$	Cubic EoS specific constant	
b^{total}	Fitted coefficient for (5.30)	
$\bar{B}$	B for mixture at its critical point	Table 2.2
C_c^I - C_c^V	Specific heat polynomial coefficients	
$\tilde{f}$	Target component flowrates (Chapter 6)	
i	Counter in Chapter 6	
$k_{i,j}$	Cubic EoS specific binary interaction parameters for species i and j	
M	large positive multiplier for big M relaxation	10
n^H	Number of cooling units (hot streams in HENS literature)	
n^H	Number of heating units (cold streams in HENS literature)	
n	Counter in Chapter 6	
N_c	Number of components	
N^{sub}	Number of subunits for heat exchanger unit decomposition	
N^+	Number of inactive trays (used in Section 4.4.2)	
$\bar{p}_c$	Pure component critical pressure for species c	
$\tilde{P}$	Target stream pressures (Chapter 6)	
R	Ideal gas constant	
$\bar{t}_c$	Pure component critical temperature for species c	
$\tilde{T}$	Target stream temperatures (Chapter 6)	
T^{crit}	Critical point of water	
T^{crit}	Critical point of water	
$T_z^{utility}$	Temperature of utility cooling in zone z	
$\Delta\underline{T}_z$	Minimum temperature difference for heat integration in zone z	
$\Delta T^{utility}$	Minimum temperature difference between streams and utility temperature	
$\bar{t}_i$	Pure component critical temperature for species i	
u	Cubic EoS specific constant	
w	Cubic EoS specific constant	
$\tilde{x}$	Target stream compositions (Chapter 6)	